UNIVERSIDADE FEDERAL DE MINAS GERAIS
Instituto de Ciências Exatas
Programa de Pós-Graduação em Física

Frederico Barros de Sousa

A BROAD OPTICAL CHARACTERIZATION OF DEFECTS AND MANY-BODY EFFECTS IN TWO-DIMENSIONAL TRANSITION METAL DICHALCOGENIDES

Belo Horizonte

2024

Frederico Barros de Sousa

A BROAD OPTICAL CHARACTERIZATION OF DEFECTS AND MANY-BODY EFFECTS IN TWO-DIMENSIONAL TRANSITION METAL DICHALCOGENIDES

Thesis presented to the Post-Graduation Program in Physics of the Intitute of Exact Sciences of the Federal University of Minas Gerais as a partial requirement to obtain the title of Doctor of Science.

Supervisor: Leandro Malard Moreira

Belo Horizonte
2024

Dados Internacionais de Catalogação na Publicação (CIP)

S725b Sousa, Frederico Barros de.
A broad optical characterization of defects and many-body effects in two-dimensional transition metal dichalcogenides / Frederico Barros de Sousa. – 2024.
240 f. : il.

Orientador: Leandro Malard Moreira.
Tese (doutorado) – Universidade Federal de Minas Gerais, Departamento de Física.
Bibliografia: f. 176 -217.

1. Semicondutores magnéticos diluídos. 2. Óptica. I. Título. II. Moreira, Leandro Malard. III. Universidade Federal de Minas Gerais, Departamento de Física.

CDU – 535 (043)

Ficha catalográfica elaborada por Romário Martins Ribeiro – CRB6 3595
Biblioteca Professor Manoel Lopes de Siqueira – Departamento de Física - UFMG

UNIVERSIDADE FEDERAL DE MINAS GERAIS
INSTITUTO DE CIÊNCIAS EXATAS
PROGRAMA DE PÓS-GRADUAÇÃO EM FÍSICA

FOLHA DE APROVAÇÃO

A presente tese, intitulada **"A Broad Optical Characterization of Defects and Many-Body Effects in Two-Dimensional Transition Metal Dichalcogenides''** de autoria de **FREDERICO BARROS DE SOUSA** submetida à Comissão Examinadora, abaixo-assinada, foi aprovada para obtenção do grau de **DOUTOR EM CIÊNCIAS**, em primeiro de março de 2024.

Belo Horizonte, 01 de março de 2024.

Prof. Leandro Malard Moreira
Orientador do estudante
Departamento de Física/UFMG

Prof. Marcio Daldin Teodoro
Departamento de Física/ UFSCAR

Profa. Ana Maria de Paula
Departamento de Física/UFMG

Prof. Victor Carozo Gois de Oliveira
Departamento de Física/PUC-Rio

Prof. Mário Sérgio de Carvalho Mazzoni
Departamento de Física/UFMG

Documento assinado eletronicamente por **Victor Carôzo Gois de Oliveira**, **Usuário Externo**, em 04/03/2024, às 11:38, conforme horário oficial de Brasília, com fundamento no art. 5º do Decreto nº 10.543, de 13 de novembro de 2020.

Documento assinado eletronicamente por **Ana Maria de Paula**, **Professora do Magistério Superior**, em 04/03/2024, às 13:13, conforme horário oficial de Brasília, com fundamento no art. 5º do Decreto nº 10.543, de 13 de novembro de 2020.

Documento assinado eletronicamente por **Mario Sergio de Carvalho Mazzoni**, **Membro**, em 08/03/2024, às 10:44, conforme horário oficial de Brasília, com fundamento no art. 5º do Decreto nº 10.543, de 13 de novembro de 2020.

Documento assinado eletronicamente por **Leandro Malard Moreira**, **Professor do Magistério Superior**, em 11/03/2024, às 13:02, conforme horário oficial de Brasília, com fundamento no art. 5º do Decreto nº 10.543, de 13 de novembro de 2020.

Documento assinado eletronicamente por **Marcio Daldin Teodoro**, **Usuário Externo**, em 12/03/2024, às 15:41, conforme horário oficial de Brasília, com fundamento no art. 5º do Decreto nº 10.543, de 13 de novembro de 2020.

A autenticidade deste documento pode ser conferida no site https://sei.ufmg.br/sei/controlador_externo.php?acao=documento_conferir&id_orgao_acesso_externo=0, informando o código verificador **3075555** e o código CRC **C810749F**.

ACKNOWLEDGMENTS

Ao Leandro Malard (*aka* Xubaka), por ter sido meu mentor, orientador, colaborador e parceiro ao longo desses anos todos. Ser aluno do Xubaka me proporcionou a segurança de ter um orientador presente e capaz de resolver qualquer problema experimental. Além disso, o Xubaka esteve sempre disposto a ouvir, discutir e incentivar minhas ideias. Por fim, a liberdade que vivenciei trabalhando com o Xubaka foi extremamente importante para desenvolver minhas habilidades e ganhar confiança para liderar projetos futuramente. Levando em conta também a personalidade tranquila e descontraída do Xubaka, eu não poderia pedir um orientador melhor!

Aos meus pais Ricardo e Edésia, por nunca terem deixado faltar amor e carinho na minha criação e por terem me proporcionado as melhores oportunidades em todas as fases da minha vida. Além de ter pais presentes que me apoiam incondicionalmente, eu também tenho o privilégio de ter nos meus pais as minhas maiores referências pessoais e profissionais. E com certeza meu doutorado se tornou bem mais fácil tendo um notável professor e uma renomada cientista dentro de casa.

A todos meus professores ao longo da minha vida, e especialmente aos que cito a seguir. Ao Ron, meu primeiro orientador de IC, por todos os ensinamentos e por ajudar a moldar meu pensamento científico. Ao Gustavo Azevedo, pela intensa e prazerosa convivência que tivemos. Ao Bira, por toda orientação no meu estágio docente. Ao Ado e Gusta, por serem referências sempre acessíveis no laboratório. Ao Waldemar, pelos conselhos e por me ajudar em certas oportunidades.

Aos meus colegas de laboratório, pela convivência leve e por estarem sempre dispostos a ajudar. Em particular, ao Lucão, por sempre estar disposto a me ensinar e ajudar com o alinhamento óptico dos experimentos. À Bárbara, pelos importantes ensinamentos sobre propriedades ópticas de semicondutores 2D quando eu estava entrando nessa área. À Katherine e ao Filó, por também terem me ajudado muito com alinhamento óptico quando entrei no laboratório. Ao Renan, Danilo, Ana Clara, Menescal, Will, Andreij, Rafael, Luquinhas, Diego, Douglas, Vitor, Matheus, Tiagão, Paula e Márcia, pela amizade, discussões e ajudas.

Aos colaboradores nacionais. Especificamente, ao Ado e Rafael do Laboratório de Nano-Espectroscopia da UFMG. Ao Leo Campos, Fábio Offredi, Lucas Liberal, Gabriel Bargas e Felipe Murta do Laboratório de Nanomateriais da UFMG. Ao Marcos Pimenta e Geovani Resende do Laboratório de Espectroscopia Raman da UFMG. Ao Bernardo, Ana Paula e Joyce do Laboratório de Nanoscopia da UFMG. Ao Chacham e ao Matheus, pelos cálculos e por tirar todas as dúvidas teóricas. À Ive Silvestre e ao Rafael Martins da UFOP. Ao Benjamin e ao seu grupo da UFJF. Ao Pedro Lana do CDTN. Ao Bruno da UFRN.

Ao Alisson Cadore do LNNano. Finalmente, ao Marcio Daldin e seus alunos Alessandra Ames, Vinicius e Gabriel pela frutífera colaboração e por gentilmente me receberem em seu laboratório na UFSCar em duas oportunidades para realizar experimentos.

To the international collaborators. Firstly, to Prof. Achim Hartschuh from the Ludwig Maximilian University of Munich. Beyond our collaboration, I am very grateful to have had the opportunity to spend 2 months in Munich learning about time-resolved experiments in Achim's group. I would also like to thank Hari, Alex, Konrad, Veit, Lucas and Sean that kindly received me in Munich. To the Penn State University collaborators. In particular, to Prof. Mauricio Terrores and his students and to Prof. Vincent Crespi and Boyang Zheng. To Prof. Prasana Sahoo from the Indian Institute of Technology Kharagpur. To Prof. Ermin Malic from the Philipps University of Marburg. And to Prof. Stephan Reitzenstein from TU Berlin.

A todos aqueles que ajudaram a tornar meus dias mais leves e felizes. Em especial, à Luiza, por todo seu amor, carinho, companheirismo e compreensão. Sua companhia para celebrar os momentos bons e para me fazer enxergar que os momentos ruins sempre podem ser superados me deu muita força ao longo desses anos. A toda minha família. Em particular, às minhas avós Conceição e Elza, por estarem sempre presentes e serem um abrigo de aconchego e ao meu irmão Gabriel, pela amizade e por eu sempre poder contar com ele. Aos meus amigos das antigas, Justin, Natan, Igor, Leo, Melão, Zoi e Netão, com quem posso viver meu lado mais moleque. Aos meus amigos da graduação, Filipe, Guilherme, Zé, Breno e Bernardo, com quem compartilho desde o início essa caminhada na física. Ao Time de Futsal da UFMG, pelas resenhas e viagens.

Ao CNPq, CAPES, FAPEMIG, INCT de Nanomateriais de Carbono e Rede 2D pelo apoio financeiro. À UFMG, ao Departamento de Física e ao LCPNano pela infraestrutura. Aos funcionários da limpeza, da secretaria e da biblioteca, e aos técnicos do LCPNano e da Criogenia.

Meu muito obrigado a todos vocês!

RESUMO

Dicalcogenetos de metais de transição (do inglês, TMDs) bidimensionais (2D) são semicondutores da família dos materiais de van der Waals com um grande potencial para serem aplicados na próxima geração de dispositivos ultrafinos devido às suas notáveis propriedades. Entre estas propriedades, eles demonstram respostas ópticas singulares por conta de suas fortes interações de muitos corpos, emissão de luz circularmente polarizada com seletividade de vales e efeitos não lineares. No entanto, essas propriedades podem ser dramaticamente afetadas pelo surgimento de defeitos nesses materiais. Por conta disto, existe uma grande preocupação em caracterizar diferentes defeitos que comumente aparecem em TMDs 2D e também em desenvolver métodos para intencionalmente inserir novos defeitos a fim de modificar ou gerar novas propriedades nesses materiais. Por exemplo, a introdução de metais de transição spin polarizados como defeitos substitucionais pode induzir um ordenamento ferromagnético à temperatura ambiente em TMDs, que é o caso das monocamadas de WS_2 e WSe_2 dopadas com vanádio. Desse modo, é fundamental a caracterização de como o vanádio afeta as propriedades ópticas desses materiais assim como é de grande interesse o estudo de como suas propriedades ópticas e magnéticas se acoplam. Além disso, apesar de defeitos que surgem não intencionalmente em TMDs 2D terem sido profundamente investigados nos últimos anos, os estudos de suas respostas nano-ópticas ainda são escassos, o que deve ser superado com o uso de técnicas ópticas de campo próximo. Finalmente, em relação às interações de muitos corpos, enquanto fenômenos excitônicos são bem estudados, estados de alta densidade de portadores de cargas — que é o caso do plasma de elétrons e buracos — ainda carecem de mais investigação. Nessa tese nós realizamos uma ampla caracterização de TMDs 2D e suas heteroestruturas focando nesses pontos mencionados acima. Mais especificamente, nós realizamos medidas ópticas e magneto-ópticas para estudar monocamadas dopadas de TMDs, utilizamos técnicas espectroscópicas amplificadas por sonda para investigar aspectos nanométricos de defeitos em monocamadas de MoS_2 e empregamos óptica não linear para provar TMDs 2D e suas heteroestruturas em regimes de altas excitações. Nosso trabalho fornece importantes contribuições para um melhor entendimento sobre estados de defeito e de altas densidades de carga em TMDs 2D, assim como ressalta as funcionalidades desses materiais.

Palavras-chave: Materiais 2D, TMDs, semicondutores magnéticos diluídos, excíton, plasma de elétrons e buracos, óptica, óptica não linear, magneto-óptica, óptica de campo próximo.

ABSTRACT

Two-dimensional (2D) transition metal dichalcogenides (TMDs) are semiconducting van der Waals materials with a great potential for the next generation of ultrathin devices due to their singular properties. Among these properties, remarkable optical responses are observed in 2D TMDs due to their strong many-body interactions, circular light emission with valley selectivity and notable nonlinear effects. Nonetheless, these properties can be dramatically affected by the emergence of defects in these materials. Therefore, there is a great concern in characterizing the distinct defects that commonly appear in 2D TMDs as well as in engineering novel defects in TMDs in order to tune or induce novel desirable properties. For instance, the introduction of spin-polarized transition metal atoms as substitutional defects in TMD monolayers can induce a room temperature ferromagnetism on them, which is the case of V-doped WS_2 and WSe_2 monolayers. Hence, there is a fundamental necessity in characterizing the optical modifications caused by the vanadium doping and a great interest in performing magneto-optical experiments to study the coupling between the semiconducting and magnetic properties of these materials. In addition, although unintentionally provoked defects have been deeply studied in 2D TMDs over the past years, the investigation of their nano-optical responses are still very scarce. Thus, near-field optical techniques play a major role to access these nanometric optical features. Finally, regarding the many-body interactions in 2D TMDs, while their excitonic effects are well-studied, a higher charge carrier density state consisted in an ionized electron-hole plasma still lacks investigation. Here in this thesis we perform a broadband optical characterization of 2D TMDs and their heterostructures focused on these mentioned opened questions. More specifically, we carried out optical and magneto-optical measurements to study doped TMD monolayers, tip-enhanced optical spectroscopies to investigate nanoscale aspects of defects in MoS_2 monolayers and nonlinear optical techniques to probe 2D TMDs and their heterostructures in higher excitation regimes. Our work provides relevant steps toward the understanding of fundamental aspects of defective and high density states in 2D TMDs as well as shed light in novel functionalities for these materials.

Keywords: 2D materials, TMDs, dilute magnetic semiconductors, exciton, electron-hole plasma, optics, nonlinear optics, magneto-optics, near-field optics.

LIST OF FIGURES

LIST OF ACRONYMS

1L	Monolayer
2D	Two-Dimensional
2L	Bilayer
3L	Trilayer
AFM	Atomic Force Microscopy
APD	Avalanche Photodiode
CBM	Conduction Band Minimum
CCD	Charge-Coupled Device
CVD	Chemical Vapor Deposition
CVT	Chemical Vapor Transport
CW	Continuous-Wave
DCP	Degree of Circular Polarization
DFT	Density Functional Theory
DMS	Dilute Magnetic Semiconductor
DT	Direct Transition
EHL	Electron-Hole Liquid
EHP	Electron-Hole Plasma
FF	Far-Field
FWHM	Full Width at Half Maximum
FWM	Four-Wave Mixing
HAADF	High-Angular Annular Dark Field
H-BN	Hexagonal Boron Nitride
IRF	Instrument Response Function

IT	Indirect Transition
LH	Lateral Heterostructure
NA	Numerical Aperture
NF	Near-Field
OPO	Optical Parametric Oscillator
PL	Photoluminescence
PMT	Photomultiplier Tube
REP	Raman Excitation Profile
SHG	Second-Harmonic Generation
SOC	Spin-Orbit Coupling
SPM	Scanning Probe Microscopy
STEM	Scanning Transmission Electron Microscopy
TEPL	Tip-Enhanced Photoluminescence
TERS	Tip-Enhanced Raman Spectroscopy
TMD	Transition Metal Dichalcogenide
TRPL	Time-Resolved Photoluminescence
VBM	Valence Band Maximum

CONTENTS

1 Introduction

When a crystal structure has one of its dimensions reduced, novel physical phenomena can emerge due to restrictions on its degrees of freedom and quantum confinement. For example, two-dimensional (2D) materials are atomic-thick materials where the in-plane bonds are stronger than the out-of-plane bonds, making them feasible to be vertically thinned from bulk (3D) materials. Therefore, the confinement of the electrons in two dimensions leads to modifications of the physical properties of these materials compared to its bulk counterparts.

The first 2D material to have a monolayer isolated and characterized was graphene, in 2004 (1). This atomically thin sheet of carbon is obtained from graphite, that is the graphene bulk structure with strong covalent in-plane bonds. On the other hand, the layers of graphite are weakly bonded by van der Waals forces, making graphene easy to be isolated by a simple mechanical exfoliation technique, also known as a micromechanical cleavage technique (1). The great interest behind this 2D material is due to its surprisingly electronic structure (2). Graphene is a semimetal due to the touching of the valence and conduction bands at K and $-$K points in the first Brillouin zone. The Dirac cone format of the band structure at K and $-$K valleys has a linear energy dispersion near these points. These and other features grant to graphene, for example, properties as high carrier mobility (3, 4), high mechanical strength (5), ambipolar field effect (6), and quantum Hall effect at room temperature (7).

With the discovery and characterization of graphene, there was a natural raise of interest in new 2D materials (8). Materials with van der Waals out-of-plane interactions were among the most searched ones due to the facility in their exfoliation down to a monolayer. The hexagonal Boron Nitride (h-BN) is one example of another layered material that has shown promising insulator properties when thinned to a single layer (9). Moreover, the transition metal dichalcogenide (TMD) family of van der Waals materials attracted a great attention of scientific researches due to their novel and surprising properties when they are isolated from bulk to a monolayer. For example, TMD monolayers are direct band gap semiconductors (10, 11), whereas in TMD bulk structures is observed an indirect band gap. Furthermore, TMD monolayers also exhibit a circularly polarized light with valley selectivity (12, 13, 14), strong many-body interactions (15, 16, 17, 18) and substantial nonlinear responses (19, 20, 21), making them a promising material for applications in optoelectronic devices and physical phenomena studies.

Regarding the many-body effects, 2D TMDs present the formation of excitons, i.e., bound electron-hole quasiparticles, even above room temperature (22, 23). In contrast to bulk semiconductors (24) and quantum well systems (25), which only display exciton

formation at low temperatures, the reduced dielectric screening in 2D TMDs lead to strong binding energies between their electrons and holes (16). Therefore, the optical responses in 2D TMDs are greatly influenced by their excitonic effects. However, these excitons can be ionized in a plasma of electrons and holes if the material charge carrier density is high enough to promote the screening of their Coulomb interactions (26), which is known as an exciton Mott transition. While excitons in 2D TMDs have been largely studied, the optical properties of the electron-hole plasma in these materials still lack investigations due to the high excitations required to form this ionized state. In particular, the few reports on the electron-hole plasma light emission of 2D TMDs were associated with specific conditions as low temperatures (27) or suspended samples (28). Therefore, to have a deeper understanding of the potential of 2D TMDs for light emitting devices in high excitation regimes is fundamental to find a method to study these states at room temperature and in supported TMD samples.

In addition to the characterization of the mentioned intrinsic properties of 2D TMDs, there are further challenging steps to achieve their application in devices in an industrial scale (29, 30). For instance, although the mechanical exfoliation method provides high-quality samples to be studied, there is no reasonable control in the shape and size of the exfoliated monolayers (31). Therefore, there is a great effort in develop and improve controllable growth techniques to overcome this demand (32, 33). However, these growth techniques are usually related with the emergence of distinct defects that can deeply affect the material optical and electronic properties (34, 35). Hence, the investigation of the induced inhomogeneities in TMD monolayers due to defective states is crucial to accomplish these steps toward their industrial application. Although a great effort has been placed in the optical study of several defects that are commonly reported in TMD monolayers, there is still a concern in further investigations into the nanoscale aspect of the optical modifications caused by defects in these 2D materials, as the conventional optical techniques only provide their μm-scale averaged response.

The same way that defects can affect TMD monolayer properties in an undesirable manner, there is also a relevant interest in the defect engineering of these 2D materials to induce novel desirable properties (34, 35). In that sense, it was theoretically predicted (36, 37, 38, 39) and then experimentally shown (40, 41, 42, 43, 44, 45) that the introduction of spin-polarized metal atoms as substitutional defects in TMD monolayers can induce a room temperature ferromagnetism in these materials, shedding light to their potential as 2D dilute magnetic semiconductors. Nonetheless, some of these recently achieved doped TMD samples still need a broad optical characterization to probe the modifications in their semiconducting properties caused by the magnetic dopants. In addition, magneto-optical investigations are promising to study novel physical phenomena in these materials. Another emerging effort in the TMDs engineering is to reassemble distinct monolayers together in order to tune their properties in 2D heterostructures (46, 47, 48, 49, 32). The

reasonable stability of these new built structures opened a wide range of applicability due to the freedom in "playing" with the electronic and optical properties of different 2D materials by assembling them together. The variety in the choice of materials, number of layers and their relative crystallographic orientation explains their large potential for applications. The great interest in these TMD heterostructures is proportional to their several reported optical studies. However, most of them are focused on the linear optical responses of these samples, which shows the necessity of further investigations into the nonlinear optical effects of TMD heterostructures. Hence, the combination of distinct linear and nonlinear optical techniques plays a significant role for a broad investigation of defective and engineered TMD materials.

In a simplified perspective, we can divide the optical properties of TMD monolayers in their vibrational and electronic aspects. The vibrational features of these 2D materials are mainly investigated by Raman spectroscopy (50), which is capable of providing information about the phonon population through the sample interaction with light and of giving a fingerprint of the material structure. For the electronic properties, while absorption measurements are mostly responsible for the study of the charge carrier excitations (51), photoluminescence (PL) spectroscopy commonly deals with the radiative recombination of these excited electrons (10, 11). However, in a more accurate analysis the vibrational and electronic responses of these TMD monolayers are coupled. Therefore, the excitation energy plays a major role in the Raman scattering process, that can be influenced by single and double electronic resonances (52, 53). Besides, in the time-resolved investigation of the excited electronic states is possible to measure the electron-phonon interactions of the material (54, 55). Nonetheless, to probe nanoscale localized optical responses these confocal optical techniques present a spatial resolution limitation lying in hundreds of nanometers due to the diffraction limit of light. To overcome this limitation, near-field techniques such as tip-enhanced Raman and PL spectroscopies are able to furnish the vibrational and electronic properties of these 2D systems with a nanometric resolution (56, 57, 58, 59). Finally, to study nonlinear effects in TMD monolayers second-harmonic generation (SHG) and four-wave mixing (FWM) measurements are generally employed (60). Beyond the nonlinear susceptibilities, polarized SHG is able to provide the crystallographic orientation of the sample (19, 20, 21), while both SHG and FWM processes can reveal vibrational and electronic resonances of the material (61). With these and other optical techniques it is possible to characterize the role of defects and many-body effects in the intrinsic properties of TMD monolayers as well as to unveil novel physical phenomena induced by them.

This thesis focus in a broad investigation of different defects and high density many-body effects in 2D TMDs by several optical techniques. Thereunto, in Chapter 2 we introduce the TMD monolayer structure and we provide a theoretical description of its many-body and spin-valley coupling effects. Subsequently, in Chapter 3 we discuss about several defects in TMDs, firstly presenting their classification and then focusing in

two specific TMD samples achieved through defect engineering: TMD dilute magnetic semiconductors and TMD heterostructures — in which their interfaces can be viewed as defective regions since they have their properties changed. In Chapter 4, we show how distinct optical techniques can be used to characterize and study novel phenomena associated with defects in 2D TMDs by a thorough review of the major reports in this field. A general theoretical description of each optical technique is also presented. Then, the specific optical setups that we used in the experiments performed for this thesis are showed in Chapter 5.

Chapters 6, 7 and 8 contain the results obtained for this thesis. In Chapter 6 we first present a broadband optical and electronic structure characterization of WS_2 monolayers doped with vanadium. Subsequently, we show our optical and magneto-optical investigations on WSe_2 monolayers doped with vanadium. Finally, we probe aged WS_2 and WSe_2 monolayers with adsorbed defects by magneto-optical measurements. In Chapter 7 we study the nanoscale aspect of several defects such as grain boundaries, strain fields and edges in grown MoS_2 monolayers by tip-enhanced optical techniques. In Chapter 8 we focus on the nonlinear responses of 2D TMDs and their heterostructures. We present a room temperature electron-hole plasma light emission of monolayer and multilayer TMD samples through a sub band gap pulsed excitation. Then, we also used pulsed excitations to generate this electron-hole plasma state in vertical and lateral TMD heterostructures and we studied their light emission in this regime as well. Lastly, we image these TMD lateral heterostructures by second-harmonic generation measurements. In Chapter 9 we discuss about the general conclusions and perspectives of the results presented in this thesis. Appendix A, B and C provide supplementary information for Chapters 6, 7 and 8, respectively.

2 Transition Metal Dichalcogenide Monolayers

The semiconducting transition metal dichalcogenide (TMD) monolayers are of the type MX_2, where M is a transition metal atom from the family VI of the periodic table (such as Mo or W) and X is a chalcogen atom (S, Se or Te). The bulk TMDs are layered van der Waals materials widely used as dry lubricants, in which each monolayer is composed by a layer of M sandwiched between two layers of X (Figure 2.1). TMD monolayers are presented in nature in three distinct crystalline configurations regarding its unit cell: one trigonal prismatic (2H phase) and two octahedral (1T/1T' phases), as shown in Figure 2.2. The crystal structure that will be presented and discussed in this thesis is the 2H phase, since it is the most stable and common one. As shown in Figure 2.2a, for the 2H phase the triangular lattices of M and X layers are arranged in a way that from a top down view they look very similar to graphene honeycomb lattice. It is worth noting that due to a mirror symmetry with respect to the M layer the resulting X-M-X covalent bonds lie down in the plane, making the TMD crystalline lattice even more like graphene.

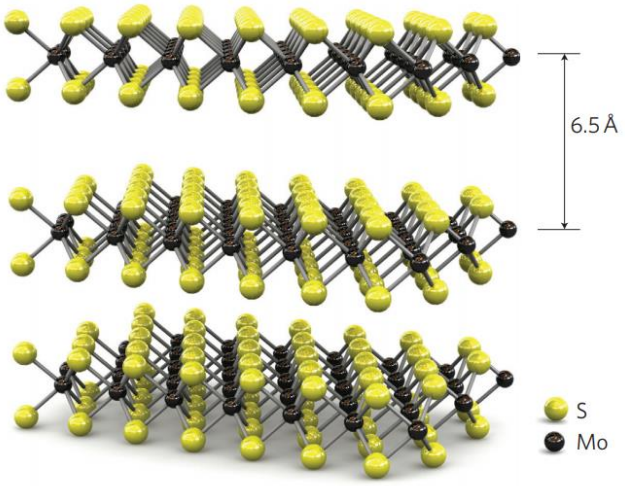

Figure 2.1 – **Crystal structure representation of a TMD.** Lateral view of MoS_2 layers showing their in-plane covalent bonds and their van der Waals out-of-plane weakly interactions. Adapted from: (62)

A TMD monolayer was first isolated by a exfoliation technique in 1986 (64). Despite that, it was only in 2010 that TMD monolayers unveiled an emerging photoluminescence and got a great attention for further studies (10, 11). They were obtained by a micromechanical cleavage method that provides high-quality monolayer samples (65, 66, 31, 67), which is hence a widely used technique for these characterization studies. On the other hand, growth techniques that give large-area monolayer flakes started to be developed given that exfoliation methods do not present a reasonable control in the samples shape and

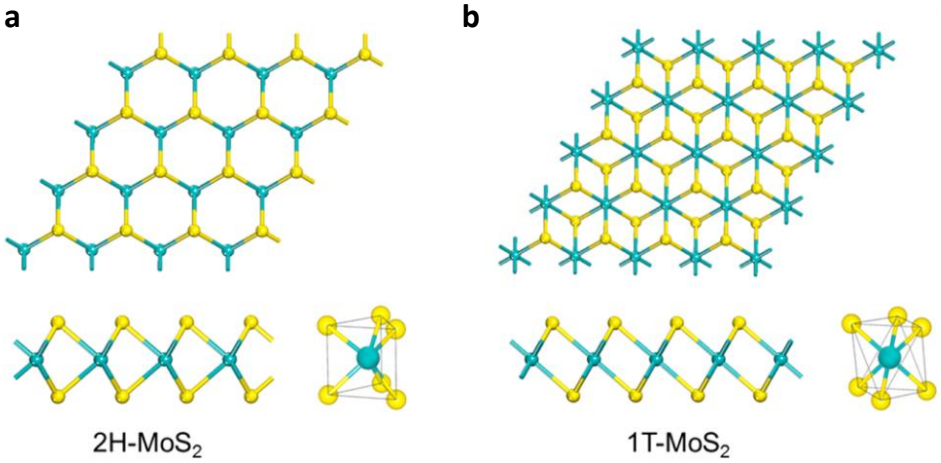

Figure 2.2 – **Top view schematic illustration of distinct TMD crystalline configurations.** (**a**) 2H and (**b**) 1T phases of a MoS_2 monolayer. It is worth to comment that there is also a 1T' phase which is a distorted version of the 1T phase. Adapted from: (63)

size. For instance, chemical vapor deposition (CVD) (68, 69, 70, 71) and molecular beam epitaxy (MBE) (72, 73, 74) are controlled growth techniques that are being extensively used to provide a step toward industrial-scale applications for the TMD monolayers. Meanwhile, it remains challenging to produce defect free samples with an uniform optical emission (34, 35, 30). Conversely, what is observed is that these synthesized samples are influenced by substrate interactions, strain fields, local defects and grain boundaries (70, 71, 75, 76, 77, 78, 79, 80, 34, 81, 82, 83) that are not found in the exfoliated samples. A detailed discussion about defects in TMDs will be presented in Chapter 3.

As the crystal lattice in the direct space of a TMD monolayer is very similar to graphene, it is expected that the reciprocal lattice of both materials would also present similarities. Figure 2.3 shows the in-plane first Brillouin zone of a TMD with the high symmetry points denominated as Γ, K and M points, with K having a degenerated −K point. Nevertheless, TMDs start to be distinguishably different from graphene when we compare their electronic band structures. As commented before, graphene's conduction and valence bands touch each other at K and −K points, making it to behave as a semimetal with a linear dispersion of momentum in energy near the K and −K valleys.

The TMD monolayers, in contrast to graphene, exhibit an energy gap between the conduction and valence bands, making them semiconductors (84, 85). This band gap in TMDs arises due to their broken inversion symmetry, that comes from their distinct atoms in the crystal lattice. The TMD monolayers band gap together with their constrained dimensionality implicate in remarkable many-body effects (86). Moreover, as can be seen in Figure 2.4, the bulk and multilayers structures of TMDs present an indirect band

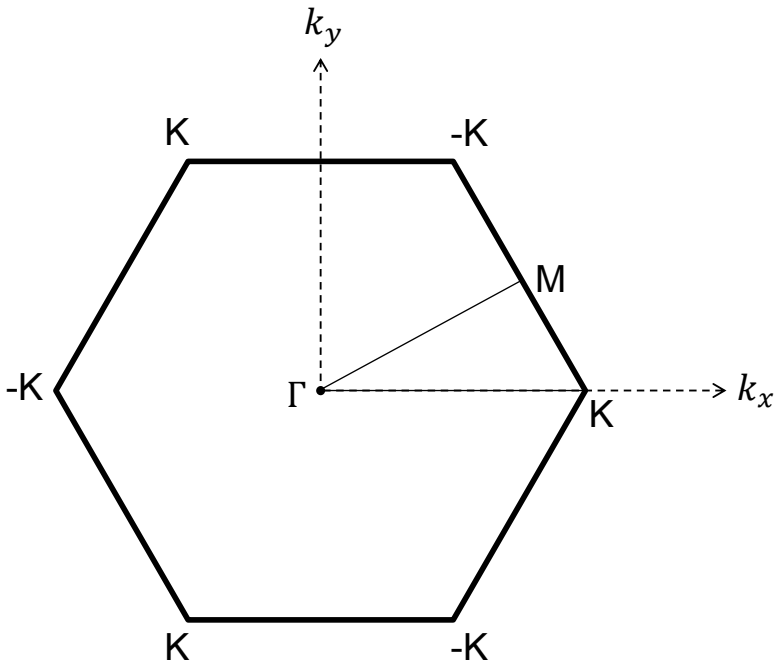

Figure 2.3 – **In-plane first Brillouin zone of a general TMD monolayer.**

gap, in which the maximum of the valence band is at the Γ point while the minimum of the conduction band is between Γ and K points. On the other hand, the monolayer has its maximum of the valence band and the minimum of the conduction band both at the K and −K points, revealing as a direct band gap semiconductor and presenting an enhanced light emission quantum yield (10, 11). Both theoretical and experimental (10, 11, 87, 88, 89) works have shown this direct band gap in the most studied group *VI* TMD monolayers such as MoS_2, $MoSe_2$, WS_2, and WSe_2. Furthermore, they all present a band gap ranging from visible to near-infrared frequency in the energy spectrum, which facilitates their optical investigations and their applications in optoelectronic devices such as light emitting diodes (90), photodetectors (91), and photovoltaic cells (92, 93). Another interesting property of TMD monolayers is their strong spin-orbit coupling due to the transition metal atom's d orbital (94). While the bottom of the conduction band d_{z^2} orbital lead to a small spin splitting of few meV, a noticeable spin splitting of 0.1-0.5 eV is observed in the valence band top owing to their hybridized d_{xy} and $d_{x^2-y^2}$ orbitals (94, 95). In the following sections we explore interesting physical phenomena of TMD monolayers related to the properties mentioned above and that we further investigate in Chapters 6, 7 and 8.

2.1 Many-body effects in TMDs

The quantum confinement of TMD monolayers in two dimensions leads to a reduction in their dielectric screening (16). Therefore, many-body Coulomb interactions

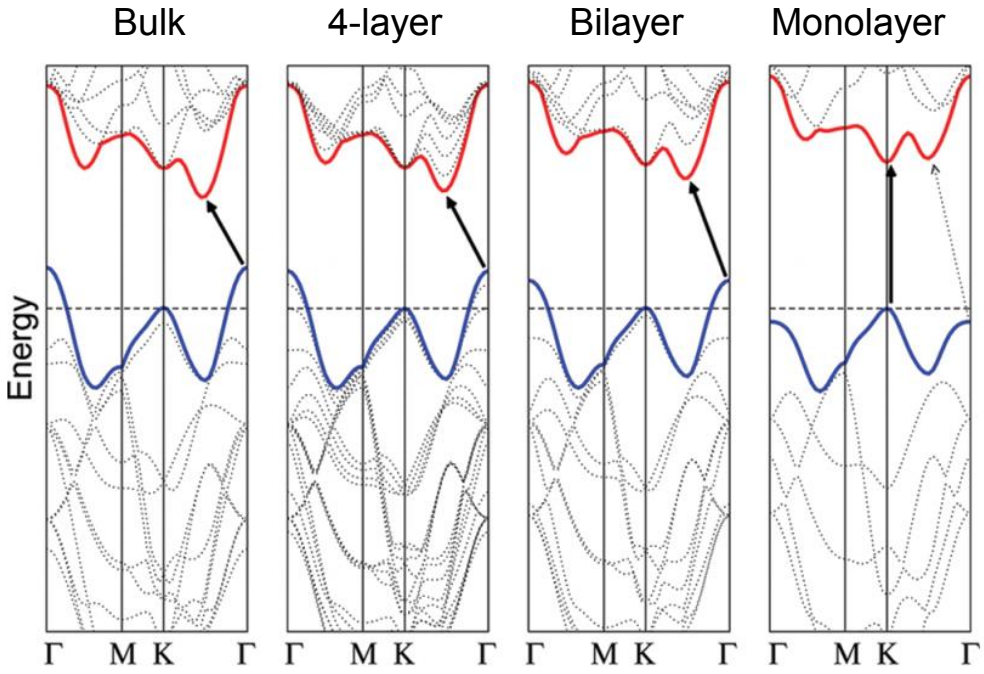

Figure 2.4 – **MoS_2 band structure for distinct number of layers.** From left to right the band structures of bulk, 4-layer, bilayer, and monolayer MoS_2, presenting its indirect-to-direct band gap transition. Adapted from: (11).

play a major role in TMD monolayers even above room temperature (86). At low excitation densities, exciton complexes dominate the optical properties of these materials (22, 23). Besides, from a certain excitation density TMD monolayers present an exciton Mott transition to electron-hole plasma and liquid phases with the emergence of novel physical phenomena (26). These charge carrier regimes and the reasons why TMD monolayers are an ideal platform for their study and application will be detailed exposed in the following sections.

2.1.1 Excitons

The exciton is an electrically neutral quasiparticle observed in nonzero band gap materials such as semiconductors, insulators and molecular crystals. When these materials absorb a photon with enough energy for an interband transition, an electron is excited from the valence band to the conduction band, leaving the lack of a negative particle. This absence of a negative particle is physically treated as a positively charged quasiparticle called hole. Therefore, after the electron excitation the oppositely charged electron and hole can attract each other through a Coulomb interaction, forming a bound electron-hole pair called exciton. As a first approach, we can consider the exciton as an hydrogen-like atomic system in which the electron is in orbit with the hole (24).

For this hydrogenic atom approximation we can distinguish two types of excitons

regarding the excitonic radius: the Wannier-Mott excitons and the Frenkel excitons. The first ones have a large radius that extend for several atoms in the crystal. This delocalization gives to the Wannier-Mott excitons a considerable mobility throughout the crystal and they are thus also called as free excitons. On the other hand, the Frenkel excitons have a radius of the order of a unit cell, which leads to the reduction in the mobility of the electron-hole pairs that are also called as tightly-bound excitons. The free excitons are usually observed in semiconductors, while the tightly-bound excitons are more noticed in insulators or molecular crystals (24). Both excitons are schematically shown in Figure 2.5.

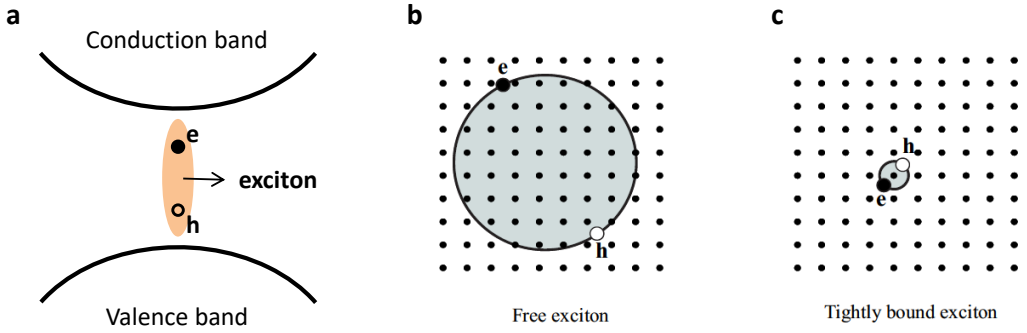

Figure 2.5 – **Schematic representation of an exciton. a** Exciton formation through the bonded electron hole pair and its types representations: (**b**) the free exciton and (**c**) the tightly bound exciton. Adapted from: (24).

Excitons in TMD monolayers are in the intermediate of Wannier-Mott and Frenkel excitons behavior. Nonetheless, the essential part of their physics can be well explained by considering it as a Wannier-Mott type (22). Hence, it will be presented here the physics of these free excitons. As mentioned, they are characterized by their large distance between the electron and the hole, that is much larger than the lattice constant. Therefore, we can model these excitons ignoring the atomic arrangement of the crystal and whereas they are moving in a uniform dielectric medium. Considering the kinetic energy of the exciton given by its center of mass motion and its internal structure described by the relative motion between the particles, we can solve its eingenvalue Schrodinger equation of the relative motion to find the energies of the exciton bound states. However, the Bohr model already provides reasonable results to understand the exciton physics and thereby we present here this model due to its simplicity. By using the reduced mass μ of the exciton with respect to the electron and hole effective masses and setting a dielectric constant ϵ_r, the Bohr model applied to the exciton gives the following energies relative to the principal quantum number n of the bound states (24):

$$E(n) = -\frac{\mu}{m_0}\frac{1}{\epsilon_r^2}\frac{R_H}{n^2} = -\frac{R_X}{n^2}, \tag{2.1}$$

in which m_0 is the free electron mass, R_H is the Rydberg energy of the hydrogen atom

(13.6 eV) and R_X is the Rydberg energy of the exciton. Moreover, the radius of this Wannier-Mott exciton orbit is given by (24):

$$r_n = \frac{m_0}{\mu}\epsilon_r n^2 a_H = n^2 a_X, \tag{2.2}$$

where a_H is the Bohr radius of the hydrogen atom (5.29×10^{-11} m) and a_X is the Bohr radius of the exciton.

For a direct band gap semiconductor, the exciton energy created by an optical interband transition is thus equal to the energy gap E_g between the valence and the conduction bands minus the exciton bound state energy. In other words, the energy of the exciton is given by the energy needed to excite and electron to the conduction band and create a hole in the valence band minus the binding energy of this electron-hole pair due to their Coulomb interaction (24):

$$E_n = E_g - \frac{R_X}{n^2}. \tag{2.3}$$

2.1.2 Excitons in a true 2D system

Besides the several properties that make the TMD monolayers unique 2D materials, being an ideal platform to study excitons in a reduced dimension is another point that attract a great interest to them. Although excitons in quasi-2D systems as GaAs or GaN quantum wells have already been deeply studied (25), the TMD monolayers excitons present a substantially stronger binding energy between the electron and the hole of almost 2 orders of magnitude due to its reduced dielectric screening from the environment (22, 23). Values ranging from $0.3 - 0.8$ eV for this huge Coulomb interaction in these bound electron-hole pairs have been calculated and measured in theoretical (96, 97, 15) and experimental (16, 17, 18) works for TMD monolayers. Therefore, the optical properties in these materials are ruled by the excitonic resonance behaviors even at room temperature.

The excitons behavior in TMD monolayers are also strongly related to its spin and valley degrees of freedom and can provide information about the optical selection rules of this spin-valley coupling (12, 14) (see Section 2.2 for further details). For instance, the strong spin-orbit coupling that cause the splitting of the valence band originates two distinct excitons in these TMDs associated to each splitted band: the A and B excitons (94, 98). The A exciton is related to the transition with respect to the highest valence band while the B exciton is associated with the transition from the less energetic splitted valence band. Furthermore, the TMD monolayers also show another strong excitonic resonance for higher energies in comparison with the A and B optical transitions. This resonance is addressed to a singularity in the joint density of states (JDOS) in a region where the valence

and conduction bands are parallel to each other (51). This parallel band feature is called "band nesting" and the increased light-matter interaction in this region is known as a C transition (in the WSe_2 case in which there are two band nesting resonaces, the transitions are usually called as A' and B' or C and D). Due to an excitonic analogy, this C transition is also referred as a "C exciton". Figure 2.6 shows the A, B and C optical transitions for a MoS_2 monolayer band structure as well as differential reflectance and photoluminescence (PL) spectra highlighting all these transitions for distinct TMD monolayers. It is worth to comment that besides differential reflectance and PL spectroscopies there are other techniques to unveil the excitonic energies such as: resonant Raman spectroscopy (RRS), resonant second-harmonic generation (SHG) and resonant four-wave-mixing (FWM), which will be further explored in Chapter 4.

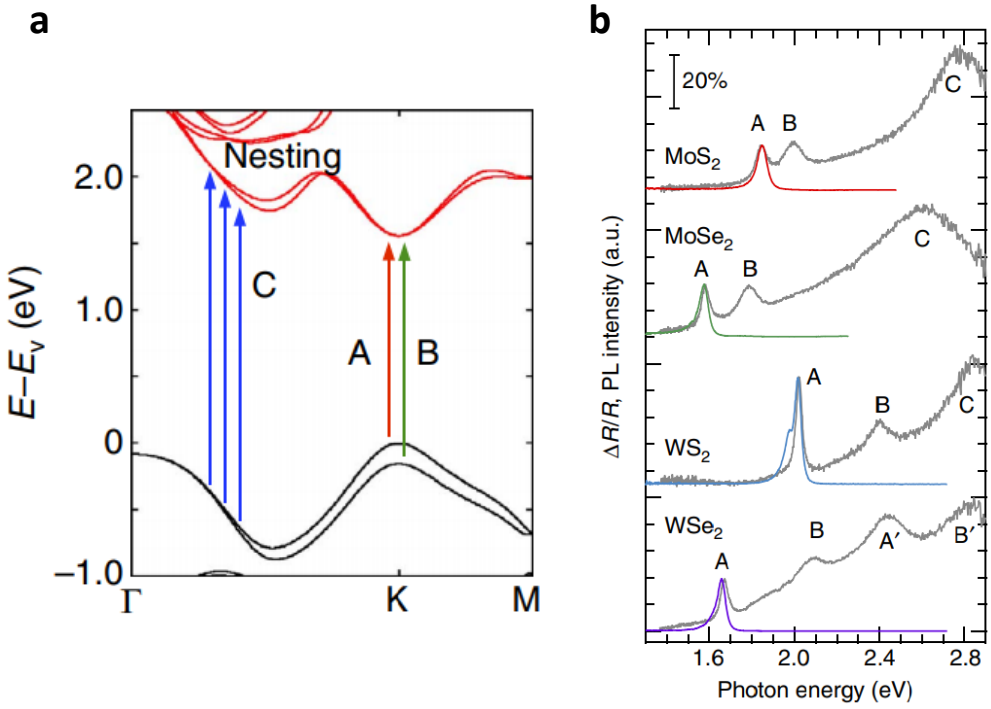

Figure 2.6 – **TMDs optical transitions. a** Schematic representation of the A, B and C transitions in the MoS_2 monolayer band structure. **b** Differential reflectance (in gray) and PL (in red, green, blue and purple) spectra for distinct TMD monolayers showing the A, B and C transition peaks. Adapted from: (51).

In addition to the linear responses of the optical transitions at a low-density regime commented above, at a moderate excitation density TMD monolayers also exhibit further many-body interactions. That is, the density of bound excitons become so large that they start to interact with each other and even form many-body quasiparticles. This is the case of biexcitons, that is a four-body quasiparticle consisted of two electron-hole pairs. Furthermore, an exciton could also interact with free charge carriers (an electron or a hole) an create a charged quasiparticle known as trion. Both biexciton (99) and trion (100, 101) have been reported to be stable in TMD monolayers under certain conditions.

2.1.3 Electron-Hole Plasma

We have seen that a semiconductor present exciton formation at a low-density excitation and other may-body quasiparticles such as biexciton and trion in a moderate excitation. However, if we continue increasing the excitation density in a semiconductor until high charge carrier densities, the dielectric screening between the formed exciton complexes becomes so relevant that these bound quasiparticles start to be ionized and there is the emergence of a plasma of free electrons and holes (102, 103). Mathematically translating it to the model of the interaction between charge carriers, at a low-density this interaction is ruled by the Coulomb attraction between an electron and a hole (103):

$$U(r) = -\frac{e^2}{4\pi\epsilon r}. \tag{2.4}$$

For a high charge carrier density, we might yet consider the screening of the Coulomb interaction between electrons and holes, and their interaction potential becomes then (103):

$$U(r) = -\frac{e^2}{4\pi\epsilon r}\mathrm{e}^{-r/\lambda_s}, \tag{2.5}$$

in which e is the electron charge, ϵ is the permittivity of the medium, r is the distance between electron and hole and $\lambda_s = \lambda_s(N)$ is the screening length that depends on the electron-hole pair density N. The screening length decreases under increasing N, and when it reaches the free exciton radius a_X, the insulating excitons become energetically unstable and are dominated by the metallic electron-hole plasma (EHP) phase. Therefore, this exciton to EHP transition is also called as an analogous excitonic Mott insulator-metal transition (102, 103). It is worth pointing that this transition is generally gradual, i.e. excitons and the EHP coexist for a certain range of charge carrier density and the EHP population gradually overcomes the excitonic population (103), as shown in Figure 2.7.

As a consequence of this excitonic Mott transition there is a reduction in the semiconductor band gap due to a renormalization of its band structure. This reduction can be demonstrated by calculating the difference between the renormalized band gap $E'_g(N)$ and the low-density band gap E_g (103):

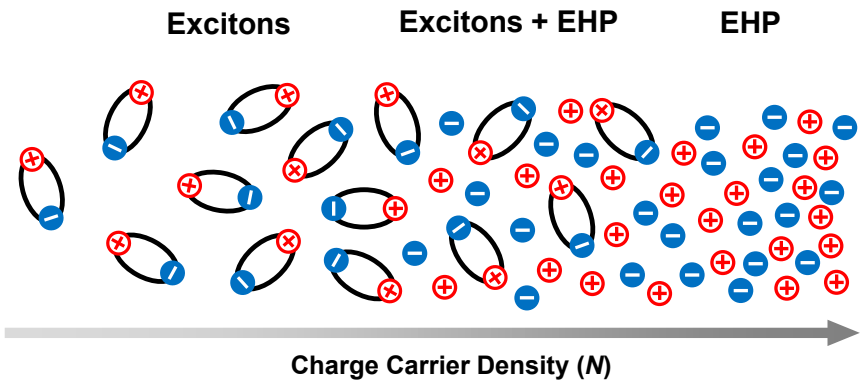

Figure 2.7 – **Exciton to EHP transition.** Under an increasing charge carrier density N, the screening length of the exciton population in a semiconductor decreases and they are gradually ionized, forming an EHP.

$$\Delta E_g(N) = E_g'(N) - E_g = \lim_{r\to 0}[U_s(r) - U(r)]$$
$$\Delta E_g(N) = \frac{e^2}{4\pi\epsilon}\lim_{r\to 0}\left[\frac{\mathrm{e}^{-r/\lambda_s} - 1}{r}\right]$$
$$\Delta E_g(N) = -\frac{e^2}{4\pi\epsilon}\lim_{r\to 0}\left[\frac{\mathrm{e}^{-r/\lambda_s}}{\lambda_s}\right]$$
$$\Delta E_g(N) = -\frac{e^2}{4\pi\epsilon}\frac{1}{\lambda_s(N)}.$$

Hence, the negative value of the $\Delta E_g(N)$ confirms the band gap reduction under increasing electron-hole pair density for the EHP regime.

Another consequence of the EHP formation is the modification of the light emission spectrum of the semiconductor material. While excitons present a narrow emission linewidth owing to their very specific energy of the bound electron-hole radiative recombination, the EHP recombination happens in a broad energy range (102, 103). This occurs because of the Pauli blocking between the charge carriers, which forbids the higher electronic states relaxation to the occupied bottom states of the conduction band, leading to a broadband radiative decay, as shown in Figure 2.8. Therefore, there is an enhanced broadening of the light emission spectrum in the EHP regime by increasing the excitation density. Also regarding the light emission properties of the EHP, this charge carrier regime plays a major role in emitting devices such as semiconductor lasers (102, 103). Since population inversion is required for a lasing process, there is a critical charge carrier density that need to be surpassed for that purpose. For these densities, excitons can present an stimulated emission through exciton-exciton scattering (104, 105), exciton-electron scattering (104), exciton-phonon scattering (106), and the exciton-polariton formation (107). However, for several systems the EHP state displays stronger stimulated emissions associated with a

higher optical gain with respect to excitons (108, 109, 110, 111, 112), being thus more appropriate for application as gain medium in lasers.

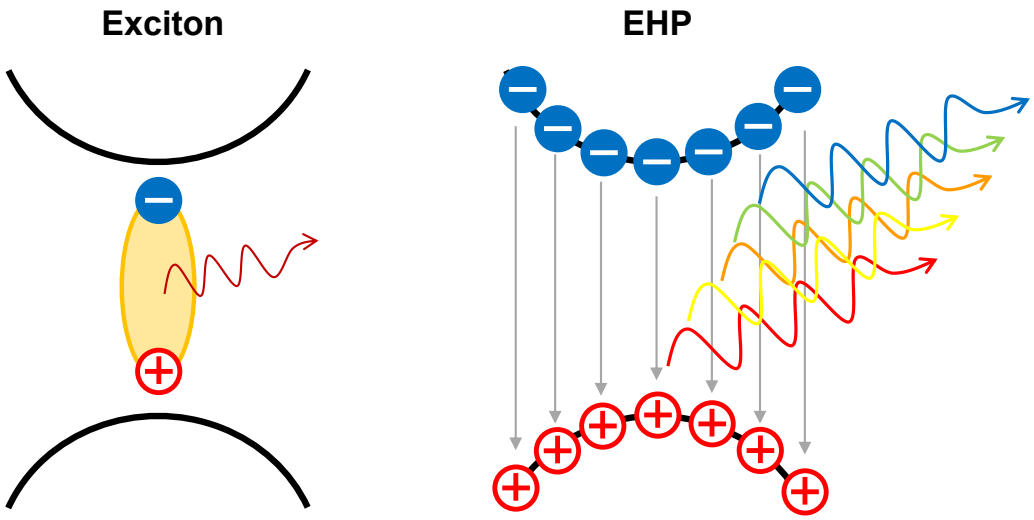

Figure 2.8 – **Exciton and EHP light emission.** Excitons present a narrow light emission due to its specific energy, while an EHP displays a broad one as its radiative recombinations happen for a large range of energies in the conduction and valence bands.

Beyond the EHP, semiconductors also present a condensed charge carrier phase at high excitation densities known as electron-hole liquid (EHL) (102, 103). As well as the classical gas condensation into a liquid droplet, the excitonic transition into an EHL consists in the formation of spherical drops of free electrons and holes (and no longer bound quasiparticles). The internal forces and the surface tension presented in these EHL states maintain the free charge carriers held together in these droplets. Distinctly from the EHP, the EHL can only occur for indirect band gap semiconductors due to the necessity of longer carrier lifetimes for the condensation be reached (102, 103). Other difference between these two states is the spectral shape invariance by increasing the excitation density for the EHL light emission. Similarly to a classical liquid, the EHL exhibits a constant volumetric density of free electrons and holes for a given temperature. Thus, instead of enlarging the volumetric density of charges by occupying higher energy states in the conduction bands, the EHL spatially dissipates under an increased density excitation (102, 103). Therefore, the EHL light emission spectrum width remains unchanged, but its intensity is enhanced and there is an enlargement in its spatial emission.

2.1.4 Electron Hole Plasma in TMDs

Both EHP and EHL phases have been largely investigated in 2D quantum well systems in traditional (III/V) semiconductor heterostructures over the past decades

(113, 114, 115, 116, 117, 118, 119, 120, 121, 122, 123, 124, 125). However, as well as to form excitons, cryogenic temperatures are required to access the excitonic Mott transition in these materials, which limits its investigation and application possibilities. As 2D TMDs are an ideal platform to study these many-body effects, there is also a great interest in probing the high density regimes in these materials. Recently, theoretical and experimental works explored EHP and EHL states in several TMD samples such as MoS_2 (126, 127, 128, 129, 28, 130, 131), WS_2 (26, 126), WSe_2 (126, 132), $MoTe_2$ (133), and also TMD heterostructures (27, 134, 135, 136). However, there are still only few studies on the light emission properties in TMDs showing their interesting optical and electronic responses at high carrier densities above the Mott critical value. Among them, Yu *et al.* (28) revealed an exciton Mott transition to an EHL state in a suspended-MoS_2 monolayer with an intermediate EHP phase under continuous-wave (CW) excitation through photoluminescence measurements as shown in Figure 2.9a. While the EHP presented a band gap redshift (as also observed on WS_2 samples (26)), a large broadening in the emission peak and no intensity modification, the transition to the EHL showed an abrupt enhancement of the photoluminescence intensity and a cease in its broadening as well as in the band gap renormalization. On the other hand, Wang *et al.* (27) demonstrated a low-temperature exciton Mott transition to an EHP phase in a $MoSe_2/WSe_2$ heterostructure that displayed no shift in the interlayer photoluminescence peak position but a strong and gradual broadening without a later transition to an EHL state, as displayed in Figure 2.9b. Furthermore, the TMD Mott transition studies reported distinct characteristic times (from few ps to hundreds of ns) for each sample and measurement conditions (26, 133, 27, 129, 132). Therefore, the investigation of the high carrier density light emission in other TMD monolayers such as $MoSe_2$ and WSe_2 as well as in distinct TMD vertical and lateral heterostructures is still lacking. Besides, finding an optical route to induce these EHP and EHL regimes in supported 2D TMDs at room temperature is a demanding task in view of future applications. Finally, the dynamics of the radiative decay of these highly excited states also needs further understanding. Among other contributions, all these efforts would shed light in the potential of the EHP state in 2D TMDs for lasing applications (137).

Here in this thesis we tackle these points in order to contribute with the understanding of the EHP regime in TMD monolayers and their heterostructures, as will be shown in Chapter 8.

2.2 Spin-Valley Coupling

As shown in Figure 2.3, the corners of the hexagonal first Brillouin zone of TMD monolayers present inequivalent K and $-$K points, similarly to graphene. Since K and $-$K valleys play a major role in the electronic structure of both graphene and TMDs,

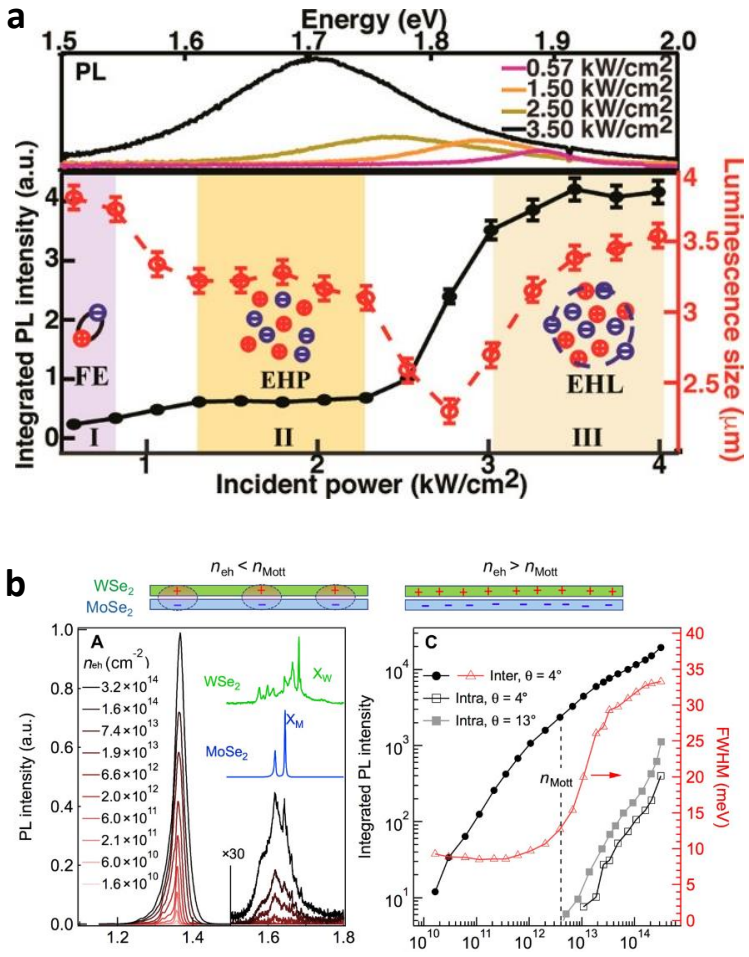

Figure 2.9 – **EHP and EHL light emission in TMDs. a** Exciton, EHP and EHL photoluminescence spectra for a suspended MoS_2 monolayer with respect to the pumping power. Adapted from: (28). **b** Low temperature photoluminescence spectra showing the transition from an interlayer exciton to an EHP under increasing charge carrier density in a $MoSe_2/WSe_2$ vertical heterostructure. Adapted from: (27).

there is a great interest in manipulating this valley index in order to offer a platform for valleytronics (138, 139, 140, 141, 98, 12, 13, 14). For instance, a valley Hall effect (141) and valley dependent optical selection rules (140) were predicted for graphene by externally breaking its inversion symmetry. In contrast, the inversion symmetry in TMD monolayers is intrinsically broken, which leads them to inherently present these valley dependent phenomena (98). Moreover, also conversely to graphene, TMD monolayers exhibit a strong spin-orbit interaction (94, 142), giving rise to a coupling in their spin and valley degrees of freedom as is going to be discussed next.

As commented, the spin-orbit coupling (SOC) induces a remarkable spin splitting at TMD monolayers K and −K valleys. To understand this splitting, Figure 2.10 shows the orbital contributions in the electronic band of a general MX_2 TMD monolayer (94, 95).

For the valence band at the Γ point, the metal atom M mainly displays a d_{z^2} orbital, while the chalcogen atom X presents a p_{z^2} orbital. Thus, the out-of-plane character of these orbitals — which is related to no z-component of the orbital angular momentum, i.e., $m_l = 0$ — leads to the absence of spin splitting at the Γ point valence band. Toward the K point, the valence band starts showing a hybridized $d_{xy} + d_{x^2-y^2}$ orbital for M and a $p_x + p_y$ orbital for X. Regarding the conduction band at K point, d_{z^2} and $p_x + p_y$ orbitals are noted for M and X atoms, respectively. As the SOC is more intense for heavier atoms, the metal atoms present a stronger contribution to the spin splitting in TMD monolayers. Therefore, the valence band at K point exhibits noticeable spin splittings of 0.1-0.5 eV (94, 95) — in which MoS_2 shows the weaker and WSe_2 the greater splitting because of their atomic weights. On the other hand, the K point conduction band displays spin splittings of one order of magnitude smaller than the valence band due to the out-of-plane feature of the metal atom orbital (142). The SOC effect in the energy splitting of MoS_2, WS_2, $MoSe_2$ and WSe_2 electronic bands can be seen in Figure 2.11.

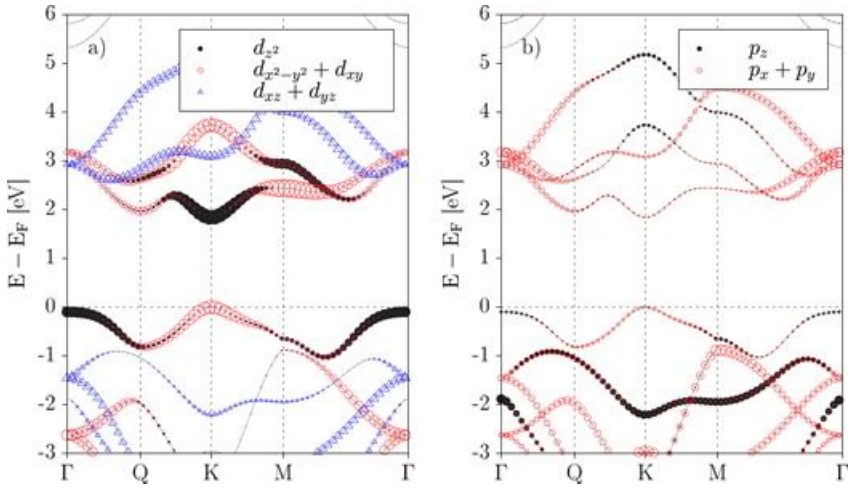

Figure 2.10 – **Atomic orbital weights of a MX_2 TMD monolayer.** Metal atom d orbitals in the left and chalcogen atom p orbitals in the right. Adapted from: (95).

The spin splitting discussed above and shown in Figure 2.11 concerns about the SOC effect at the K point. Hence, the natural question that arises from this is: does −K valley experience the same spin splitting? As K and −K points present opposite momenta $\boldsymbol{k}$, they are connected by time reversal symmetry (98), which gives:

$$E_{\uparrow}(\boldsymbol{k}) = E_{\downarrow}(-\boldsymbol{k}), \tag{2.6}$$

where E is the energy of the electronic state with spin up (↑) or down (↓). Therefore, the spin splitting at K and −K valleys must be opposite, leading to a spin-valley coupling in TMD monolayers (98). In terms of the generated excitons, the electrons of excitons A (B)

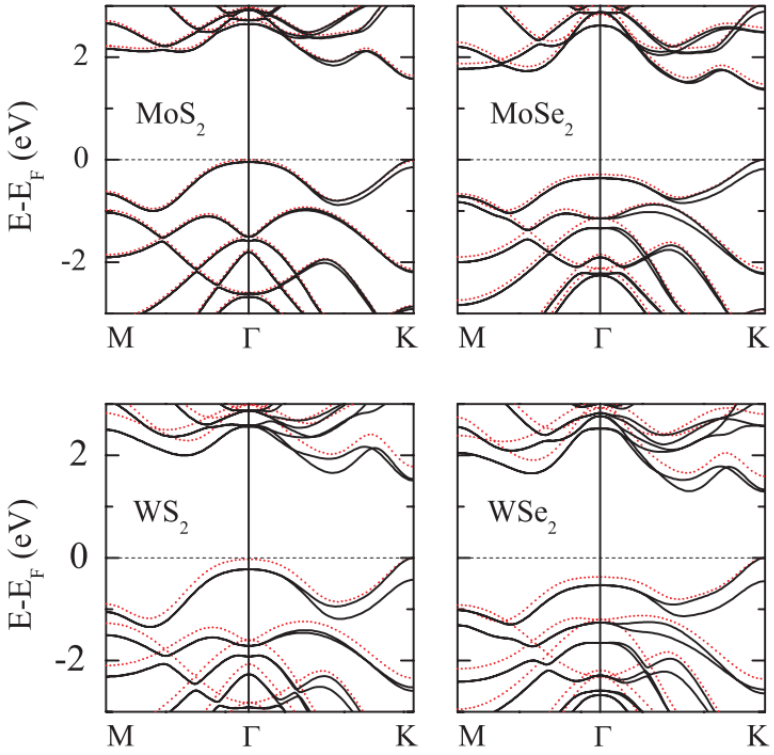

Figure 2.11 – **Electronic band structures of TMD monolayers with SOC.** The solid lines represent the band structures calculated with the inclusion of SOC, while the dotted red lines are without SOC. Thus, it can be observed that the spin splitting at the K valley is induced by the spin-orbit interaction. Adapted from: (94).

in the K valley are spin up (down) polarized, while the electrons of excitons A (B) in the −K valley are spin down (up) polarized.

2.2.1 Valley Selective Circular Dichroism

To explore the spin-valley coupling physics in TMD monolayers, a route to separately access each valley is mandatory. As shown by Figure 2.12a, besides the opposite spins, valence and conduction bands in these 2D semiconducting materials also present contrary z-components of their total angular momentum (m_j) (12). It can be noted that optical transitions in K and −K valleys display variations in m_j of $\Delta m_j = \pm 1$ (12), in which the sign corresponds to the valley index, whereas the electron spin is conserved in the transition. Therefore, the required angular momentum conservation leads to optical selection rules that can be used to selectively excite the valleys. These selection rules can be satisfied by light with circular polarization, which exhibts $\Delta m_j = 1$ for right circularly polarized (σ^+) and $\Delta m_j = -1$ for left circularly polarized (σ^-) light (24), as displayed in Figure 2.12b. Hence, K and −K valleys can be individually accessed by σ^+ and σ^- excitations, respectively.

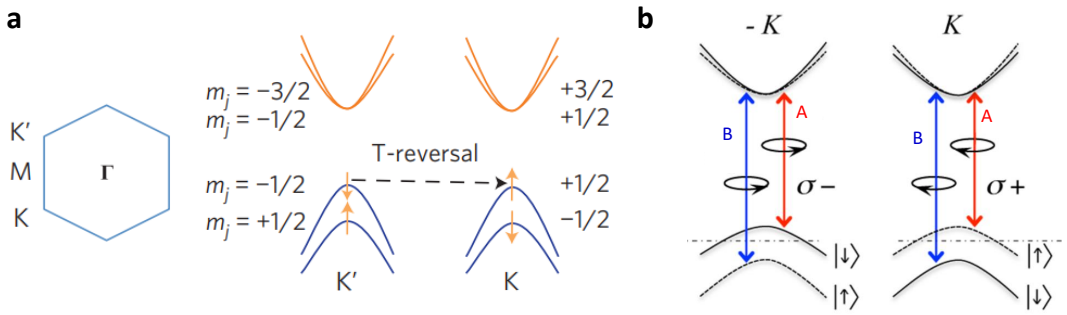

Figure 2.12 – **Valley selectively by circularly polarized light. a** z-components of the total angular momentum (m_j) for valence and conduction bands at K and −K valleys. Adapted from: (12). **b** Selective excitation of A and B excitons at K and −K valleys by circularly polarized light. Adapted from: (98).

By pumping the material with circularly polarized light and with enough energy to excite both A and B excitons, charge carriers with spin up and down would be generated in the same valley (12). Moreover, the relaxation process of the hot electrons to the bottom of conduction bands could lead to a loss in the spin polarization (143). Therefore, in order to induce a spin polarized population of charge carriers with long lifetimes, near-resonant excitations are recommended (12, 13). Figure 2.13 shows photoluminescence spectra of a MoS_2 monolayer for distinct σ^- excitation energies and detecting both σ^- and σ^+ emissions. It can be observed a great degree of circular polarization by exciting near the A exciton energy and similar σ^- and σ^+ spectra for the out-of-resonance excitation. For a σ^- excitation, the degree of circular polarization can be calculated as follows (for a σ^+ excitation is the inverse):

$$DCP(\%) = \frac{I_{\sigma^-} - I_{\sigma^+}}{I_{\sigma^-} + I_{\sigma^+}}, \tag{2.7}$$

in which I_{σ^-} and I_{σ^+} are the intensity of σ^- and σ^+ light emissions, respectively. It is worth to point that these photoluminescence measurements probe the emitted photons. To study the absorbed photons other optical techniques such as differential reflectance spectroscopy can be employed. Further details about these optical measurements are going to be discussed in Chapter 4.

2.2.2 Valley Zeeman Effect

Controlling spin and valley indexes by circularly polarized light opens a variety of possibilities for spintronics and valleytronics in TMD monolayers (144, 145). Nonetheless, the energy degeneracy between K and −K valleys restricts their use in applications that require an energy threshold to distinguish the distinct spin and/or valley charge carrier populations. To overcome this issue, it has been previously shown that an external magnetic

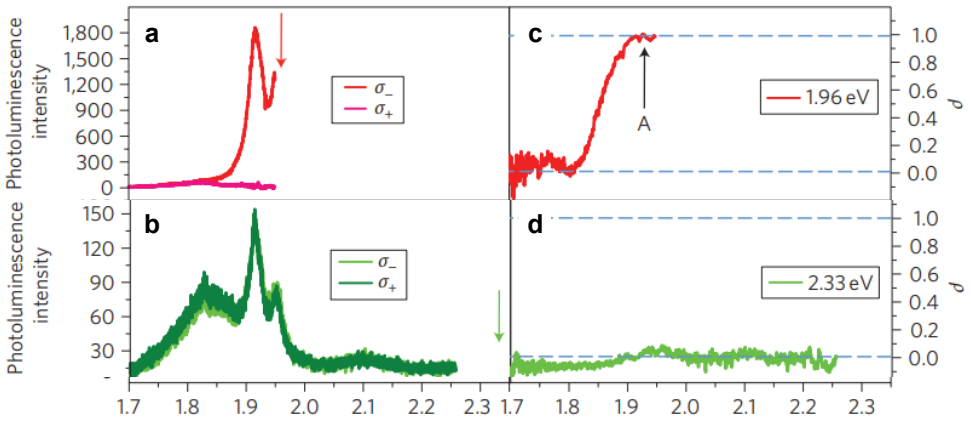

Figure 2.13 – **Degree of circular polarization for a MoS_2 monolayer. a,b** Resonant (**a**) and non-resonant (**b**) σ^- excitation photoluminescence spectra for σ^- and σ^+ detection. The arrows indicated the excitation energy. **c,d** DCP (ρ) for the resonant (**c**) and non-resonant (**d**) excitations. Adapted from: (12).

field perpendicular to the TMD monolayer can break its valley degeneracy through an analogous Zeeman effect, known as valley Zeeman effect (146, 147, 148, 149).

The Zeeman effect consists in the energy splitting of atomic levels in the presence of an external magnetic field. The Hamiltonian (H_Z) related to the magnetic field (B) for a single electron is given by (150):

$$H_Z = -\boldsymbol{\mu} \cdot \boldsymbol{B}, \tag{2.8}$$

where $\boldsymbol{\mu} = \boldsymbol{\mu_l} + \boldsymbol{\mu_s}$ is the magnetic moment of the atom composed by its orbital ($\boldsymbol{\mu_l} = -\frac{e}{2m}\boldsymbol{L}$) and spin ($\boldsymbol{\mu_s} = -\frac{e}{m}\boldsymbol{S}$) magnetic moments. Thus, the magnetic field Hamiltonian can be written as (150):

$$H_Z = \frac{e}{2m}(\boldsymbol{L} + 2\boldsymbol{S}) \cdot \boldsymbol{B}, \tag{2.9}$$

in which e, m, $\boldsymbol{L}$ and $\boldsymbol{S}$ are the charge, mass, orbital angular momentum and spin angular momentum of the electron. H_Z can be treated as a perturbation, and solving the Schrodinger equation by time-independent perturbation theory the energy Zeeman contribution is (150):

$$E_Z = \mu_B g_j m_j B, \tag{2.10}$$

where $\mu_B = \frac{e\hbar}{2m} \approx 5.788 \times 10^{-5}$ eV/T is the Bohr magneton, g_j is the Landé g-factor and m_j is the z-component of the total angular momentum. Therefore, the degeneracy of the energy levels is broken for different m_j, leading to a splitting of the atomic spectral lines.

For TMD monolayers, an external magnetic field would interact with their atomic orbital (μ_l), valley orbital (μ_v) and spin (μ_s) magnetic moments (146, 147, 148, 149, 151). The valence and conduction bands at K and $-$K valleys present no splitting associated with the magnetic field, as they are explicitly splitted with respect to the distinct m_j values because of the SOC (94). However, the magnetic field causes a further energy shift of the electronic bands that depends on those cited magnetic moments. Orbital, valley and spin magnetic moments are opposite in K and $-$K valleys. Therefore, the magnetic field energy shifting in these valleys must also be opposite, breaking the valence and conduction bands degeneracy in K and $-$K points (146, 147, 148, 149). But if the valence and conduction bands presented identical energy shifts at the same valley, the band gap would remain the same for both valleys, then not breaking their band gap degeneracy. However, as is going to be discussed now, the magnetic moments of the valence and conduction bands are not all equal, leading to the valley Zeeman splitting effect in TMD monolayers (146, 147, 148, 149).

The energy shift due to an external magnetic field is given by: $E = -\boldsymbol{\mu} \cdot \boldsymbol{B}$, with $\boldsymbol{\mu} = \boldsymbol{\mu}_l + \boldsymbol{\mu}_v + \boldsymbol{\mu}_s$. Hence, the band gap modification (ΔE_g) is the difference between the energy shifts in the valence and conduction bands:

$$\Delta E_g = (-\boldsymbol{\mu}_l^{\mathrm{c}} + \boldsymbol{\mu}_l^{\mathrm{v}}) \cdot \boldsymbol{B} + (-\boldsymbol{\mu}_v^{\mathrm{c}} + \boldsymbol{\mu}_v^{\mathrm{v}}) \cdot \boldsymbol{B} + (-\boldsymbol{\mu}_s^{\mathrm{c}} + \boldsymbol{\mu}_s^{\mathrm{v}}) \cdot \boldsymbol{B}, \tag{2.11}$$

in which the c and v uppercases are related to conduction and valence bands. The valence and conduction bands that are linked by an allowed optical transition — i.e. by an exciton formation between their electrons and holes — have the same spin magnetic moment ($\mu_s^{\mathrm{c}} = \mu_s^{\mathrm{v}}$), leading thus to an identical Zeeman shift and no band gap modification. Besides, the valley magnetic moment in TMD monolayers can be written as $\mu_v^{\mathrm{c(v)}} = \pm(m_0/m_{e(h)})\mu_B$, where $m_{e(h)}$ is the electron (hole) effective mass at the conduction (valence) band, m_0 is the bare electron mass and the sign is respective to K and $-$K valleys. For a simple tight-biding model, $m_e = m_h$ and the band gap modification due to a Zeeman shift related to the valley magnetic moments is also negligible (151). Finally, the atomic orbital magnetic moments of valence and conduction bands at the same valley in TMD monolayers are not the same (94). While their d_{z^2} conduction band orbital has a zero magnetic moment, their hybridized $d_{x^2-y^2} \pm id_{xy}$ valence band orbitals have orbital magnetic moments of $\mu_l = \pm 2\mu_B$, related to the K and -K valleys, respectively. For this approach, the total band gap modification is $\Delta E_g = -2\mu_B B$ at K valley and $\Delta E_g = +2\mu_B B$ at $-$K valley. Therefore, the perpendicular external magnetic field causes a band gap degeneracy breaking in TMD monolayers — known as the valley Zeeman splitting —, and the expected energy difference (ΔE) between the gap in their K and $-$K valleys is $\Delta E = -4\mu_B B$. To correlate this with the former Zeeman effect, we can write this valley Zeeman splitting as:

$$\Delta E = g\mu_B B, \tag{2.12}$$

in which the g-factor g is used to measure the TMD response to a magnetic field. Figure 2.14 shows the band structure schematic representation of the valley Zeeman effect for a TMD monolayer.

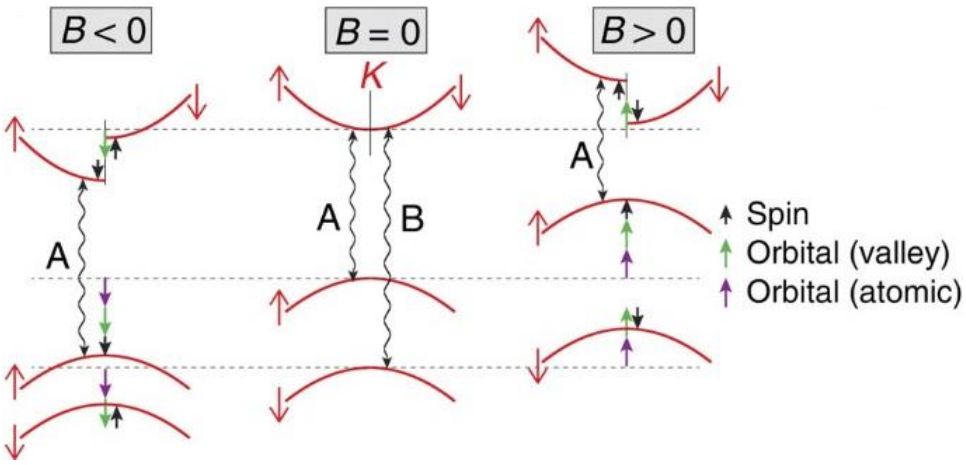

Figure 2.14 – **Valley Zeeman effect for a TMD monolayer.** By applying an external magnetic field, the valence and conduction bands are shifted due to a Zeeman effect depending on their spin, atomic orbital and valley orbital magnetic moments. This band shifting results in a splitting of the band gap in K and −K valleys, known as the valley Zeeman splitting effect. Adapted from: (151).

Exciton complexes in distinct TMD monolayers have previously shown g-factors close to the expected value of $g = -4$ (146, 147, 148, 149, 151, 152, 153, 154, 155). In a first analysis, small deviations in this value can be understood as corrections to the simple tight-biding model, where $m_e \neq m_h$ (156). However, recent theoretical studies showed a more thorough analysis for the g-factor calculation (157, 158). Through first-principle calculations, the orbital angular momenta associated with a specific exciton are summed over hundreds of bands, allowing a more precise estimation of the g-factor for excitons in TMD monolayers as well as interlayer excitons in TMD heterostructures. These interlayer excitons are going to be discussed in Chapter 3. Besides, in Chapters 3, 4 and 6 we will present how the defect engineering of TMDs can potentialize TMD magnetic properties resulting in enhanced g-factor values.

3 Defects in TMD Monolayers

The quantum description of the band theory of solids in the first half of the 20th century (159, 160) provided a step toward the understanding of the semiconducting properties probed by that time. Thus, with the development of the former semiconductor junction devices — such as the p-n junction diode (161) and the junction transistor (162) — it was realized the importance of the crystallinity as well as the pristineness of the materials in order to provide high quality devices (163). In addition, it was also known that the operation mechanism behind these p-n juctions is deeply dependent on intentional and controlled doping of semiconductors to provide the n- and p-type regions (163). Therefore, it should be noted that defects play a major role since the beginning of the semiconductor applications, acting as "villains" or "heroes" depending on the circumstances (164).

The increasing interest on 2D TMDs for the next generation of ultrathin devices also led to a natural concern about defects in these materials (34, 35). The spatial inhomogeneity of TMDs properties caused by several possible defects can deeply affect their applicability (34, 35). In this context, there is a great effort and interest of the community to characterize all distinct defects that are commonly displayed in TMDs systems and to understand their impact on electronic, optical, mechanical, magnetic, and physicochemical properties (34, 35). Also, if on the one hand defects can lead to undesirable modifications in the TMDs properties, on the other hand it is possible to engineer certain types of defects to achieve new desirable features. For instance, the introduction of spin polarized metal atoms as substitutional defects in TMD monolayers induce a room temperature ferromagnetic ordering in these materials (165, 166). Furthermore, the stacking and stitching methods to fabricate vertical and lateral TMD heterostructures showed to be a playground for tuning TMD properties and thus unveil novel physical phenomena associated with their interlayer effects (46, 47, 48, 49, 32). It is worth commenting that although these heterostructures are not a typical semiconductor defect, their interfaces are usually treated as defective regions since the potentials introduced in the sample lead to modifications in the material properties at these interfaces. In this Chapter, firstly we will introduce a classification of defects and their origin in 2D TMDs, also showing their identification through scanning microscopy measurements such as scanning probe microscopy (SPM) and scanning transmission electron microscopy (STEM) (167, 168). SPM can investigate surface properties as topography, friction, electrostatic and magnetic forces and work function, while STEM measurements are employed to image surfaces at the atomic level. Then, we will focus our discussion on two examples of TMD systems achieved through defect engineering: 2D dilute magnetic semiconductors and TMD heterostructures. It is worth pointing that the optical features associated with defects in TMDs will be

superficially commented in this Chapter, as they are going to be extensively explored in Chapter 4.

3.1 Types of Defects in TMDs

An ideal semiconductor free of defects would be a single crystal absent of imperfections in its chemical composition. Therefore, any modification in these features can be called as a "defect". It is very to common classify defects in TMDs accordingly to their dimension, i.e., zero-dimensional (0D), one-dimensional (1D), two-dimensional (2D) or three-dimensional (3D) defects (34). However, here we are more concerned about the impact of these irregularities on the optical responses of 2D TMDs. Therefore, we will introduce now defects that are related with the experimental investigations performed for this thesis. They are: atomic vacancies, adsorbed atoms (adatoms) or molecules, substitutional dopants, passivation, grain boundaries and edges. Besides, we will also comment about strain fields in TMD samples, which can be caused by different agents. These defects are schematically represented in Figure 3.1.

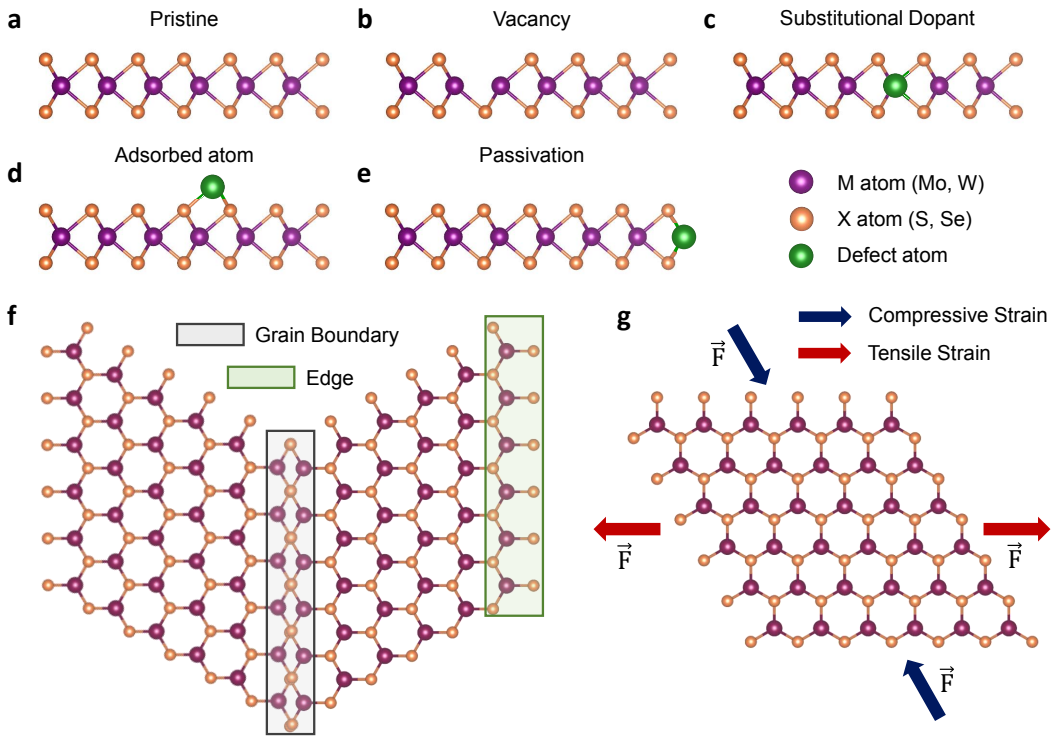

Figure 3.1 – **Types of defects in a TMD monolayer.** Lateral view of the atomic structure of a TMD monolayer with no defects (**a**), vacancy (**b**), substitutional dopant (**c**), adsorbed atom (**d**) and defect passivation (**e**). Top view of a TMD monolayer showing grain boundary and edge defects highlighted in gray and green areas (**f**), and submitted to compressive and tensile strains (**g**).

Atomic vacancies are the most reported defects in TMD monolayers (34, 35).

Different single and joint vacancies have been observed in these materials. For example, MoS_2 monolayers have shown monosulfur vacancies (V_S), disulfur vacancies (V_{S2}), a vacancy complex of one molybdenum nearby three monosulfur (V_{MoS3}), a vacancy complex of one molybdenum with three nearby disulfur vacancies (V_{MoS6}), an antisite of molybdenum occupying a V_{S2} (Mo_{S2}) and an antisite of disulfur occupying a molybdenum vacancy ($S2_{Mo}$) (169), as shown in the annular dark field (ADF) STEM measurements of Figure 3.2. Among these point defects, the V_S is the most likely to show up since it displays the lowest formation energy (169). On the other hand, the antisite (Mo_{S2}) and ($S2_{Mo}$) defects are less observed, presenting the highest formation energies (169). This implies that vacancies do not tend to modify the trigonal structure of the sample (34) (at least when they are not linked with other defects). Nonetheless, vacancies induce relevant band structure modifications, which affects the light emission and the dynamics of the optical transitions in TMD monolayers (83, 170, 171). Although vacancies commonly appears during the fabrication process, there are also methods to deliberately generate these point defects in 2D TMDs, as annealing (172) and He-ion treatment (173), which can originate single photon emitters in TMD monolayers (174, 175).

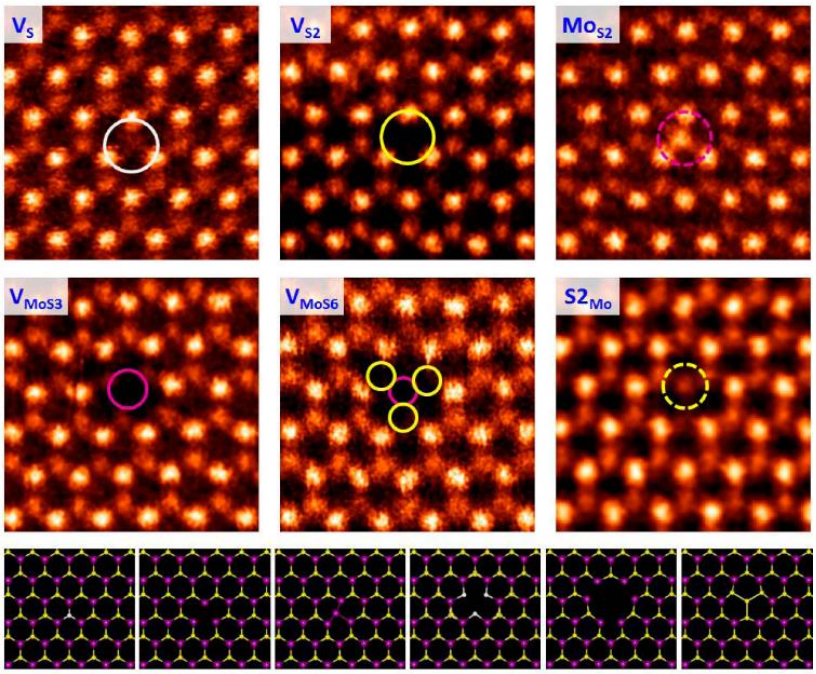

Figure 3.2 – **Types of vacancies in a MoS_2 monolayer.** ADF-STEM measurements showing the most common vacancies of a MoS_2 monolayer and their atomic representation. Adapted from: (169).

In addition to the lack of an atom in the crystal structure, it is also possible that other atoms fill these vacant sites. And when these foreign atoms are introduced in the crystal lattice we call them substitutional dopants. These dopants can replace both metal and chalcogen atoms (34, 176, 177). Several metal atoms have been theoretically predicted

to be energetically favorable to substitute host metal atoms sites (176, 177), leading to n-type, p-type or isoelectronic dopings, as shown in Figure 3.3. Optical, electronic, chemical and magnetic properties have been shown to be tuned by these dopants (176). In the next section we will further explore this defect engineering for magnetic functionalities. Experimentally, n-type Mn-, Fe-, Co-, Ni-, and Re-doped TMD monolayers have already been fabricated, introducing donor states at the material band structure (176, 177). For p-type dopants, the introduction of V and Nb atoms was also achieved, leading to acceptor states (176, 177). These dopants are usually *in-situ* introduced, i.e., they occur during the sample growth process. While unintentionally doping can happen due to impurities presented in the chemical reaction environment (178), they can also be intentionally inserted to tune the TMD monolayer properties (44, 43). Regarding the isoelectronic doping, the W replacement of Mo as well as the contrary are also reported (176, 177). Finally, the chalcogen substitution is observed for less different atoms (only other chalcogens). Beyond the substitution of S by Se and Se by S, the other atom that play a major role in the this chalcogen substitution is oxygen (176, 177). Again, these substitutional dopings can naturally occur or can be artificially introduced. As an example, the post treatment of a grown MoS_2 monolayer with an hydrogen plasma followed by a Se evaporation can lead to a complete replacement of one layer of S by Se, known as Janus monolayer (179). Besides, oxygen doping can also be induced by a plasma treatment, causing significant modifications in the material electrical and optical properties (180, 181). It is worth pointing that oxygen is also often incorporated in TMDs through defect passivation (177). This occurs mostly at edges (182), and it shown to be a mechanism to suppress nonradiative recombinations.

In addition to foreign atoms taking place of host atoms in the crystal lattice, atoms and molecules can also be adsorbed to the monolayer surface (183, 34) — and when is an atom being adsorbed, it is also called an adatom. A variety of adsorbents have shown low formation energies for TMDs, including metal atoms, oxygen, hydrogen, water molecules and organic molecules (184, 183, 185, 186). These adsorbents are predicted to modify the TMD monolayers band structure, leading to n- or p-type dopings as well as inducing magnetic properties in these materials (184, 183, 185, 186). However, although several theoretical works have studied these adsorptions, experimental works still find challenges to reliably assign their chemical composition (187, 188, 170, 189). Scanning microscopy and X-ray photoelectron spectroscopy measurements provide indications of possible adsorbents, but it is usually complex to differentiate similar species (189, 178). These defects are usually related to the air exposition of the sample, being thus observed in aged TMD monolayers (188, 189). Nonetheless, controlled gas environments (187, 188) and h-BN encapsulation (190) are methods to protect the sample from these external agents.

Beyond these chemical defects, i.e., defects associated with the sample chemical composition, TMD monolayers also display structural defects as grain boundaries and

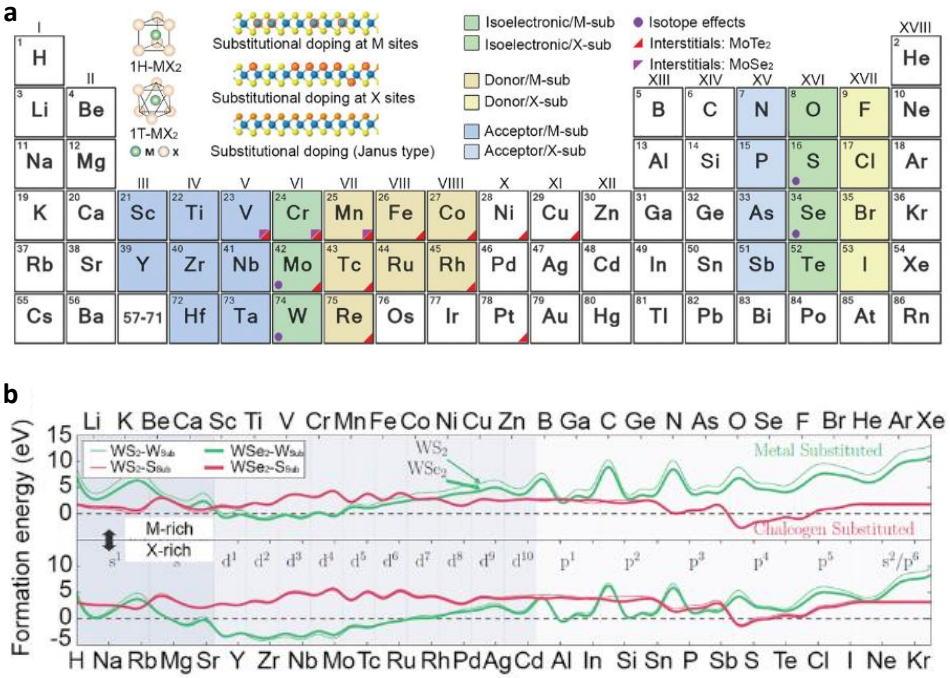

Figure 3.3 – **Theoretical overview of potential dopants for TMD monolayers. a** Periodic table showing the potential substitutional dopants for the metal and chalcogen atoms in TMD monolayers and their doping type (associate with their induced acceptor or donor states). **b** Formation energies for distinct dopants substituting atoms in different TMD monolayers. Adapted from: (176).

edges (34). As commented, a perfect structure would be related to a single crystal. However, grown TMD monolayers commonly report multi crystalline domains (71, 169, 191). Each of these domains, called as grains, present a certain crystallographic orientation. Therefore, for multi crystalline TMD monolayers the boundary between two grains is thus a defective region in which the mismatched atoms present a distinct localized geometrical structure that depends on the relative orientation of the grains as well as the direction of their junction (zigzag or armchair) (71, 169, 191). The relative orientation and direction of the grain boundary can be probed by ADF-STEM measurements (71, 169, 191), as shown in Figures 3.4a,b. Moreover, AFM measurements have shown modifications in the grain boundary topography (178), as presented in Figure 3.4c. Regarding the optical responses, these grain boundaries can also be probed by polarized second harmonic generation microscopy (192, 193, 178) and display an enhanced light emission (194, 192, 178). While grain boundaries only show up in multi crystalline samples, edges are obviously present in every TMD flake. Distinct features noticed at edges are associated with the interruption of the crystal periodicity, which depend on the edge termination (169). In general, edges can be either zigzag or armchair terminated — as well as chalcogen or metal terminated (or a mixture of both) (169). The edge termination can be probed by STEM measurements (169), whereas distinct topographic response has also been noted at TMD monolayer edges

by AFM (195), as displayed in Figure 3.4d. Moreover, the incomplete chemical bonds of the edge atoms make them probable to be passivated by external atoms (182), as mentioned before.

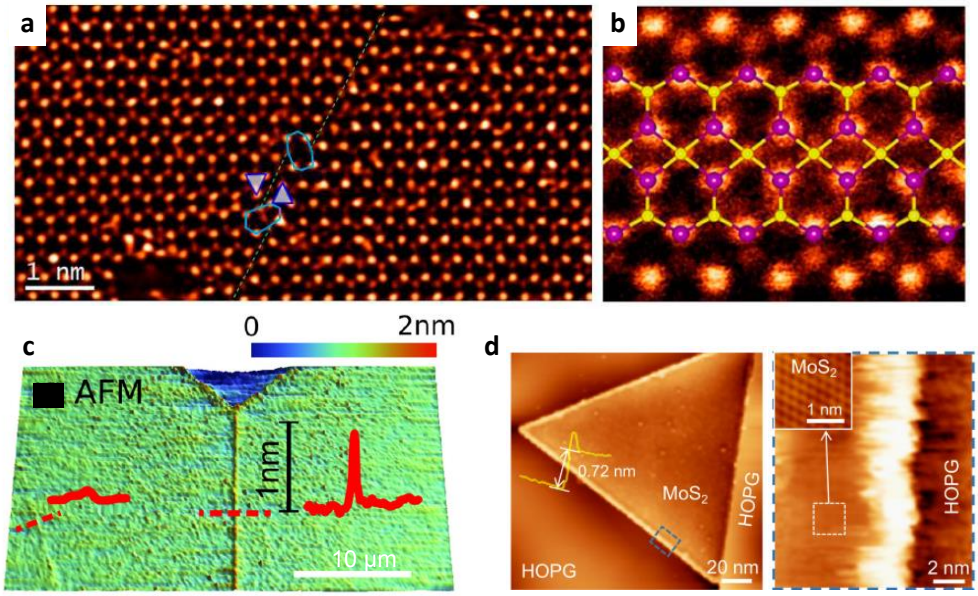

Figure 3.4 – **STEM and SPM measurements of grain boundaries and edges in TMD monolayers. a,b** ADF-STEM measurements showing a grain boundary and the relative orientation of 60° between the adjacent grains in a MoS_2 monolayer. Adapted from: (169). **c,d** AFM measurements presenting the higher topography of a WS_2 monolayer grain boundary and a MoS_2 edge, respectively. Adapted from: (178) and (195).

Finally, strain fields are another source that modifies the intrinsic properties of TMD monolayers, since they are able to disturb the pristine crystalline geometry (196, 197). Strains can have several origins. Some defects commented above, such as grain boundaries and edges, are occasionally the cause of strain fields in the sample, since their topography distortions can lead to local tensions. Besides, strain can emerge from the expected thermal expansion coefficient and lattice constant mismatch between the monolayer and the substrate (196), which plays a major role in the growth process. Finally, strain can also be engineered by bending or stretching the TMD, which enables a modulation of TMD properties by controlling the compressive or tensile tension applied on the material (198).

3.2 2D Dilute Magnetic Semiconductors

Dilute magnetic semiconductors (DMS) are a class of materials formed when a non-magnetic semiconductor is doped with transition metal atoms. The great interest in this type of material lies in joining both semiconducting and magnetic properties in the same system, enhancing its application possibilities for spintronics or data storage

devices (199, 200, 201). Bulk Mn-doped GaAs is the most prominent example of a bulk dilute magnetic semiconductor (199, 201), which has shown great functionalities for spintronics devices due to its induced ferromagnetism. However, at room temperature this ferromagnetic ordering is only locally observed, not presenting thus a long-range spin-polarization (199, 201). On the 2D scale, some materials have also attracted attention due to their magnetic responses. For instance, VSe_2 (202) and $MnSe_2$ (203) monolayers have shown room-temperature ferromagnetic ordering, but their metallic character do not allow carrier density control. Besides, 2D semiconducting CrI_3 (204, 205, 206) and $Cr_2Ge_2Te_6$ (207) materials display an intrinsic ferromagnetism, but it is restricted to cryogenic temperatures.

As 2D TMDs present unique semiconducting features, there was also a natural interest in engineering 2D DMSs by doping TMD monolayers with distinct transition metal atoms (208, 166). Firstly, theoretical works predicted finite magnetic moments for different TMD monolayers doped with distinct metal atoms such as V, Nb, Ta, Cr, Mn, Re, Fe, Co, Ni, Cu, Zn, Cd and Hg (36, 37, 38, 39, 209, 210, 211, 212, 213, 214, 215, 216, 217, 218, 219, 220). Nonetheless, the experimental realization of these samples with a ferromagnetic ordering showed to be challenging (165, 166). To our knowledge, V-doped WS_2 (44), WSe_2 (42, 43) and $MoSe_2$ (221) as well as Fe-doped MoS_2 (222) are the only TMD DMS monolayers that presented room temperature ferromagnetism until now. The magnetism in these samples were probed by vibrating sample magnetometry and magnetic force microscopy measurements, as shown in Figure 3.5. It can be observed that V-doped WS_2 and WSe_2 monolayers present a tunable magnetism by varying the dopant concentration, with optimal vanadium concentrations of 2% and 4% (44, 43), respectively.

Figure 3.6 schematically shows the introduction of spin-polarized vanadium atoms in a TMD monolayer and the subsequent dopants spin alignment. This magnetization can occur by a direct or indirect mechanism. The first one is related to the direct exchange between localized dopant states (223), while the later one is associated with the indirect exchange mediated by free carriers of the host material (which is described by the RKKY (224) or the Zener model (225)). For instance, scanning tunneling microscopy and transport measurements in the vanadium-doped WSe_2 monolayer showed the hybridization between the vanadium dopant states with the host valence band and the presence of free holes in the hybridized band (226), giving an experimental evidence of the Zener-type itinerant magnetism, which was previously predicted by DFT calculations (220). On the other hand, V-doped WS_2 monolayers still require experimental confirmation of their magnetization mechanism. In addition, among the significant challenges to be overcome in this field such as the gate-tunability manifestation and the necessity of enhanced magnetic moments in these materials (165, 166), there is also a fundamental necessity for broadband optical, magneto-optical and electronic structure characterization of these doped 2D semiconductors.

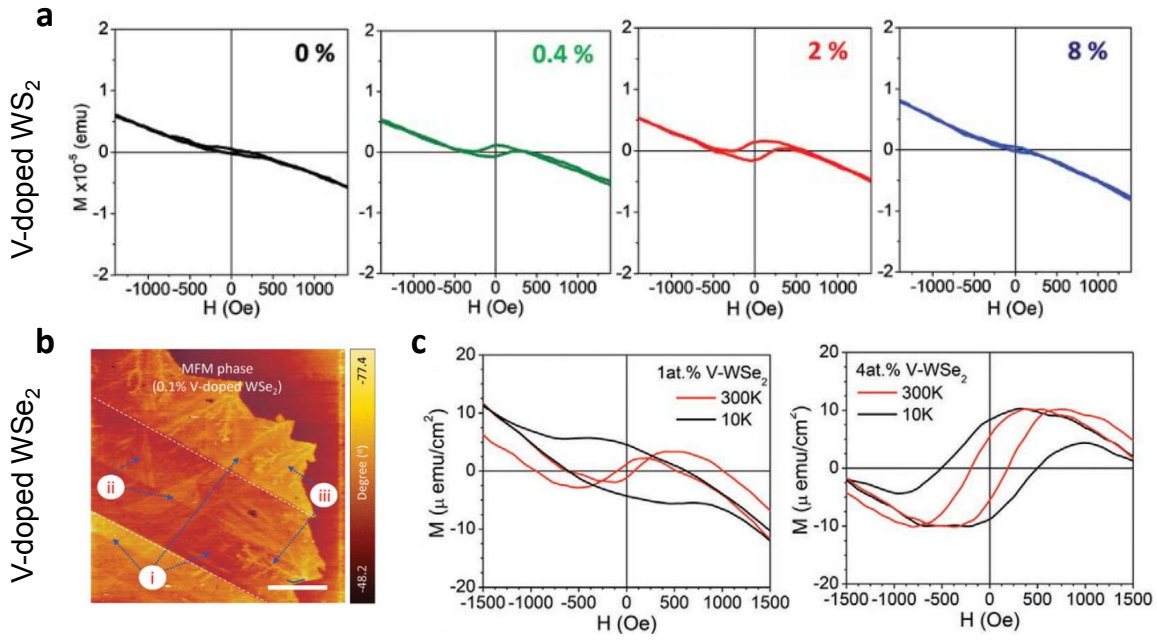

Figure 3.5 – **Room temperature ferromagnetism in vanadium-doped TMD monolayers. a** Room temperature magnetometry measurements for V-doped WS_2 monolayers showing the tunable magnetic response under increasing V doping. Adapted from: (44) **b,c** Magnetic force microscopy and magnetometry measurements for V-doped WS_2 monolayers. Adapted from: (42) and (43).

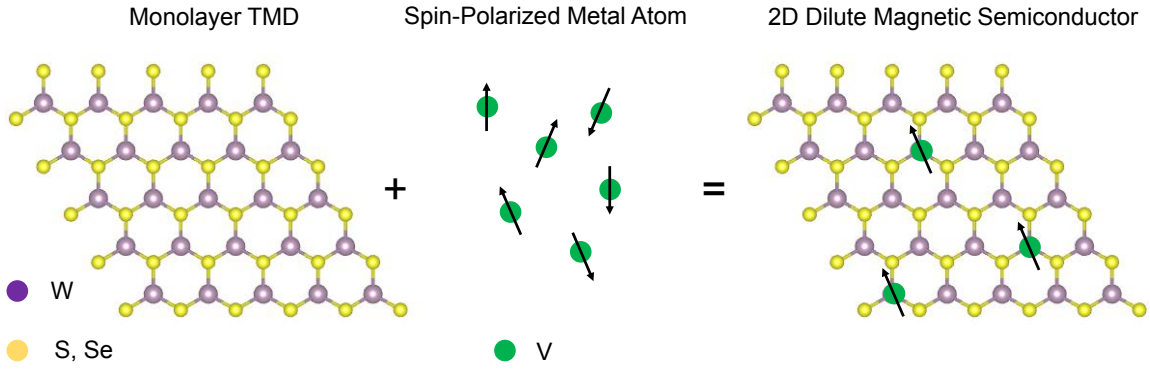

Figure 3.6 – **Schematic representation of a TMD DMS monolayer.**

3.3 2D Heterostructures

While 2D materials were being extensively studied and characterized, there was also a great effort on thinking of new ways to apply and discover novel physical phenomena using them. Thus, the idea of vertically stack distinct layered materials together and tune their properties emerged and ever since it is attracting a great interest due to the large possibilities of building new structures (46, 47, 48, 49, 32). For these vertical heterostructures, after isolating the monolayers of the chosen materials, they are assembled one on top of each other in the desired sequence by a transfer process (46). This

Lego-like atomically thin building blocks is schematically shown in Figure 3.7. The first heterostructure of 2D materials to be introduced was a monolayer of graphene stacked on top of few layers of h-BN, in 2010 (9). It was shown that h-BN is a good substrate because it is flat and has a smooth surface with a small number of dangling bonds and charge traps. After that, other heterostructures started to be experimentally introduced showing potential to be used beyond than for a substrate improvement (227, 228, 229).

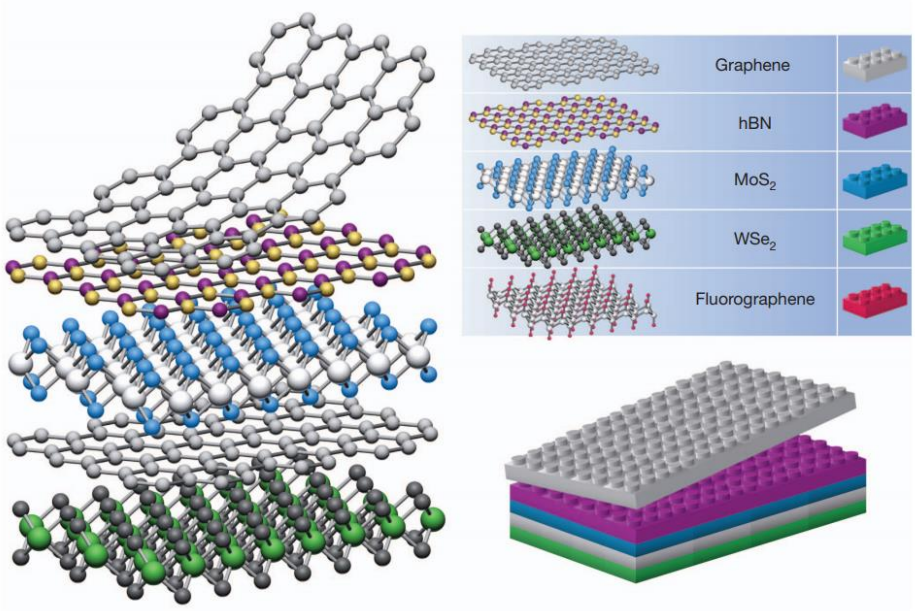

Figure 3.7 – **Vertical assembling representation of 2D materials in a heterostructure building process.** Adapted from: (46).

Likewise, the idea of building TMD vertical heterostructures have also attracted a great interest since their electronic properties as band gap, work function and spin-orbit coupling strength considerably vary between different TMD monolayers (230, 231, 98, 232), raising the possibility of tuning these properties in distinct ways. Therefore, several works started to be done on these heterostructures and theoretical results presented strong modifications in their electronic band structure with respect to each pristine monolayer that constitutes these stacked materials (233, 234, 142, 235). For instance, it has already been shown a moiré periodic potential due to a lattice mismatch or rotation between layers (234), expanding their engineering potential. Moreover, because of the band alignment between each TMD layer, the valence band maximum and the conduction band minimum can be placed in different monolayers. Hence, there is an emergence of a bound electron-hole pair where the electron and hole are in different layers, called as interlayer exciton (236, 237). In particular, interlayer excitons exhibit distinct properties that are not presented by conventional direct excitons, such as a longer lifetime (238, 239), electrical control of the optical and transport properties (240, 241, 242) and a quantum manipulation of a trapping periodic potential that arises from the moiré pattern(243). All these features make the

TMD heterostructures an excellent platform for exploring these new phenomena.

Beyond the vertical heterostructures, that is also another family of 2D assembled materials known as lateral heterostructures (LHs). While vertical heterostructures present an out-of-plane heterojunction between the layers, in the LHs this heterojunction is in-plane, which makes them useful for different applications. The heterojunctions are the lateral interfaces between the 2D materials in these heterostructures and they play a major role in the novel physical phenomena observed. For instance, the heterojunctions of TMD based LHs revealed themselves great candidates to be used as a p-n junction building blocks (49, 244) in optoelectronic devices. Besides, it has been probed a charge transfer phenomenon at the heterojunction of these LHs, which facilitates exciton dissociation and charges propagation (245). Figure 3.8 schematically shows the TMD lateral and vertical heterostructures as well as their charge transfer, interlayer exciton and moiré exciton features.

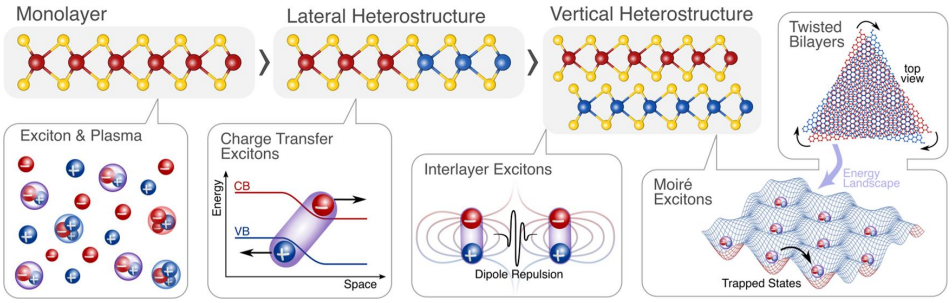

Figure 3.8 – **TMD heterostructures and their charge transfer, interlayer exciton and moiré exciton phenomena.** Adapted from: (246).

Despite all the effort in the past years to develop the TMD LHs fabrication, a high-quality and controllable growth method able to provide sharp and defect free heterojunctions remained challenging. The first and most reported growth technique of 2D TMD LHs is the sequential edge-epitaxy through chemical vapour deposition that have been implemented in distinct ways, such as: single-step (247, 248, 249), two-step (250, 251), multi-step (252), and one-pot (253) methods. The reasonable small lattice mismatch between the distinct TMD materials allows this epitaxial growth. However, to achieve a high standard growing process is not that simple. In the single step method, for example, there is a significant alloy formation in the heterojunctions, a limitation in the chosen pair of TMDs and a lack of control in the growth process. It happens because the single-step method place both TMD powders in the same boat and they are simultaneously heated to their vapour phase and condensed side by side in the substrate. Therefore, besides the noticeable absence of control, the simultaneously condensation do not enable a sharp transitions in the heterojunctions and requires TMDs that have similar growth parameters. On the other hand, the two- and multi-steps methods improved these points

by growing distinct materials domains separated in different chambers. Therefore, they present a larger growth control, a smaller formation of alloy and more freedom in the materials choice in comparison with the single-step method. Nonetheless, the chambers exchange exposes the edges to ambient contamination, compromising the purity of the heterojunctions. Recently, the one-pot method has experimentally shown to provide pure and atomically sharp heterojunctions in a controllable fabrication of these heterostructures (253). As in the single-step method, it uses a single solid source of TMD powders. The difference is the selectively growth of each material domain only by switching the carrier gas, allowing a pure and abrupt transition in the heterojunctions.

Until now, MoS_2−$MoSe_2$ (247), MoS_2−WS_2 (248, 254, 50, 253), MoS_2−WSe_2 (251), $MoSe_2$−WS_2 (252), $MoSe_2$−WSe_2 (249, 250, 50, 253, 255) and WS_2−WSe_2 (247, 252) are types of 2D TMD LHs already synthesized by those different growth methods. The heterojunctions of these LHs have been widely investigated by different techniques such as scanning transmission electron microscopy (STEM) (247, 248, 254, 50, 253, 251, 252, 249, 250, 255) and scanning probe microscopy (SPM) (254, 256), as well as Raman and photoluminescence (PL) spectroscopy (247, 248, 254, 50, 253, 251, 252, 249, 250, 255). Nevertheless, high excitation density phenomena and nonlinear effects have been barely explored in such heterostructures (50, 251, 246). Hence, these are subjects of study in this thesis.

4 Optical Techniques

In Chapter 2 we showed that many of the remarkable properties of 2D TMD materials are associated with their optical phenomena and electronic structure. Subsequently, in Chapter 3 we discussed about defects that are commonly present in TMD samples. Now, we will focus on how these defects can affect the optical and electronic properties of these materials. Thereunto, we will introduce some of the main linear and nonlinear optical techniques used to study TMDs. For each technique, we are going to show their potential for characterization and investigation of 2D TMDs, providing a review on the optical responses of distinct TMD defects and how they manifest through these different optical techniques.

4.1 Absorption Spectroscopy

In a classical perspective, light is described as an oscillating electric field. The electric field propagation depends on the refractive index of the medium, in which the imaginary part of the refractive index is related to the attenuation of the electric field amplitude (24), i.e., the absorption of light by the medium. In a dipole approximation, the Lorentz oscillator model shows that the absorption coefficient present resonances when the light frequency matches with the normal vibrational modes (24). However, although this approach reasonably explain some qualitative features of the light absorption, to understand the interband optical transitions in semiconductors we need to consider the particle behavior of light and the material band structure (24). As shown in Figure 4.1, semiconductors present a band gap between their valence and conduction bands, which can be direct or indirect in momentum. For a direct band gap semiconductor, an optical interband transition might only happen if the photon energy $\hbar\omega$ is greater than the band gap energy E_g. In an indirect band gap semiconductor, besides the energy threshold there is also a momentum conservation to be satisfied. As the photon momentum can be neglected in this scenario, the indirect interband transition should be mediated by a phonon, which diminishes the absorption quantum yield.

The transition rate for a direct optical absorption can be given by the Fermi golden rule (24):

$$W_{i\to f} = \frac{2\pi}{\hbar}|M|^2 g(\hbar\omega), \tag{4.1}$$

in which $W_{i\to f}$ is the transition rate between initial and final electronic quantum states, $M = \langle f|\,|H'|\,|i\rangle$ is the matrix element that describes the effect of the light perturbation

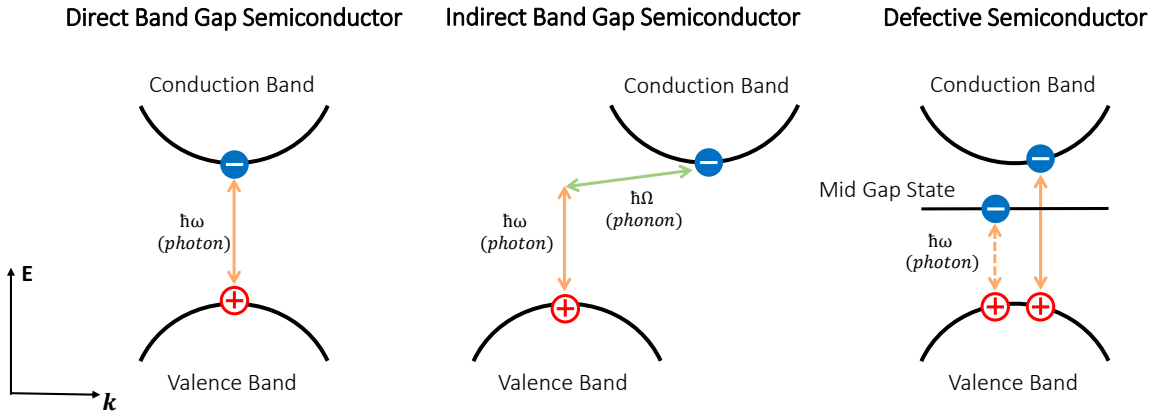

Figure 4.1 – **Light absorption and emission processes in direct, indirect and defective semiconductors.**

Hamiltonian H' on the electrons and $g(\hbar\omega)$ is the joint density of states that depend on the energy difference $\hbar\omega$ between the initial and final states. Hence, we can observe that this description consider the quantum character of the light-matter interaction as well as the band structure of the material. In an experimental point of view, for 2D materials both sample and substrate will contribute in the light absorption. Therefore, the material absorption coefficient $\alpha(\hbar\omega)$ can be calculated from the relative difference between the sample and substrate reflection spectra R_{sample} and $R_{substrate}$, respectively, being known as a differential reflectance (or contrast reflectance) measurement (257):

$$\frac{\Delta R}{R} = \frac{R_{sample} - R_{substrate}}{R_{substrate}} = \frac{4n_{sample}}{n_{substrate}^2 - 1}\alpha(\hbar\omega), \tag{4.2}$$

where n_{sample} and $n_{substrate}^2$ are the sample and substrate refractive indexes, respectively.

Figure 4.2 shows the differential reflectance spectra of distinct 2D TMDs (258). Conversely to the threshold behavior with respect to the band gap commented above, these 2D materials present resonant absorption responses even below the band gap (257, 258). As discussed in Chapter 2, these observed peaks are related to excitons in these materials, which displays an energy smaller than the energy of the band-to-band transition (Equation 2.3). Moreover, as we discussed in Chapter 3 several reported defects in TMD monolayers introduce mid gap states in these materials (see Figure 4.1), modifying the electronic transitions in these materials. Hence, defective TMDs can also present additional lower energy peaks in their absorption spectra related to the optical transitions to the mid gap states (259). Thus, absorption measurements are capable of probing excitonic features as well as defect states in 2D TMDs.

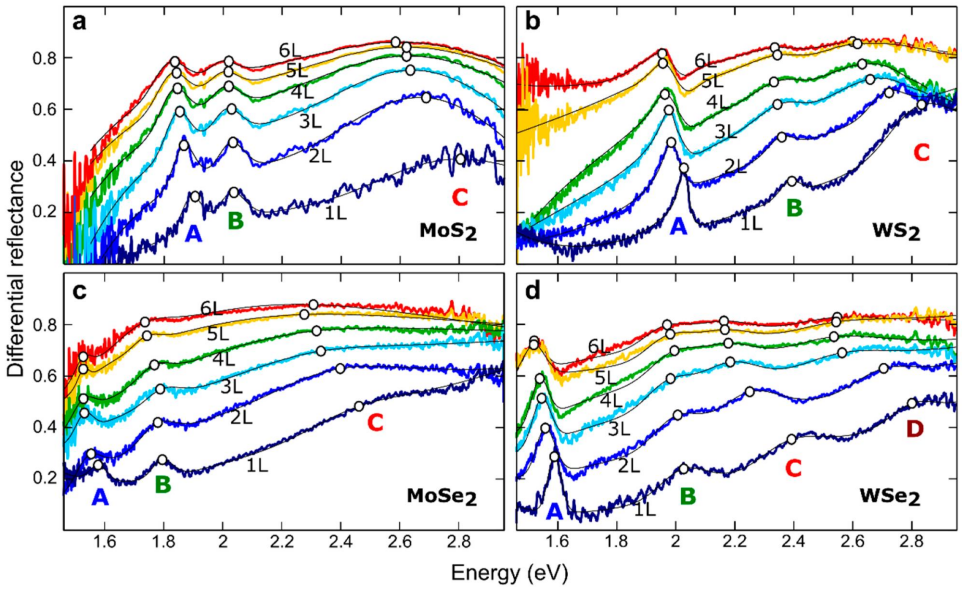

Figure 4.2 – **Differential reflectance spectra of different TMDs with distinct thicknesses, showing their excitonic resonances.** MoS_2, $MoSe_2$ and WS_2 mono and fewlayer samples exhibit absorption peaks related to their A, B and C excitons, while WSe_2 samples also present a forth absorption resonance that is being called as a D transition. Adapted from: (258).

4.2 Photoluminescence Spectroscopy

Excited electrons in the conduction band of a semiconductor always tend to return to their fundamental state, i.e., to the valence band. Thereunto, two distinct transition mechanisms can happen: radiative and/or nonradiative recombinations. The transition is radiative when the electron energy loss occurs through a photon emission, while the nonradiative does not involve light and is generally related to the creation of phonons. If the electron is excited above the conduction band minimum, there are usually multi-step nonradiative intraband relaxation processes until it reaches the bottom of the conduction band. From this point, for a pristine sample the interband transition to the valence band maximum must be direct (in the sense of a single-step transition), and there is a probability dispute between the radiative and nonradiative decays. For direct band gap semiconductors, the radiative recombination probability overcomes the non-radiatiive path, presenting thus optical transitions strongly associated with light emission. On the other hand, the radiative transition in indirect semiconductors is less efficient, resulting in a lower light emission. These processes are also represented in Figure 4.1 and they depict why the direct band gap TMD monolayers present a remarkable light emission with respect to the indirect band gap multilayers.

The light emission phenomenon associated with an optical transition have different names depending on the origin of the electronic excitation. For instance, when the excitation

comes from an electric current, this luminescence process is called electroluminescence. In this thesis we are more interested in another process: when the light emission follows light absorption, which is known as the photoluminescence (PL) effect. As well as for the light absorption, the light emission intensity in a direct semiconductor is also proportional to the square of the matrix element and to the joint density of states (Equation 4.1). However, the PL intensity will also depend on the occupancy level of the conduction band where the transition comes from.

Since excitons play a significant role in 2D TMDs, their PL is also dominated by excitonic responses. And similarly to the absorption transitions, defects can also modify the electronic decays in these materials. Distinct defects will affect the TMD PL in different ways, but their main modifications are usually related to the PL emission intensity, energy, spectral shape, dynamics and new peaks. Defects can act both as introducing or suppressing nonradiative decay channels, which impacts the radiative transition probability and therefore the PL intensity. As defects can change the structural parameters of TMDs, a band structure renormalization might happen, leading to a distinct band gap and an energy shift in the PL peaks. The PL spectral shape should also reveal the presence of defects, as the broadening of the PL linewidth can be related to the inhomegeneity of the electronic properties over the sample. The dynamics of the optical transition would also be modified by defects, as will be discussed in section 4.5. Besides, the introduction of defective mid gap states can lead to lower energy PL peaks, that are in general highly dependent on the temperature and the pumping power. Regarding the optical transition associated with the conduction band, in a low excitation regime there will always be unoccupied states for electrons to be excited. Therefore, doubling the pumping power means doubling the occupancy level at the conduction band, which will also double the PL intensity. On the other hand, defective mid gap states are localized, which means that they present few empty states. Hence, from a certain pumping power there is an occupancy level saturation, and the defective PL peak will not linearly increase with the incident power (260). Also because of the localization character of the defective mid gap states, at higher temperatures electrons might escape from these levels through thermally induced nonradiative recombinations. Therefore, the lower energy PL peaks associated with defects are usually more intense (or are only present) at low temperatures.

Carozo *et al.* (83) have probed the impact of vacancies in an as-grown WS_2 monolayer through PL measurements. They have shown a higher presence of sulfur vacancies at the monolayer edges corresponding to a lower energy PL peak, as shown in Figure 4.3a. Later, Mitterreiter *et al.* (170) performed annealing and He-ion bombardment in a MoS_2 monolayer to study how the desorption of adsorbents and the generation of vacancies impact the sample light emission. As displayed in Figure 4.3b, they showed a broad PL peak associated with adsorbed atoms and molecules in contrast to a narrow PL response coming from the localized vacancy states. The PL emission related to atomic and

molecular adsorbents was also investigated in aged WS_2 monolayers (189). While fresh samples presented no defective PL peaks, the aged samples displayed a broad lower energy PL peak due to the adsorption of oxygen and organic molecules. This broad character of the light emission associated with these adsorbents was explained by the large number of defective states that they introduced in the material gap (189). Oxygen also play a major role in the TMD monolayer light emission by passivating defects. Its adsorption at MoS_2 and WS_2 edges and/or vacancy sites suppresses nonradiative decay channels and promotes an exchange between trion and exciton populations owing to changes in the sample doping, inducing an enhancement of the PL intensity (77, 182).

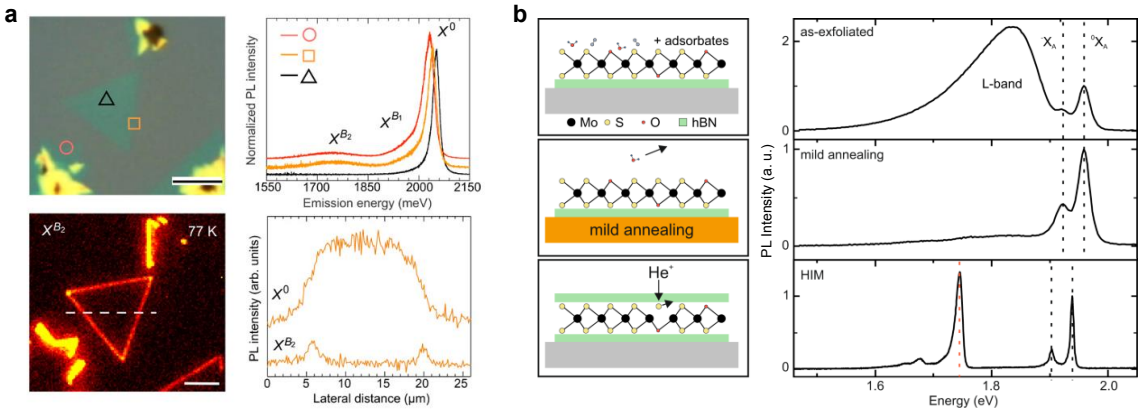

Figure 4.3 – **Low temperature PL spectra of MoS_2 monolayers with sulfur vacancies and adsorbents. a** Optical image, low temperature PL spectra, PL mapping and PL intensity profiles of a MoS_2 monolayer with sulfur vacancies showing a low energy peak at the sample edges. Adapted from: (83). **b** Low temperature PL spectra of a MoS_2 monolayer with adsorbents and sulfur vacancies after annealing and He-ion bombordment. Adapted from: (170).

Substitutional dopants can also deeply affect the light emission of TMD monolayers. Beyond the introduction of donor or acceptor levels, these dopants might also shift the valence and conduction bands of the TMD sample, leading to modifications in the intensity and energy of PL peaks. For instance, Nb-doped MoS_2 (261) and WS_2 (262) monolayers display an enhanced, broadened and redshifted PL emission with respect to the pristine samples. Co-doped MoS_2 monolayers present a blueshifted A exciton PL peak with a reduced intensity and the emergence of a higher energy PL peak (40). A PL quenching is noted for Re- (263) and Mn-doped (264) MoS_2 monolayers as well. However, MoS_2 monolayers doped with Re present an energy redshifting, while the Mn-doped samples show a blueshifting in its PL emission. A reduction in the PL intensity is also observed for Fe-doped MoS_2 and WS_2 monolayers, corresponding to a blueshift and a redshift in energy, respectively (222, 41, 265). In a V-doped WSe_2 monolayer the trion PL peak overcomes the exciton emission, whereas a lower energy PL peak emerges due to V defective levels inside the gap (266, 267). Finally, V-doped WS_2 monolayers also exhibit two quenched PL peaks in contrast with the single A exciton PL peak from the pristine WS_2 (44, 268).

Nonetheless, the origin of these peaks still lacks investigation and were thus object of study of this thesis as it is going to be presented in Chapter 6. Figure 4.4 shows some of these PL modifications related to substitutional dopants commented above.

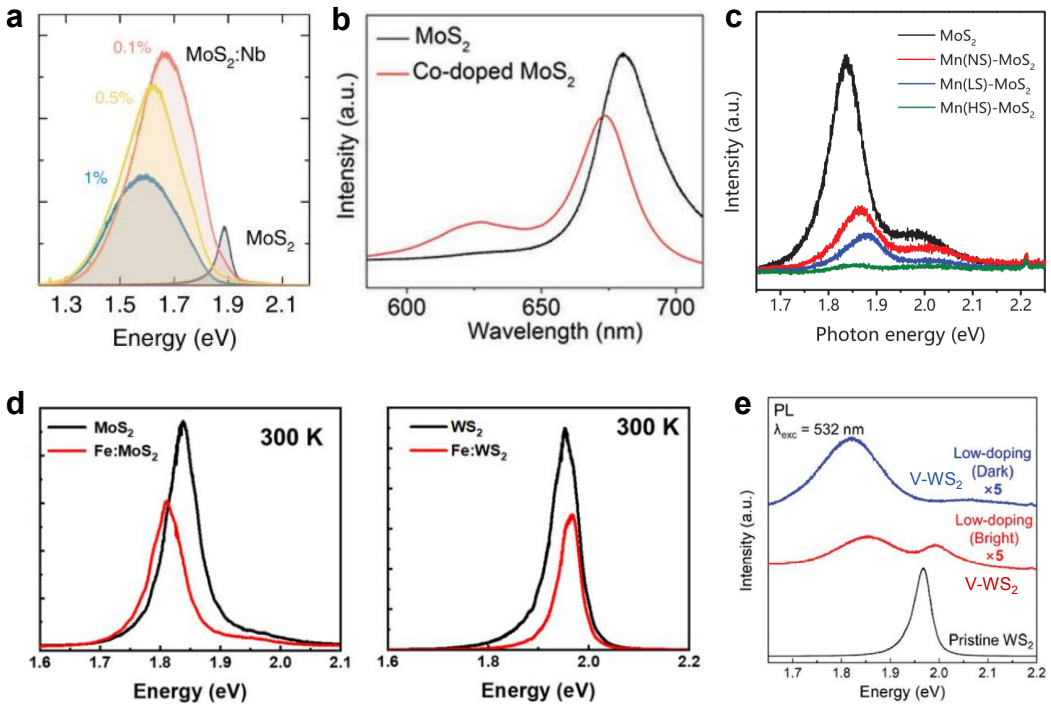

Figure 4.4 – **PL spectra of TMD monolayers doped with transition metal atoms.** Adapted from: (261) (**a**), (40) (**b**), (264) (**c**), (265) (**d**), and (268) (**e**).

Another defect that impacts the PL features of TMD monolayers is grain boundaries. To investigate the modifications in the light emission of TMD samples due to defects restricted to a specific region — such as grain boundaries —, PL mappings are usually employed. As discussed in Chapter 3, the relative orientation and the edge termination of the grains influence the grain boundary properties. However, in general the PL emission of grain boundaries is enhanced and blueshifted with respect to the middle of the grain (71, 79, 192, 178), as shown in Figure 4.5. PL mappings are also performed to investigate other spatial inhomogeneities related to defects. For instance, through PL mapping we revealed that CVD grown WS_2 monolayers present a line from the flake center to their convex vertexes in which the introduction of dopants is energetically favorable (178). Although confocal PL mapping is a powerful tool, it is worth to comment that it presents a spatial resolution limitation of hundreds of nanometers due to the diffraction limit of light. To overcome this limitation, near-field optical techniques can be used, as will be discussed in section 4.4.

Strain fields are another source of disturbance in the light emission of TMDs. Strain causes a renormalization of the band structure of TMD samples, and thus shifts in the PL emission are generally related to this defect (269, 270, 198). As shown in Figure

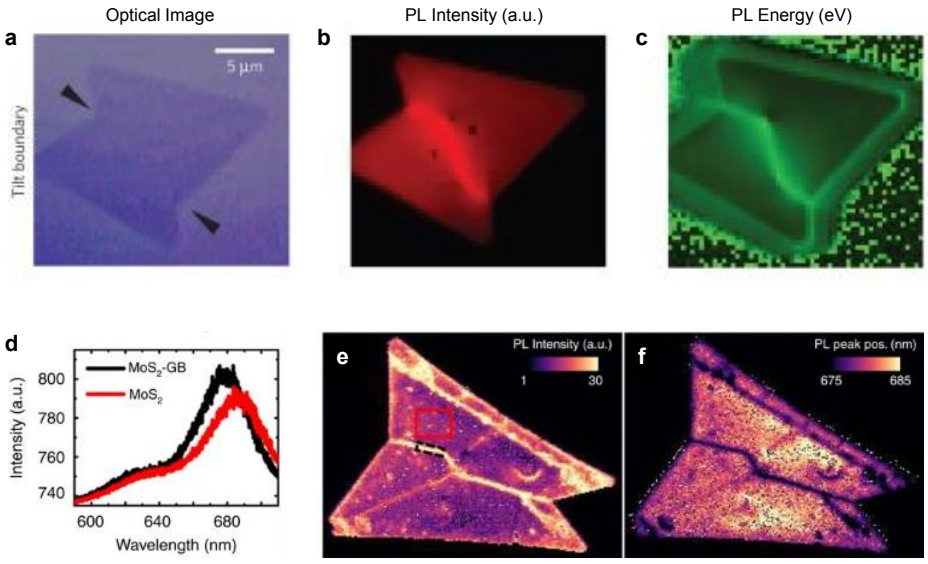

Figure 4.5 – **PL mapping of MoS_2 monolayers showing an enhanced and blueshifted emission from grain boundaries.** Adapted from: (71) (**a-c**) and (192) (**d-f**).

4.6a, it is possible to engineer strain field in TMDs, providing an external control of the energy of the PL peaks of these materials (269, 270, 198). Moreover, as the renormalization of the electronic bands is not the same for distinct valleys, it is possible to induce a transition from an indirect to a direct band gap (or the contrary) by applying a tension in the sample. For instance, WSe_2 multilayers have shown a remarkable enhancement in their PL emission from a certain percentage of strain due to a transition to a direct band gap (271), as displayed in Figure 4.6b.

4.3 Raman Spectroscopy

When light interacts with matter distinct phenomena can happen beyond absorption, such as reflection, transmission, refraction, diffraction and scattering. The later one is usually an elastic process, i.e., the scattered light has the same energy of the incident light. This elastic scattering is called as Rayleigh scattering. Besides, although less efficient, there is also an inelastic scattering of light that provides information about the medium. This inelastic effect is known as Raman scattering and it is employed to investigate vibrational properties of several materials, since the energy difference between the incident light and the Raman scattered light is related to the energy of the normal vibrational modes of the material. In a classical analysis, the scattered light will depend on the material polarization $\boldsymbol{P}$ induced by its interaction with the incident oscillating electric field $\boldsymbol{E} = \boldsymbol{E_0}\cos(\boldsymbol{kr} - \omega t)$, in which $\boldsymbol{k}$ is the wave vector and ω is the frequency of the incident light. This relation is mediated by the material susceptibility tensor $\boldsymbol{\chi}$ (272):

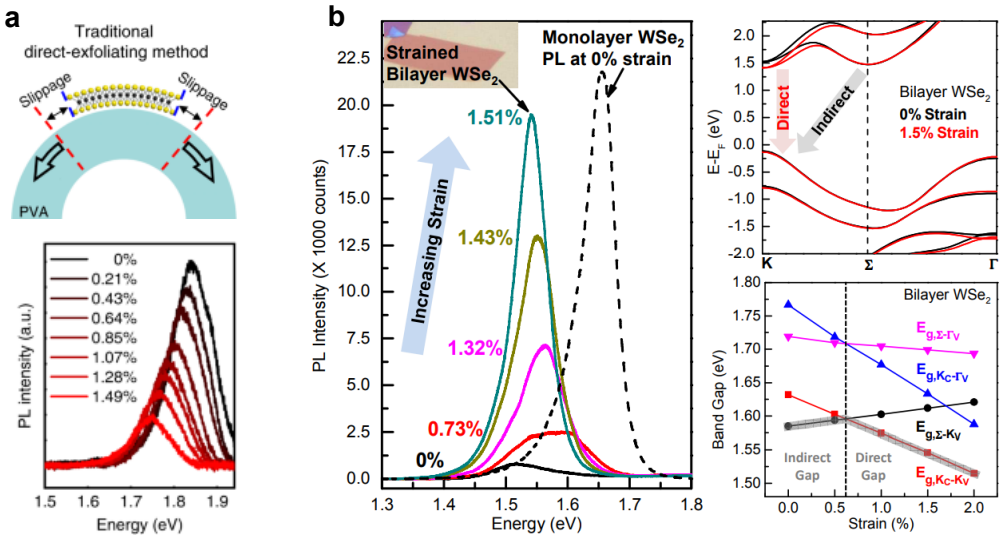

Figure 4.6 – **Strain engineering in 2D TMDs. a** PL spectra of a MoS_2 monolayer revealing a controlled energy redshifting under increasing tensile strain. Adapted from: (198). **b** Indirect to direct band gap transition in a WSe_2 bilayer induced by strain. Adapted from: (271).

$$\boldsymbol{P} = \epsilon_0 \boldsymbol{\chi} \boldsymbol{E}, \tag{4.3}$$

where ϵ_0 is the free space permittivity. The susceptibility tensor, in its turn, is dependent on the the electric field frequency ω and the material oscillations $\boldsymbol{Q} = \boldsymbol{Q_0} \cos(\boldsymbol{qr} - \omega_0 t)$, in which $\boldsymbol{q}$ is the wave vector and ω_0 is the frequency of a normal vibration mode of the material. In a first approximation we can expand $\boldsymbol{\chi}(\omega, \boldsymbol{Q})$ in a Taylor series and consider the first two terms. Hence, the material polarization can be written as (272):

$$\boldsymbol{P} = \epsilon_0 \left[\boldsymbol{\chi(\omega, 0)} + \left(\frac{\partial \boldsymbol{\chi}}{\partial \boldsymbol{Q}} \right) \Bigg|_{Q=0} \boldsymbol{Q_0} \cos(\boldsymbol{qr} - \omega_0 t) \right] \boldsymbol{E_0} \cos(\boldsymbol{kr} - \omega t), \tag{4.4}$$

in which $\left(\frac{\partial \boldsymbol{\chi}}{\partial \boldsymbol{Q}}\right)$ is the polarizability of the material. Following, the polarization equation can be expanded as (272):

$$\boldsymbol{P} = \epsilon_0 \boldsymbol{\chi(\omega, 0)} \boldsymbol{E_0} \cos(\omega t) + \epsilon_0 \left(\frac{\partial \boldsymbol{\chi}}{\partial \boldsymbol{Q}} \right) \Bigg|_{\boldsymbol{Q}=0} \boldsymbol{Q_0 E_0} \cos(\boldsymbol{qr} - \omega_0 t) \cos(\boldsymbol{kr} - \omega t). \tag{4.5}$$

The first term of Equation 4.5 presents the same frequency ω of the incident electric field, being thus associated with the Rayleigh scattering. On the other hand, by multiplying the cosine functions of the second term we have:

$$\cos(\boldsymbol{qr} - \omega_0 t) \cos(\boldsymbol{kr} - \omega t) = \frac{1}{2} (\cos[(\boldsymbol{k} + \boldsymbol{q})\boldsymbol{r} - (\omega + \omega_0)t] + \cos[(\boldsymbol{k} - \boldsymbol{q})\boldsymbol{r} - (\omega - \omega_0)t]).$$

Therefore, the second term of the polarization vector is related to the Raman scattering, that presents scattered frequencies of $\omega - \omega_0$ (Stokes shift) and $\omega + \omega_0$ (anti-Stokes shift), which can be used to investigate the vibrational modes ω_0 of the material. Looking at Equation 4.5, we should note that a vibrational mode is active in Raman only if its polarizability is nonzero, making the active Raman and infrared modes different (272). Furthermore, as the susceptibility tensor is also dependent on the incident light frequency ω, the intensity of the Raman scattering should also vary with the excitation energy. However, to have a better understanding of this excitation energy dependence a quantum description of the Raman scattering is required.

In a quantum perspective, the Raman scattering can be understood in terms of the creation or annihilation of a phonon. A first order Raman effect involves three quantum processes: an electronic transition from an initial state $|i\rangle$ to an intermediate state $|a\rangle$, a phonon creation or annihilation leading the system to another intermediate state $|b\rangle$, and an electronic decay to a final state $|f\rangle$. Solving the Schrodinger equation of this third order process with time dependent perturbation theory, the Raman intensity can be given by the following Fermi golden rule (273):

$$I(E_{pump}) = C \left| \sum_{a,b} \frac{\langle f|H_{e-r}|b\rangle\langle b|H_{e-ph}|a\rangle\langle a|H_{e-r}|i\rangle}{(E_g - E_{pump} + i\gamma)(E_g - E_{pump} + E_{ph} + i\gamma)} \right|^2, \tag{4.6}$$

in which the numerator present the matrix elements of the absorption of the incident photon, the creation of one phonon and the emission of the scattered photon mediated by the Hamiltonians of the electron-radiation (H_{e-r}) and electron-phonon (H_{e-ph}) interactions. The resonant behavior of the first order Raman scattering is presented in the two terms of the denominator, in which there is an enhancement of the Raman intensity when the energy of the incident (E_{pump}) or scattered ($E_{pump} - E_{ph}$) photons matches with the allowed electronic transitions energies (E_g). Finally, E_{ph} is the phonon energy related to an specific Raman mode and γ is the damping factor associated with the inverse lifetime of the excited electronic state. This resonant Raman process is schematically represented in Figure 4.8. For 2D TMDs, Raman resonances are strongly dependent on excitonic effects, in which E_g are thus the energies of the exciton states. For instance, Del Coro *et al.* (52, 274) have investigated the Raman excitation profile of WSe_2 and WS_2 samples, revealing enhanced Raman intensities in resonance with distinct excitons of these materials, as shown in Figure 4.7.

The quantum processes associated with the first order Raman scattering are presented in Figure 4.8. It is worth commenting that the momentum of the incident and scattered photons is negligible in comparison with the momenta of the phonons outside the Γ point in the Brillouin zone of TMDs. Therefore, first order Raman processes in pristine TMD samples only create or annihilate phonons close to the Γ point (i.e., with

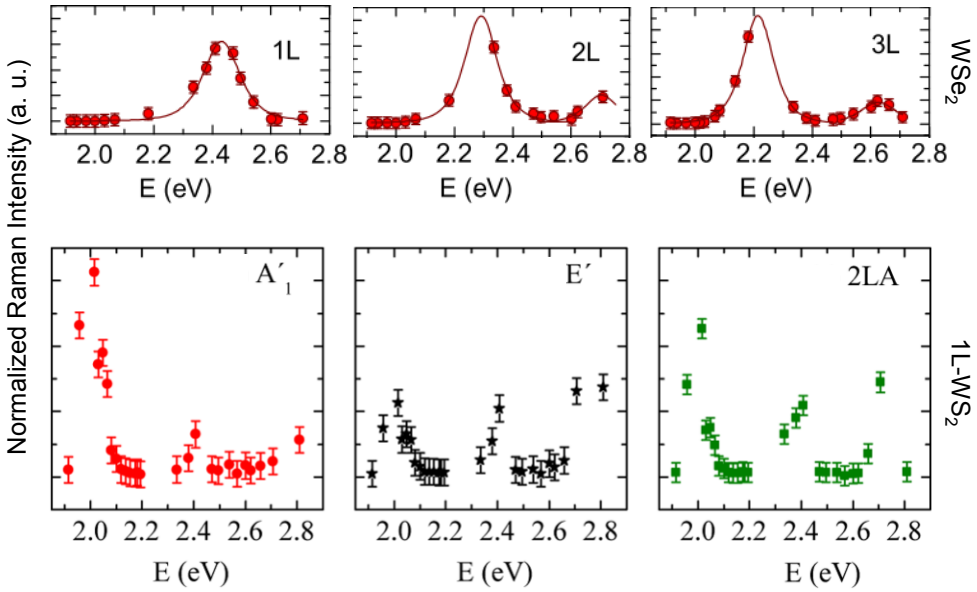

Figure 4.7 – **Raman excitation profiles (REPs) of 2D TMDs.** Top graphs: WSe_2 monolayer, bilayer and trilayer REPs related to their degenerated A_{1g}+E_{2g} modes. Adapted from: (52). Bottom graphs: WS_2 monolayer REPs related to its A_{1g}, E_{2g} and 2LA modes. Adapted from: (274).

$q \sim 0$) to obey the momentum conservation (273). Phonons outside the Γ point can be created or annihilated in a second order Raman effect, represented in Figure 4.8. This second order scattering involves two phonons, and if their wave vectors q present opposite directions it is possible to conserve momentum (273). This momentum conservation can also be respected for phonons with finite q in a first order Raman process in a defective TMD sample, since defects can scatter electrons with the required momentum (273). Thus, Raman spectroscopy is a powerful tool to probe defects in 2D TMDs. To exemplify these commented features, Figure 4.9 shows Raman spectra of a pristine and defective MoS_2 monolayers. While the pristine sample only displays the first order $E_{2g}(\Gamma)$ and $A_{1g}(\Gamma)$ modes and the second order 2LA(M) mode, defective monolayers also presented the first order LA(M) mode (275).

Beyond the emergence of first order Raman modes outside the Γ point, defects can also affect the intensity, frequency and linewidth of Raman peaks in 2D TMDs. Similarly to PL, strain engineering can be used to tune the frequency of Raman modes in TMD samples (276, 277, 270, 198), as shown in Figure 4.10a. The E_{2g} mode displays a stronger frequency shifting with respect to the A_{1g}. Besides, from a certain strain value the E_{2g} Raman peak is splitted in two due to a lattice symmetry breaking (276, 277, 270, 198). Electrical doping provokes Raman frequency shifting and broadening as well. But contrary to strain, the frequency and linewidth of the A_{1g} peak are more sensitive to doping effects than the E_{2g} mode (278), as displayed in Figure 4.10b. Finally, other defects such as vacancies (279), substitutional dopants (176) and grain boundaries (192) are also commonly related to

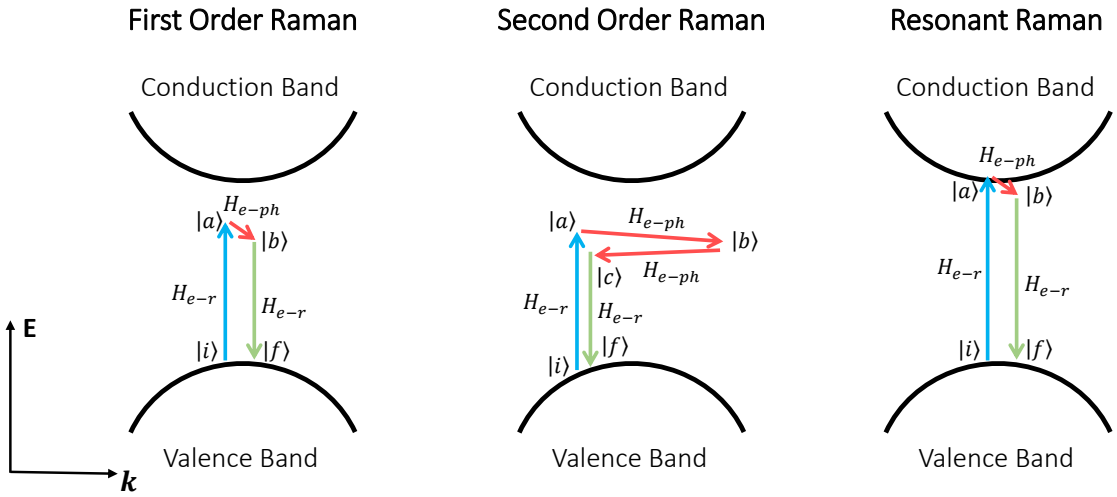

Figure 4.8 – **First order, second order and resonant Raman processes representation.**

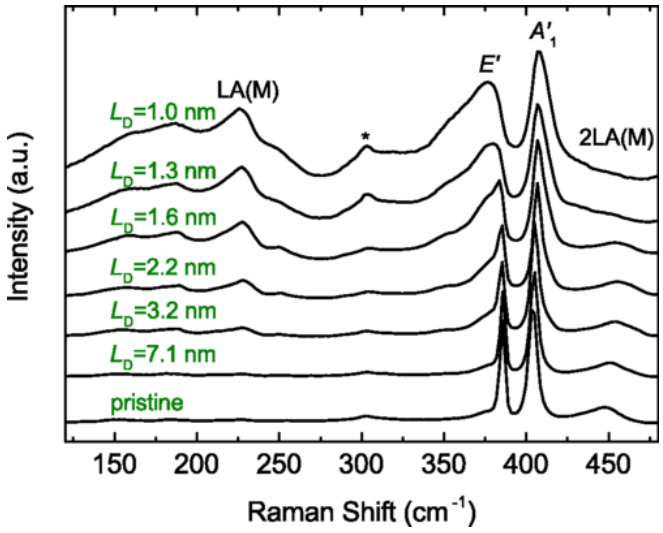

Figure 4.9 – **Raman spectra of MoS_2 monolayers showing an increased intensity of the LA mode with respect to the defect concentration.** The defect concentration is indirectly given by L_D, that is the mean distance between defects. Adapted from: (275).

modifications in the Raman modes, since they might induce doping effects and changes in the TMD lattice parameters.

4.4 Tip-Enhanced Photoluminescence and Raman Spectroscopies

As discussed so far, confocal optical techniques such as PL and Raman spectroscopies are ideal for probing optical features that exhibit a μm-scale uniform response in 2D TMD samples. However, when these samples present a nanoscale inhomogeneity,

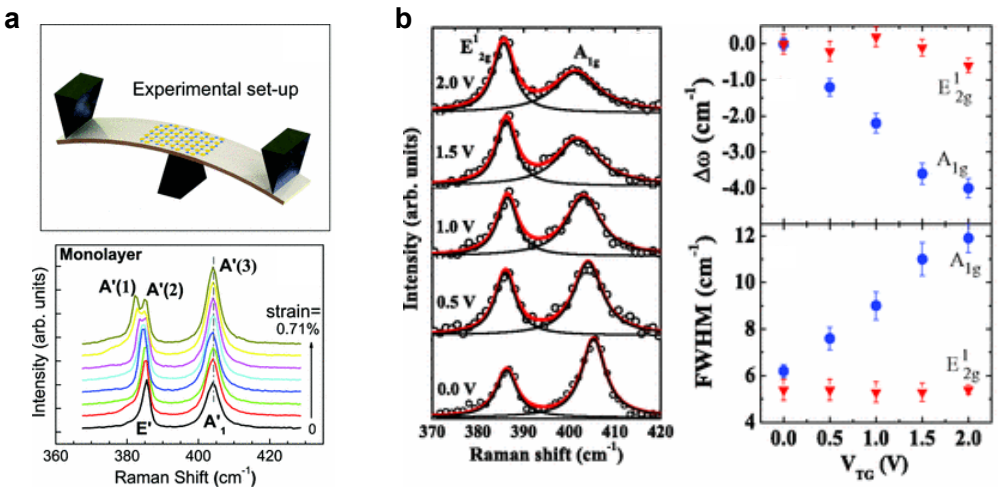

Figure 4.10 – **Strain and doping effects in the Raman spectra of MoS_2 monolayers.** **a** Raman spectra of a MoS_2 monolayer revealing an energy shift and splitting of the E_{2g} mode under increasing strain. Adapted from: (276). **b** Raman spectra of a MoS_2 monolayer showing an energy shift and broadening of the A_{1g} mode under increasing doping. Adapted from: (278).

we might consider the diffraction limit of light. According to Abbe (280), two punctual objects can be resolved if their distance Δx is greater than:

$$\Delta x > \frac{0.61\lambda}{n \sin\theta}, \tag{4.7}$$

where λ is the wavelength of light, n is the refractive index of the medium and θ is the maximum angle with respect to the normal direction in which light is collected. Besides, $n \sin\theta$ is also called the numeric aperture (NA) of an objective lens. Therefore, by using light with a lower wavelength and objective lens with high NA to collect more wave vector components of the emitted light it is possible to improve the spatial resolution of the measurement. However, for excitations in the visible range, the best spatial resolution that can be achieved is still in the hundreds of nanometers (even using oil immersion objectives with NA values greater than 1). This happens because there is also an evanescent part of the wave that does not propagate far from the vicinity of the emitting source (280), which is thus not detected by confocal measurements. And as the evanescent field intensity exponentially decays in few nanometers, there is no superposition between the evanescent components from emitting sources that are spatially separated by more than a dozen of nanometers (280). Therefore, a possible mechanism to improve the spatial resolution involves collecting this near-field light emission (280).

There are distinct near-field optical techniques that have shown an improvement in the spatial resolution, such as scanning near-field optical microscopy (SNOM) and tip-enhanced photoluminescence (TEPL) and Raman spectrocopy (TERS). In this thesis

we will focus on the tip-enhanced optical spectroscopies. This tip-enhanced technique combines a confocal spectroscopy with a scanning probe microscopy, as schematically represented in Figure 4.11. The objective lens focus the incident light on the sample, while the scanning probe tip — placed few nanometers above the sample — acts like an antenna that enhances and propagates the near-field component of the emitted light due to a plasmonic effect (280). As the near-field amplitude becomes much stronger than the far-field signal, the detected light in this tip-enhanced measurements is dominated by the evanescent field. Therefore, the measured optical response is dominated by the localized emission that interacts with the antenna, and the spatial resolution of the measurements is thus determined by the tip diameter (280). Hence, these tip-enhanced optical techniques are powerful tools to investigate nanometric features associated with defects in 2D TMDs (56, 57, 58, 59).

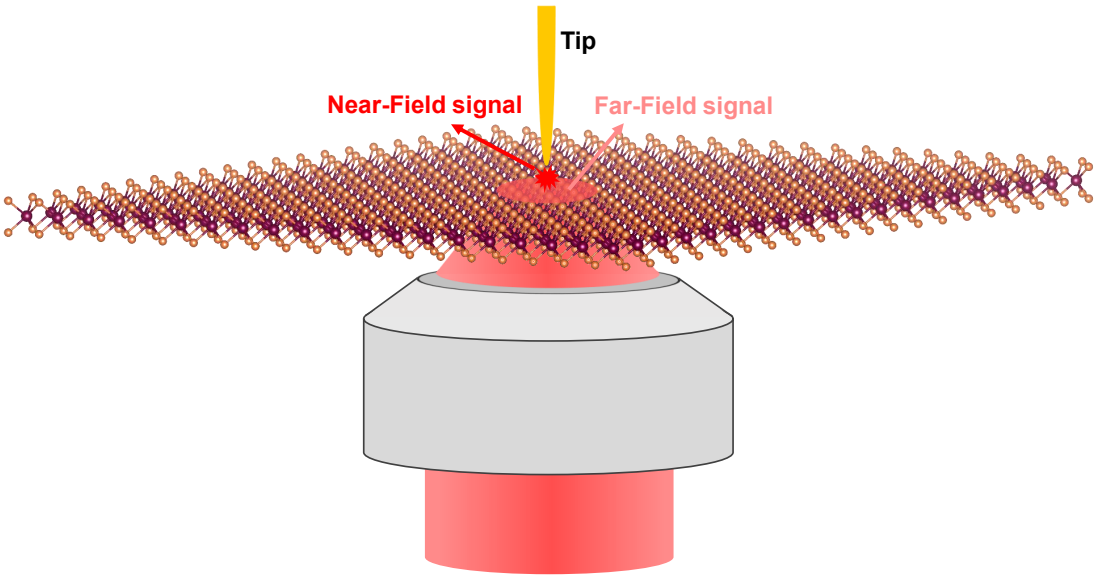

Figure 4.11 – **Representation of the tip-enhanced optical spectroscopy concept.**

Grain boundaries, edges, strain, wrinkles, lateral interfaces and other inhomogeneities are examples of defects that have already been probed by TEPL and TERS measurements in TMD samples (56, 57, 58, 59). For instance, a distinct light emission was observed in nanometric width regions at MoS_2 monolayer edges. As shown in Figures 4.12a,b, TEPL measurements revealed an enhanced and blueshifted PL emission at these edges (281). TERS measurements was also employed to study the electron-phonon interactions at 2D MoS_2 edges. It was demonstrated that edges in a MoS_2 bilayer and between MoS_2 monolayers and bilayers can induce a Raman mode at 396 cm^{-1} activated by a double resonance Raman scattering process (282). Moreover, the distinct A_{1g} mode frequency shifting at different MoS_2 edges showed a new method to determine the edge termination type in these materials (282), as displayed in Figure 4.12c. Another defect that has also been investigated by TERS and TEPL measurements is strain. Nanoscale

strain fields can be either engineered in TMD samples by transferring them on top of a nanostructure (283) as well as occasionally generated by the emergence of wrinkles or bubbles during the exfoliation process (284, 285). TERS and TEPL mapping showed to be capable of measure the strain magnitude induced by Au nanostructures in a MoS_2 monolayer (283) and probe a very narrow wrinkles in a WSe_2 monolayer (285), MoS_2 monolayer (284) and MoS_2 twisted bilayer (286), as shown in Figure 4.13. TEPL and TERS measurements also revealed optical features from nanoscale heterojunctions of TMD lateral heterostructures. For instance, Shao *et al.* (287) studied the atomic diffusion in a bilayer WS_2/MoS_2 heterojunction with TERS and TEPL mapping, while Sahoo *et al.* (256) determined the alloy formation and analyzed aging effects in distinct interfaces of a monolayer $WSe_2/MoSe_2$ lateral heterostructure through TEPL measurements.

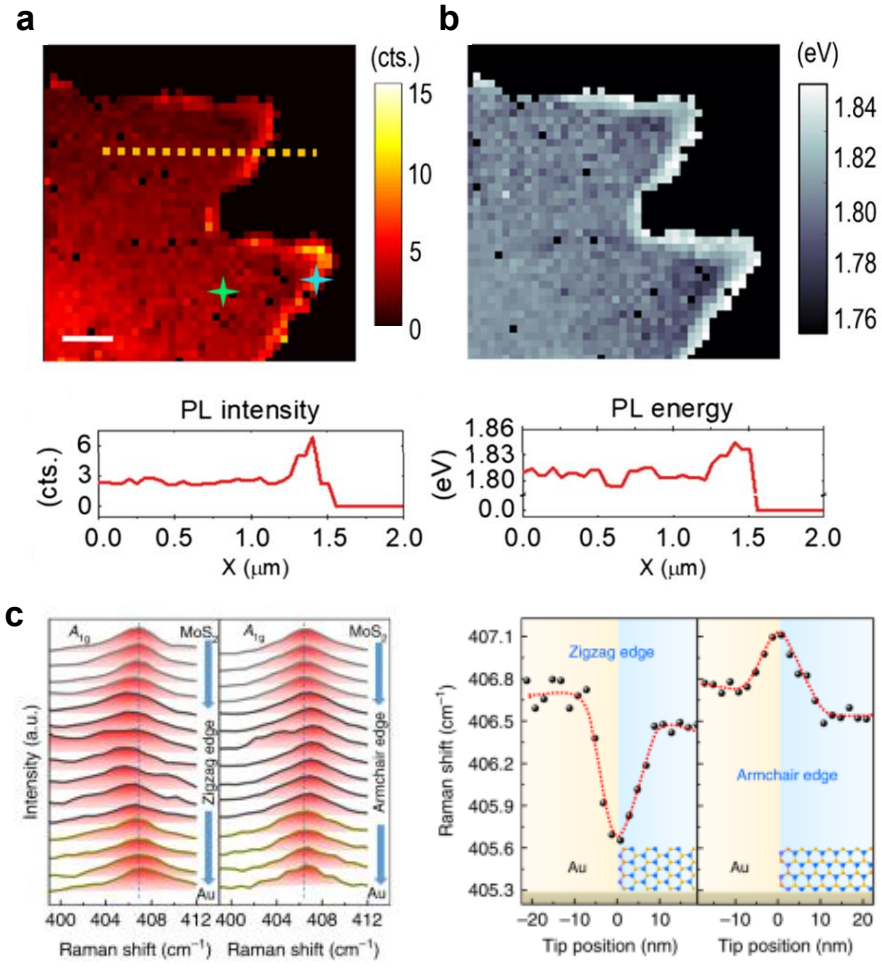

Figure 4.12 – **Tip-enhanced optical techniques probing edges in MoS_2 monolayers. a,b** TEPL mapping of a MoS_2 monolayer showing an enhanced and blueshifted emission at its edges. Adapted from: (281). TERS spectra along MoS_2 monolayer edges revealing the distinct frequency shifting of the A_{1g} mode in zigzag and armchair edges. Adapted from: (282).

As commented in section 4.2, although confocal PL measurements probed optical

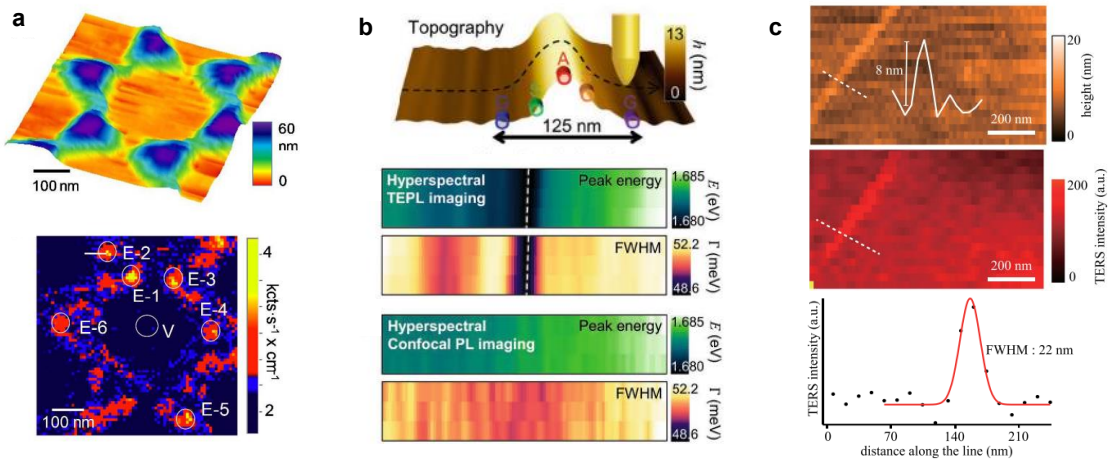

Figure 4.13 – **Nanoscale strain engineering in TMD monolayers probed by tip-enhanced optical techniques. a** AFM measurement and TERS intensity map of a MoS_2 monolayer on top of Au nanostructures showing an enhanced Raman intensity in the strained regions. Adapted from: (283). **b** TEPL mappings of a WSe_2 monolayer showing a redshifted and narrower light emission at a wrinkle region. Adapted from: (285). **c** TERS intensity map of a MoS_2 monolayer showing an enhanced Raman intensity at a wrinkle. Adapted from: (284).

modifications in grain boundaries, their spatial resolution limitation lead to averaged responses of a μm-scale region that contains this defect. Therefore, to specifically probe the grain boundary light emission TEPL and TERS mapping should be employed. However, sometimes the challenges behind these sophisticated techniques difficult the achievement of desired outcomes. Although grain boundaries have already been investigated by tip-enhanced optical measurements, we can note that the optimal spatial resolution was not reached in some reports (288). Moreover, other studies that achieved reasonable spatial resolution only showed the absence of light emission from grain boundaries (289, 290, 291) — in contrast with previous PL measurements —, which is presumably due to the fracture of the material in these regions. These TEPL and TERS mappings of TMD monolayers grain boundaries are shown in Figure 4.14.

In summary, TEPL and TERS revealed themselves as leading techniques to study nanoscale defects in 2D materials. However, the diversity of these localized defects are still much greater than their tip-enhanced optical investigations on account of experimental challenges. Hence, it is of a great importance to continue developing and employing TEPL and TERS measurements to explore hindered optical features in TMDs.

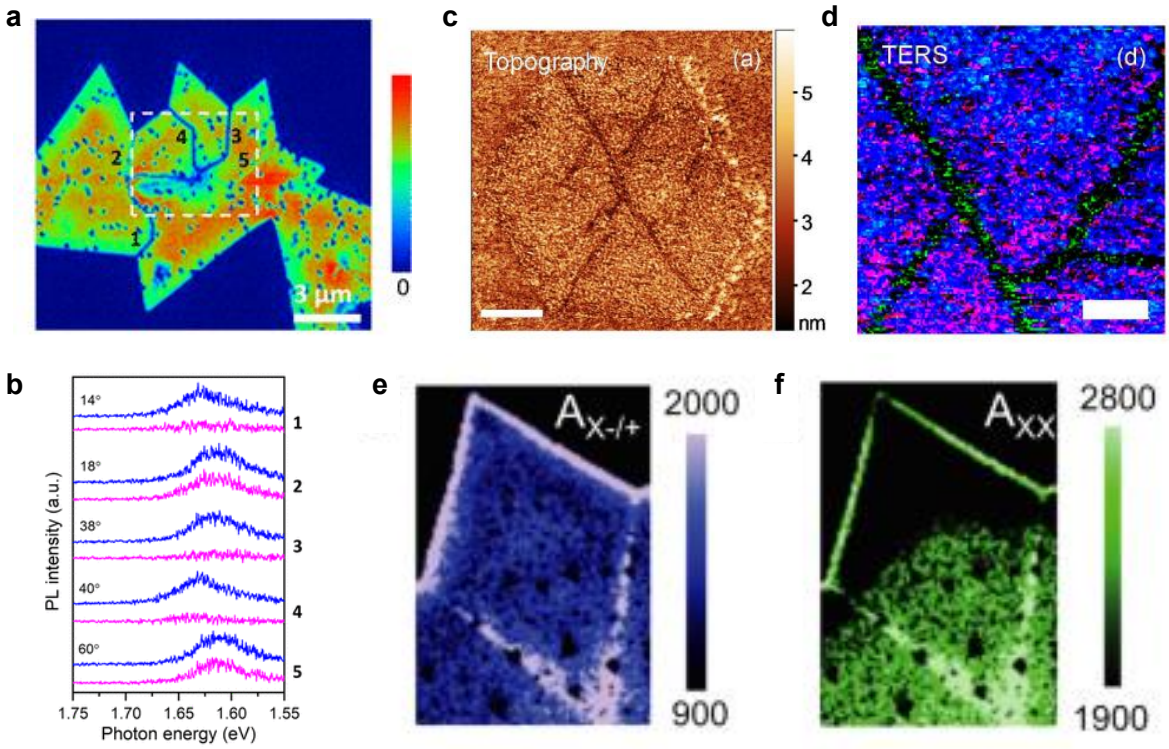

Figure 4.14 – **Tip-enhanced optical mapping of grain boundaries in 2D TMDs.** **a,b** TEPL intensity map and TEPL spectra from a WSe_2 monolayer showing a light emission quenching at their grain boundaries. Adapted from: (291). **c,d** AFM measurement and TERS intensity map of a $MoSe_2$ monolayer presenting cracked grain boundaries with a reduced Raman intensity. Adapted from: (290). **e,f** TEPL intensity maps of trion and biexciton peaks in a $MoSe_2$ monolayer. Adapted from: (288).

4.5 Magneto-Optics

In Chapter 2 we discussed about the rich spin-valley physics of TMD monolayers. As commented, K and $-$K valleys can be separately accessed by circularly polarized light. However, to probe the valley Zeeman effect in these materials external magnetic fields are also required. Moreover, spin-forbidden "dark" excitons can also be accessed by applying magnetic fields. Hence, magnetic-optics is a fundamental tool to study relevant phenomena in 2D TMDs.

Magneto-PL and magneto-absorption spectroscopies are optical techniques widely used to investigate the valley Zeeman effect and dark excitons in 2D TMDs. The valley Zeeman effect consists in the breaking of the band gap degeneracy between K and $-$K valleys by applying an external perpendicular magnetic field (see Chapter 2, section 2.22). This energy splitting is fundamental for valleytronics and spintronics applications, and its strength can be valued by the g-factor for each optical transition (Equation 2.12). Circularly polarized PL (or absorption) measurements can provide the optical transition

energies from K and −K valleys individually. Thus, circularly polarized magneto-PL measurements are able to provide these transition energies as a function of the applied magnetic field. As shown in Figure 4.15, PL spectra of a TMD monolayer detected with σ^+ and σ^- circular polarization are similar at 0 T (149), as expected. At 7 T, σ^+ and σ^- PL spectra are shifted in opposite directions due to the valley Zeeman effect (149). And plotting the difference between σ^+ and σ^- PL energies (i.e., the valley Zeeman splitting) for all measured magnetic fields it is possible to extract the respective g-factor by the linear fit of the data (149) (Figure 4.15). Several works have measured g-factor values close to −4 for the exciton A, exciton B, trion and biexciton transitions in distinct TMD monolayers (146, 147, 148, 149, 151, 152, 153, 154, 155). For that magnitude of valley splitting, strong magnetic fields would be required for application purposes. Therefore, there is a great interest in the defect engineering of these materials to tune their magnetic properties in order to achieve higher g-factors.

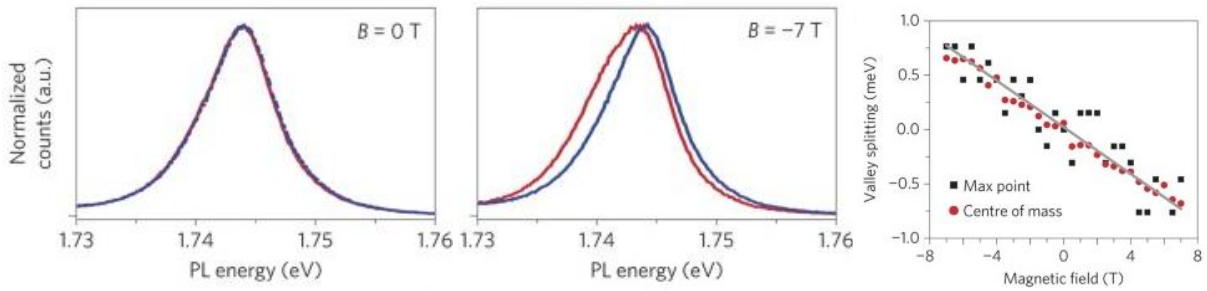

Figure 4.15 – **Magneto-photoluminescence measurements showing the valley Zeeman splitting for a WSe_2 monolayer.** Adapted from: (149).

As mentioned in Chapter 3, the introduction of spin-polarized metal atoms as substitutional defects in TMD monolayers can induce magnetic responses on them. Regarding the valley Zeeman effect, the A exciton of Co-doped MoS_2 monolayers showed an enhanced g-factor of −15 (40), while Fe-doped MoS_2 monolayers revealed g-factors as high as −20 for their A exciton (41), as shown in Figures 4.16a,b. This greater magnetic response owns to the interaction between the MoS_2 electronic bands with the localized magnetic moments of the dopants. Moreover, Wang *et al.* (292) also studied the valley Zeeman splitting associated with defect-bound excitons in a MoS_2 monolayer with sulfur vacancies. Contrary to the doped samples, the A exciton showed no enhancement in its g-factor value. On the other hand, the lower energy optical transition related to the vacancy mid gap state presented a greater g-factor value of −6.2, as displayed in Figure 4.16c. This higher value is due to the increased effective electron mass at the mid gap state as well as its distinct orbital magnetic moments with respect to the conduction band. Heterostructures are also being engineered to provide stronger magnetic effects in TMDs. For instance, interlayer excitons in a $MoSe_2/WSe_2$ vertical heterostructure with a 60° (AB) stacking angle showed enhanced g-factor values ranging from −10 to

−15 (154, 293) and opposite helicities between singlet and triplet states (293). The AB stacking leads to interlayer optical transitions between K and −K valleys, which explains the increased valley Zeeman splitting (that can be quenched by the effect of moiré patterns (294)). Besides, a magnetic proximity effect in a $WSe_2/NiPS_3$ heterostructure induced quantum light emitters with a high degree of circular polarization and a g-factor value of approximately −5 (295). Finally, it was demonstrated an increased g-factor value of −14 for a phase engineered WSe_2 monolayer owing to the exchange interaction between the 2H phase WSe_2 with the local induced magnetic moments of the T phase domain (296). Thereby, these reports show the potential of the defect engineering in tuning the valley Zeeman effect in TMDs.

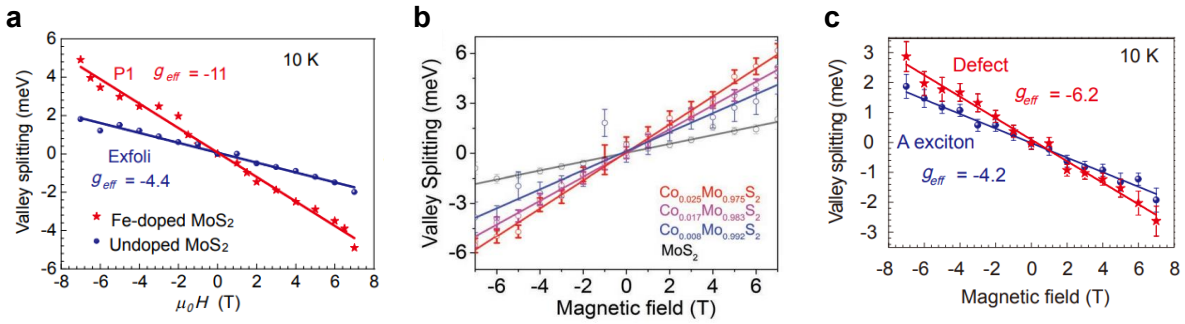

Figure 4.16 – **Valley Zeeman splitting of Fe-doped, Co-doped and sulfur vacancy MoS_2 monolayers.** Adapted from: (40) (**a**), (41) (**b**) and (292) (**c**).

Another possibility that magneto-optical experiments open up is to study the light emission from spin-forbidden dark excitons. TMD monolayers present two types of dark excitons: momentum- and spin-forbidden excitons. In the momentum-forbidden exciton the electron and hole occupy distinct valleys, and thus their radiatively recombination only occurs if assisted by a phonon. Besides, when the electron and hole are in the same valley but in bands with opposite spins — that are perpendicular to the material surface —, the radiative transition is also forbidden. However, this transition can be brightened by applying an external magnetic field parallel to the sample plane, which leads to spins tilted away from the surface normal direction. Therefore, the spins will share a component in the same direction, being able to radiatively recombine. This magnetic brightening of the spin-forbidden dark exciton has already been reported for distinct TMD monolayers (297, 298).

4.6 Time-Resolved Optics

Until now we have only discussed stationary optical effects, i.e., when the sample is continuously excited and its emission is acquired over long periods of time (>> ns). However, from the moment that the sample is pumped by an incident photon to the

moment that the respective emitted or scattered photon is released, distinct phenomena that impacts the material optical properties happen. Therefore, time-resolved optical measurements are of a great importance to study this electronic dynamics. Now we will comment about the charge carriers dynamics in 2D TMDs, the different measurements that are able to probe it and the role of defects in these phenomena.

Figure 4.17 summarizes the electronic dynamics in a direct gap semiconductor, and a detailed discussion about the following description of this dynamics can be found in Refs. (299, 300). When a semiconductor is pumped by a monochromatic laser with an energy greater than the band gap, electrons from a narrow energetic range in the valence band are excited to a narrow energetic range in the conduction band, leaving holes at their initial states. In a first moment, the carrier-carrier scattering promotes the thermalization of these hot electrons in the conduction band. Meanwhile, in 2D TMDs it is observed the formation of excitons in these excited states. In the subsequent time domain, there is an excitonic and electronic relaxation owing to the carriers interaction with phonons. When carriers and excitons achieve a thermal quasi-equilibrium with the lattice, they are found at the band edges and at the fundamental $1s$ state, respectively. Finally, during these dynamics electrons and holes recombine both radiatively and nonradiatively. It is important to comment that although each of these phenomena display distinct time scales, they can happen in parallel. That is, relaxation also occurs over the electronic thermalization, as well as hot carriers can recombine before their full relaxation. The time scale in which these effects are noted in 2D TMDs is faster than in bulk semiconductors or quantum-wells, as they show strong Coulomb interactions due to their reduced dielectric screening. For instance, it have been reported carrier thermalization (301) and exciton formation (302, 303) time scales of tens of fs for 2D TMDs, while their cooling process showed characteristic times of hundreds of fs (301, 304). Lastly, there are distinct reported time domains for excitonic recombination depending on their mechanism and the sample crystallinity as will be discussed later. Moreover, these time scales can also change due to the charge carrier dynamics dependence on the excitation power and energy (305, 302, 306) — as well as on temperature (307, 308).

Different optical techniques are able to probe this electronic dynamics in TMD samples, such as pump-probe spectroscopy and time-resolved photoluminescence (TRPL) (309). As they are related to the time resolving of the optical responses, ultra-short pulsed lasers are generally required to perform these techniques, in which the laser pulse should be at least as fast as the time scale of the phenomenon that will be investigated. Pump-probe spectroscopy consist in pumping the sample with a higher power beam to generate non-equilibrium electronic states and then use a delayed lower power probe beam to study the induced modifications in the material optical responses with respect to the delay time (309). Therefore, the time resolution in pump-probe measurements is basically determined by the temporal pulse width of the laser. On the other hand, TRPL spectroscopy is based

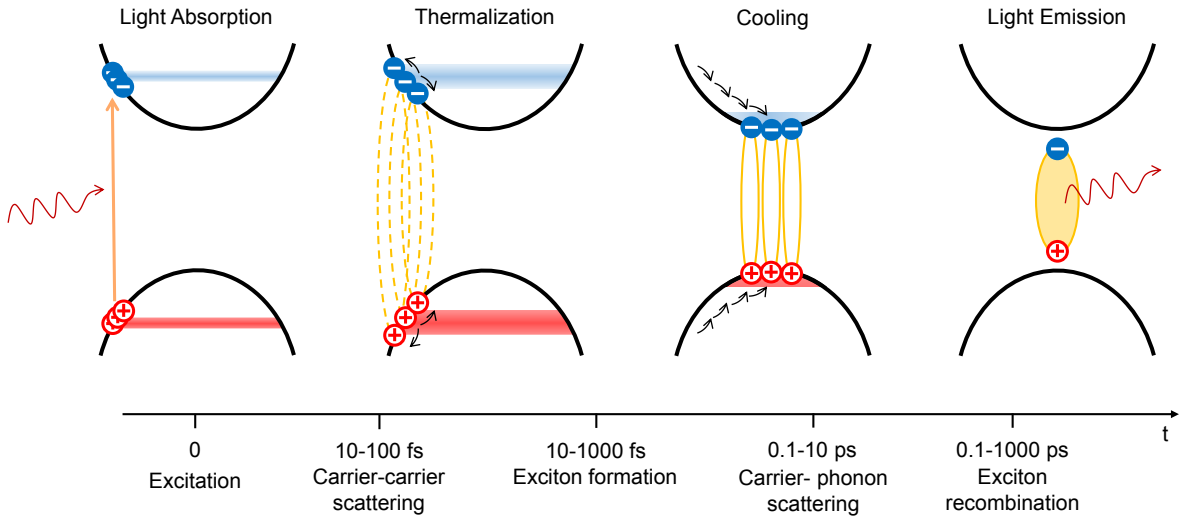

Figure 4.17 – **Schematic representation of the exciton dynamics in a TMD monolayer.** The time scales presented at the bottom of the Figure are based on Ref. (300).

on directly measuring the sample light emission as a function of time (309). Hence, the time resolution of these TRPL measurements is usually defined by the temporal accuracy of the detection equipment.

As mentioned, excitons can recombine over a large temporal scale due to the different possible mechanisms of recombination they present. TRPL measurements in TMD monolayers have shown that the radiative recombination of their A excitons happens in few ps (307, 310, 311, 308), while trions exhibit lifetimes of tens of ps (311, 308). Defective TMDs also present lower energy optical transitions associated with mid gap states, which radiatively recombine in hundreds of ps (311, 310). These defective levels are also called as trap states owing to this long-lived character of defect-bound excitons. Moreover, their long lifetimes favor the light emission quenching due to nonradiative recombinations by phonon scattering. TRPL spectra of exciton, trion and defect-bound exciton states are shown in Figure 4.18. Beyond the radiative path, excitons can also recombine through different nonradiative mechanisms, such as Auger recombination and exciton-exciton annihilation. The exciton-exciton annihilation is a nonlinear many body effect in which an exciton recombines transferring energy to another exciton instead of emitting a photon. Therefore, the exciton-exciton annihilation rate is strongly dependent on the charge carrier density, and can be calculated from the temporal evolution of the exciton population through pump-probe measurements (312, 305, 313, 314). A similar effect is the Auger recombination, that is related to the energy absorption of an electron hole recombination by a free carrier. For instance, it has been shown that defects can assist the electron hole nonradiative recombination by Auger processes (315). Time-resolved optical measurements are thus a powerful tool to investigate the expressive impact of

defects in the exciton dynamics in TMDs.

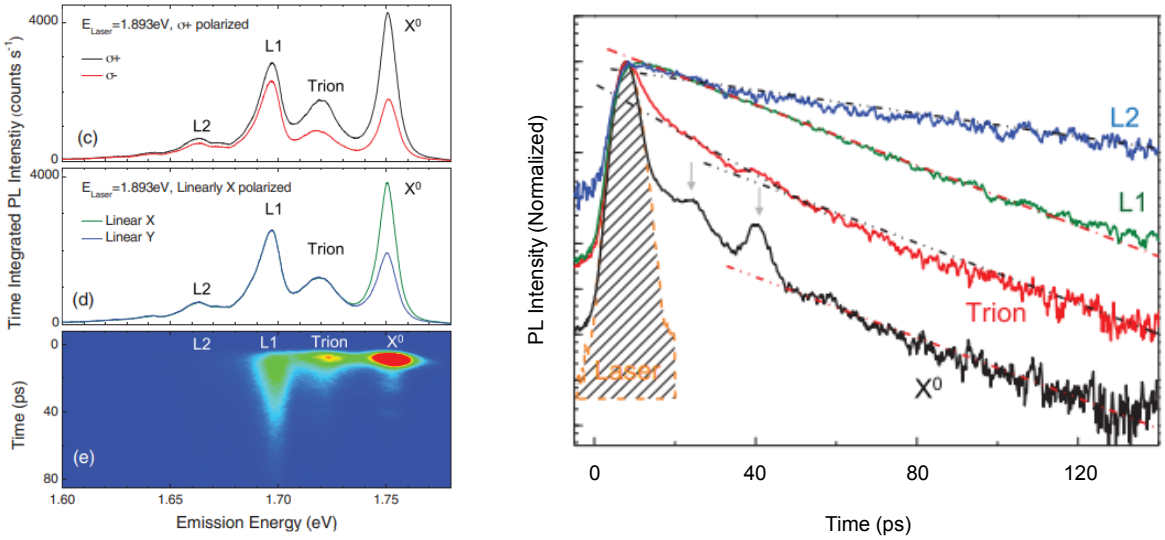

Figure 4.18 – **PL spectra and time-resolved PL measurements showing the lifetimes of the exciton, trion and defect-bound excitons states.** Adapted from: (311).

4.7 Second-Harmonic Generation

The development of high power pulsed lasers also allowed a broad research on the nonlinear optical responses of distinct types of nonlinear materials (316). Since these nonlinear phenomena happen due to the modifications in the properties of an optical medium by its interaction with light, they require large intensities that are usually only reached by pulsed lasers. In these cases, the optical response of the material becomes not just linear with respect to the intensity of the applied electric field, but also shows nonlinear dependencies. As commented in the Raman section, for a conventional linear response, the time-varying polarization $P(t)$ is related with the electric field strength $E(t)$ by (317):

$$P(t) = \epsilon_0 \chi^{(1)} E(t), \tag{4.8}$$

in which $\chi^{(1)}$ is the linear susceptibility. However, this expression could be generalized to also account the nonlinear effects by expanding it in a power series of $E(t)$ (317):

$$\begin{aligned} P(t) &= \epsilon_0 \left(\chi^{(1)} E(t) + \chi^{(2)} E^2(t) + \chi^{(3)} E^3(t) + \cdots \right) \\ &\equiv P^{(1)}(t) + P^{(2)}(t) + P^{(3)}(t) + \cdots , \end{aligned} \tag{4.9}$$

with $\chi^{(2)}$ and $\chi^{(3)}$ being the second- and third-order nonlinear susceptibilities, respectively. Note that we are now considering the polarization and electric field vectors as scalars just for simplicity, but their vector character will be included later.

The second-harmonic generation (SHG) is an example of a nonlinear optical process in which two photons with the same frequency interact with a nonlinear optical medium and generate a new photon with twice the frequency, as it is schematically shown in Figure 4.19. To better understand this nonlinear effect, we shall determine the the second-order nonlinear polarization $P^{(2)}$ in terms of an incident oscillating electric field given by (317):

$$E(t) = Ee^{-i\omega t} + c.c., \tag{4.10}$$

in which ω is the angular frequency and *c.c.* is the complex conjugate. Thus, the second-order nonlinear polarization can be derived from (4.9) as (317):

$$P^{(2)}(t) = 2\epsilon_0\chi^{(2)}EE^* + (\epsilon_0\chi^{(2)}E^2e^{-i2\omega t} + c.c.). \tag{4.11}$$

Hence, the second-order polarization has a frequency independent term accounted to an optical rectification process and a double frequency term that generates the second harmonic radiation.

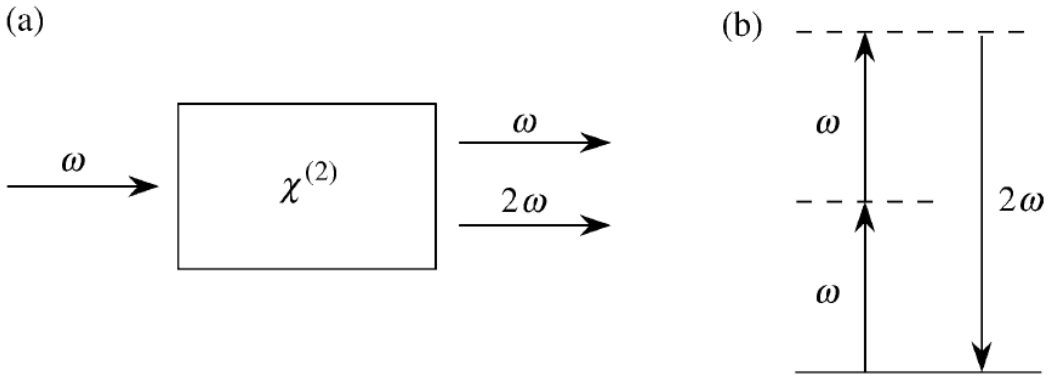

Figure 4.19 – **Schematic representation a the second harmonic generation process** (**a**) An incident photon interacting with a nonlinear medium generating a double frequency emission and (**b**) its diagram level representation. Adapted from: (317).

It can be seen from (4.11) that the SHG contribution is finite only for $\chi^{(2)} \neq 0$. Moreover, the SHG and any other even-order nonlinear process is only allowed for noncentrosymmetric media, i. e., systems that do not exhibit an inversion symmetry. In the particular case of second-order optical effects, we can demonstrate this result by looking for its polarization term (317):

$$P^{(2)}(t) = \epsilon_0 \chi^{(2)} E^2(t). \tag{4.12}$$

Considering an optical medium with an inversion symmetry, if we change the electric field sign it is expected that the polarization also has its sign changed. Thereby (317):

$$-P^{(2)}(t) = \epsilon_0 \chi^{(2)} [-E(t)]^2 = \epsilon_0 \chi^{(2)} E^2(t). \tag{4.13}$$

By comparing (4.12) with (4.13), we realize that both expressions would only be simultaneously true if $\chi^{(2)} = 0$. Consequently, no second-order optical process would be generated for this electric dipole approximation (317).

Although the polarization and electrical fields were so far presented as scalars for simplicity, they are vectors quantities. Therefore, the susceptibility terms are in fact tensors. For instance, $\chi^{(1)}$ is a second-rank tensor, $\chi^{(2)}$ is a third-rank tensor, an so on. The polarization vector components are thus (317):

$$P_i = \epsilon_0 \left(\chi_{ij}^{(1)} E_j + \chi_{ijk}^{(2)} E_j E_k + \chi_{ijkl}^{(3)} E_j E_k E_l + \cdots \right), \tag{4.14}$$

and the SHG polarization components can be specifically depicted as (317):

$$P_i^{(2)}(2\omega) = \epsilon_0 \chi_{ijk}^{(2)}(2\omega, \omega, \omega) E_j(\omega) E_k(\omega). \tag{4.15}$$

As can be seen, the $\chi^{(2)}$ that describes the SHG has $3 \times 3 \times 3 = 27$ components. However, due to symmetry restrictions the number of independent terms is significantly reduced and fortunately we can replace the third-rank susceptibility tensor by a d matrix (317):

$$d_{is} \equiv \chi_{ijk}^{(2)}, \tag{4.16}$$

with i being a three term index representing x, y and z, and s a six term index defined as (317):

jk:	11	22	33	23,32	31,13	12,21
s:	1	2	3	4	5	6

By also applying the Kleinman symmetry condition (317), it only remains 10 independent terms in the d_{is} matrix for a negligible dispersion and the SHG polarization matrix equation can be written as (317):

$$\begin{pmatrix} P_x(2\omega) \\ P_y(2\omega) \\ P_z(2\omega) \end{pmatrix} = 2\epsilon_0 \begin{pmatrix} d_{11} & d_{12} & d_{13} & d_{14} & d_{15} & d_{16} \\ d_{16} & d_{22} & d_{23} & d_{24} & d_{14} & d_{12} \\ d_{15} & d_{24} & d_{33} & d_{23} & d_{13} & d_{14} \end{pmatrix} \begin{pmatrix} E_x^2(\omega) \\ E_y^2(\omega) \\ E_z^2(\omega) \\ 2E_y(\omega)E_z(\omega) \\ 2E_x(\omega)E_z(\omega) \\ 2E_x(\omega)E_y(\omega) \end{pmatrix}. \tag{4.17}$$

Hence, possessing the crystal symmetry and the incident electric field, it is possible to obtain the second harmonic polarization behavior of the material.

SHG has been used to investigate a variety of condensed matter systems, ranging from bulk to nanomaterials (318, 319, 320). In particular, SHG has also been used to probe interfaces in materials that are centrosymmetric due to the symmetry breaking at the surfaces and interfaces (321, 322, 323) and to identify modifications in the nonlinear optical susceptibility of layered materials (324). Moreover, polarization-resolved SHG measurements have also shown to provide information about the crystallography orientations of TMD monolayers (19, 20, 21, 325). As can be seen in Figure 4.20, the hexagonal symmetry of these 2D materials is revealed by the SHG six-fold intensity pattern.

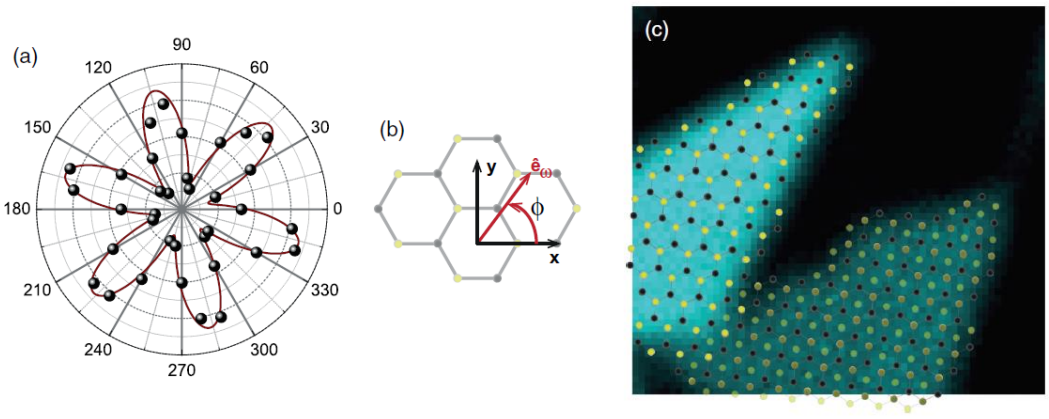

Figure 4.20 – **TMD angular dependence in the second harmonic emission.** (**a**) The six-fold pattern of a polarization-resolved SHG measurement, (**b**) the ϕ angle relative to the armchair direction and (**c**) two TMD domains showing distinct crystallographic orientations. Adapted from: (20)

This SHG angular dependence can be derived from (4.17). For TMD monolayers with D_{3h} point-group symmetry, the second-order susceptibility has only one independent nonzero term (20):

$$\chi^{(2)} \equiv \chi^{(2)}_{xxx} = -\chi^{(2)}_{xyy} = -\chi^{(2)}_{yyx} = -\chi^{(2)}_{yxy}, \tag{4.18}$$

and hence the d matrix could be written as:

$$\begin{pmatrix} 0 & 0 & 0 & 0 & 0 & d_{16} \\ d_{16} & -d_{16} & 0 & 0 & 0 & 0 \\ 0 & 0 & 0 & 0 & 0 & 0 \end{pmatrix}. \tag{4.19}$$

Therefore, for an incident electric field with a linear polarization the polarization vector is given by:

$$\begin{pmatrix} P_x(2\omega) \\ P_y(2\omega) \\ P_z(2\omega) \end{pmatrix} = \epsilon_0 \chi^{(2)}_{xxx} \begin{pmatrix} 2E_x(\omega)E_y(\omega) \\ E_x^2(\omega) - E_y^2(\omega) \\ 0 \end{pmatrix}. \tag{4.20}$$

And by placing a fixed analyzer before the detector, the polarization vector will present the following dependence with the angle ϕ between the TMD armchair and the electromagnetic polarization directions (20):

$$\boldsymbol{P}(2\omega) \cdot \hat{e}_\phi = \epsilon_0 \chi^{(2)}_{xxx} E^2(\omega) \cos(3\phi). \tag{4.21}$$

As the SHG intensity $I(2\omega)$ is proportional to $P^2(2\omega)$, it will present a $\cos^2(3\phi)$ dependency, unveiling the six-fold pattern shown in Figure 4.20. Therefore, for a known incident polarization field direction, it is possible to found the relative crystallographic orientation of the sample. This measurement can be done in two distinct ways: by fixing the same direction for the incident polarization and the analyzer before the detector and rotating the sample, or by letting the sample fixed and rotating the incident polarization and the analyzer directions together. However, there is a simpler measurement that consists in fixing the TMD sample and the analyzer direction and only rotate the incident polarization direction. For simplicity, but without loosing the generality, let consider the analyzer in the x direction and θ being the angle between the incident polarization direction and the x direction. Therefore, $E_x(\omega) = E(\omega)\cos(\theta)$ and $E_y(\omega) = E(\omega)\sin(\theta)$. Substituting these relations to Equation 4.20 and applying some trigonometric identities, we can write the detected polarization vector as:

$$\boldsymbol{P}(2\omega) \cdot \hat{e}_x = P_x(2\omega) = \epsilon_0 \chi^{(2)}_{xxx} E^2(\omega) \cos(2\theta). \tag{4.22}$$

In that case, the SHG intensity $I(2\omega)$ would be thus proportional to $\cos^2(2\theta)$, presenting a four-fold pattern. Although it does not provide the hexagonal symmetry of the TMDs, it is an easier way to determine the relative crystal orientations over distinct TMD domains.

Beyond the crystal orientation determination, SHG measurements can also provide information about excitonic phenomena as well as defective states in TMD monolayers. For instance, there is an enhancement of the SHG intensity when any of its virtual transitions is

in resonance with a real excitonic state (61), which was also used to study interlayer excitons in TMD vertical heterostructures (326). And since SHG is a coherent effect, interference phenomena have been probed in these vertically stacked samples (327, 328, 329, 330). Moreover, polarized SHG microscopy can reveal grain boundaries in TMDs, as different grains with distinct crystallographic orientations would present distinct intensities with respect to the incident polarization (331, 332). These grain boundaries can be identified by dark-field SHG imaging as well, since this technique is able to separate the spatial components of the emitted light (333). Besides, polarized SHG is also employed to measure strain fields in TMD monolayers, which affects the symmetry of the SHG polar intensity dependence (334). A summary of these SHG results in TMDs is shown in Figure 4.21, shedding light in the potential of this nonlinear effect to investigate defects in these materials.

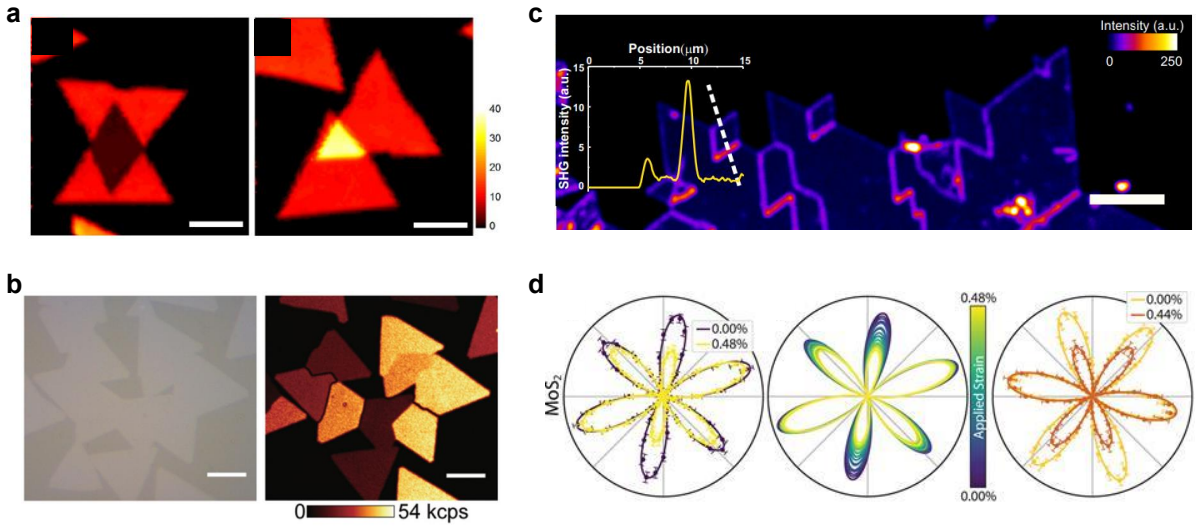

Figure 4.21 – **SHG measurements in TMD heterostructures and defective TMDs.** **a** SHG imaging of artificially stacked MoS_2 bilayer showing a constructive interference emission for a bilayer with a 2° stacking and a destructive one for a bilayer with 54° stacking. Adapted from: (327). **b** Polarized SHG imaging revealing distinct grains and grain boundaries in a polycrystalline MoS_2 monolayer by their different SHG intensity. Adapted from: (332). **c** Dark-field SHG imaging of a $MoSe_2$ monolayer presenting an enhanced signal at grain boundaries. Adapted from: (333). **d** Polarization-resolved SHG measurement in a MoS_2 monolayer showing an intensity asymmetry in the six-fold pattern for a strained sample. Adapted from: (334).

4.8 Four-Wave Mixing

Four-wave mixing (FWM) is a another nonlinear effect that consists in the interaction of three incident photons in a nonlinear material generating a forth photon. As it is a third-order nonlinear effect, it is described by the third-order polarization $P^{(3)}$

(Equation 4.9). The distinct possible frequencies of the generated forth photon (ω_4) in a FWM process comprehend the absolute values of the linear combination of the three incident photon frequencies (with coefficients ± 1), i.e., $\omega_4 = |\pm\omega_1 \pm \omega_2 \pm \omega_3|$ (317). However, due to the simplicity in using only two laser lines, it is common to observe degenerate FWM measurements, in which two incident photons have the same frequency (ω_1) and interact with a third photon (ω_2) in the nonlinear material to generate the FWM photon (ω_{FWM}) with frequency:

$$\omega_{FWM} = 2\omega_1 - \omega_2. \tag{4.23}$$

As well as for the SHG effect, FWM processes are usually related to virtual states. Nonetheless, when any of its transition energies match with a real state, there is also an enhancement in the FWM intensity. Therefore, this resonance effect can be used in 2D TMDs to study their excitonic states (61). Figure 4.22 shows the diagram levels for both SHG and FWM resonant and nonresonant processes as well as the comparison between PL spectra of distinct TMD monolayers and their SHG and FWM intensity profiles with respect to the emitted photon energy. As mentioned, it is clearly noted a nonlinear resonant effect at the excitonic energies in these materials.

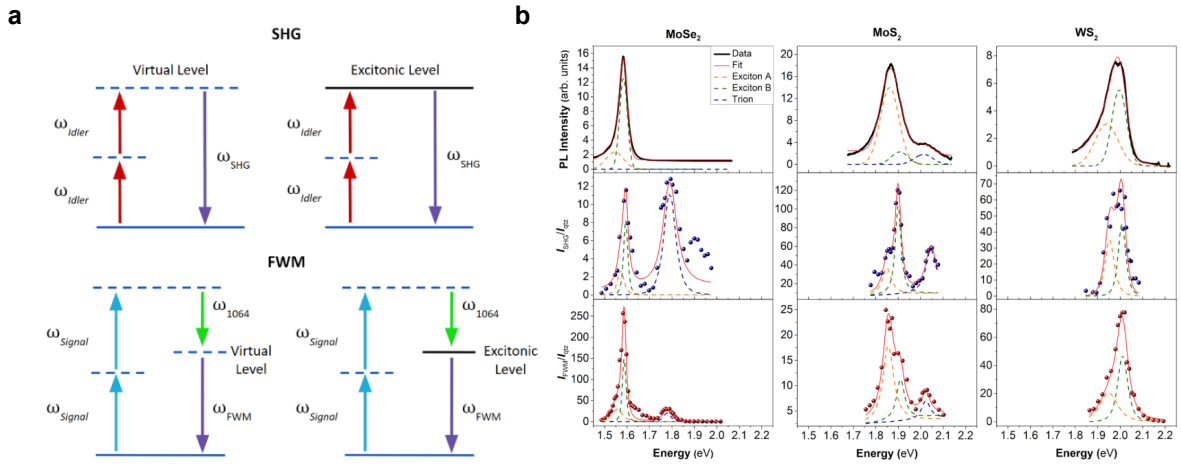

Figure 4.22 – **Resonant SHG and FWM processes in TMD monolayers. a** Diagram level representation of nonresonant and resonant SHG and FWM processes. **b** SHG and FWM excitation profiles for distinct TMD monolayers revealing resonant features corresponding to their PL spectra peaks. Adapted from: (61).

5 Experimental Methodology

In this thesis we investigated different 2D TMD samples. Most of them were grown by a chemical vapor deposition (CVD) method by different collaborators. Besides, we have also studied exfoliated samples, in which the majority of them was also fabricated by other groups. Therefore, we will let the details of the sample fabrication to the cited references, and here we will focus on the different experimental setups of the optical characterizations performed in this work. Several optical setups were used to perform spectroscopy and microscopy photoluminescence (PL), magneto-PL, electron-hole plasma (EHP) PL, Raman, tip-enhanced PL and Raman, second-harmonic generation (SHG), four-wave mixing (FWM) and two-pulse excitation correlation measurements. In this Chapter we present the experimental instrumentation used in these measurements by dividing the linear, nonlinear and time-resolved optical setups in different sections. Most of the experiments were carried out at the Nano-Spectroscopy Laboratory (LabNS) at the physics department of UFMG, and the measurements performed outside LabNS will be pointed out.

5.1 Linear Optics Setup

Figure 5.1 represents the optical setup used in the confocal PL and Raman spectroscopy experiments performed in this thesis. In general, for these measurements a continuous-wave (CW) laser beam was focused on the sample by an objective lens. The backscattered signal was collected by the same objective, reflected by a dichroic mirror and directed to a spectrometer that diffracts the signal to a charge-coupled device (CCD) which records the spectrum. However, the optical specifications were different for the spectroscopy measurements carried out at LabNS, for the resonant Raman spectroscopy experiments and for the hyperspectral measurements. For the spectroscopy experiments carried out at LabNS we used 488, 561 and 785 nm diode lasers to excite the sample through a 40× objective lens with numerical aperture (NA) = 0.95. The signal was detected in a single monochromator spectrometer (*Andor* Shamrock 303i) equipped with a sensitive CCD camera (*Andor* IDUS DU401A-BV) and using 600 and 1200 grooves/mm diffraction gratings for PL and Raman measurements, respectively. In a single monochromator spectrometer, the signal focused by an external lens is spatially selected by a slit and directed to a diffraction grating that spectrally disperses it to the CCD. Hence, the spectrometer resolution depend on the slit aperture, the number of grooves/mm of the diffraction grating and the distance between the grating and the CCD camera. Moreover, it is necessary a long pass (or a notch) filter in front of the spectrometer to block the Rayleigh scattered signal of the

laser. The resonant Raman spectroscopy measurements were carried out at the Raman spectroscopy laboratory at the physics department of UFMG. They were performed on a *HORIBA* Jobin Yvon T64000 triple monochromator spectrometer also equipped with a CCD detector and using a 1800 grooves/mm diffraction grating. The samples were excited by a CW Ar-Kr laser that displays 12 laser lines that cover excitation energies (wavelengths) from 1.92 to 2.81 eV (from 441 to 647 nm) and by a CW Ti-Sa laser with excitation energies (wavelengths) ranging from 1.38 to 1.70 eV (from 730 to 900 nm). A 100× objective lens with NA = 0.9 was used to focus the laser beam and collect the backscattered signal. Conversely to the single monochromator, the triple monochromator presents three diffraction gratings, in which the first two gratings are used to reject the laser signal and the third one disperses the filtered signal to the CCD. Hence, in that configuration it is possible to collect emissions much closer to the laser energy than with a single monochromator spectrometer. It is important to comment that both standard and resonant Raman measurements were punctual, i.e., the sample was placed in a stage that remained fixed during the measurements. Nonetheless, we were also interested in mapping PL and Raman spectra over TMD samples. Thereunto, we performed hyperspectral PL and Raman measurements in the *Witec* Alpha 300RA equipment at the LCPNano, a multiuser laboratory of the physics department of UFMG. This equipment has three CW laser lines (457, 532 and 633 nm) that were focused on the sample by a 100× objective lens with NA = 0.9. In contrast to the punctual measurements, the *Witec* equipment displays a piezoelectric translation stage that, together with the single monochromator spectrometer, can be controlled by an integrated software. Therefore, it was possible to map the PL emission and the Raman scattering of the sample by taking several spectra over a delimited region with determined spatial steps, that is, a hyperspectral measurement. Finally, tip-enhanced PL and Raman hyperspectral measurements were carried in a *FabNS* Porto-SNOM equipment. The confocal part of the setup is very similar to the setup of *Witec* Alpha 300RA, in which the most relevant difference lies in the 100× oil immersion objective lens with NA = 1.4 used in the *FabNS* system. Thus, the tip-enhanced measurements required samples in a transparent substrate. Besides, there is also the scanning probe part of the Porto-SNOM setup, which utilizes a Au Plasmon-Tunable Tip Pyramid (PTTP) (335) in a configuration as represented in Figure 4.11.

Beyond PL and Raman measurements presented above, we have also employed magneto-PL experiments at the semiconducting nanostructures laboratory at UFSCar. Figure 5.2 shows the optical setup representation for these measurements. The major difference from the other linear spectroscopy experiments is that in this case the sample was placed inside a closed cycle helium magneto-cryostat (*Attocube* attoDRY1000) with an ultra low vibration. In this cryostat it is possible to reduce the sample environment temperature to 3.5 K, and we performed measurements varying this temperature from 4 to 80 K. Moreover, the superconducting magnet inside the cryostat is able to apply uniform

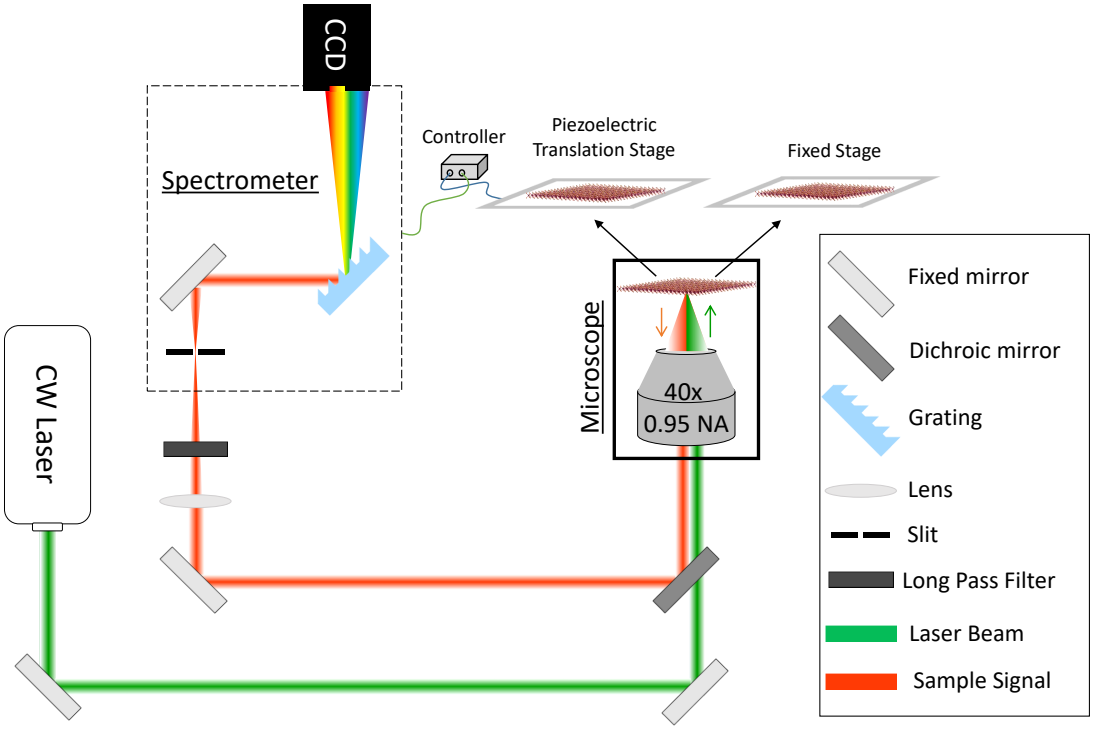

Figure 5.1 – **Schematic illustration of the linear spectroscopy setup.** For the linear spectroscopy experiments we used a CW laser to excite the sample. For this setup, the laser beam is focused on the sample by an objective lens and the backscattered signal is collected by the same objective. The signal is directed to a spectrometer equipped with a sensitive CCD camera for the detection. The sample was placed in a microscope in two possible stages, a fixed one for punctual measurements and a piezoelectric translation stage for mapping experiments.

magnetic fields from -9 to 9 T, which were applied perpendicular to the sample plane in our experiments (Faraday geometry). To control the incident laser linear polarization we placed a half-wave plate before the cryostat. The laser beam was focused on the sample by a objective lens with NA $= 0.69$ and the backscattered signal was collected by the same objective. Before being directed to a single monochromator spectrometer (*Andor* Shamrock) equipped with a sensitive CCD (*Andor* Idus), the signal passed by a quarter-wave plate and then by a linear polarization analyzer to select the right or left circularly polarized component of the sample emission. This optical setup presents a circular polarization confidence superior to 98%.

5.2 Nonlinear Optics Setup

The optical setup used to perform FWM, SHG and EHP PL microscopy imaging in 2D TMDs is schematically shown in Figure 5.3. These nonlinear experiments were employed by exciting the samples with an optical parametric oscillator (OPO) system

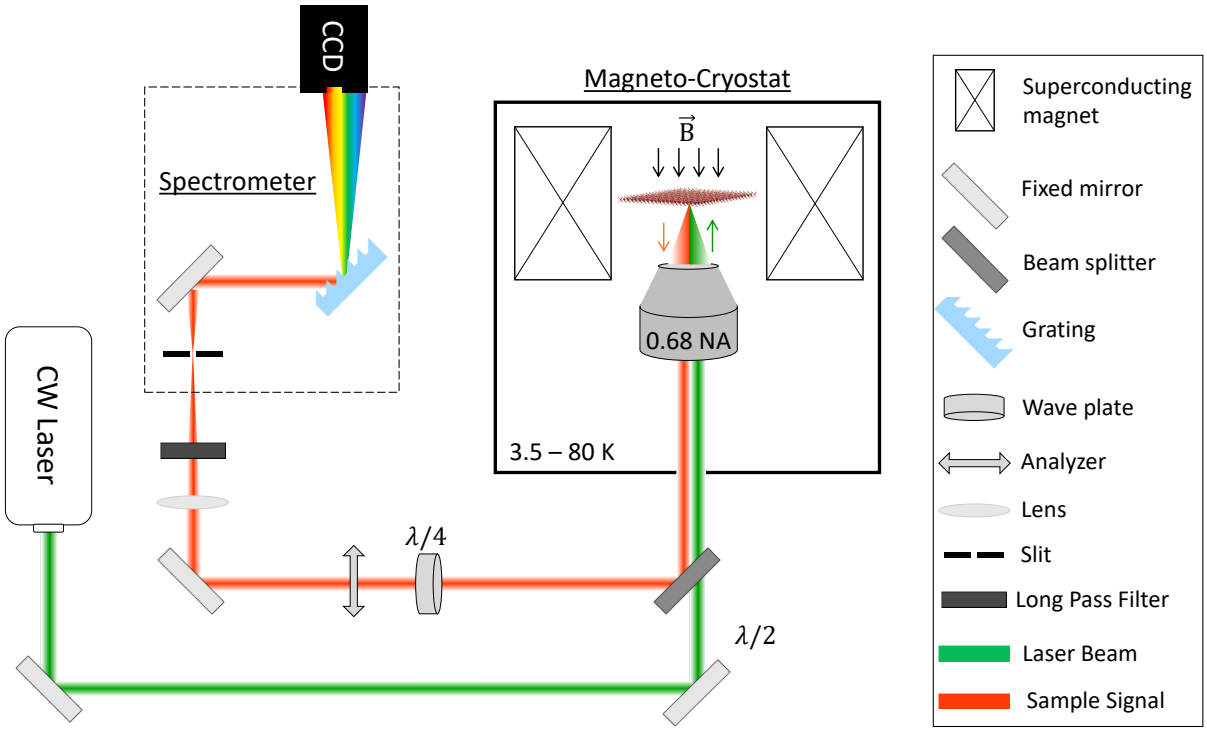

Figure 5.2 – **Schematic illustration of the magneto-PL setup.** For the magneto-PL experiments we used a CW laser to excite the sample. For this setup, the laser beam is focused on the sample by an objective lens and the backscattered signal is collected by the same objective. The signal is directed to a spectrometer equipped with a sensitive CCD camera for the detection. The sample is placed in a magneto-cryostat that is able to reduce the temperature down to 3.5 K and apply magnetic fields ranging from −9 to 9 T. In addition, half-wave and quarter-wave plates were used to control the linearly polarized excitation and to detect the circularly polarized components.

(*APE* picoEmerald) that provides three pulsed laser lines: the signal beam tunable from 750 to 950 nm, a fixed 1064 nm beam and an idler beam tunable from 1210 to 1830 nm. All of them present a pulse width of 7 ps and a repetition rate of 80 MHz. In general, SHG and EHP PL measurements were done with the signal beam, while the degenerated FWM measurements used both signal and 1064 nm beams as ω_1 and ω_2, respectively. To perform the nonlinear microscopy imaging, the samples were scanned by these pulsed laser beams with a set of galvanometric mirrors (*LaVison BioTec*) in a *Nikon* microscope. The pumping beams were focused on the sample by a 40× objective lens with NA = 0.95. The backscattered nonlinear signal was collected by the same objective, reflected by a beam splitter and then directed to a photomultiplier tube (PMT). For each experiment (SHG, FWM or EHP PL) it was used a distinct band pass and/or short pass filters to block any other optical contribution. Finally, the nonlinear images were obtained by an image acquisition software (*LaVision BioTec* Imspector Pro). Some SHG and EPL PL measurements were also performed using a pulsed Ti:Sa laser (*Coherent* Mira Optima

900-F) tunable from 700 to 980 nm, with a repetition rate of 76 MHz and a pulse width of 300 fs.

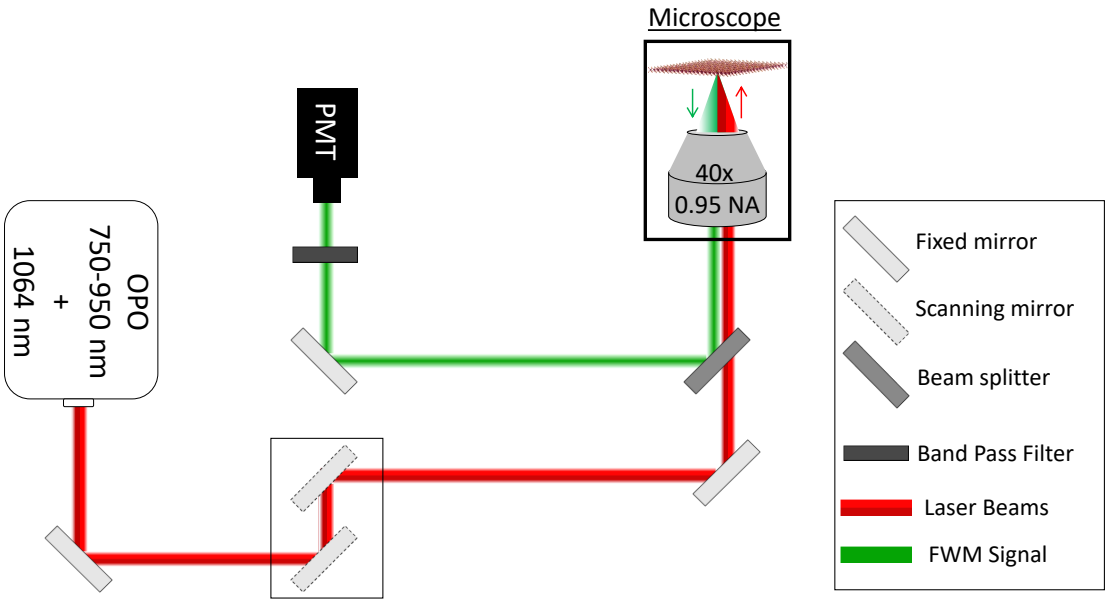

Figure 5.3 – **Schematic illustration of the nonlinear imaging microscopy setup.** For the nonlinear imaging experiments we used a pulsed laser to excite the sample. We used two pulsed laser lines, the signal beam tunable from 750 to 950 nm and a fixed 1064 nm beam. For this setup, the laser beams are focused on the sample by an objective lens and the backscattered signal is collected by the same objective and directed to a PMT for its detection. A set of galvanometric mirrors are used to scan the samples with the laser beams and perform the nonlinear imaging experiments.

Furthermore, it was also performed polarization-resolved SHG imaging in 2D TMDs. The experimental setup for these measurements was very similar to the standard nonlinear imaging presented above. The difference was the addition of two optical elements as presented in Figure 5.4: a rotable half-wave plate (690-1200 nm) before the objective to control the laser linear polarization on the sample and a fixed analyzer in front of the PMT in the horizontal direction. It is worth to point out that although the emitted signal also pass through the half-wave plate, its polarization is not noticeably affected as our generated SHG wavelengths (400-450 nm) are significantly below the half-wave plate working range. The polarized SHG images were obtained by rotating the half-wave plate in steps of 2^o, ranging from 0^o to 90^o (which represents steps of 4^o from 0^o to 180^o in the incident polarization). As the SHG dependence with the incident laser polarization for this measurement is $\sin^2(2\theta)$, the measured angle range was sufficient to provide all the relative orientation information.

Finally, we also performed nonlinear spectroscopy experiments to measure the resonant SHG and FWM profiles as well as to take EHP PL spectra. For these measurements

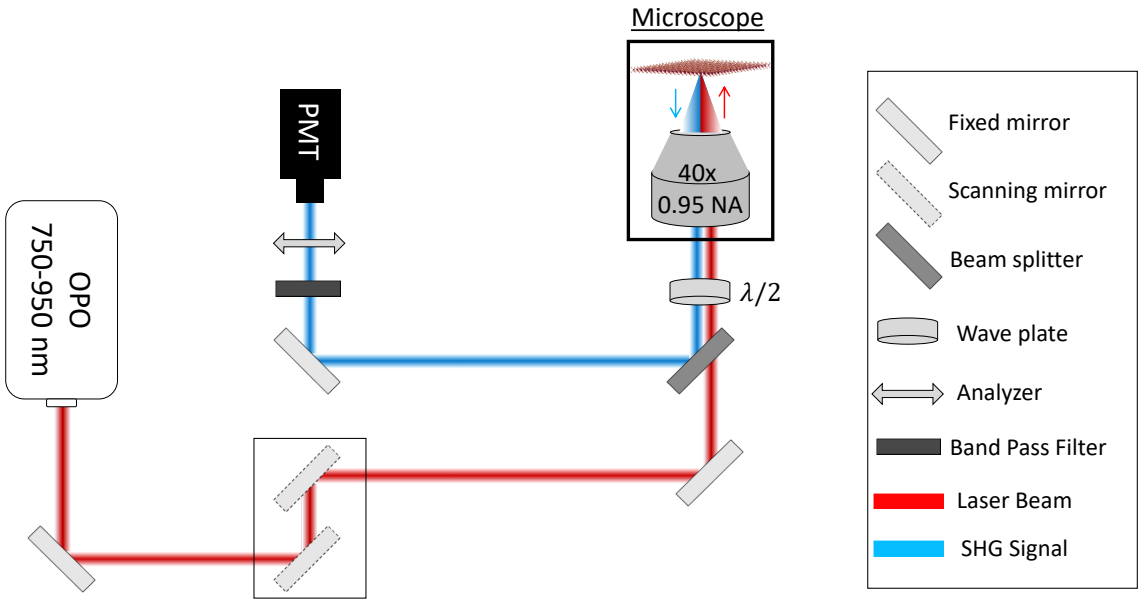

Figure 5.4 – **Schematic illustration of the polarization-resolved SHG imaging setup.** For the polarization-resolved SHG imaging experiments we used the tunable pulsed laser beam (750 to 950 nm) to excite the sample. For this setup, the laser beam is focused on the sample by an objective lens and the backscattered signal is collected by the same objective and directed to a PMT for its detection. A half-wave plate and an analyzer are used to control the linearly polarized excitation and select the detected polarization.

we used a similar setup shown in Figure 5.1 for the standard linear spectroscopy, but pumping the sample with the OPO or MIRA pulsed lasers instead of the CW ones.

5.3 Time-Resolved Optics Setup

The time-resolved measurements presented in this thesis were performed at the Nano-optics laboratory at the Ludwig Maximilian University (LMU) of Munich. Although we employed distinct time-resolved experiments, here we will present the technique that provided the most relevant results: the two-pulse excitation correlation, a degenerated pump-probe measurement. As represented in Figure 5.5, the samples were excited by a pulsed Ti:Sa laser (*Coherent* Mira Optima 900-F) tunable from 700 to 980 nm, with a repetition rate of 76 MHz and a pulse width of 300 fs. A polarized beam splitter was used to separate the laser beam in two pulses with the same fluence and crossed polarizations, in which the time delay between the pulses was controlled by an optical delay line with a linear translation stage. The delayed beams were then reunited again by another beam splitter and focused on the sample by an immersion oil objective with NA = 1.49 (limiting again to samples in a transparent substrate). The backscattered signal was collected by the same objetive and directed to an avalanche photodiode (APD) after passing through

short pass and/or band pass filters. The two-pulse excitation correlation measurements were done by measuring the correlated EHP PL emission of the samples for different delay times in the range of few ps.

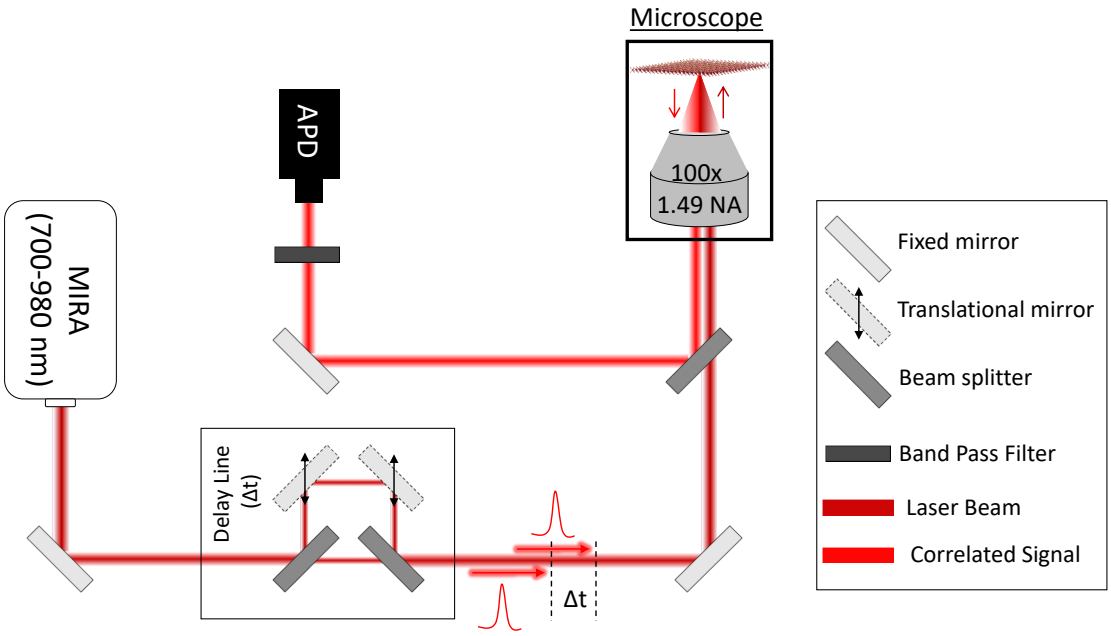

Figure 5.5 – **Schematic illustration of the two-pulse excitation correlation setup.** For the two-pulse excitation correlation experiments we used the tunable pulsed laser beam (700 to 980 nm) to excite the sample. For this setup, the laser beam pass through a polarized beam splitter to separate the laser beam in two pulses with the same fluence and crossed polarizations. In the sequence, the laser pulses are focused on the sample by an objective lens and the backscattered signal is collected by the same objective and directed to an APD for its detection. A delay line stage is used to control the pulses temporal delay.

6 Optical and Magneto-Optical Properties of WS_2 and WSe_2 monolayers

As presented in Chapter 3, tuning the electronic, optical, magnetic, and/or physicochemical properties of two-dimensional (2D) transition metal dichalcogenides (TMDs) through defect engineering provides multiple pathways for diverse applications (34, 22, 35). For instance, a dilute magnetic semiconductor (DMS) (201) can be achieved by incorporating transition metal atoms as substitutional defects in TMD monolayers (37, 213, 42, 43, 44). Vanadium-doped WSe_2 (42, 43) and WS_2 (44) samples have shown a long-range ferromagnetic ordering even above room temperature, thus opening possibilities for spintronic devices fabrication. However, among the significant challenges to be overcome in this field such as the gate-tunability manifestation and the necessity of enhanced magnetic moments in these materials (165, 166), there is a fundamental need for broadband optical and electronic structure characterization of these doped 2D semiconductors. Moreover, the lack of magneto-optical investigations in these materials is possibly hindering distinct responses associated with their valley Zeeman effect.

In section 6.1 we show an extensive optical and electronic structure characterization of pristine and V-doped WS_2 monolayers. Subsequently, the section 6.2 focus in the optical and magneto-optical characterization of V-doped WSe_2 monolayers, which showed a strong valley Zeeman effect. Finally, we also present magneto-optical results in aged WS_2 and WSe_2 monolayers in section 6.3, revealing a giant g-factor associated with a defect mid gap state transition. The samples used for the works presented in this Chapter were synthesized by Prof. Mauricio Terrones group from Penn State University.

6.1 Optical and electronic structure characterization of V-doped WS_2

Here we study pristine and V-doped WS_2 monolayer samples with three different atomic percentages (at%) of vanadium to explore its dependence on the optical response near the three main excitonic energies (A, B, and C excitons), using power-dependent photoluminescence (PL), resonant Raman, resonant four-wave mixing (FWM), resonant second-harmonic generation (SHG), and differential reflectance spectroscopies. Density functional theory (DFT) calculations for the band structure of V-doped WS_2 with a Hubbard U correction ($U = 0$ to 5 eV) for vanadium, including transition dipole moments, were performed by our collaborators to elucidate the optical transitions observed in the experiments. The following results were accepted to be published in the *Advanced Optical Materials* journal and its preprint version is published in Ref. (337).

6.1.1 Power-dependent photoluminescence in V-doped WS_2

The pristine and V-doped WS_2 monolayers used in this work were synthesized by single-step chemical vapor deposition (CVD) as described by Zhang *et al.* (44). To confirm the presence of substitutional V atoms at W sites and to determine their concentration, high-angular annular dark-field scanning transmission electron microscopy (HAADF-STEM) imaging was performed in 4 distinct samples as shown in Appendix Figure A.1. A statistical analysis from the HAADF-STEM measurements revealed vanadium concentrations of 0.4 at%, 2.0 at%, and 8.0 at%, respectively. In order to experimentally study the electronic band structure modifications in these samples due to vanadium doping, we employed power-dependent PL measurements with a 561 nm laser excitation wavelength as shown in the normalized spectra of Figures 6.1a-d. The normalization of the PL spectra was performed with respect to the higher-energy PL peak (from the A exciton in the case of pristine WS_2). While the pristine sample exhibits a single PL peak at 1.96 eV related to A exciton emission,(338, 80) the doped samples display one peak in the energy range of 1.8–1.9 eV (we call P_1) and a second peak around 2.0 eV (P_2), as reported by Zhang *et al.* (268). It can be noted that after increasing vanadium doping the lower energy peak P_1 redshifts — in agreement with the band gap reduction predicted from previous DFT calculations (44). In addition, the higher-energy PL peak P_2 blueshifts. Moreover, the substitutional defects broadened the PL peak and quenched the integrated PL intensity, similar to other works (32, 339, 178). All PL spectra were fitted by two Gaussian peaks and their intensities as a function of laser power are shown in Figures 6.1e-h. Beside the expected linear power dependence of the A exciton peak in pristine WS_2, there is a linear (for P_2) and sublinear (for P_1) power dependencies for V-doped samples. According to Refs. (260, 340), the power-dependent PL measurements reveal that the P_2 peak is associated with an exciton formation and the P_1 peak is related to a radiative recombination process from a donor or to an acceptor level. However, previous DFT calculations showed no mid gap states for V-doped WS_2 monolayers (44), while HAADF-STEM data present no indication of higher S mono-vacancy defects for the V-doped samples. Therefore, this sublinear power dependence might be related to an acceptor state instead of a donor defect level. In order to gain more experimental evidence about the nature of these new electronic states, we next perform FWM and differential reflectance spectroscopy experiments.

6.1.2 Resonant four-wave mixing in V-doped WS_2

As shown by Lafeta *et al.*,(61) nonlinear optical techniques such as FWM can be used to determine excitonic energies (Figure 6.2). FWM is a third-order nonlinear optical process in which three photons interact in a nonlinear material to generate a fourth photon at a linear combination of the three incident photon frequencies (with coefficients ± 1). Here we measured a degenerate FWM in which two incident photons with the same

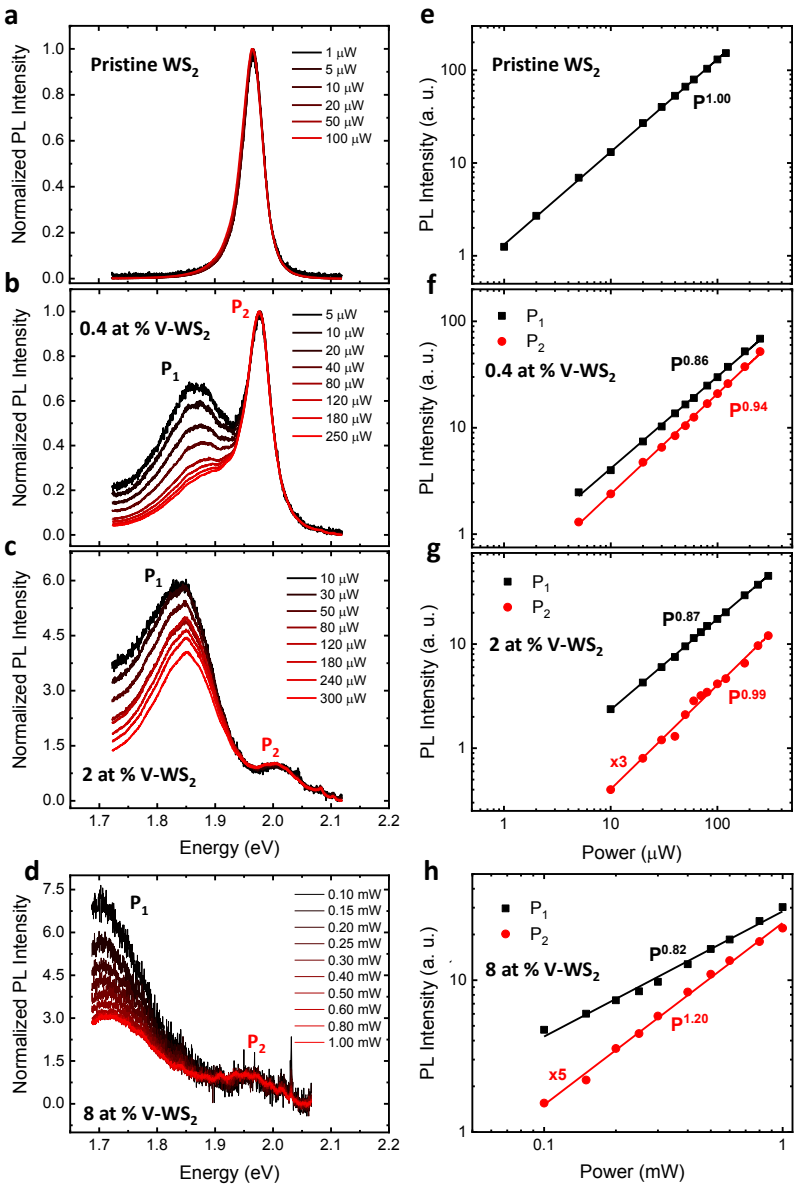

Figure 6.1 – **a-d** Normalized PL spectra for a pristine (**a**) and 0.4 at% (**b**), 2.0 at% (**c**) and 8.0 at% (**d**) vanadium doped WS_2 monolayers for distinct pump powers. All spectra were taken with an excitation wavelength of 561 nm and are normalized by the higher energy peak maximum. **e-h** Power-dependent PL intensity showing a linear power dependence for the pristine WS_2 peak and V-doped WS_2 higher energy peaks (P_2) and a sublinear dependence for the V-doped WS_2 lower energy peaks (P_1).

variable frequency ω_{pump} (from 720 to 950 nm) interact with a third photon of a fixed frequency ω_{1064} (1064 nm) to generate a fourth photon with frequency:

$$\omega_{\text{FWM}} = 2\omega_{\text{pump}} - \omega_{1064}. \tag{6.1}$$

The wide wavelength range of the resulting ω_{FWM} (544 to 858 nm) allowed us to probe resonant responses over the energy window of the WS_2 monolayer A exciton (600 to 680 nm). Figures 6.2a-c show the PL spectra and the FWM resonant profiles with their Gaussian

fits for three samples (pristine and doped WS_2 with 0.4 at% and 2.0 at% vanadium). The resonant behavior of the FWM measurement for the pristine WS_2 monolayer (Figure 6.2a) is in good agreement with its single PL peak. The few meV energy shift between the FWM resonant response and the PL peak is presumably due to a Stokes shift (88, 341). Figures 6.2b,c show that both 0.4 at% and 2.0 at% vanadium-doped WS_2 monolayers present a strong FWM resonant response at the energy of the P_2 PL peak, as well as the same Stokes shift. The 0.4 at% doped sample shows no resonance close to the lower-energy P_1 PL peak, while the 2.0 at% doped sample displays a weak FWM resonant feature around the P_1 PL peak energy. As shown by Equation 6.1 and Figures 6.2d-f, the FWM process requires energy conservation as it brings the electron back to the same occupied electronic band from which it was excited, meaning that the FWM allowed processes have final states below the Fermi level. Therefore, the final state of the P_2 peak is occupied, while the absence of a relevant FWM resonance close to the P_1 peak energy suggests a lower occupancy level of its final state. Since vanadium doping introduces free holes in TMD monolayers (44, 220, 336), the final electronic state associated with the P_1 peak could be these itinerant holes. The FWM results for WS_2 monolayers at 8 at% vanadium concentration are not shown due to its weak intensity. In addition, differential reflectance measurements presented in Appendix Figure A.2 — which also probe electronic excitations only from occupied bands — only clearly show the P_2 peak for doped samples, in agreement with the results described above.

6.1.3 Resonant Raman scattering in V-doped WS_2

In order to further characterize the electronic band structure modifications in the monolayer WS_2 due to vanadium doping, we performed resonant Raman spectroscopy measurements to probe the B exciton energy range. Figure 6.3 shows Raman spectra of these pristine and V-doped WS_2 monolayers for 14 different laser lines in the 250–550 cm^{-1} spectral range (lower frequency Raman spectra were also measured and are shown in Appendix Figure A.3). All spectra were normalized by the silicon peak intensity (520 cm^{-1} peak), considering its Raman cross section (342) for each laser line. A strong dependence of the Raman peaks intensities on the excitation energy can be observed. This dependence, plotted as a Raman excitation profile (REP) in Figure 6.4, varies with the doping concentration, indicating different resonant excitation behaviors among samples. The intensity of a first-order Raman mode is (273)

$$I(E_{\text{pump}}) = C \left| \sum_{m,n} \frac{\langle f|H_{e-r}|n\rangle\langle n|H_{e-ph}|m\rangle\langle m|H_{e-r}|i\rangle}{(E_{exciton} - E_{\text{pump}} + i\gamma)(E_{exciton} - E_{\text{pump}} + E_{ph} + i\gamma)} \right|^2, \qquad (6.2)$$

where the numerator holds matrix elements for electron-radiation (H_{e-r}) and electron-phonon (H_{e-ph}) interactions between the initial (i), intermediate (m and n), and final (f) quantum states. Resonance occurs when the incident (E_{pump}) or scattered ($E_{\text{pump}} - E_{ph}$)

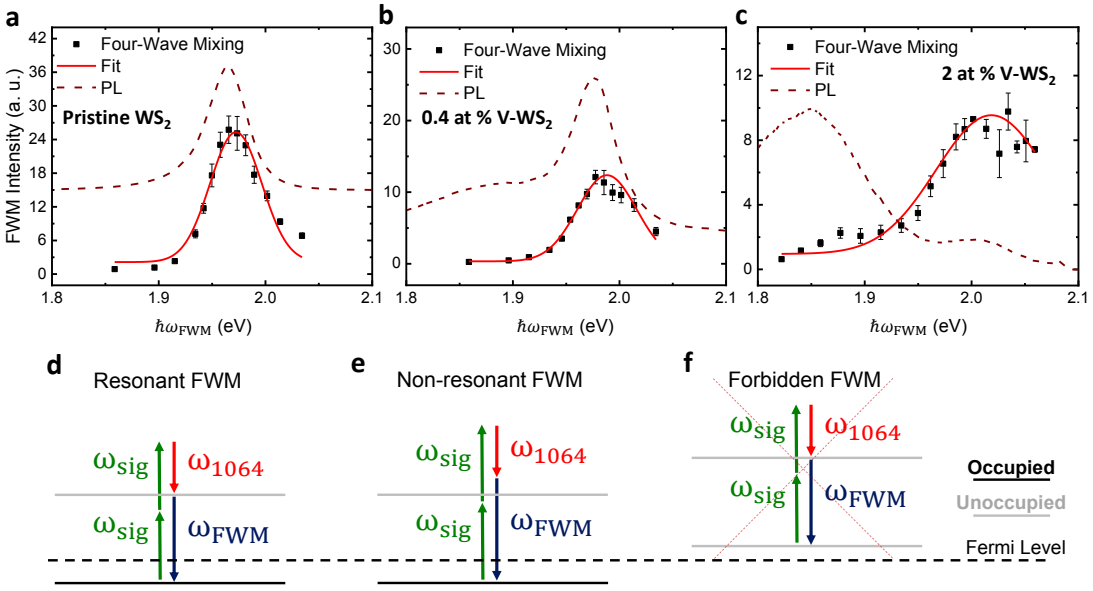

Figure 6.2 – **a-c** FWM resonant profile (black squares) and its Gaussian fits (red line) together with the PL spectra (dashed brown line) for the pristine (**a**), 0.4 at% (**b**) and 2.0 at% (**c**) vanadium doped WS_2 monolayers. The FWM resonances align with the higher energy PL peak for the V-doped samples. **d-f** FWM energy diagrams for resonant (**d**), non-resonant (**e**), and forbidden (**f**) conditions. The colored arrows correspond to the photons of the FWM process as described by Equation 6.1. The black lines are associated with occupied states, the gray lines with unoccupied states and the dashed line with the Fermi level.

photon energy matches the electronic transition energy ($E_{exciton}$). γ is a damping factor relating to the inverse lifetime for the resonant scattering process (273).

To plot a REP, we need to choose a Raman mode whose intensity can be easily tracked over a wide range of excitation energies. Figure 6.4a shows the Raman spectrum of a pristine WS_2 monolayer with 521 nm excitation. Peak positions and their Raman mode assignments have been investigated by other researchers (343, 344). Among these peaks, only the 2LA(M), E_{2g1}, and A_{1g} modes do not quickly lose discernable signals out of resonance, as shown in Figure 6.3. However, 2LA(M) and E_{2g} are not ideal for plotting a REP because their energies are almost degenerate, making it difficult to separate their signals, leaving A_{1g} as the best choice for plotting the REP.

The A_{1g} intensities for all Raman spectra in Figure 6.3 (normalized by the Si peak and accounting for its Raman cross section) were fitted by Lorentzian functions and the resulting A_{1g} REP is shown in Figures 6.4b-e. These data points were further fitted by Equation 6.2, with the A_{1g} frequency for each sample being the phonon energy E_{ph}, and then plotted in red curves. As the pristine, 0.4 at%, and 2.0 at% samples present two resonant responses (one centered around 2.4 eV and another at higher energies), we have used two distinct values of $E_{exciton}$ to fit their data. The ascertainment of the resonant energy value around 2.4 eV is not affected by the uncertainty of the value of

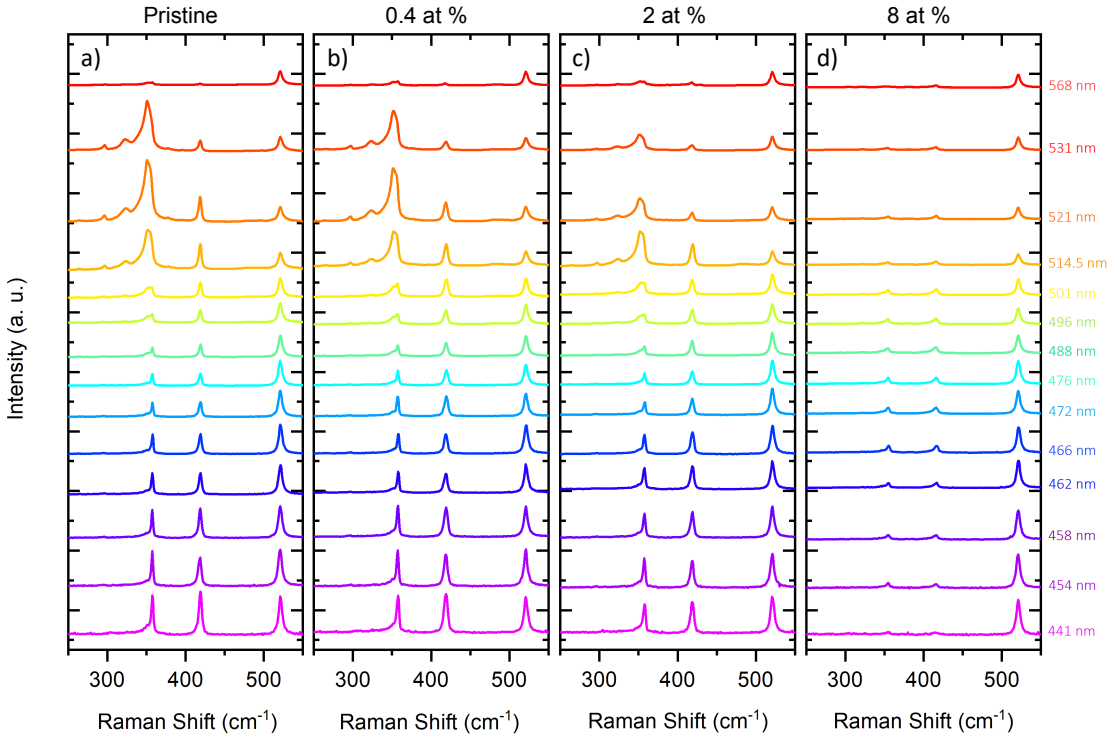

Figure 6.3 – **a-d** Raman spectra for pristine WS_2 (**a**) and 0.4 at% (**b**), 2 at% (**c**), and 8 at% (**d**) vanadium doped WS_2 monolayers under 14 different excitation energies. The excitation wavelengths are on the right side of each spectrum of the 8 at% V-doped WS_2 monolayer (**d**). All spectra were normalized by the silicon peak intensity considering its Raman cross section for each laser line.

the higher-energy resonance because of their large spectral distance. The WS_2 monolayer with 8.0 at% of vanadium concentration shows only one resonant feature and thus was fitted to a single value of $E_{exciton}$. The lower (B exciton) resonance energies produced by the fittings are 2.42, 2.44, 2.49 and 2.57 eV for the pristine, 0.4 at%, 2.0 at% and 8.0 at% samples, respectively. For the pristine sample, the 2.42 eV peak agrees with reported values for the WS_2 monolayer B exciton energy measured by other groups with the same (274) and different (345) techniques. Therefore, it is reasonable to assign the REP peak energy as the B exciton energy in each sample, and we observe thus a B exciton blueshift under increasing vanadium concentration. This blueshifting feature is also observed in differential reflectance measurements and in the REP of the LA mode of those samples, as shown in Appendix Figures A.2 and A.4.

Resonant SHG was also used to probe the higher-energy transitions in pristine and V-doped WS_2 samples. As shown in Figure 6.5, the pristine sample presents a clear resonance due to the C exciton (20, 346). Furthermore, the V-doped WS_2 samples show a similar resonance energy, indicating that the vanadium doping did not cause any substantial modification to this transition. Hence, beyond the electronic characterization of the samples, the results discussed above also demonstrate an optical method to identify the vanadium doping level in WS_2 monolayers by measuring the energy splitting of P_1 and P_2 PL peaks

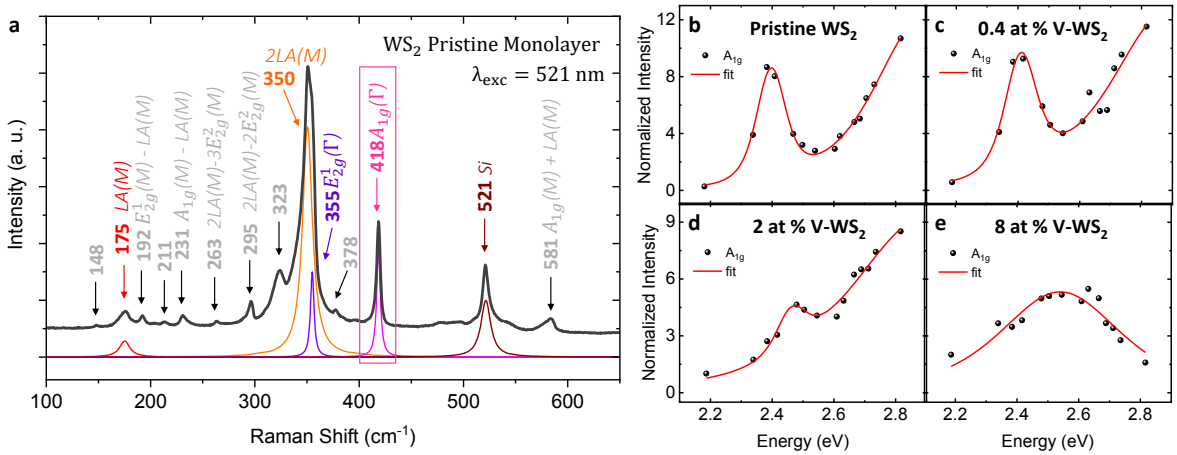

Figure 6.4 – **a** Raman spectra of a pristine WS_2 monolayer for 521 nm laser excitation. The peak positions and some of the Raman modes are assigned. The Lorentzian peak fits of selected Raman modes are shown in different colors below the spectra. **b-e** Raman excitation profiles of the A_{1g} Raman mode (highlighted in pink in (**a**)) for the (**b**) pristine, (**c**) 0.4 at%, (**d**) 2 at%, and (**e**) 8 at% V-doped WS_2 monolayers. The solid red curves show the fits to Equation 6.2.

as well as by probing the B exciton energy. To summarize these experimental results, Figure 6.6 shows P_1, P_2, B exciton and C exciton energies for WS_2 monolayers with respect to their vanadium concentration obtained from all optical techniques used in this work.

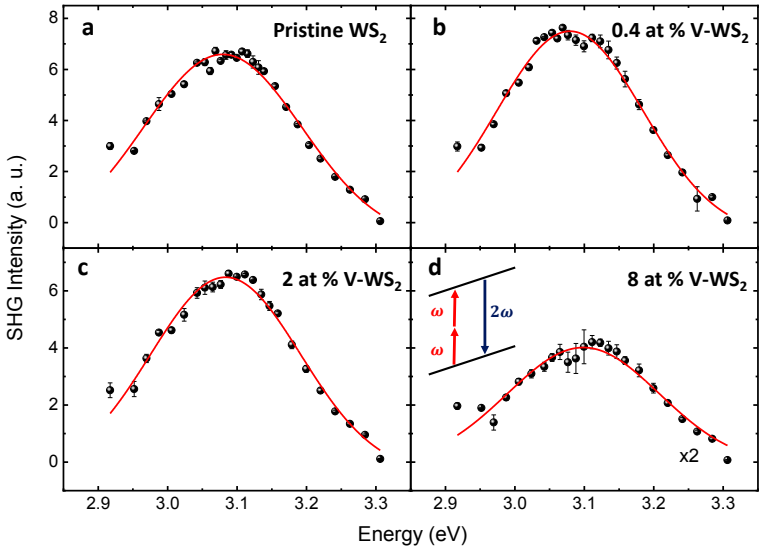

Figure 6.5 – **a-d** Second-harmonic generation intensity profile in the C exciton energy range for the (**a**) pristine, (**b**) 0.4 at%, (**c**) 2 at%, and (**d**) 8 at% V-doped WS_2 monolayers. The SHG resonance with the C exciton transition is represented in the inset scheme in (**d**). A similar C exciton energy for all samples can be noted.

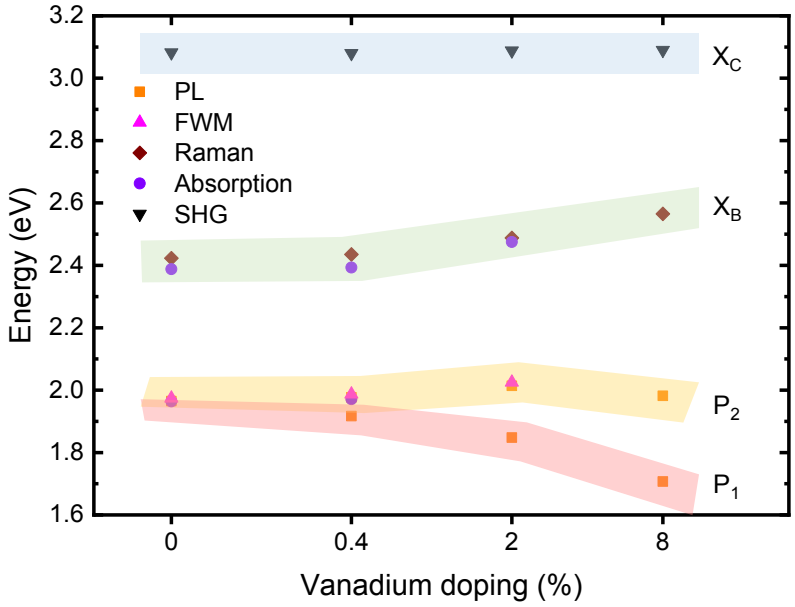

Figure 6.6 – Summary of P_1, P_2, B exciton (X_B) and C exciton (X_C) energies for WS_2 monolayers with respect to their vanadium doping concentration measured by PL, resonant FWM, resonant Raman, absorption (differential reflectance) and resonant SHG measurements. The shadowed areas are guide to the eyes.

6.1.4 Electronic structure calculation for V-doped WS_2

To understand the optical properties observed in experiment, we examined the band structures (Appendix Figure A.5) of V-doped WS_2 with a Hubbard U correction $U = 0$ to 5 eV for vanadium and the transition dipole moments to identify candidate transitions, as summarized in Figure 6.7. These calculations were performed by our theoretician collaborators Prof. Vincent Crespi and Boyang Zheng from Penn State University. The optical transitions in WS_2 mainly relate to the d_{x^2}/d_{xy} orbitals at the valence band maximum (VBM) and the d_{z^2} orbitals at the conduction band minimum (CBM) at the K or $-$K valleys (347). The defect states from the vanadium dopant mainly have the character of vanadium d_{z^2} (see Figure 6.8a), so their hybridization with the CBM is plausible. When U is small ($U \leq 2$ eV), the defect state in the conduction band is far from the band edge, thus it does not hybridize well with the CBM. However, the defect state still shows a non-negligible optical coupling to the valence bands at the K valley. In this case ($U = 0$, 1 and 2 eV), the A and B excitons can be easily identified and we find a valley degeneracy breaking of ~ 0.02 to ~ 0.1 eV, A exciton redshifts of ~ 0.05 to ~ 0.10 eV, and B exciton redshifts of ~ 0.13 to ~ 0.20 eV as U increases. If U further increases, the defect state in the conduction band drops in energy and hybridizes with the spin-up CBM (i.e. the same spin as the defect state). The resulting hybridized states both show large optical transition matrix elements with the d_{x^2}/d_{xy} valence bands. When $U \geq 3$ eV, we cannot identify the A exciton at the K valley or the B exciton at the $-$K valley, so we tentatively call them "upper" and "lower" spin-up transitions; we will discuss these later.

This hybridization explains why the spin-up transitions are sensitive to the value of U. On the other hand, the spin-down defect states are far from the CBM and consequently do not hybridize with it, thus the spin-down transitions are insensitive to the value of U.

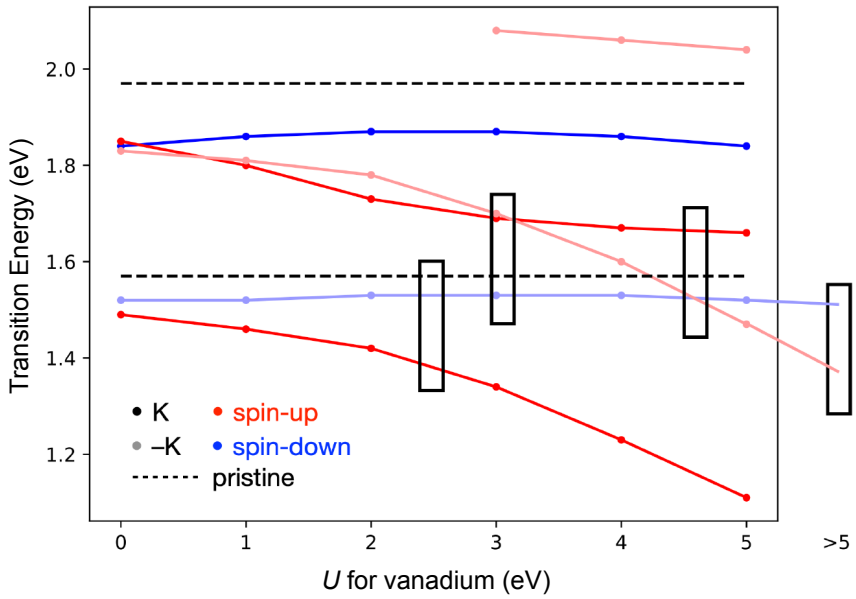

Figure 6.7 – Transition energies with largest dipole moments in V-doped WS_2 (1 vanadium in a 5×5 supercell). The dashed line shows the calculated A, B exciton energies in pristine WS_2. The extensions to $U > 5$ eV are drawn schematically following the trend from the plot. Valley degeneracy breaking is non-negligible even without a Hubbard U correction for vanadium. The bandstructure and consequently the optical properties are sensitive to the value of U. As the Hubbard U increases, the transitions associated with spin-up states redshift while those associated with spin-down states are relatively insensitive to the Hubbard U. The rectangles highlight four possible scenarios to explain the ~ 0.13 eV energy difference between the P_1 and P_2 peaks. Adapted from: (337).

Identifying the origin of the experimental peaks is not straightforward due to the sensitivity of the band structure to the value of U in addition to the underestimation of optical transition energies in DFT at the PBE level (348). We therefore focus on the ~ 0.13 eV splitting of P_1 and P_2 around the A exciton energy region in Figure 6.1 and find 4 possible scenarios with $U \sim 2.5$, ~ 3, ~ 4.5, and > 5 eV, as highlighted in the inset black rectangles of Figure 6.7. In the $U \sim 2.5$ eV scenario, the P_1–P_2 energy difference is from the valley degeneracy breaking of the A exciton. In the $U \sim 3$ eV scenario, P_1 is the A exciton at $-$K and P_2 could be the upper spin-up transition at K and/or the lower transition at $-$K since their energies coincide. In the $U \sim 4.5$ eV scenario, the A exciton and the lower transition energies at $-$K have similar energies, so they both could explain the P_1 peak, while the upper spin-up transition at K could be the P_2 peak. In the $U > 5$ eV scenario, P_1 is the lower spin-up transition and P_2 is the A exciton at $-$K. Among these scenarios, $U \sim 3$ and ~ 4.5 eV can qualitatively explain the blueshift of the P_2 peak relative to the pristine A exciton. In the $U \sim 3$, ~ 4.5, and > 5 eV

scenarios, the high energy of the upper spin-up transition could qualitatively explain the blueshift of the B exciton while the transition with the lowest energy (the lower spin-up transition at K) may lead to PL emission with further lower energy, however we could not observe this emission given our instrument sensitivity. Moreover, the $U \sim 3$ eV scenario shows occupied/unoccupied VBM at K/−K, that is in agreement with our power-dependent PL, resonant FWM, and differential reflectance measurements in which radiative recombinations to unoccupied/occupied bands for P_1/P_2 PL peaks are shown (the band structure representation of these recombinations is schematically depicted in Figures 6.8c-d). The linear power dependence of P_2 could also be explained since the electron state of the P_2 at −K shows non-negligible dispersion, meaning this state has a significant contribution from the WS_2 basal plane which can support the linear power dependence. Although none of these scenarios can fully explain all of the optical responses observed in the experiments, they provide relevant insights into the electronic structure modifications by the introduction of vanadium on a WS_2 monolayer as well as its dependence on the Hubbard U correction.

In summary, by applying broadband optical characterization through the use of several optical tools we studied the electronic band structure and optical transitions, as well as their dependence on vanadium doping, of WS_2 grown by single-step CVD. Power-dependent PL measurements showed that the A exciton PL peak of the pristine WS_2 monolayer split into two PL peaks after vanadium doping — one (P_1) redshifted and another (P_2) blueshifted with respect to the pristine A exciton PL peak. The linear/sublinear power dependence of P_2/P_1, together with the fact that FWM resonant profiles only show the P_2 peak, indicated that the P_2/P_1 PL peak is associated with a radiative recombination to an occupied/unoccupied electronic band. Resonant Raman spectroscopy measurements revealed a blueshift in the B exciton energy under increasing vanadium doping, while the SHG resonant profile presented no modifications in the C exciton energy. First-principle calculations showed valley degeneracy breaking after vanadium doping and a strong dependence of the band structure on the Hubbard U parameter for vanadium. Both our experimental and computational results indicated the presence of free holes in V-doped WS_2, suggesting a similar magnetic exchange mechanism as in the case of V-doped WSe_2 (220, 226) . Our work shows the great potential of broadband optical characterization to study the impact of defect in 2D materials.

6.2 Optical and magneto-optical characterization of V-doped WSe_2

In this section we show optical and magneto-optical properties of a CVD grown 4% vanadium doped WSe_2 monolayer. Room temperature PL and Raman spectroscopy measurements were performed in pristine and V-doped WSe_2 samples to study the effects of the defect on their electronic and vibrational properties. Raman spectroscopy measurements

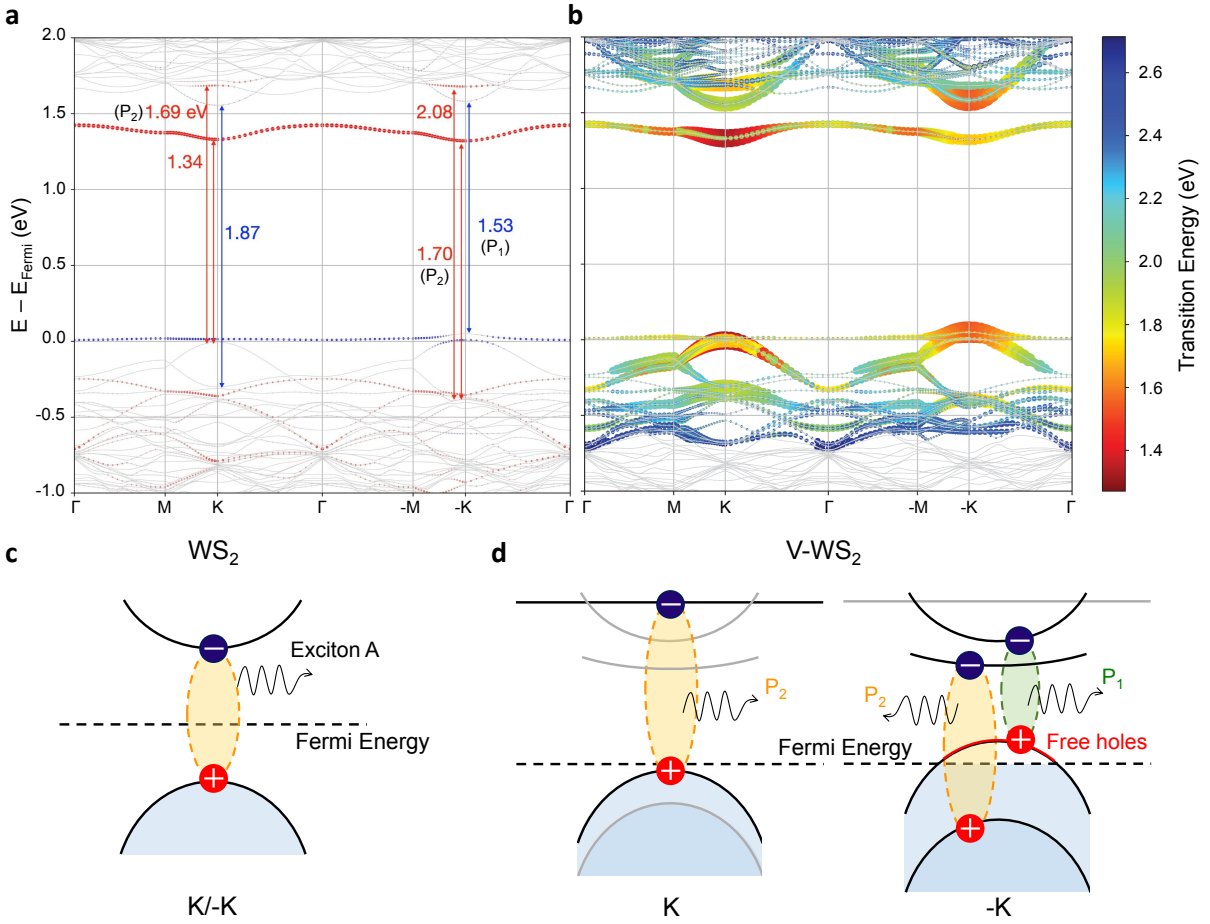

Figure 6.8 – **a** Band structure of V-doped WS_2 with $U \sim 3$ eV for vanadium. For each state, a circle is plotted with size proportional to the projection onto the vanadium d_{z^2} orbital and color indicating the spin (red–up, blue–down). The vanadium defect state in the conduction band, mainly with d_{z^2} character, has spin up and hybridizes with the spin-up conduction band minimum. As the Hubbard U increases, these two spin-up states decrease in energy, while the spin-down defect states remain far away from the conduction band edge. **b** Band structure and transition dipole moments of V-doped WS_2 with $U \sim 3$ eV for vanadium. The energy of transitions at K with the largest transition dipole moments are 1.34, 1.69 and 1.87 eV. The energy of transitions at $-$K with the largest transition dipole moments are 1.53, 1.70 and 2.08 eV. **c-d** Schematic illustration of band structure and optical transitions close to the pristine A exciton energy for the pristine and V-doped WS_2 monolayers with $U \sim 3$ eV for vanadium. The pristine sample presents its degenerate A exciton recombination at K and $-$K valleys (**c**), while the V-doped WS_2 monolayer displays valley degeneracy breaking with the valence band minima below and above the Fermi level at K and $-$K, respectively, showing the presence of free holes at the $-$K valley. The black bands are associated with P_1 or P_2 optical transitions, while the gray bands are not related to them. Adapted from: (337).

were carried for distinct laser lines in the visible and NIR spectral range to also study the excitonic resonances of the samples, which was probed by resonant FWM measurements as well. Furthermore, circularly polarized low temperature magneto-PL measurements were performed to investigate the valley Zeeman splitting in the 4% V-doped WSe_2

monolayer. Our theoretician collaborators from UFMG and UFOP are finishing the electronic structure calculation of the vanadium-doped WSe_2 to ascertain the origin of these concluded experimental results.

6.2.1 Optical Characterization of a CVD grown V-doped WSe_2 monolayer

The modifications in the optical properties of V-doped WSe_2 monolayers were previously reported for chemical vapor transport (CVT) grown samples (266, 267) with distinct vanadium concentrations lower than or equal to 1%. However, the optimal ferromagnetic response observed for these samples was in a 4% V-WSe_2 monolayer (43). Moreover, the experiments that showed a room temperature ferromagnetism in these materials were carried out on CVD grown samples (42, 43). Therefore, it is of great importance to carry a broad optical characterization in a CVD grown 4% V-WSe_2 monolayer as the growth method plays a major role in the optical responses of the material (166). Hence, we firstly performed room temperature PL and Raman spectroscopy measurements in CVD grown pristine and 4% V-doped WSe_2 monolayers. The samples were grown by the same method described by Pham *et al.* (43). Figures 6.9a,b show the PL spectra for pristine and 4 at% vanadium concentration WSe_2 monolayers for a 561 nm excitation. As well as for CVT grown samples, the CVD grown 4% V-doped WSe_2 monolayer also exhibits a defect lower energy PL peak besides the exciton and trion peaks (266, 267). Moreover, the trion peak also dominates the PL spectrum for the V-doped sample, which is explained by its p-type doping. However, distinctively from CVT grown V-doped WSe_2 monolayers, the PL quenching by increasing the vanadium concentration is significantly lower in the CVD grown samples. While the PL quenching for the CVT grown 0.3% and 0.5% V-doped WSe_2 monolayers was greater than 100 and 500 times (266), respectively, the CVD grown 4% V-doped WSe_2 displays a PL quenching less than 7 times with respect to the pristine monolayer PL intensity. Figures 6.9c,d show the power dependence of the exciton, trion and defect PL peaks for pristine and 4% V-doped WSe_2 monolayers. While the intensity of the exciton (X_0) and trion (X_+) peaks present a linear power dependence, the defect peak shows a sublinear dependence, which is related to a vanadium mid gap bound-exciton state (X_V) (266, 267).

Raman spectroscopy measurements were also employed to compare pristine and 4% V-doped WSe_2 monolayers. Figure 6.9e shows the Raman spectra of both samples for a 514 nm excitation, presenting a quenching in the Raman intensity under vanadium doping but no measurable shift in the Raman frequencies for the degenerate first-order modes (E_{2g} and A_{1g}) and the 2LA second-order mode. The Raman spectra were also taken for distinct laser lines. Figures 6.9f,g display the Raman spectra for several visible laser lines for pristine and 4% V-doped WSe_2 monolayers, whereas Raman spectra performed with NIR laser lines are shown in Appendix Figure A.6. As shown in Figure 6.10a,b, from the

Raman experiments with NIR excitation we extracted the convoluted $E_{2g} + A_{1g}$ intensities and plotted their REPs for both samples, revealing strong resonant responses even for the V-doped monolayer. The REPs were fitted by the Raman Equation 6.2 with a single $E_{exciton}$ value, as we are not able to resolve the exciton, trion and defect resonances in these REPs. In addition, remarkable resonances were also noticed in resonant four-wave mixing measurements performed in pristine and 4% V-doped WSe_2 monolayers, as displayed in Figures 6.10c,d, which exhibits the noticeable nonlinear optical response of this CVD grown V-doped sample. In contrast to the REPs, the FWM data were fitted by 2 Gaussian peaks. Both Raman and FWM resonant responses are in agreement with the energy position of the PL peaks shown in Figure 6.9.

6.2.2 Enhanced magneto-optical response of a V-doped WSe_2 monolayer

To study the influence of the vanadium doping on the valley Zeeman effect of WSe_2 monolayers we performed low temperature (4 K) circularly polarized magneto-PL measurements in both pristine and 4% V-doped WSe_2 monolayers. Although circularly polarized magneto-PL measurements have already been reported for CVT grown V-doped WSe_2 monolayers (267), they were carried out on samples with vanadium concentrations lower than 1%. Therefore, it is extremely important to also probe the optical responses of the optimal 4% vanadium concentration sample under an external magnetic field. Figure 6.11a displays PL spectra for a 4% V-doped WSe_2 monolayer with a linear polarized excitation and a right circularly polarized (σ_+) detection at external magnetic fields of -9 and 9 T. The external magnetic fields were all applied perpendicular to the sample plane. At 4 K the X_+ peak dominates even more the PL spectra, while the X_0 emission becomes almost negligible. Moreover, there is a giant energy shift in the X_V PL peak between the spectra taken at 9 and -9 T. This shift is better noticed in Figure 6.11b, in which normalized PL spectra performed at distinct external magnetic fields from -9 to 9 T are displayed. The logarithm scale of the PL intensity axis highlights the X_V emission, revealing its strong dependence with the magnetic field. PL spectra were performed by varying the external magnetic field from -9 to 9 T with steps of 0.1 T. All PL spectra are shown in the PL intensity 2D plots of Figures 6.11c,d, respective to σ_+ and σ_- detections. The spectra were normalized by their maximum intensity related to the X_+ emission. While there is a small energy shift in the X_+ peak position, a larger shift in the X_V emission is observed. To measure these shifts, all spectra of Figures 6.11c,d were fitted by Gaussian peaks. Figure 6.11e displays the energies of the X_V peak from -9 to 9 T for both σ_+ and σ_- detections, which were extracted from the fitted parameters. Opposite shifts of almost 30 meV for this magnetic field range are noted between both circular polarized detections. The X_V Zeeman splitting given by the energy difference between σ^+ and σ^- emission ($\Delta E = E_{\sigma^+} - E_{\sigma^-}$) is presented in Figure 6.11f. As discussed in Chapter 2, the ΔE can

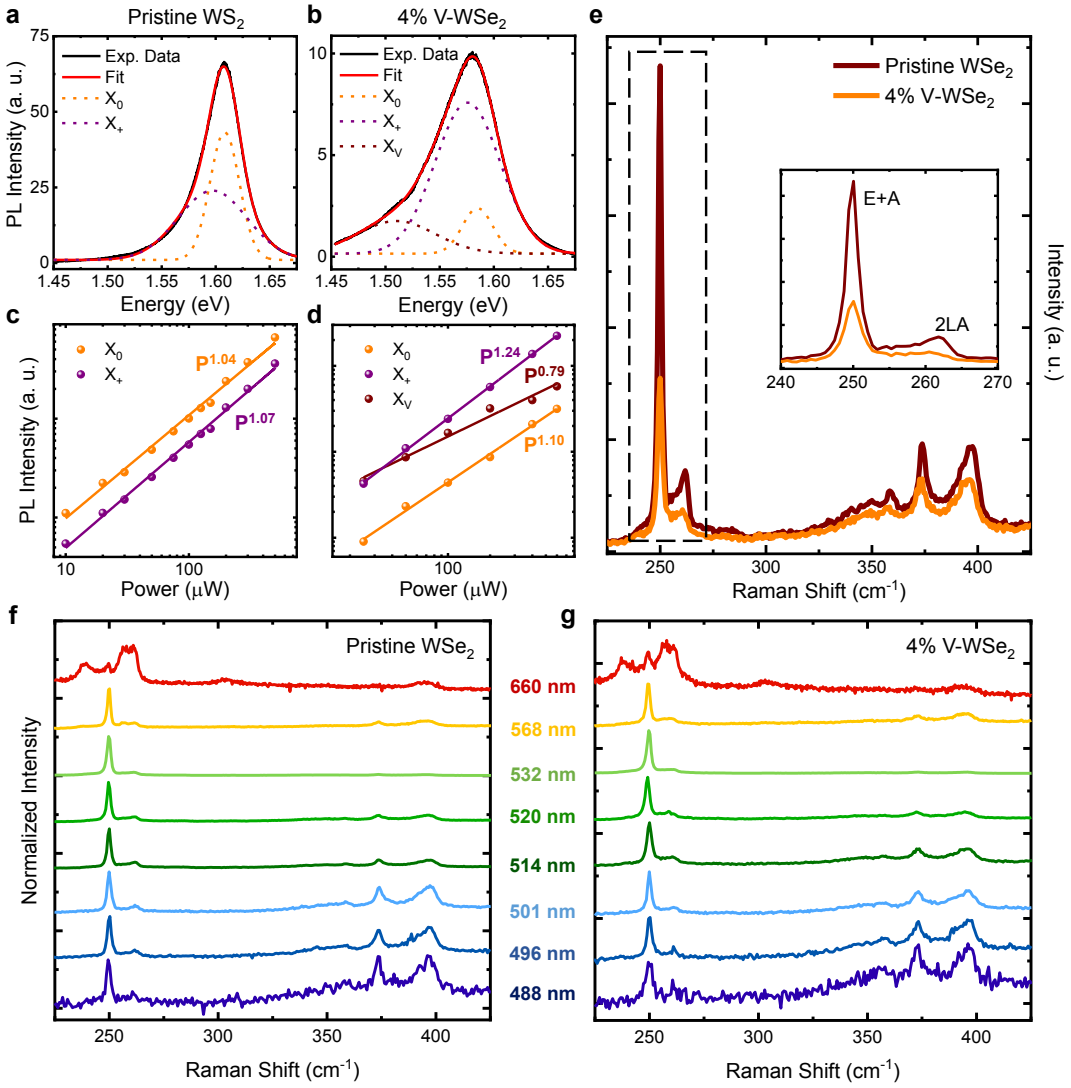

Figure 6.9 – **Optical characterization of CVD grown pristine and 4% V-doped WSe_2 monolayers. a,b** Room temperature PL spectra of pristine (**a**) and 4% V-doped (**b**) WSe_2 monolayers for a 561 nm excitation. The red curves display the cumulative fit of the experimental data (in black). The dashed lines are related to the exciton, trion and defect peaks of the fit. **c,d** Power dependence of the PL peaks intensity for the pristine (**c**) and 4% V-doped (**d**) WSe_2 monolayers. The exciton and trion peaks show a linear power dependence, while the defect peak shows a sublinear dependence. **e** Raman spectra of pristine and 4% V-doped WSe_2 monolayers for a 514 nm excitation. The inset highlights the E^1_{2g}, A^1_{1g} and 2LA Raman modes. **f,g** Raman spectra for distinct visible laser lines of pristine (**f**) and 4% V-doped (**g**) WSe_2 monolayers.

be written as a function of the magnetic field as: $g\mu_B B$, in which $\mu_B = 0.05788$ meV/T is the Bohr magneton and g is the g-factor. A g-factor value of -51.6 for the X_V emission was extracted for the 4% V-doped WSe_2 monolayer by a linear regression of its Zeeman splitting. However, since there is a convolution between the PL peaks due to their large linewidths, it is worth to comment that the X_V fitted parameters can be overestimated. Therefore, we performed these magneto-PL measurements in different points of distinct 4%

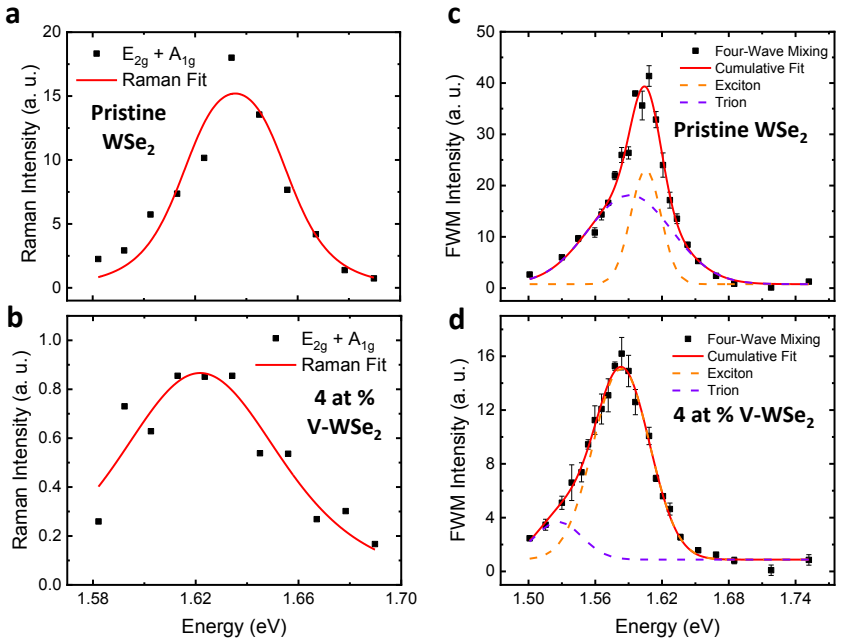

Figure 6.10 – **Raman and FWM resonant profiles of pristine and V-doped WSe_2 monolayers. a,b** REPs of pristine (**a**) and 4% V-doped (**b**) WSe_2 monolayers. The scattered experimental data (in black) were fitted by the Raman equation 6.2 (red curve). **c,d** Resonant FWM intensity profile for the pristine (**c**) and 4% V-doped (**d**) WSe_2 monolayers. The FWM data were fitted by 2 Gaussian peaks, which are related to exction and trion for the pristine sample and trion and defect mid gap state for the V-doped sample.

V-doped WSe_2 monolayer flakes and we fitted them fixing distinct values for the X_V peak linewidth (see Appendix Figure A.7). With this analysis we found distinct g-factor values ranging from -26.7 to -69.0. In any case, although there is not a precisely value for the X_V peak g-factor, it can be observed an evident giant Zeeman splitting for this vanadium defect emission. This low precision can be improved by encapsulating the sample in 2D h-BN flakes, as it causes a narrowing in the PL peaks.

In addition to the valley Zeeman splitting associated with the X_V peak, we have also analyzed the Zeeman effect in the X_+ peak. As the pristine WSe_2 monolayer PL spectra also presents a strong X_+ emission at 4 K, it is possible to compare the modifications in the valley Zeeman splitting under vanadium doping. Figure 6.12 shows the X_+ energy and Zeeman splitting for both pristine and 4% V-doped WSe_2 monolayers for external magnetic fields from -9 to 9 T. Conversely to the nonlinear g-factor reported for the CVT grown 0.3% V-doped WSe_2 monolayer (267), we observed expected linear g-factors for the CVD grown pristine and 4% V-doped WSe_2 monolayers. While the pristine sample presented a g-factor value of -3.2, the V-doped monolayer displayed an enhanced g-factor of -5.2.

Enhanced g-factors have also been reported for distinct dilute magnetic semiconductors. Fe-doped (41) and Co-doped (40) MoS_2 monolayers also presented higher

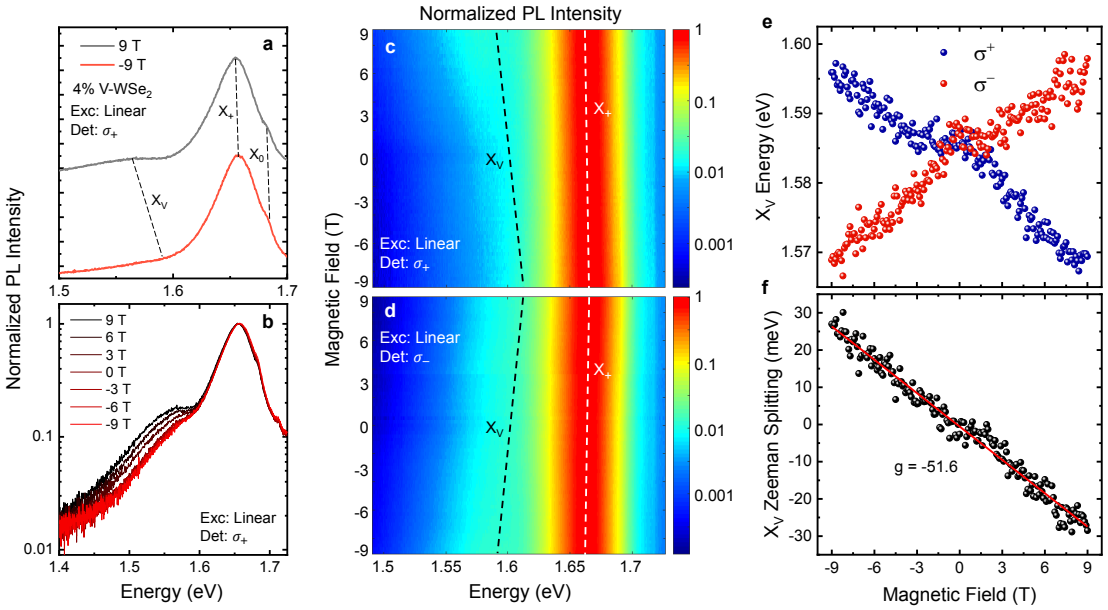

Figure 6.11 – **Low temperature magneto-PL measurements for a 4% V-doped WSe_2 monolayer. a,b** Normalized PL spectra of a 4% V-doped WSe_2 monolayer performed with linear polarized excitation and σ_+ detection for distinct external magnetic fields ranging from -9 to 9 T and at 4 K. The PL spectra present a major contribution from the X_+ recombination, a lower energy emission related to the X_V peak and a minor signal related to the X_0 peak. A remarkable shift in the X_V peak is observed by varying the external magnetic field from -9 to 9 T. This feature is well noticed in (**b**), in which the intensity axis is plotted in log-scale. **c,d** Normalized 2D plot of the 181 PL spectra ranging from -9 to 9 T with steps of 0.1 T for σ_+ (**c**) and σ_- (**d**) detections. **e** Magnetic field dependence of the X_V peak energy for σ_+ and σ_- detections. The energy values were extracted from the fitting of the PL spectra. **f** Valley Zeeman splitting associated with the X_V peak, showing a giant g factor calculated from the linear fit shown in red.

g-factor values for their exciton emission due to the interaction between the MoS_2 electronic bands with the localized magnetic moments of the dopants. Nonetheless, although they also displayed a lower energy defect peak, this peak was not associated with a Zeeman splitting. As V-doped WSe_2 monolayers exhibit a magnetic ordering, the mechanism that leads to their enhanced Zeeman effect associated with the trion emission should also be related to the hybridization between the WSe_2 valence and conduction bands with the magnetic moments of the vanadium states. In addition, in contrast to the Fe- and Co-doped MoS_2 samples, the defect mid gap state in the V-doped WSe_2 monolayers might have an expressive magnetic moment, leading to the giant g-factor observed for the X_V peak. To confirm these hypothesis and further understand the origin of these notable Zeeman splittings, our theoretician collaborators Prof. Helio Chacham and Prof. Matheus Matos from UFMG and UFOP are calculating the electronic structure and the respective magnetic moments of a vanadium-doped WSe_2 monolayer.

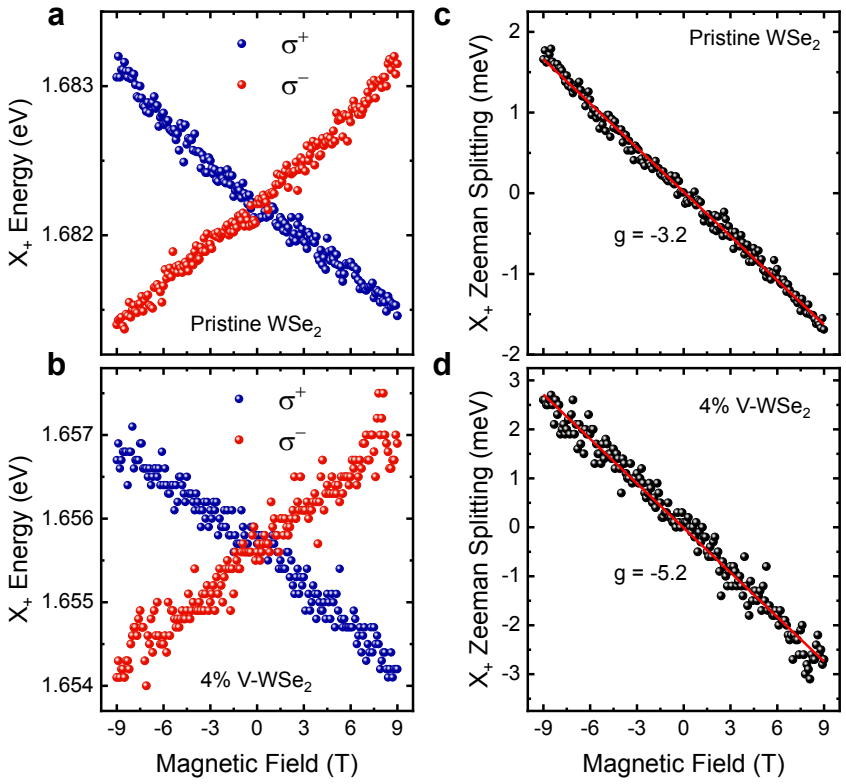

Figure 6.12 – **Trion valley Zeeman splitting of pristine and 4% V-doped WSe_2 monolayers. a,b** Magnetic field dependence of the X_+ peak energy for σ_+ and σ_- detections of pristine (**a**) and 4% V-doped (**b**) WSe_2 monolayers. The energy values were extracted from the fitting of the PL spectra. **c,d** Valley Zeeman splitting associated with the X_+ peak of pristine (**c**) and 4% V-doped (**d**) WSe_2 monolayers. The doped samples presented an enhanced g-factor value of -5.2 with respect to the -3.2 g-factor of the pristine monolayer. The g-factors were calculated from the linear fit presented in red.

6.3 Giant g-factor and magnetic field induced spin-polarization in aged WS_2 and WSe_2 monolayers

In addition to the intentionally doped TMD monolayers, there are several other defects that can affect the TMDs optical and magneto-optical properties, such as the commonly reported adsorbed atoms and molecules due to the sample aging. Therefore, there are possible hidden valley Zeeman responses in these defective TMDs that still lack magneto-optical investigations. Here we investigate the valley Zeeman effect in aged CVD grown WS_2 and WSe_2 monolayers by magneto-PL measurements with circularly polarized light detection. The following results are submitted as a manuscript and its preprint version is published in Ref. (349).

6.3.1 Magneto-optical measurements in aged WS_2 monolayers

To probe the presence of defects in an aged TMD sample and study the consequent modifications in its light emission, we firstly performed power dependent PL measurements in a 2-year aged CVD grown WS_2 monolayer, as shown in Figures 6.13a,b. The power-dependent PL spectra of Figure 6.13a were taken at 4 K and are normalized by the free exciton (X_0) peak ($\sim$ 2.02 eV), revealing a lower energy PL peak with a distinct intensity and energy position features. While the exciton PL peak presents no relevant shift in its energy and a linear increasing of its intensity with respect to the incident power, the lower energy peak displays a sublinear power dependence and a noticeable energy blueshift, as highlighted in Figure 6.13b. Moreover, Figure 6.13c shows the temperature dependent PL spectra of the WS_2 monolayer, in which the lower energy PL peak presents an intensity quenching and an energy redshift under increasing temperature. Additionally, in Appendix Figure A.8 it is possible to note that this lower energy peak vanishes at room temperature. A lower energy PL emission with sublinear power and temperature dependencies is commonly related to defect-bound localized excitons (X_L) (350). Nonetheless, this feature is reported for a variety of possible defects in TMDs, such as vacancy (170), substitutional doping (177) and adsorbed impurities (351, 34, 352, 353, 170, 189). On the other hand, the significant energy shift displayed for both power and temperature variation as well as the large spectral linewidth and its peak position was previously related to the adsorption of oxygen and organic molecules due to an aging process (351, 34, 352, 353, 189).

In order to further characterize these samples, our collaborators from CDTN have performed XPS measurements. The valence state of each element present in the WS_2 sample was investigated using the high-resolution XPS spectra analysis. The analysis was used to validate the existence of a minor fraction of adsorbent defect sites within their structures, as done in Ref. (189). Figure 6.13d displays the spectrum of W 4d, which reveals the presence of two asymmetric responses associated with W $4d_{5/2}$ and W $4d_{3/2}$ orbitals (354). Each one of these asymmetric orbital responses were fitted with two Voigt peaks. While the predominant fitted peaks (in blue) at 244.8 and 257.2 eV are related to the chemical state doublet of the W-S bond, the orange fitted peaks at 249.2 and 261.3 eV indicate the presence of a distinct chemical state doublet in a higher binding energy. Moreover, XPS high-resolution spectra of the aged WS_2 monolayer for the W 4f orbitals also exhibit an asymmetric response due to the presence of a defective chemical state doublet (see Appendix Figure A.9). Similar XPS results were previously reported for an aged WS_2 monolayer and were related to a loss of sulfur atoms and a higher oxidation state for tungsten atoms as well as to the presence of non-identified adsorbed organic molecules (351, 189). Therefore, our XPS measurements give an indication that the defects responsible for the lower energy PL peak are similar to those found in Refs. (351, 189).

In order to investigate the circular dichroism of the X_L peak and its dependence

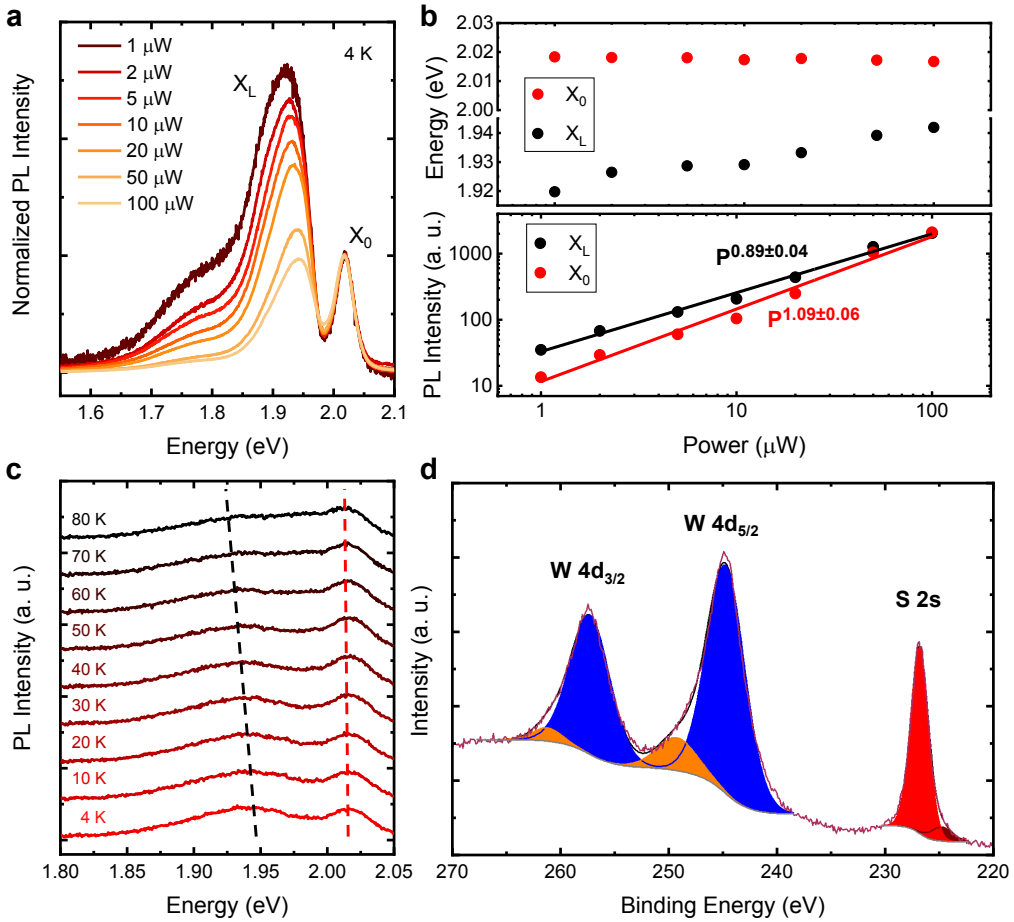

Figure 6.13 – **a** Power dependent PL spectra at 4 K for an aged WS_2 monolayer showing free exciton and defect-bound exciton peaks. PL spectra are normalized by the intensity of the free exciton peak. **b** PL energy (top graph) and intensity (bottom graph) dependencies on the incident power for both defect and exciton PL peaks. **c** Temperature dependent PL spectra for a 100 μW incident power. All measurements were performed with a 532 nm laser. **d** XPS spectrum of W 4d and S 2s core-level peaks. The W 4d displays two W $4d_{5/2}$ and W $4d_{3/2}$ doublets associated to W of the main WS_2 structure (blue fitted peaks) and to W at defect sites (orange fitted peaks).

with an external magnetic field we performed circular polarization magneto-PL measurements in the aged CVD grown WS_2 monolayer at 4 K. The sample was excited by a linearly polarized laser beam, with an incident power of 100 μW and applying a perpendicular external magnetic field tunable from -9 to 9 T (with steps of 0.1 T), while its PL emission was detected for both right (σ^+) and left (σ^-) circular polarizations. Figures 6.14a,b exhibit the PL spectra for -9, 0 and 9 T for both σ^+ and σ^- detections. An opposite energy shift with respect to the magnetic field for σ^+ and σ^- emissions can be observed for both X_0 and X_L peaks. A wider perspective of this shifting can be noted in the PL intensity 2D plots of Figures 6.14c,d, which contains all 181 PL spectra measured varying the external magnetic for both polarizations. This opposite energy shifting occurs due to the Zeeman effect, that displaces each valley in opposite directions in energy as they

present inverse spins. Besides, Figures 6.14a-d also display the great broadening of the X_L peak corresponding to its redshifting with magnetic field. The magnetic field dependence of the valley Zeeman splitting ΔE - denoted as the energy difference between σ^+ and σ^- emission ($E_{\sigma^+} - E_{\sigma^-}$) - is given by $\Delta E = g\mu_B B$, in which $\mu_B = 0.05788$ meV/T is the Bohr magneton and g is the g-factor. Thus, first we extracted the energy position of X_0 and X_L peaks for all PL spectra, as shown in Figures 6.14e,f. From the energy values, we plotted the valley Zeeman splitting for X_0 and X_L peaks and calculated their associated g-factors from the data linear fit, as presented in Figure 6.14g,h. A g-factor of -3.6 is noted for the X_0 peak, that is in agreement with previously reported values (146, 147, 148, 149). On the other hand, an enhanced g-factor of -25.0 can be observed for the X_L peak, which correspond to its noticeable energy shifting shown in the magneto-PL spectra of Figures 6.14a-d. We performed similar measurements in another aged WS_2 monolayer and we noticed this enhanced X_L g-factor for it as well, as displayed in Appendix Figure A.10. Besides, we also probed an aged WS_2 monolayer with a 1 μW incident power to study the power influence on this giant X_L g-factor, as shown in Appendix Figure A.10. A significant Zeeman shifting for the defect-bound exciton for this lower pumping power is also observed.

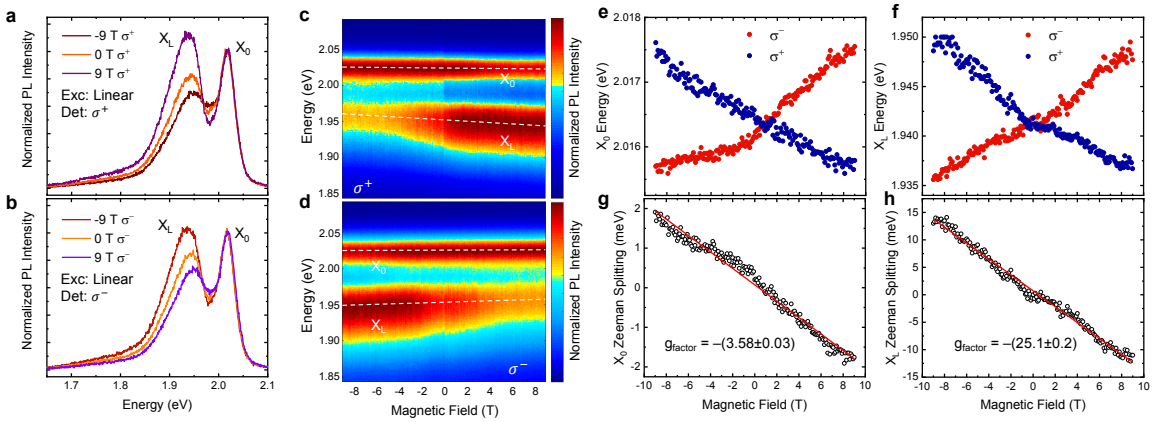

Figure 6.14 – **a,b** PL spectra of an aged WS_2 monolayer for a linearly polarized excitation and σ^+ (**a**) and σ^- (**b**) detections with external magnetic fields of -9, 0 and 9 T. **c,d** PL intensity 2D plots of an aged WS_2 monolayer for a linearly polarized excitation and σ^+ (**a**) and σ^- (**b**) detections with external magnetic fields ranging from -9 to 9 T. The spectra in (**a-d**) are normalized by the free exciton peak intensity to highlight the intensity and energy modifications in the defect-bound exciton peak. **e,f** Exciton (**e**) and defect-bound (**f**) PL peak energies with respect to the magnetic field and their respective valley Zeeman splitting (**g,h**) showing g-factors of -3.6 (**g**) and -25.0 (**h**). All measurements were carried out at 4 K and with an incident power of 100 μW.

6.3.2 Magneto-optical measurements in aged WSe_2 monolayers

To have a better understanding of the defect role in the optical properties of other aged TMDs, we investigated a 3-year aged CVD grown WSe_2 monolayer by the same measurements carried out for the WS_2 monolayer. Figure 6.15a shows the power dependent PL spectra at 4 K for the WSe_2 monolayer normalized by the exciton peak intensity. Beyond the exciton emission, it can also be observed a lower energy PL peak with a sublinear power dependence. Figures 6.15b,c show the power dependence of both exciton and defect PL peaks with respect to their energy and intensity, respectively. Similarly to the aged WS_2 monolayer, an energy blueshift and a sublinear intensity power dependence are noted for the defect-bound exciton peak in the WS_2 sample. Moreover, temperature dependent PL measurements shown in Figure 6.15d reveals another similar behavior with respect to the WS_2 monolayer. As XPS measurements of this aged WSe_2 monolayer also shows the presence of an extra chemical bond (see Appendix Figure A.9), it is suggestive that both WS_2 and WSe_2 lower energy PL peaks have the same defect source, since they were similarly grown and aged. Low temperature magneto-PL measurements with linear polarized excitation and circular polarized detection were also performed for the aged WSe_2 monolayer. Figures 6.15e,f respectively show the σ^+ and σ^- detected PL spectra for all 181 measured external magnetic fields between -9 and 9 T (with steps of 0.1 T). The separated PL spectra for -9, 0 and 9 T are displayed in Appendix Figure A.11. The energy of X_0 and X_L peaks were extracted for all PL spectra and are presented in Figures 6.15g,h. Besides the well-known Zeeman shifting of the X_0 peak, it is also noted a remarkable shift in the X_L PL peak for this aged WSe_2 monolayer. From the energy shifting data it was calculated the valley Zeeman splitting for both exciton and defect-bound peaks, which are respectively shown in Figures 6.15i,j. A g-factor value of -3.2 is noted for the X_0, whereas the X_L presents an notable g-factor of -19.1. Furthermore, Figures 6.15e,f also display the significant spectral broadening of the circular polarized X_L emission corresponding to its energy redshift with magnetic field.

As observed in Figures 6.14 and 6.15, beyond the giant Zeeman shifting of the X_L peak, this defect-bound exciton emission also presents a great circularly polarized intensity dependence on the magnetic field for both aged WS_2 and WSe_2 monolayers. To further investigate this dependence, Figure 6.16a shows the degree of circular polarization (DCP) of the aged WSe_2 monolayer for -9, 0 and 9 T, given by:

$$\mathrm{DCP}(\%) = 100\frac{I_{\sigma^+} - I_{\sigma^-}}{I_{\sigma^+} + I_{\sigma^-}},$$

in which I_{σ^+} and I_{σ^-} are the PL intensities for both σ^+ and σ^- polarizations, respectively. A negligible DCP can be observed for the whole PL spectral range at 0 T, that is a consequence of the similar PL spectra for both σ^+ and σ^- detection at 0 T. This absence of DCP is related to the symmetric band structure with anti-symmetric spin moments at

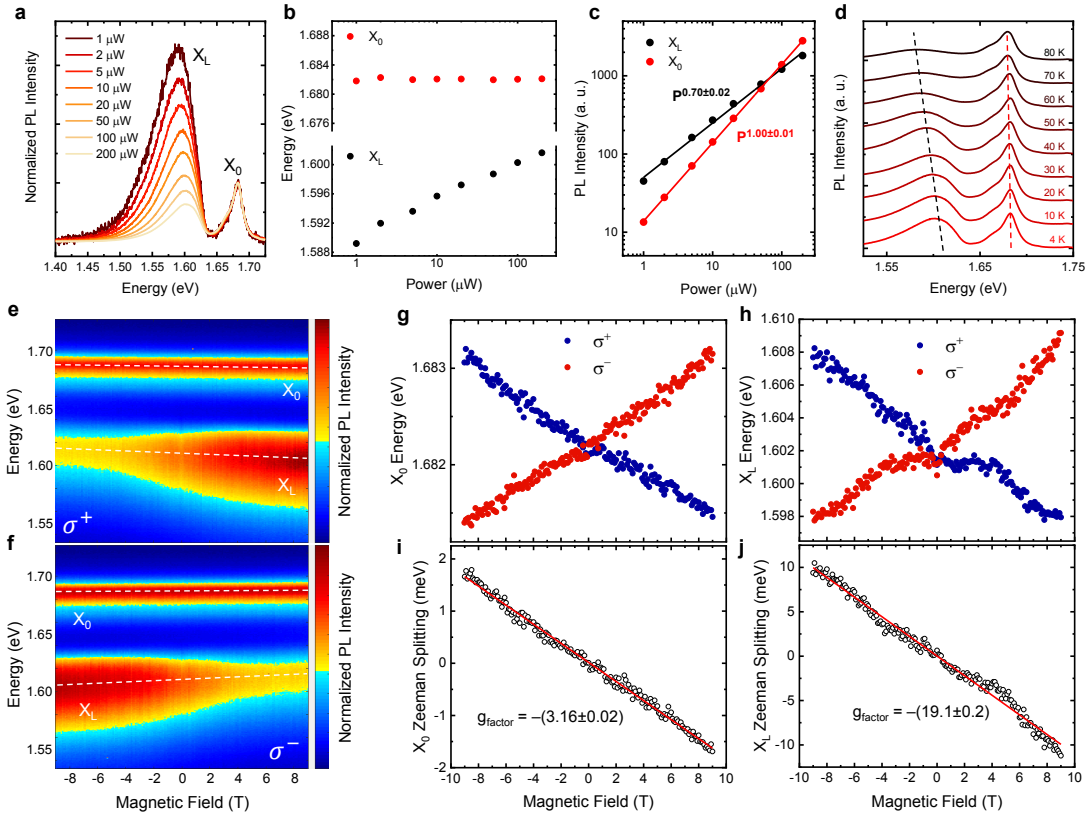

Figure 6.15 – **a** Power dependent PL spectra at 4 K for an aged WSe_2 monolayer showing free exciton and defect-bound exciton peaks. PL spectra are normalized by the intensity of the free exciton peak. **b,c** PL energy (**b**) and intensity (**c**) dependencies on the incident power for both defect and exciton PL peaks. **d** Temperature dependent PL spectra for a 100 μW incident power. **e,f** PL spectra of an aged WSe_2 monolayer for a linear polarized excitation and σ^+ (**e**) and σ^- (**f**) detection with external magnetic fields ranging from -9 to 9 T. The spectra were normalized by the free exciton peak intensity to highlight the intensity and energy modifications in the defect-bound exciton peak. **g,h** Exciton (**g**) and defect (**h**) PL peak energies with respect to the magnetic field and their respective valley Zeeman splitting (**i,j**) showing g-factors of -3.2 (**i**) and -19.1 (**j**). All magneto-PL measurements were carried out at 4 K and with an incident power of 100 μW.

0 T between K and $-$K valleys. On the other hand, we can observe a significant variation of the DCP for -9 and 9 T with respect to the emission energy. While there is a DCP of $\sim 7.5\%$ in the X_0 spectral range, the X_L peak energy shows an increased DCP of $\sim 40\%$, more than 5 times greater compared to X_0. Besides, the full PL intensity dependencies on the external magnetic field for both X_0 and X_L are displayed in Figures 6.16b,c. The σ^+ and σ^- PL intensities of the free exciton are maximum close to 0 T and decrease for both positive and negative magnetic fields. Conversely, the defect-bound exciton PL intensity dependence on the magnetic field is approximately linear, with a positive (negative) slope for σ^+ (σ^-) emission. While σ^+ and σ^- polarized X_L emissions have similar intensities at $B = 0$, for $B = 9$ T the X_L σ^+ polarized intensity is 2.5 times greater than the X_L σ^- polarized intensity (and the opposite is valid for B =-9 T), revealing a significant

magnetic field induced spin polarization of the mid gap states. In addition, the aged WS_2 monolayer also shows a noticeable DCP for the X_L peak, as shown in Appendix Figure A.12. Therefore, we can note a correspondence of the magnetic field dependence between the X_L peak energy shifting, spectral broadening and spin polarization. These relationships will be further explored to explain the observed giant g-factor of the defect-bound exciton peak.

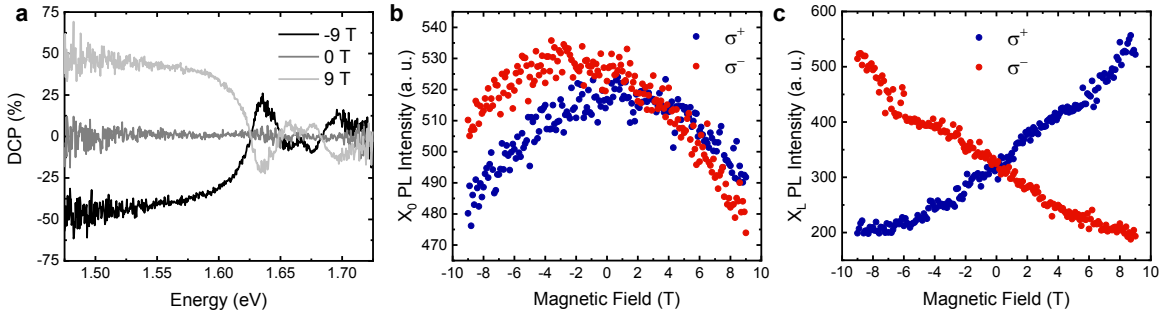

Figure 6.16 – **a** Degree of circular polarization of an aged WSe_2 monolayer for −9, 0 and 9 T between σ^+ and σ^- PL spectra. **b,c** Free exciton (**b**) and defect-bound exciton (**c**) PL intensities with respect to the magnetic field. A parabolic dispersion for the exciton PL intensity can be noted, while the defect PL intensity presents a X pattern between σ^+ and σ^- emission.

6.3.3 Multiple mid gap states model

As mentioned in Chapter 2, the Zeeman shifting in TMDs happens due to the orbital, spin and valley magnetic moments of the valence and the conduction bands of the material. The reported g-factors of the X_0 state related to the valley Zeeman splitting between K and −K valleys is around $-4\mu_B$ (146, 147, 148, 149). However, as defect-bound exciton PL peaks are associated with the optical transition from defect mid gap states to the valence band, a distinct valley Zeeman splitting is expected (292). Although spin magnetic moments remain the same, orbital and valley magnetic moments can be modified, since the mid gap states can present distinct hybridized orbitals and effective masses with respect to the valence band. For instance, a −6.2 g-factor associated with vacancy defect levels in MoS_2 monolayers was previously explained by their distinct magnetic moments. Nonetheless, the giant g-factor values of −25.0 and −19.1 that we observed for the aged monolayers require a distinct explanation.

Comparing the power dependent PL spectra (Figures 6.13a and 6.15a) with the magnetic field dependent PL spectra (Figures 6.14a-d and 6.15e,f) it is clearly noted a similar dependence of the X_L peak with power and magnetic field. As previously reported, the adsorbent defects can induce the emergence of distinct mid gap states in the material band structure (189), leading to the observed broad PL peaks (353, 170, 189). Therefore, by varying the incident power there are modifications in the charge carrier occupation of

these mid gap states, resulting in a significant peak energy shift. Figure 6.17 schematically represents this light emission power dependence by showing the band structure of a direct gap semiconductor with two mid gap states at low and high excitation power regimes. For low excitation powers, the lower energy defect level is more occupied due to the charge carrier relaxation, leading to a lower energy defect-bound exciton emission. For high incident powers, the electronic occupation of the lower energy mid gap state is saturated, resulting in a larger occupation of the higher energy mig gap state and a blueshift in the defect-bound exciton emission. Therefore, these multiple mid gap states might also influence the observed magneto-optical responses.

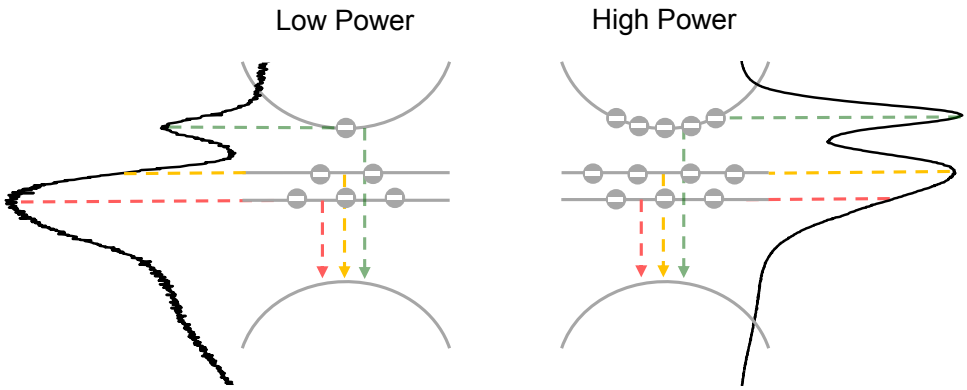

Figure 6.17 – **Representation of the radiative recombinations from the conduction band and mid gap states for a low and high incident power regime in an aged TMD monolayer.**

Figure 6.18a summarizes the dependence of the aged WS_2 and WSe_2 monolayers optical responses on the external magnetic field, in which the σ^+ polarized light emission at the K valley is represented for negative, zero and positive magnetic fields. For positive magnetic fields, the radiative recombinations from the mid gap states — related to the X_L PL peak — exhibit an intensity enhancement, an energy redshifting and a spectral broadening compared to the emission without an external magnetic field. Conversely, for negative magnetic fields there is an intensity quenching, an energy blueshifting and a spectral narrowing of the X_L peak emission. The opposite is valid for the σ^- polarized light emission at the $-$K valley. Considering this scenario, we next propose a spin-flip mechanism to explain these experimental observations, as represented in Figure 6.18b.

Distinct relaxation pathways are reported in the electronic dynamics of TMD monolayers. For instance, intervalley and intravalley scattering of excited carriers can happen due to electron-phonon and spin-orbit interactions, respectively (355, 356). The intravalley scattering is associated with a spin-flip of the carrier state, and can also be induced by an external magnetic field (357, 355). For mid gap states, similar relaxations can occur as well. As our reported aging defects are presumably non-magnetic, it is expected that their states exhibit weaker spin-orbit couplings with respect to the TMDs conduction

and valence bands, and thus smaller spin splittings, as shown in Figure 6.18a. Therefore, as the spin splitted defect mid gap states are closer in energy, it is reasonable to expect a greater probability of electronic relaxation among them. In addition, the electronic recombination of electrons in these trapping states is notably slower than of free excitons (311, 310), which also favors the relaxation processes in the mid gap levels. Therefore, we presume that the external magnetic fields induce significant spin-flip transitions between the spin splitted mid gap states. As shown in Figure 6.18b, while there is no relevant spin-flip transition in the absence of an external magnetic field, positive (negative) magnetic fields cause spin-flip transitions from spin-down (-up) to spin-up (-down) states, leading to a strong spin polarization in the mid gap states. Hence, for positive (negative) magnetic fields there will be a dominant population of spin-up (-down) states, which is in agreement with the enhanced (quenched), redshifted (blueshifted) and broadened (narrowed) σ^+ polarized light emission observed in the experimental results and depicted in Figure 6.18a. It is important to comment that the defect levels are also shifted by the external magnetic fields, as shown in 6.18a. Therefore, the measured X_L g-factor is due to a combination of the Zeeman splitting and the polarized electronic occupation of the mid gap states.

In summary, we studied aged WS_2 and WSe_2 monolayers by low temperature power dependent PL, temperature dependent PL and low temperature circularly polarized magneto-PL measurements. The power and temperature dependent PL spectra showed a lower energy peak related to a defect-bound exciton. XPS measurements were carried out and related this lower energy PL peak to the presence of an extra chemical bond to the W atom that might be associated with the adsorption of oxygen and organic molecules in the material structure. Finally, low temperature circular polarized PL measurements with an applied varied external magnetic field were performed to study the Zeeman effect in the defect-bound exciton. A significant energy shift of the defect emission corresponding to an intensity enhancement and a spectral broadening was observed for both aged monolayers under magnetic field variation. Besides, from their Zeeman splitting we extracted g-factor values of -25.0 and -19.1 for the defect-bound exciton emission in WS_2 and WSe_2 monolayers, respectively. These giant g-factors emerge from the combination of the valence band Zeeman shift and the spin polarization of the defect mid gap states due to a magnetic field induced spin-flip transition. Therefore, our work highlights how adsorbed defects related to an aging process can potentialize the Zeeman splitting and carriers spin polarization in TMD monolayers for spintronics and valleytronics applications.

6.4 Partial Conclusions

The defect engineering of TMD monolayers is a powerful method to improve and generate novel properties in these materials. Among several possibilities, defects can induce singular magnetic responses in TMDs, such as a room temperature ferromagnetism by

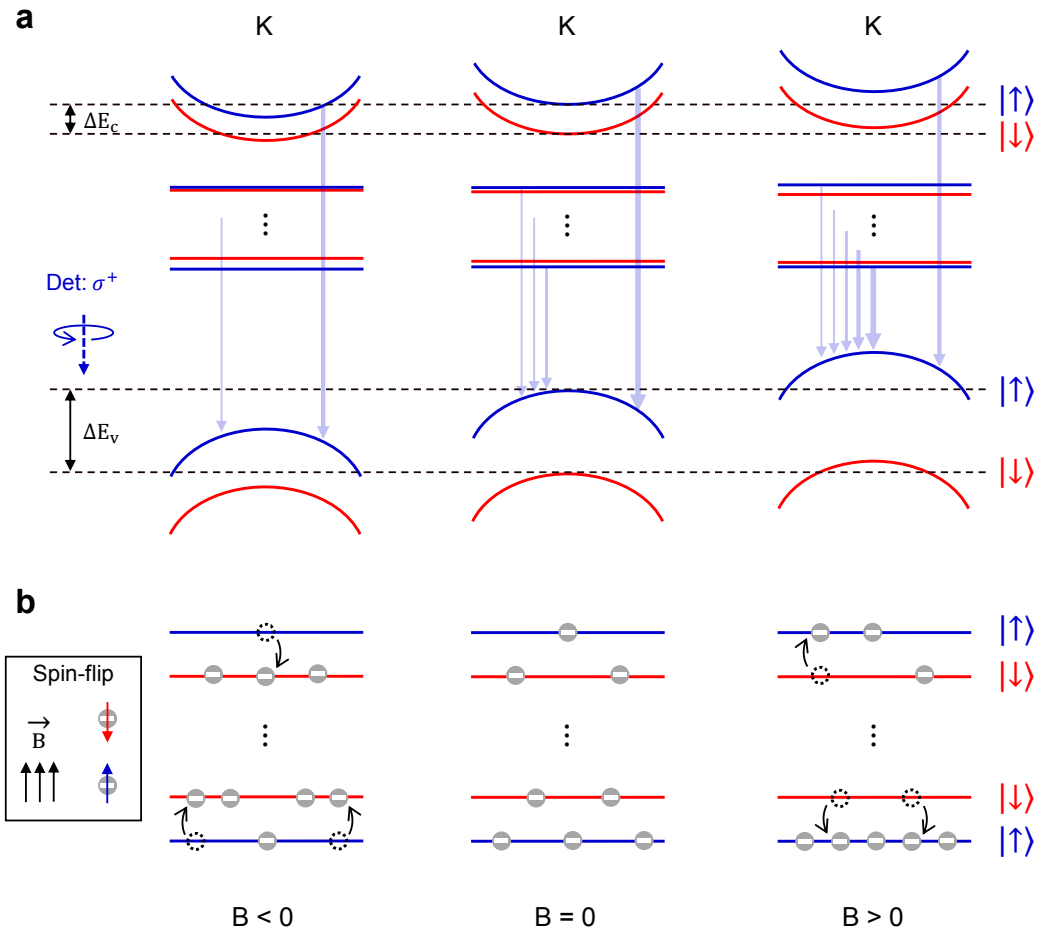

Figure 6.18 – **a** Band structure representation of an aged WS_2 or WSe_2 monolayer for negative, zero and positive magnetic fields, showing the conduction and valence bands Zeeman shifting and the multiple spin splitted mid gap states. **b** Spin-flip relaxation in the mid gap states induced by the external magnetic fields. The spin polarized population of these defect levels lead to their magnetic dependent light emission shown in (**a**).

introducing spin polarized metal atoms as substitutional defects. Besides, the adsorption of atoms and molecules in the TMD monolayers surface might also affect their magnetic properties. Therefore, as TMDs are attractive materials due to their semiconducting properties, it is fundamental to characterize their optical and electronic modifications in the presence of these defects. In addition, the investigation of the coupling between magnetic and optical responses in these defective TMDs is promising to reveal novel functionalities for these materials. Here we provided the first broadband optical and electronic structure characterization of V-doped WS_2 monolayers by combining several spectroscopy techniques and thorough DFT calculations. V-doped WSe_2 monolayers have also been investigated by optical and magneto-optical experiments, revealing a strong magnetic response from vanadium defect states. Finally, aged WS_2 and WSe_2 monolayer were probed by magneto-optical measurements as well, in which a great spin polarization of their defect-bound excitons was observed, leading to a giant effective g-factor associated

with these defect states.

Beyond the results presented here, we have further studied these samples during this thesis. For instance, together with a former master student we mapped the optical responses throughout V-doped WS_2 monolayers by PL and Raman hyperspectral experiments. They showed distinct light emission and scattering phenomena along the narrow regions that connect the center of the monolayer with their vertexes, which is related to a higher vanadium concentration. These results are shown in the master dissestation of Felipe Menescal. In addition, preliminary magneto-optical measurements have also been carried out in V-doped WS_2 monolayers, presenting an anomalous asymmetry in their valley Zeeman shifting at K and $-$K valleys.

7 Nano-optical investigation of defects in CVD grown MoS_2 monolayers

As discussed in Chapter 4, the characterization of defects that unintentionally emerge during the growth process of TMD monolayers is essential to both help the development of the large-area of growth methods as well as to study novel properties. To investigate the role of these defects in the inhomogeneity of the optical properties throughout the grown samples there is a spatial resolution limitation of hundreds of nanometers due to the diffraction limit of light. Therefore, confocal optical techniques as photoluminescence (PL) and Raman spectroscopy are only able to provide averaged electronic and vibrational responses over a μm-scale area. Hence, the precise determination of localized optical modifications should be given by near-field optical measurements such as tip-enhanced PL and Raman spectroscopies (TEPL and TERS, respectively) (56, 57, 58, 59). Investigations of excitonic effects (358, 359), grain boundaries (289, 290, 291), edge defects (281, 282, 306), strain (283), wrinkles (284, 286), lateral interfaces (244, 287), hybrid heterostructures (360) and defect-bound localized states (361, 306) have already been carried out by TEPL and TERS measurements. However, due to the implementation challenges of these optical techniques, it is possible to observe that several of these works have not reached the optimal spatial resolution of few dozens of nanometers. Moreover, as defects in grown TMDs can show distinct optical modifications depending on further factors as growth parameters and substrate (362, 363), a broad nanoscale characterization with combined electronic and vibrational information of different defects in TMD grown monolayers is still a demanding task.

In this Chapter we study several defects in chemical vapor deposition (CVD) grown MoS_2 monolayers by TEPL and TERS measurements with spatial resolutions down to $\sim$24 nm. We investigate the localized PL emission and Raman scattering along distinct MoS_2 monolayers grain boundaries and edges. The following results are submitted as a manuscript and its preprint version is published in Ref. (364).

7.1 Localized light emission from a MoS_2 monolayer grain boundary

The MoS_2 monolayer samples A1 and A2 investigated here were synthesized by a CVD method by our collaborators Prof. Ive Silvestre and Rafael Martins from UFOP in two different batches that led to distinct optical characteristics as we will show along this Chapter. Further growth details are described in Ref. (364). We first studied a multi-sided polygonal shaped MoS_2 monolayer of A1 sample. It is well-known that these CVD grown multi-sided TMD monolayers present grains with distinct crystallographic orientations (71, 169). The boundary between the two grains is thus a defective region in which

the mismatched atoms present a distinct localized geometrical structure that depends on the relative orientation of the grains. These grain boundaries have been studied for different TMD monolayers in the past years (71, 169, 191, 365, 79, 192, 178). While SPM measurements are capable of determining the nanoscale features of the modified atomic structure along the grain boundaries (71, 169, 191), conventional optical measurements only give the averaged response of μm-areas containing these defects (71, 365, 79, 192, 178). Therefore, although intensity enhancements and peak shifts had been reported for TMD monolayers grain boundaries by confocal PL and Raman measurements, they were not able to ascertain the area in which the optical properties are affected due to their limited spatial resolution. More recently, TEPL and TERS measurements have also been carried out in monolayer TMDs in order to provide a wider comprehension of the nanoscale character of the grain boundaries optical features (289, 290, 291). However, these few existent reports showed quenched Raman and PL intensities along the grain boundaries, contrary to previously reported features and in accordance with a likely sample cracking at these defects. Hence, a careful nano-optical investigation of TMD grain boundaries is required for a deeper understanding of the roles of defects in monolayer TMDs.

Figure 7.1a shows a polarized second-harmonic generation (SHG) image of the multi-sided polygonal shaped MoS_2 monolayer. Since the SHG in monolayer TMDs is sensitive to the material crystallographic orientation (20), polarized SHG measurements are capable of determining the grain orientations and thus reveals the presence of grain boundaries (331). Hence, the different SHG intensities in Figure 7.1a shows the distinct grains and their boundaries throughout the MoS_2 monolayer. Appendix Figure B.1 displays the entire polarization dependence of the observed grains and their relative crystallographic orientations. Figure 7.1b shows the intensity map of a confocal PL hyperspectral measurement performed in the red squared region displayed in Figure 7.1a. In agreement with previously reports (71, 79, 192, 178), PL intensity enhancements are observed at grain boundaries. Therefore, in order to ascertain the localization and the real magnitude of the optical modifications in these grain boundaries, we performed TEPL measurements along distinct grain boundaries regions highlighted in colored rectangles in Figure 7.1b. To show the spatial resolution and signal enhancements of the technique, all TEPL and TERS measurements in this work were carried out with the tip up and down, respective to their far-field (FF) and near-field (NF) responses. Figure 7.1c displays PL intensity maps of 4 TEPL hyperspectral measurements along MoS_2 monolayer grain boundaries regions. The underlined color around each TEPL hyperspectral map is respective to the rectangular areas of the same color in Figure 7.1b. A localized PL intensity enhancement is noted for all probed grain boundaries. Moreover, an energy blueshift is also observed at the grain boundaries, as shown in Figure 7.2a,c. To quantify the spatial width of the optical modifications in these defects probed by the NF measurements and compare them with the spatial resolution of the FF measurements, Figure 7.1d shows PL intensity profiles

taken along the black dashed arrow in Figure 7.1b and orange and purple dashed arrows in Figure 7.1c. The top intensity profile graph of Figure 7.1d reveals the remarkable increase in spatial resolution given by the tip. While the grain boundaries in the FF measurement presents spatial widths of $\sim$ 650 nm, the bottom intensity profile graphs unveil that the region affected by these defects can be as narrow as 49 nm. Distinct grain boundaries present different structural modifications, hence it is natural that they also display different affected regions. For instance, the grain boundary presented in the brown underlined TEPL map of Figure 7.1c shows two separated enhanced lines, that correspond to a broader brighter region in the FF PL map of Figure 7.1b. Figures 7.1e,f compare the FF and NF PL spectra, respectively, of grain boundary and grain middle regions. The FF spectra present a PL energy blueshift and an intensity enhancement at the grain boundary. However, these features are emphasized in the NF spectra, which gives the real magnitude of the spectral modifications. As shown in Figure 7.1f, it can be observed that the grain middle region present a PL spectrum composed by trion and exciton peaks with similar intensities. At the grain boundary, the exciton peak presents a noticeable enhancement while the trion peak is quenched, which is responsible for the observed PL energy blueshift. The exciton/trion peak intensity ratio map and profile shown in Figures 7.2b,d reveals a relative enhancement up to 9 times of the exciton intensity with respect to the trion at the grain boundary. This exciton emission increase due to a suppressed trion formation was previously associated to an electrical doping effect (366), which can be locally probed by these near-field measurements (367, 368). In fact, a commonly reported feature at MoS_2 monolayer grain boundaries is the presence of electrical doping effects at these regions (71, 369, 192), related with defects such as sulfur vacancies (369) or chemical doping (192). Thus, our results shed light in the nanoscale aspect of the electrical and optical properties modifications of the mismatched grain boundary regions.

7.2 Localized strain fields over a MoS_2 monolayer

Subsequently, we performed TEPL and TERS measurements in the A2 sample in order to study further local heterogeneities. Figure 7.3a shows the optical image of a triangular shaped MoS_2 monolayer from the A2 sample. The topography of the 500x500 nm squared region in the center of the monolayer highlighted in red in Figure 7.3a was probed by a non-contact mode AFM measurement, as displayed in Figure 7.3b showing no large topographical variations along the sample area. Moreover, Figure 7.3c shows FF and NF spectra with Raman and PL peaks taken in the middle of the MoS_2 flake. Spectral enhancement factors of $\sim$ 3.5 and $\sim$ 7 for PL and Raman intensities, respectively, were observed by engaging the tip. Hyperspectral measurements were also performed in the same region measured by AFM (Figure 7.3b) to investigate local optical features. The Raman hyperspectrum displayed an uniform response throughout this region in both FF

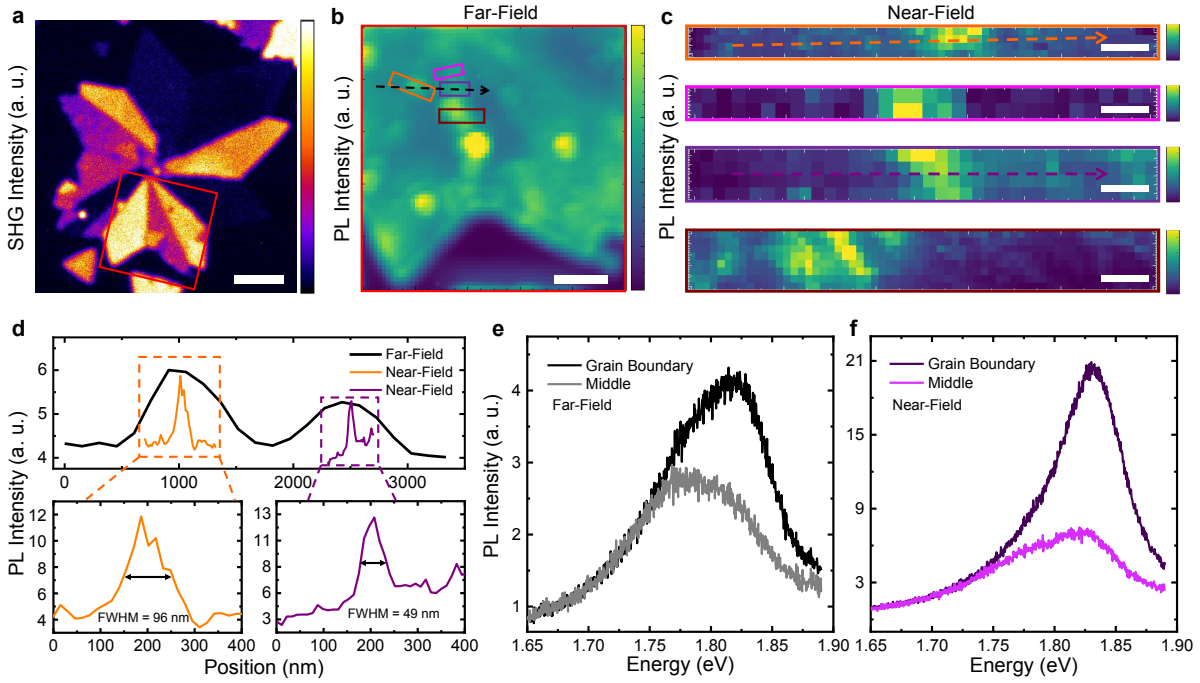

Figure 7.1 – **a** Polarized SHG imaging of a multi-sided polygonal MoS_2 monolayer. The regions with distinct SHG intensities represent grains with different crystallographic orientations, showing all grain boundaries present in the sample. Scale bar in (**a**): 5 μm. **b** PL intensity map of a FF hyperspectral measurement taken in the red squared area highlighted in (**a**). The grain boundary regions show a PL intensity enhancement. Scale bar in (**b**): 2 μm. **c** TEPL intensity maps of 4 NF hyperspectral measurements taken in the colored rectangular areas highlighted in (**b**) also showing a PL intensity enhancement at the grain boundaries. The colors of the rectangular areas in (**b**) are respective to the same underlined colors around the TEPL maps in (**c**). The FF hyperspectral measurements were performed with steps of 150 nm, while NF measurements were carried with steps of 16 nm. Scale bars in (**c**): 50, 100, 40 and 100 nm (from the top to the bottom). **d** PL intensity profiles along grain boundaries for FF and NF measurements. The top graph shows the FF PL intensity profile in black (taken along the black dashed arrow of **b**) and the NF PL intensity profiles in orange and purple (taken along the orange and purple dashed arrows of **c**). The spatial width of the PL enhancement at the grain boundaries are shown in the bottom intensity profile graphs. **e,f** FF and NF PL spectra, respectively, of grain boundary and grain middle regions. The spectra are respective to the grain boundary region shown in the purple squared region of (**b**) and (**c**). NF measurements reveal the real magnitude of the PL enhancement at the grain boundaries, also showing the exciton emission dominance over the trion emission suppression.

and NF measurements, as shown in Appendix Figure B.2. However, Figures 7.3d-g reveal nanoscale modifications in the PL emission over this area. While the FF PL hyperspectrum showed uniform exciton peak intensity (Figure 7.3d) and energy (Figure 7.3e) maps, the NF PL hyperspectrum presented local islands of an enhanced exciton intensity (Figure 7.3f) that matches to an exciton energy blueshift (Figure 7.3g). To better visualize these features, PL spectra of two distinct positions - p1 (black dot) and p2 (red dot) - are

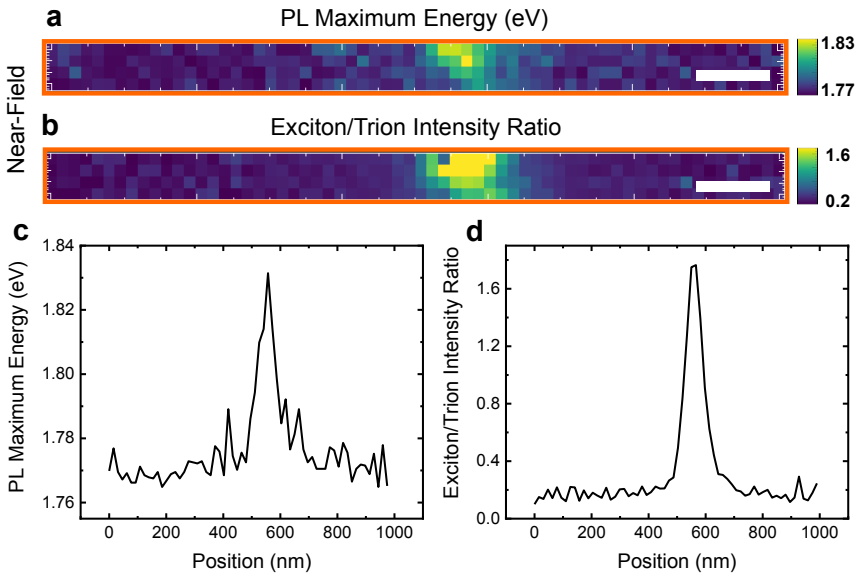

Figure 7.2 – **a,b** Near-field PL maximum energy and exciton/trion intensity ratio maps at a grain boundary of MoS_2 monolayer sample A1. These maps are from the orange rectangle region highlighted in Figure 7.1. Scale bars: 50 nm. **c,d** PL maximum energy and exciton/trion intensity ratio profiles along the grain boundary of MoS_2 monolayer sample A1.

displayed in Figures 7.3h,i for both FF and NF measurements, respectively. The p1 and p2 position are shown in the PL hyperspectral maps and are related to an enhanced PL signal spot and to a decreased PL signal spot, respectively. Figure 7.3h presents similar FF PL spectra for p1 and p2, as observed in FF hyperspectral maps. On the other hand, Figure 7.3i evidences that the NF PL spectra shows an intensity enhancement and energy blueshift at the p1 position. Furthermore, Figure 7.3i also shows the fitted PL spectra by two Gaussian peaks, respective to the exciton - higher energy peak - and trion - lower energy peak. Figures 7.4a-d displays the FF and NF PL maps for the trion emission, presenting a similar behavior with respect to the exciton. It is worth mentioning that all spectra of both FF and NF hyperspectral measurements were fitted by two Gaussian peaks and the hyperspectral maps were made with these fitted parameters.

As already mentioned, PL intensity enhancements and energy shifts in MoS_2 monolayers can be associated with doping effects. However, as shown in Figures 7.4e,f, the exciton/trion peak intensity ratio along the measured area is approximately uniform (variations lower than 35%), which is not consistent with a doping hypothesis. Another common feature reported in TMDs that induces PL energy blueshift and intensity enhancement is the variation of strain fields (370, 371, 270, 41) along the sample. CVD grown MoS_2 monolayers have previously presented shifts around 40 meV/% of strain for the exciton emission (370, 270). As we observe shifts up to ~ 4 meV for the exciton peak, it would be associated with a strain of $\sim 0.1\%$. Indeed, this strain is not sufficient to be probed by Raman, as it would induce shifts of ~ 0.21 cm^{-1} and ~ 0.07 cm^{-1}

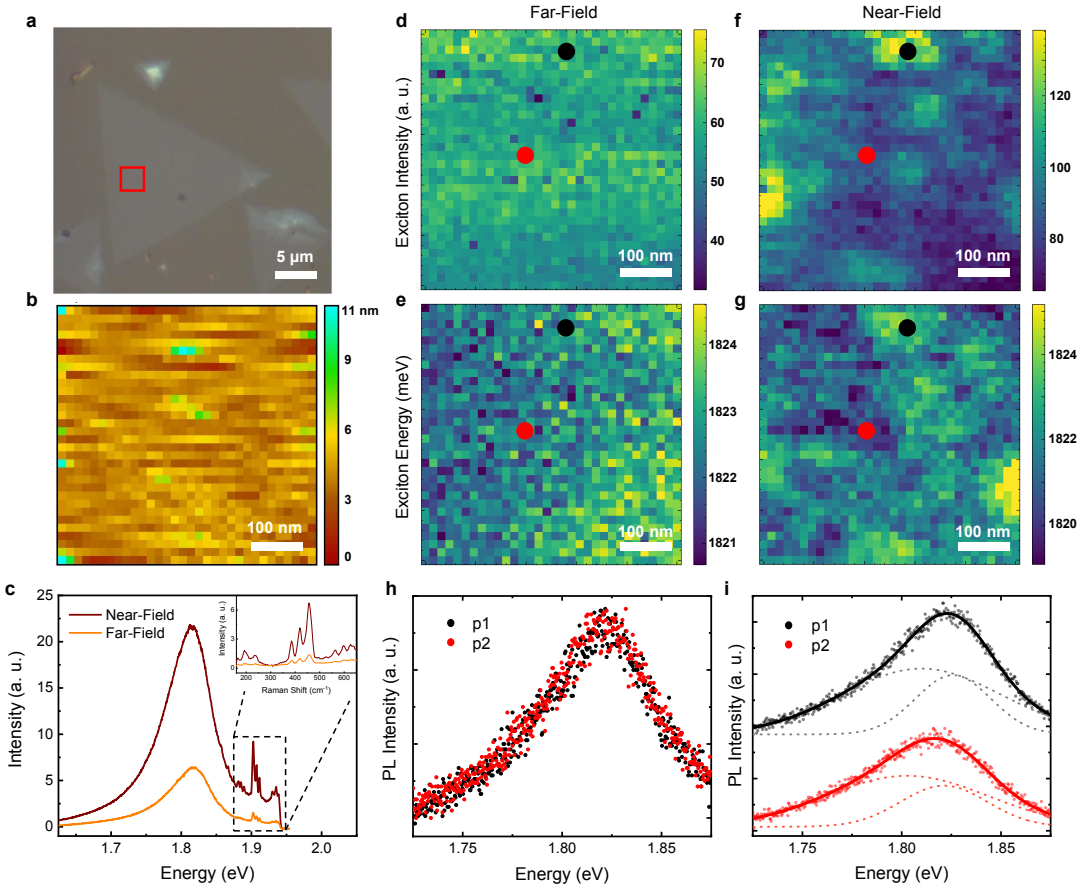

Figure 7.3 – **a** Optical image of a triangular shaped MoS_2 monolayer from sample A2. **b** AFM measurement of the 500x500 nm red squared region shown in (**a**). **c** NF and FF PL and Raman spectra of the MoS_2 monolayer showing the intensity enhancement of the NF measurement. **d-g** PL hyperspectral maps of the FF exciton intensity (**d**), FF exciton energy (**e**), NF exciton intensity (**f**) and NF exciton energy (**g**) in the same red squared region shown in (**a**). The NF maps reveal nanoscale features associated with localized strain fields. The hyperspectral measurements were performed with steps of 16 nm. FF (**h**) and NF (**i**) PL spectra of p1 and p2 points shown by black and red circles in the TEPL hyperspectral maps (**d-g**). The measured spectra are displayed in the dotted data, while the two Gaussian peaks fitting is presented in the solid curves. The trion and exciton Gaussian peaks are highlighted in the dashed curves.

in the E_{2g} and A_{1g} peaks (270), respectively, that is below our spectrometer resolution. Moreover, the PL intensity enhancement is also in accordance with the 0.1% strain. As there is no coincidence between the AFM measurement and the local variation presented in the NF PL maps, the suggestive strain is not accounted on a topographic reason. As shown in Appendix B.3, these strained islands are also observed in another region of the flake. Therefore, the noted non-uniform localized strain is presumably due to an expected thermal expansion coefficient and lattice constant mismatch between the monolayer and the substrate (196), which plays a major role in the growth process. Although strain is a well studied characteristic of TMDs, unveiling strained responses at this nanoscale can

raise the understanding of the substrate and growth method roles in the optical properties of these 2D semiconductors.

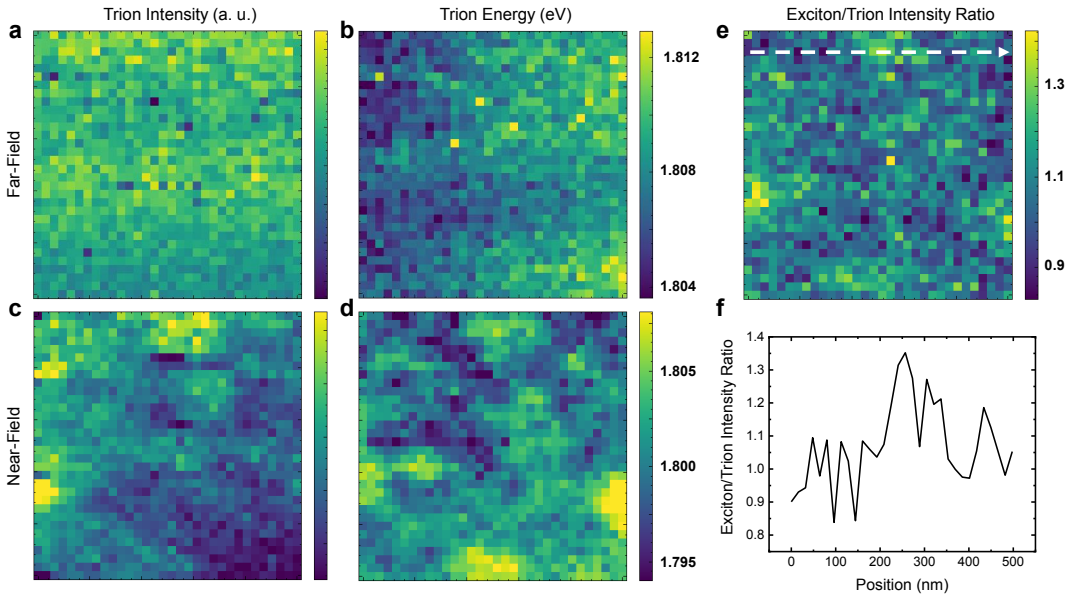

Figure 7.4 – **a,b** Far-field trion intensity (**a**) and trion energy (**b**) maps of MoS_2 monolayer sample A2. **c,d** Near-field trion intensity (**c**) and trion energy (**d**) maps of MoS_2 monolayer sample A2. These maps are from the same region of the exciton maps of Figure 2. **e** Near-field exciton/trion intensity ratio map of MoS_2 monolayer sample A2. These maps are from the same region of the exciton maps of Figure 7.3. **f** Exciton/trion intensity ratio profile taken along the dashed white arrow shown in (**e**).

7.3 Nanoscale optical responses at a MoS_2 monolayer edge: A2 sample

Another frequent heterogeneity reported in monolayer TMDs is associated to their edges (34). Thereby, we have also performed TEPL and TERS hyperspectral measurements in an edge region of the same MoS_2 flake shown in Figure 7.3. Figures 7.5a,b display the exciton peak intensity and energy maps for the NF PL hyperspectral measurement in this edge region. An intensity enhancement and an energy blueshift of the exciton peak are noted at the edge within a spatial width of less than 100 nm, which was not observed in the FF measurements as shown in Appendix Figure B.4. These features are also presented in Figure 7.5e, in which the PL spectra taken at the middle (p1) and at the edge (p2) of the sample confirm the intensity enhancement and energy shift at the edge. Moreover, Appendix Figure B.5 also shows similar results for another edge region of the same sample. Unlike the PL energy shift in the inferred strained regions throughout the monolayer (Fig. 7.3), the observed energy shift at the edges are larger. As can be noticed in the exciton energy profile in Figure 7.5f, there is an energy shift of 25 meV at the edge. Moreover, this blueshift follows a PL enhancement of ~ 1.5, as can also be seen in Figure 7.5e. If this

observed PL energy shift was also due to strain, it would be associated with measurable Raman shifts. However, a NF Raman hyperspectral measurement showed no significant shift for the E_{2g} mode at the edge as shown in Figure 7.5c. On the other hand, the 2LA Raman mode presented a noticeable blueshift of ~ 4 cm^{-1} as displayed in the TERS peak position map (Figure 7.5d). Frequency profiles along the edge for the E_{2g} and 2LA modes are presented in Appendix Figure B.6, showing the features observed in Figures 7.5c,d. In addition, the absence of frequency shifting of the first order Raman modes as well as the blueshift of the 2LA mode is also shown in the Raman spectra of the middle p1 position and at the edge p2 position shown in Figure 7.5g. As shown by Carvalho *et al.* (53), the MoS_2 monolayer 2LA Raman mode is in fact composed by different Raman peaks that are highly dependent with electronic resonances. As these peaks present distinct resonances by varying the laser wavelength (53), a similar behavior is expected if the material band gap is modified. Therefore, the observed 2LA frequency shift at the edge is probably related to a modification in the relative intensities of the 2LA peaks due to the band gap shift noticed in the PL measurements. Previous reports (372, 373, 182, 281) have observed different PL features at MoS_2 monolayer edges due to distinct defects. Water and oxygen passivation of vacancies at the edges also result in an enhancement in the PL intensity, but it corresponds to a redshift in the PL energy (372, 182). On the other hand, a similar nanoscale edge response was recently probed by hyperspectral TEPL measurements (281). However, an assertive determination of the defect responsible for these optical modifications at the edges is still lacking. Therefore, the association of this local PL enhancement and blueshift at the edges with a frequency shift of the 2LA mode brings more information of the influence of the edge defect states in the MoS_2 monolayer optical properties.

7.4 Nanoscale optical responses at a MoS_2 monolayer edge: A1 sample

In order to further investigate other types of optical responses at the edges, we have measured MoS_2 monolayer edges from the A1 sample. Figures 7.6a,b shows the measured NF PL hyperspectrum of a A1 MoS_2 monolayer edge. Contrary to the observed features of sample A2, the PL intensity map of Figure 7.6a presents no clear modification, whereas the PL energy map of Figure 7.6b reveals a significant redshift in an edge region of less than 50 nm of width. TEPL measurements in distinct edge regions of different monolayer flakes of the same A1 sample presented a similar PL energy redshift, as displayed in Appendix Figure B.7. Figure 7.6c shows PL intensity and energy profiles along the edge, in which the energy redshift of 25 meV can be observed. Moreover, in the intensity profile it is possible to extract the spatial resolution of the measurement, that is around 20 nm (see Appendix Figure B.8). PL spectra at the middle (p1 position) and at the edge (p2 position) of the sample are shown in Figure 7.6d, clearly showing the PL redshift presented in the TEPL hiperspectral map and profile, but no clear spectral modification. Although

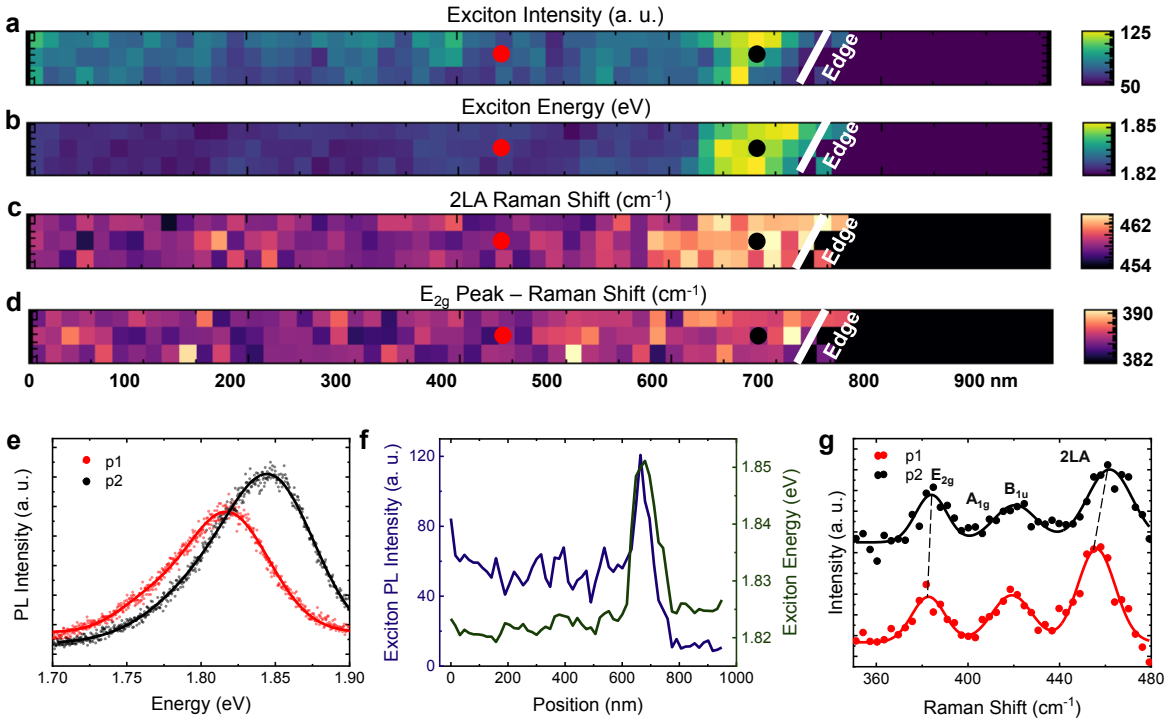

Figure 7.5 – **a,b** NF TEPL hyperspectral maps of the exciton intensity (**a**) and energy (**b**) at an edge region of the MoS_2 monolayer shown in Figure 7.3. An intensity enhancement and an energy blueshift of the PL is observed at the edges. **c,d** NF TERS hyperspectral frequency map of the E_{2g} (**c**) and 2LA (**d**) modes, respectively revealing an uniform frequency and a blueshift of ~ 4 cm^{-1} at the edge. The PL and Raman hyperspectral measurements were performed with steps of 16 nm. **e** NF PL spectra of p1 and p2 points shown by black and red circles in the hyperspectral maps (**a-d**). The measured spectra are displayed in the dotted data, while the spectra fitting is presented in the solid curves. **f** Exciton PL intensity and energy profiles along the edge, highlighting its enhancement and blueshift of ~ 25 meV. Moreover, the intensity profile reveal a spatial resolution of ~ 30 nm. **g** NF Raman spectra of p1 and p2 points shown by black and red circles in the hyperspectral maps (**a-d**). The measured spectra are displayed in the scattered data, while the spectra fitting is presented in the solid curves.

there is a PL energy redshift associated with oxygen and water passivation at the edges (372, 182), the absence of a strong PL intensity enhancement suggests a different reason for this observed edge response. On the other hand, if this intense PL energy modification at the edge is related with strain, a shift in the first order Raman modes should be observed.

Therefore, we also performed a NF Raman hyperspectral measurement in the same region as the measurements of Figure 7.6. The Raman intensity maps of the E_{2g} and 2LA modes are displayed in Figures 7.7a,b, while the frequency maps of these peaks are presented in Figures 7.7c,d. For both peaks it is observed an intensity quenching and a frequency redshift at the edge. To better quantify these responses, the intensity and frequency profiles of E_{2g} and 2LA modes along the edge are shown in Figures 7.7e,f. In addition, Figure 7.7g shows Raman spectra taken in the middle of the monolayer (p1) and

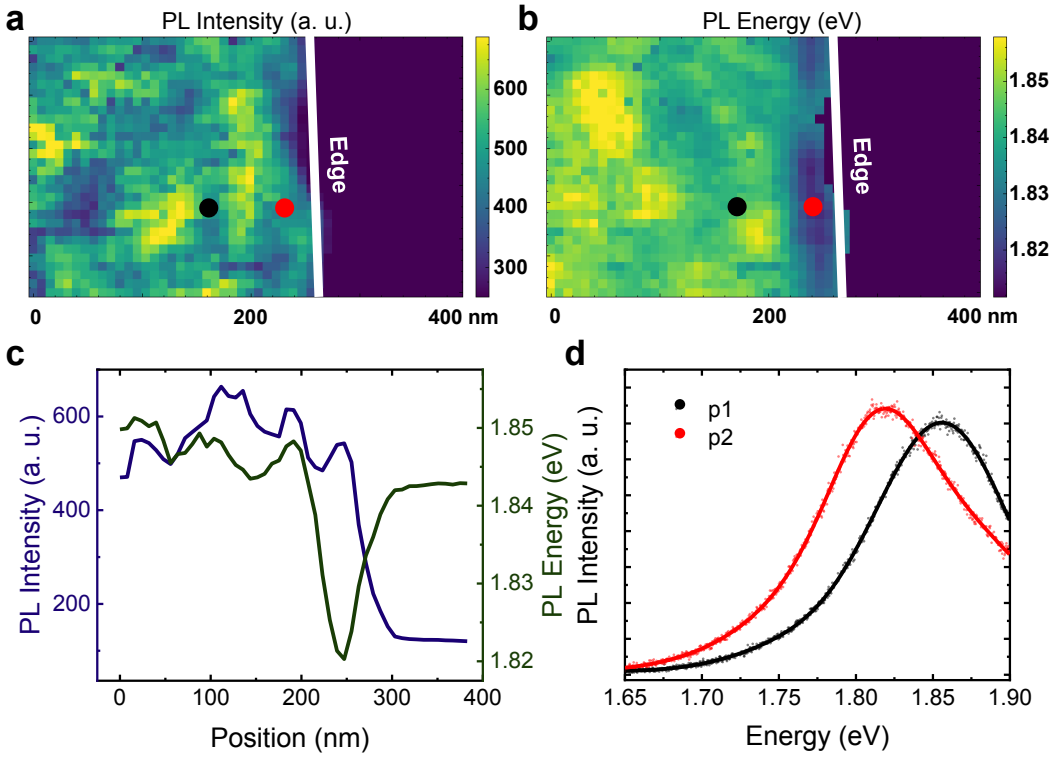

Figure 7.6 – **a,b** NF TEPL hyperspectral maps of the PL intensity (**a**) and energy (**b**) at an edge region of a MoS_2 monolayer from A1 sample. An energy redshift of the PL is observed in at the edges. The hyperspectral measurements were performed with steps of 8 nm. **c** Exciton PL intensity and energy profiles along the edge, highlighting its redshift of $\sim$ 25 meV. Moreover, the intensity profile reveal a spatial resolution of $\sim$ 20 nm. **c** NF PL spectra of p1 and p2 points shown by black and red circles in the TEPL hyperspectral maps (**a,b**). The measured spectra are displayed in the dotted data, while the spectra fitting is presented in the solid curves.

at its edge (p2), highlighting the features noted in the Raman maps. It can be observed a -1.5 cm^{-1} shift at the edge for the E_{2g} peak and a -8.5 cm^{-1} for the 2LA mode. As discussed for the A2 sample, this 2LA shift can also be associated with the modification in the relative intensities of the 2LA peaks due to their distinct resonant responses (53). Moreover, it is worth commenting that the PL blueshift at the edge of A2 sample related to a 2LA frequency blueshift is in accordance with the PL redshift of the A1 sample at its edge corresponding to a 2LA redshift. Besides, for a strain hypothesis, the 1.5 cm^{-1} redshift of the E_{2g} mode is in agreement with the observed PL redshift of 25 meV (270), which would be associated with a strain of approximately 0.7%. Another commonly reported feature associated with strain with this magnitude in MoS_2 monolayer is the splitting of the E_{2g} mode in two peaks due to a lattice symmetry breaking (277). Although we did not have the spectral resolution to resolve these two peaks, the broadening of the E_{2g} mode observed in the edge Raman spectrum of Figure 7.7g is another indication of strain. Furthermore, the Raman intensity and frequency maps and profiles of the A_{1g} mode are shown in Appendix Figure B.9. Whereas there is an intensity enhancement at the edge,

no substantial shift is noted for the A_{1g} peak. The expected A_{1g} shift for a 0.7% strain is -0.5 cm^{-1}, which was probably not detected due to our measurement spectral resolution and its convolution with the B_{1u} mode.

In order to further corroborate the strain field responsible for the nanoscale optical features at the edge we performed AFM measurements in the A1 sample to probe possible topographic disorders. Simultaneously with the acquisition of the TEPL and TERS measurements, the topographic response of the tip (non-contact mode AFM) was also measured as shown in Figure 7.7h. A noticeable suspension in the edge region of less than 50 nm of width can be observed, indicating the presence of a strain field there. In order to confirm this result, high resolution AFM experiments were employed as displayed in Figure 7.7i. The left image of Figure 7.7i presents the AFM for the whole monolayer flake, while the right image shows the AFM for the edge region highlighted in the inset black square. Besides the surface roughness across the monolayer, both measurements presented a distinct topographic response at the edge, underlined by the height profile in the inset of the left image in Figure 7.7i. Thus, the sample indeed displays a localized topographic variation at the edges that can generate the observed strain fields that could be only probed by NF PL and Raman measurements.

7.5 Partial Conclusions

In summary, we studied local defects in distinct CVD grown MoS_2 monolayers by NF optical measurements. Electronic structure modifications in nanoscale regions along MoS_2 monolayer grain boundaries were probed by TEPL, in which a remarkable intensity enhancement of the exciton peak related to a quenching in the trion peak emission due to a doping effect was revealed. Besides, local strain fields were observed throughout a MoS_2 monolayer by TEPL and TERS measurements, revealing the role of the lattice mismatch between sample and substrate. Finally, edge defects were investigated by TEPL and TERS in MoS_2 monolayers. While one of the grown MoS_2 monolayer presented an PL intensity enhancement and energy blueshift at the edges, the other grown sample showed a PL energy redshift in the edge regions. Moreover, this last sample displayed a frequency redshift in the E_{2g} and 2LA Raman modes as well as a topographic suspension revealed by the AFM measurement, which suggest a strong localized strain field at the edges. Our work highlights the importance of utilizing optical spectroscopies with nanometric resolution to probe localized defects and reveal the optical properties in two-dimensional materials, that would be otherwise hindered in typical micrometer resolved spectroscopies.

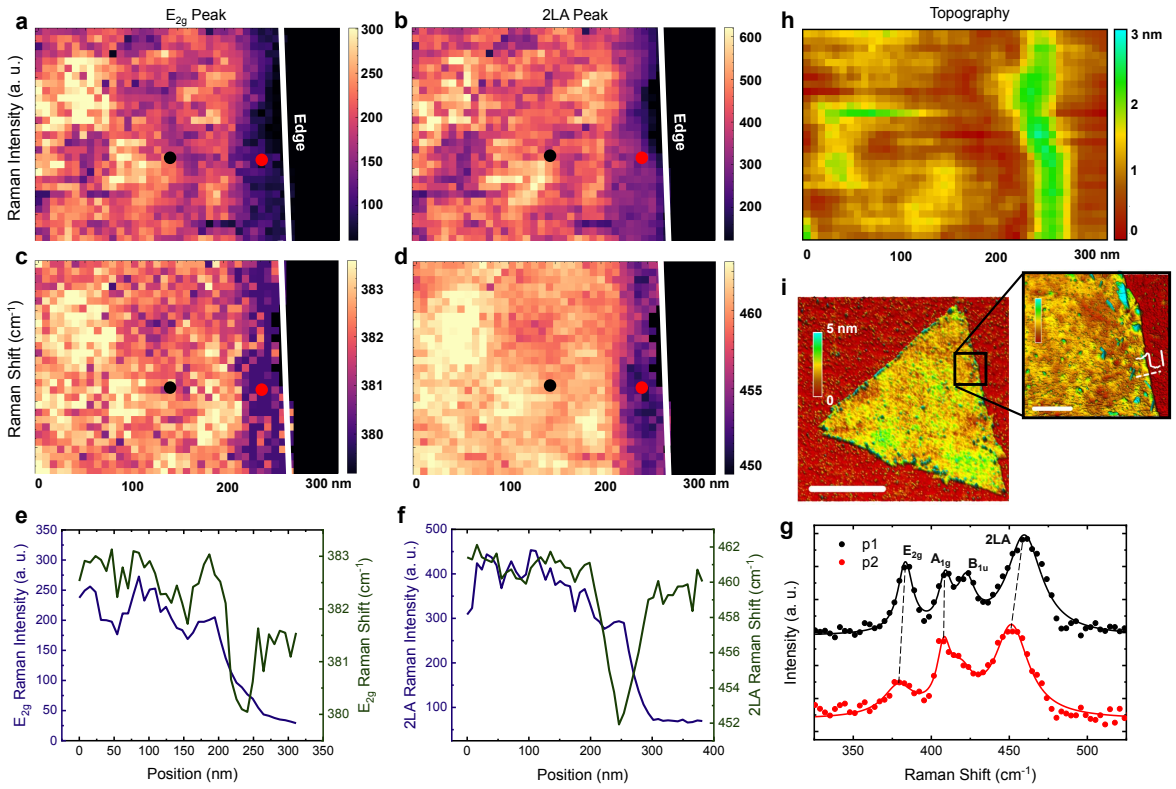

Figure 7.7 – **a-d** NF TERS hyperspectral maps of the E_{2g} Raman intensity (**a**) and Raman shift (**c**), and 2LA Raman intensity (**b**) and Raman shift (**d**) for a A1 MoS_2 monolayer. The TERS hyperspectral measurements were performed with steps of 8 nm and in the same region of the TEPL hyperspectral measurements of Figure 7.6. **e,f** E_{2g} (**e**) and 2LA (**f**) intensity and frequency profiles along the edge of the MoS_2 monolayer. They highlight the remarkable frequency redshift for both E_{2g} and 2LA Raman modes, that is also shown in NF Raman spectra of p1 and p2 points (**g**). These points are indicated by black and red circles in (**a-d**) maps and are related to an inner and an edge spot of the sample, respectively. **h** Topography measurement in the same region of the hyperspectral maps using the TERS tip height. The edge shows a noticeable suspension that is directly associated with a strain field. **i** AFM measurement of the whole monolayer (left image) and of the region underlined in the black square (right image), presenting the edge topographic response. The inset height profile in the right AFM image of (**i**) confirms the edge suspension. Scales bar in the left and right AFM images of (**g**): 5 μm and 500 nm, respectively. Scale bar of the height profile in the right AFM image in (**i**): 3 nm.

8 Nonlinear Optical Investigation of 2D TMDs

As discussed in Chapters 2 and 4, TMDs exhibit distinct optical responses under high pumping regimes. For instance, from a certain charge carrier density there is an exciton Mott transition to an electron-hole plasma (EHP) state, which modifies the optical and electronic properties of the TMD sample (26). However, the reported studies on the EHP light emission in TMDs are restricted to specific conditions such as cryogenic temperatures (28) or suspended samples (27). Moreover, for a broad comprehension of the optical properties of 2D TMDs subjected to this high excitation regime it is essential the investigation of the EHP light emission in TMD multilayers and heterostructures as well. Beyond the ionization of excitons, strong incident electric fields can also lead to further nonlinear optical responses in 2D TMDs, as a second-harmonic generation (SHG). Although SHG has been widely used to probe distinct TMDs and their vertical heterostructures (320), this second-order nonlinear response at heterojunctions of TMD lateral heterostructures still demands investigation.

In section 8.1 we show that a pulsed excitation is capable of inducing an EHP state in supported monolayer and multilayers WSe_2 and $MoSe_2$ samples at room temperature. Power-dependent photoluminescence (PL) measurements present the charge carrier dependence of the EHP emission in these materials, while two-pulse excitation correlation experiments provide information about its dynamics. The EHP light emission is also studied in section 8.2, in which TMD lateral and vertical heterostructures are imaged at high excitation densities, showing an enhanced PL intensity in comparison with the isolated TMDs. Finally, section 8.3 presents a SHG investigation of TMD lateral heterostructures. Excitation wavelength dependent SHG imaging reveals a constructive interference at the samples heterojunctions, that occurs due to a coherent superposition of the SHG fields from each TMD.

8.1 Electron-hole plasma emission of exfoliated 2D TMDs

Here, we investigate the carrier density dependence of the room temperature PL of as-exfoliated monolayer, bilayer, trilayer, and bulk WSe_2 and monolayer $MoSe_2$ samples under CW and pulsed excitations. In addition, a theoretical model was used to calculate the PL emission from unbound electrons and holes by our theoretician collaborators to compare with our experimental results. Finally, the dynamics of the light emission of the EHP regime for monolayer (WSe_2 and $MoSe_2$) and bulk (WSe_2) was investigated by two-pulse excitation correlation measurements. The following results are published in Ref. (374).

8.1.1 Room temperature EHP emission in WSe_2 monolayers

To study the carrier density dependence of the excitonic to metallic electron-hole phase transition we performed excitation power dependent PL measurements under CW and pulsed excitations in an exfoliated WSe_2 monolayer. These measurements were carried out with a pump excitation energy of 1.58 eV (below the material band gap energy of 1.65 eV) and with a notch filter placed before the spectrometer to block laser signal detection. Figure 8.1a displays the PL spectra under CW excitation for distinct pump powers and Figure 8.1b shows the same spectra normalized revealing no change in the shape of the emission peak. On the other hand, by pumping the sample with a femtosecond pulsed laser (Figures 8.1c,d) both intensity and shape of the PL peak present distinct behaviors with respect to the CW. We observe an apparent maximum peak intensity saturation and a clear broadening in the spectra above a certain pump power, that has been previously attributed to an EHP phase (27, 28). While the EHP is characterized by its carrier density dependence of the spectral width of the PL emission (375), the incompressibility of the charge carriers in the EHL phase does not let their density increase (103), leading to a constant PL peak width. As we observe a large broadening of the PL spectra with pump power, it is clear that we are not observing an EHL phase. Our observation is thus an indication for a gradual exciton Mott transition to an EHP phase. Moreover, our findings also reveal that pulsed excitation allows one to probe this effect even at room temperature and pump energies below the band gap resonance in an as-exfoliated TMD monolayer, while other authors reported this electronic phase transition only for peculiar conditions that involve suspended samples (28) or low temperatures (27). It is worth to discuss here if with the sub band gap excitation generates the EHP PL by one or two-photon absorption. As shown in Appendix Figure C.1, for CW excitation we note a linear power dependence for the PL intensity, which exclude the two-photon absorption hypothesis. Therefore, this sub band gap excitation consists in one photon process with a multi-phonon upconversion (376). Besides, to evaluate only on the WSe_2 PL contribution, background emission from the quartz substrate around 1.4 eV was removed from the spectra of Figures 8.1c,d as described in Appendix Figure C.2.

The broadening feature that is only observed in the PL generated by pulsed excitation can be better noticed in Figure 8.1f, in which the full width at half maximum (FWHM) of the spectra shown in Figures 8.1a-d are plotted with respect to the incident powers (top label). For the data measured under pulsed excitation the equivalent pump fluence values are also shown in the bottom label. We note that the PL under CW excitation shows an approximately constant FWHM value for all incident powers. For the spectra under pulsed excitation, we observe a similar constant value of the FWHM up to pump fluences around 10 J/m^2. In contrast, for greater fluences there is a noticeable enlargement of the PL width. For our measurement conditions, we can calculate the carrier density by

(27):

$$n_0 = \frac{P.\sigma}{A.f_{rep}.E}, \tag{8.1}$$

in which P is the incident laser power (W), σ is the absorptance taken from Yiley *et al.* (377), A is the area (cm^2) of the spot of the laser at the sample, f_{rep} is the laser pulse repetition rate (s^{-1}), and E is the incident photon energy (J). In addition, the pump fluence is the ratio between P with the product of A with f_{rep}, being A in m^2 in this case. Therefore, with the transition pump fluence value we calculated the Mott critical density as 10^{13} cm^{-2}, that is in agreement with previously reported values for TMD samples (126, 129, 132). Figure 8.1e displays a schematic representation of the emission in the excitonic and EHP phases. While the exciton presents a sharp emission well defined by its binding energy, the EHP has its luminescence broadened by the carrier density enhancement that leads to the electronic occupation of a larger range of energies, resulting in the observed broadening of the PL peak towards high energies. The broadening towards low energies is a fingerprint of the strong band gap renormalization that occurred during the measurement time. In summary, we observed a gradual transition induced by the excitation power in the luminescence emission of an as-exfoliated WSe_2 monolayer, in which its line width begins to continuously increase without a significant shift in the peak position. Our results help to corroborate the previously reported trend of a progressive exciton Mott transition into the EHP phase (27), unlike the abrupt one into the EHL (28).

8.1.2 Room temperature EHP emission in WSe_2 multilayers

In order to obtain a better understanding of the Mott transition in TMD materials we also probed multilayer WSe_2 samples in the same way as done for the monolayer. Figures 8.2a-i show the CW and pulsed excitation PL spectra of exfoliated bilayer, trilayer and bulk WSe_2 for distinct pump powers. It can be noted once again that under CW excitation (left side graphs) all samples preserve the PL line shape despite the intensity enhancement under increasing pump power. Furthermore, as well as observed in the monolayer, the multilayer samples exhibit a considerable broadening in the PL emission under pulsed excitation above a certain power, revealing their exciton Mott transition into an EHP (that is confirmed in the pump fluence dependent FWHM graphs shown in Appendix Figure C.3). Nonetheless, a slight difference in this effect for these multilayer samples can be noticed. While the monolayer shows no substantial shift in the energy of the PL peak maximum, there is a noticeable change in the peak position of the multilayers — mainly seen in the trilayer and bulk. Figures 8.2f,i show that the trilayer and bulk PL emission start centered at 1.46 and 1.38 eV, respectively. Above the Mott transition, new contributions around 1.59 for trilayer and 1.52 eV for bulk arise and exhibit an

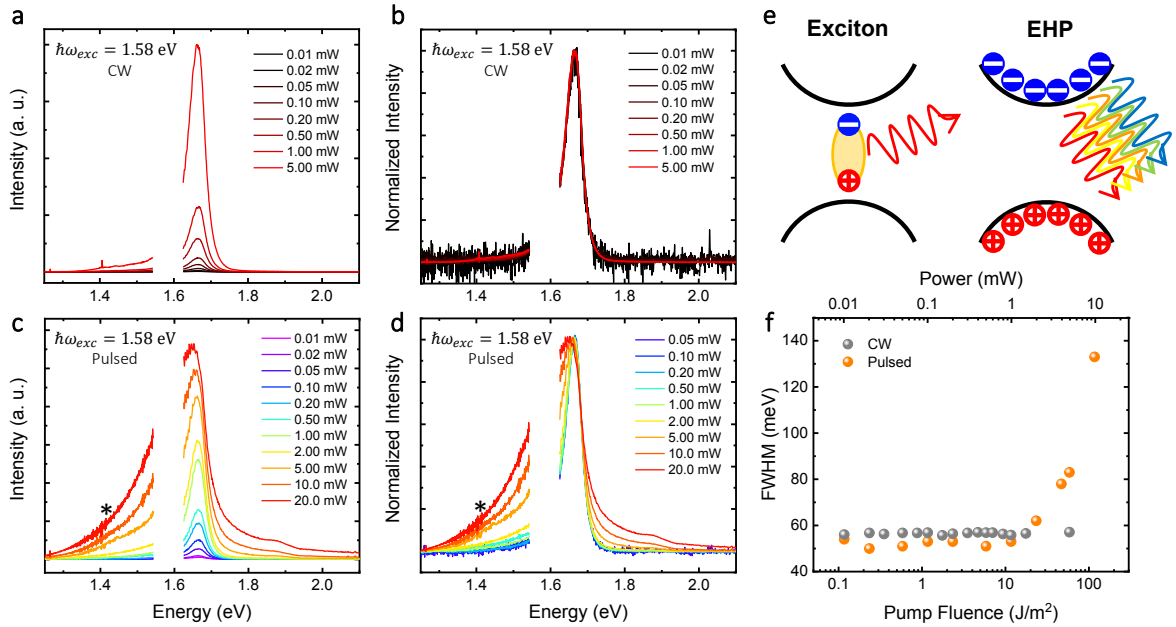

Figure 8.1 – **Excitation power dependent PL in a monolayer WSe_2. a** CW excitation PL spectra for distinct pump powers. **b** Normalized spectra from **(a)** showing that there is no modification in the peak shape. **c** Pulsed excitation PL spectra for distinct pump powers. **d** Normalized spectra from **(c)** revealing that for a pulsed laser excitation the light emission is notably broadened by increasing the pump power. **e** Schematic illustration of exciton and electron-hole plasma (EHP) emissions in a general TMD monolayer. **f** Power dependence (top label) of the PL full width at half maximum (FWHM) for the CW (gray) and pulsed (orange) excitations. For the pulsed excitation the bottom label also shows the equivalent pump fluence scale. The power and the fluence axis are displayed in a logarithm scale. It can be noted that the Mott transition happens for a pump fluence around 10 J/m^2 under the pulsed excitation. This value corresponds to a carrier density around 10^{13} cm^{-2}. The asterisks in the pulsed excitation measurements around 1.4 eV indicate where the substrate peak was removed from. The empty regions in the spectra are due to a notch filter used to block the detection of the 1.58 eV laser signal.

enhancement greater than the former peak until it dominates the spectrum. It is known that the high carrier density can result in a renormalization of the band structure due to carrier-carrier interactions (378). Moreover, as shown by Wilmington *et al.* (131), high excitation densities can also lead to sample strain in these TMDs. Besides, it has been reported by Desai *et al.* (271) that strain in multilayer WSe_2 induces an indirect to direct band gap transition. As the peak positions highlighted by the dashed curves displayed in Figures 8.2f,i are in agreement with the well known values of the energies of the indirect (IT) and direct (DT) optical transitions (379, 338, 380) of these materials, it is suggestive that the high carrier density generated by the pulsed excitation induced this band gap renormalization. As a consequence, Figure 8.3 shows that the PL intensity emitted by these multilayer WSe_2 samples in this high excitation regime becomes comparable with

the monolayer emission, enlarging the possibilities of application for these multilayers by tuning their carrier densities. Moreover, although the notch filter blocked the PL peak maximum region of the bilayer making the energy shift hard to be perceived, the great enhancement in its PL intensity similar to the trilayer and bulk samples indicates that the band gap renormalization should also be happening for the bilayer. These results reveal an opposite behavior with respect to the direct to indirect band gap transition in the exciton Mott effect of monolayer MoS_2 shown by Yu *et al.* (28). As reported, the indirect band gap drove the MoS_2 to large carrier lifetimes, which enabled the system evolution to a liquid phase (375). Conversely, we expect faster lifetimes for the WSe_2 samples, since we did not observed the emergence of the EHL state.

8.1.3 Calculation of the EHP emission in WSe_2 monolayers

To obtain a better insight into our experimental results and the underlying physics, our theoretician collaborators Prof. Ermin Malic and Raul Perea-Causin from the Philipps University of Marburg have modeled the PL emission spectra using the density matrix formalism considering a system of interacting electrons, holes and photons (381, 382, 383, 384, 385). At low densities, the PL is governed by the radiative recombination of bright excitons and is given by (386, 55):

$$I_{\mathrm{PL,x}}(\omega) \propto \sum_{\nu} \frac{|\phi^{\nu}(\mathbf{r}=0)|^2 n_{\nu}}{(\hbar\omega - E_{\nu})^2 + \gamma^2}. \tag{8.2}$$

The PL thus displays a Lorentzian line shape centered at the resonance energy E_ν of the exciton state ν with a broadening γ that is mainly governed by scattering with phonons in the low density regime. The intensity of the PL is determined by the product of the exciton population n_ν with the oscillator strength $|\phi^{\nu}(\mathbf{r}=0)|^2$, where $\phi^{\nu}(\mathbf{r})$ is the exciton wave function. In thermal equilibrium the PL is thus dominated by the recombination of excitons occupying the lowest (*i.e.* 1s) bright state. Note that the shape of the 1s PL peak in the excitonic regime is not affected by the temperature of the exciton population, as only excitons from the light cone with negligible center-of-mass momentum can recombine radiatively. The lattice temperature, *i.e.* the temperature of the phonon bath, determines rather the (symmetric) spectral broadening γ.

At densities above the Mott transition, excitons in WSe_2 dissociate into an EHP. In order to understand the effect of the carrier temperature in this regime, the interaction between charge carriers is neglected. The interactions in the plasma regime are strongly screened and lead mainly to a renormalization of the bands and an increase of the broadening γ via excitation-induced dephasing (387, 388). The PL for the EHP reads (382):

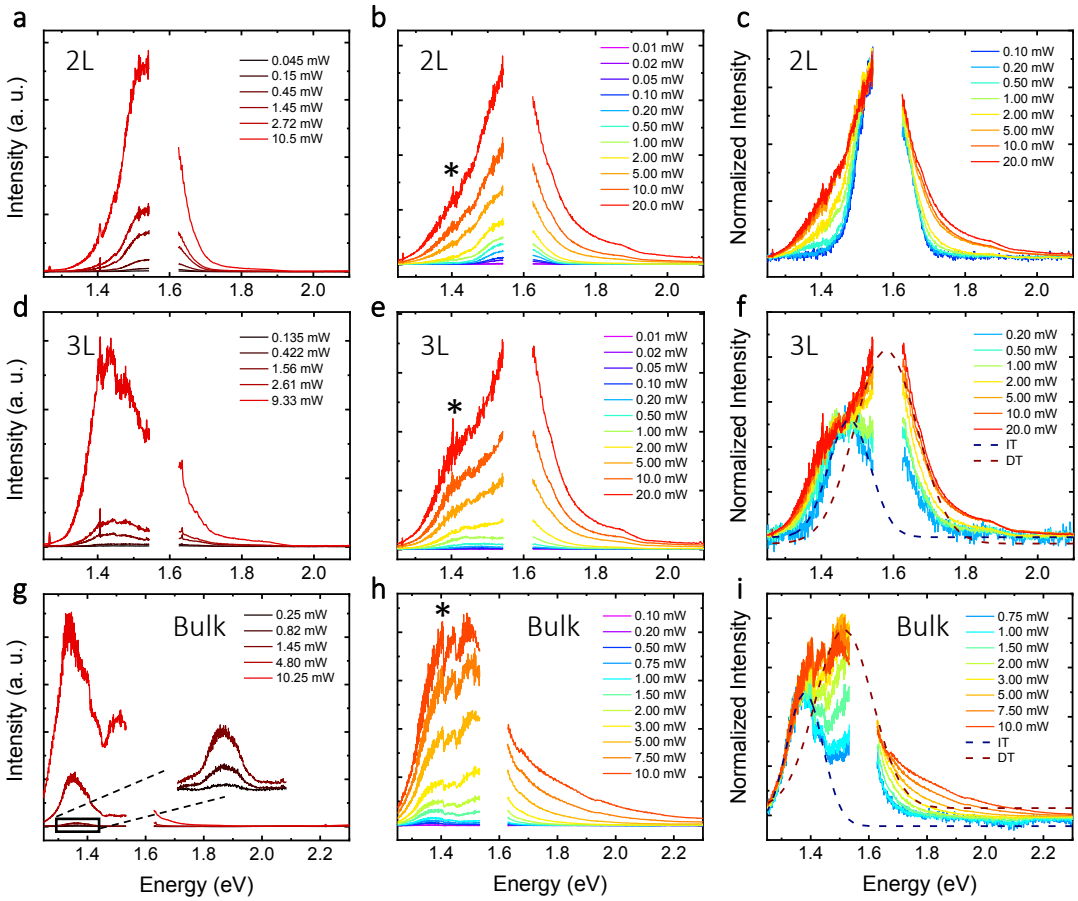

Figure 8.2 – **Excitation power dependent PL in multilayer WSe_2 samples. a,d,g** CW excitation PL spectra for distinct pump powers in a bilayer **(a)**, trilayer **(d)**, and bulk **(g)** WSe_2. No modifications in the PL peak shape for the CW excitation can be noticed. **b,e,h** PL spectra for pulsed excitation for distinct pump powers in a bilayer **(b)**, trilayer **(e)**, and bulk **(h)** WSe_2. **c,f,i** Normalized spectra from **(b,e,f)** revealing that for pulsed laser excitation the PL is notably broadened by increasing the pump power. Moreover, a shift in the peak position that is probably resulting from a indirect (IT) to direct (DT) band gap transition in these multilayer WSe_2 samples can also be observed. The asterisks in the pulsed excitation measurements around 1.4 eV indicate where the substrate peak was removed from. The empty regions in the spectra are due to a notch filter used to block the detection of the 1.58 eV laser signal.

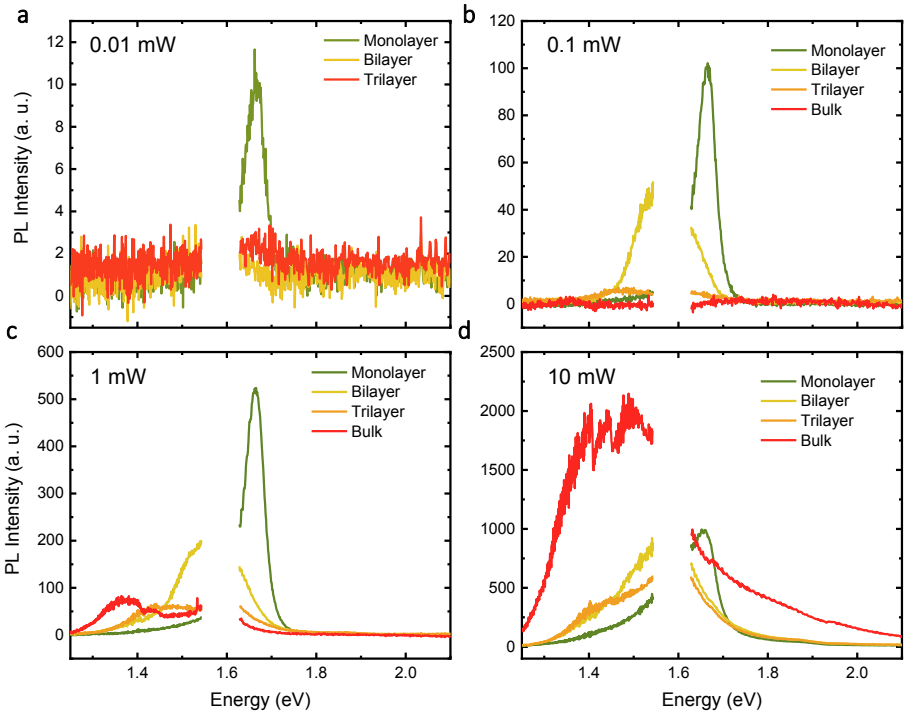

Figure 8.3 – Sample thickness dependence of the PL intensity under a pulsed excitation. **a-d** PL spectra of a monolayer, bilayer, trilayer and bulk WSe_2 for an incident power of 0.01 mW (**a**), 0.1 mW (**b**), 1.0 mW (**c**), and 10 mW (**d**). It can be noted that while the monolayer present a much greater PL intensity with respect to the multilayer samples for a low carrier density regime, the intensities of all samples become similar when they are excited to the EHP phase.

$$I_{\text{PL,e-h}}(\omega) \propto \sum_{\mathbf{k}} \frac{\rho^{\text{e}}_{\mathbf{k}} \rho^{\text{h}}_{\mathbf{k}}}{(\hbar\omega - E_{\mathbf{k}})^2 + \gamma^2}, \tag{8.3}$$

where $\rho^{\text{e(h)}}_{\mathbf{k}}$ is the electron (hole) occupation probability for the state with momentum $\mathbf{k}$, and $E_{\mathbf{k}} = E_{\text{g}} + \frac{\hbar^2\mathbf{k}^2}{2\mu}$ is the energy of the recombining electron-hole pair, with E_{g} and μ being the band gap and the electron-hole reduced mass, respectively. If the occupation is sufficiently low, electron and hole follow a Boltzmann distribution, resulting in $\rho^{\text{e}}_{\mathbf{k}} \rho^{\text{h}}_{\mathbf{k}} \propto \text{e}^{-\beta E_{\mathbf{k}}}$ with $\beta^{-1} = k_B T$. Considering a small γ, the PL reads $I_{\text{PL,e-h}}(\omega) \propto \text{e}^{-\beta(\hbar\omega - E_{\text{g}})}\Theta(\hbar\omega - E_{\text{g}})$. This expression clearly illustrates that the PL decays exponentially at energies above the band gap, with the slope of the exponential decay being determined by the thermal broadening of the carrier distribution, $k_B T$.

Figure 8.4a shows the computed PL in the excitonic (Eq. (8.2)) and EHP (Eq. (8.3)) regimes with $\gamma = 25$ meV for a monolayer WSe_2. While the excitonic PL displays a symmetric broadening and is unaffected by the temperature of the exciton distribution, the PL in the EHP regime displays a strongly asymmetric broadening towards higher energies, reflecting the thermal distribution of charge carriers. Considering a presumable renormalization of the band gap and an even greater broadening in the PL that are both not accounted here due to the neglected carrier-carrier interaction for the EHP,

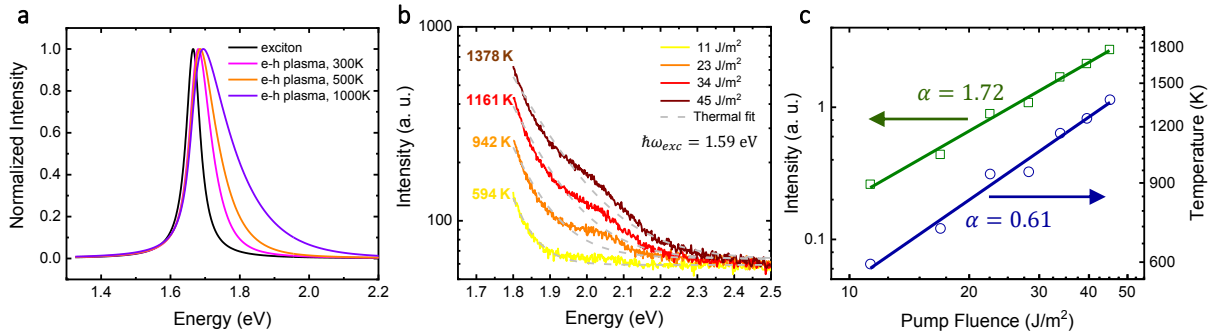

Figure 8.4 – **Excitonic and electron-hole plasma PL regimes. a** Computed PL of both regimes. While the exciton is formed by a low density excitation and therefore emits a symmetric Lorentzian peak, the electron-hole plasma is strongly affected by the high carrier population thermal distribution that generates a broad asymmetric light emission. Adapted from: (374). **b** PL spectra above the monolayer WSe_2 band gap of four distinct pump fluences with their exponential decay fits (gray) indicating their relative carrier temperatures. **c** Power dependence of the integrated PL intensity (green) and temperature (blue) with their power law fits indicating 1.72 and 0.61 exponents, respectively. The y-axis of (**b**) and both axes of (**c**) are displayed in a logarithm scale.

there is a reasonable qualitative agreement between our theoretical and experimental results. As mentioned, in the EHP regime an exponential decay of the PL determined by the carrier temperature for higher energies is expected. In order to relate that thermal distribution with the pump fluence, we performed more PL measurements in a monolayer WSe_2 focusing only on this higher energy range and for carrier densities above the Mott transition. The spectra for four distinct pump fluences are shown in Figure 8.4b together with their exponential decay fit, where it was possible to extract its carrier temperatures related to the different pump fluences. Moreover, Figure 8.4c shows the power law of the integrated PL intensity and extracted temperature with respect to the pump fluence. A nonlinear dependence of the light emission intensity with respect to fluence and a sublinear dependence for the temperature can be noted. These findings are in agreement with the reported EHP hot luminescence from graphene (389, 390, 391), which was observed for pump pulsed fluences similar to those presented in our work. In addition, similar results for a monolayer $MoSe_2$ are also shown in Appendix Figure C.4, revealing the same EHP behavior for this other TMD 2D material.

8.1.4 EHP dynamics in WSe_2 mono and multilayers

After exploring the pump-power dependence and the spectral characteristics of the EHP we now focus on the thermalization dynamics of the EHP. Different works reported on the dynamics of the electron-hole plasma and liquid phases in TMDs. For instance, Bataller (129), Chernikov (26) and Wang (27) *et al.* performed differential reflectance pump-probe measurements to access the electron-hole recombination lifetimes. While

Bataller revealed an ultralong charge lifetime of 100's of ns for the MoS_2 EHL, Chernikov and Wang observed a time scale of few picoseconds for the EHP lifetime in WS_2 and $MoSe_2/WSe_2$ heterostructure samples, respectively. Moreover, Siday *et al.* (132) have measured the exciton and EHP formation times by time-resolved terahertz nearfield microscopy in a WSe_2 bilayer, while Arp *et al.* (133) have presented the Mott transition by the nonlinearity in a photocurrent pump-probe measurement. However, despite the great impact of these results, the dynamics of the EHP thermalization and the possible physical processes behind have not been discussed so far.

Thus, in order to investigate the dynamics of the broadband luminescence in the EHP regime we performed two-pulse excitation correlation measurements in monolayer, bilayer, trilayer and bulk WSe_2 samples, and in a monolayer $MoSe_2$ sample. For this experiment the 375 fs pulsed laser beam was split in two beams with the same fluence of 15 J/m^2 and the PL signal was measured as a function of the temporal pulse separation. To focus only on the EHP emission we collected only the emitted energies above the band gap by using shortpass and bandpass filters. Figures 8.5b,c show the intensity profiles of the two-pulse excitation correlation measurements in the monolayer and bulk WSe_2 samples with respect to the temporal delay between the pulses for 1.67 eV excitation. Since this is an excitation correlation measurement, it provides information about the nonlinear dependence of the EHP light emission with the absorbed power, which is also related to its electronic thermalization dynamics. At zero delay time, the energies from the two laser pulses are transferred to material, generating the hot EHP with a given electronic temperature that leads to PL emission with the highest intensity. For increasing delay times, the electronic temperature decays and subsequently the PL intensity diminishes with two different characteristic times as can be observed in Figures 8.5b,c. Similar correlation measurements have already been performed to probe the EHP PL dynamics in graphene by Lui *et al.* (389) where two time responses were observed: a faster one due to the electronic thermalization with optical phonons and a slower one coming from the thermalization of the electrons and optical phonons with the system lattice bath - the electronic thermalization from the electron-electron scattering is ignored here since its characteristic time (392) is expected to be faster than the temporal resolution of our measurement. To determine the electronic tempearature as a function of time, one can use a two-temperature model (389). However, it is beyond the scope of our work to calculate the multiple different parameters needed, such as the electron and phonon heat capacities in the EHP regime, where changes in the electronic structure are expected due to high electronic temperatures. Therefore, in order to have an approximate value for the thermalization time scales, we use an empirical equation for the time dependent electronic temperature $T_{el}(t)$ given by:

$$T_{el}(t) = T_1 \cdot e^{-\frac{t}{\tau_1}} + T_2 \cdot e^{-\frac{t}{\tau_2}} + T_0, \tag{8.4}$$

in which $T_1+T_2+T_0$ are the "initial" electronic temperature reached upon pulsed excitation (after the electron-electron scattering thermalization), T_2+T_0 is the electronic temperature after the thermalization with the optical phonons (that happens in a time scale of τ_1) and T_0 is the final electronic temperature after thermalization with the system lattice bath (that happens in a time scale of τ_2). Hence, the optical phonon temperature can be written as: $T_{op}(t) = T_2 \cdot (1 - e^{-\frac{t}{\tau_1}}) \cdot e^{-\frac{t}{\tau_2}} + T_0$, and the system lattice bath temperature can be written as: $T_{bath}(t) = T_0 \cdot (1 - e^{-\frac{t}{\tau_2}})$. To illustrate these dependencies, Figure 8.5a shows a schematic representation of the temporal evolution for T_{el}, T_{op} and T_{bath}. Finally, to extract the time scales of each thermalization process, the intensity profiles of the two-pulse excitation correlation measurements shown in Figures 8.5b,c were fitted (in red) by the convolution of the IRF (Instrument Response Function) with the following expression that represents the electronic temperature dependent PL intensity:

$$I(T_{el}(t)) = 2I + I^{'} e^{-\frac{E}{k_B T_{el}(t)}}, \tag{8.5}$$

in which I is the uncorrelated PL intensity generated by each beam separately, $I^{'}$ is the maximum correlated intensity value, E is the emission energy and k_B is the Boltzmann constant. A detailed description of the signal deconvolution with the IRF is presented in Appendix Figure C.5. It is worth noting that while we measured the PL intensity in a time integrated fashion, its value is mainly determined by the peak electronic temperature reached (390). We observe a time decay faster than our experimental temporal resolution of 100 fs (orange) in both samples, while a slower one of $\sim$ 4 ps (purple) was mainly noticed in the monolayer and showed a minor contribution in the bulk. The optical phonons lifetime - that is the time in which the optical phonons loose their energy to acoustic phonons and to the lattice - has been previously measured by Jeong *et al.* (393) in a WSe_2 monolayer and showed a similar value of 4.5 ps. Therefore, we presume that the WSe_2 samples present an ultrafast thermalization of the plasma with the optical phonons around one hundred femtoseconds and that the electrons and optical phonons achieve in sequence a thermal equilibrium with the lattice bath in a time scale of few picoseconds. Finally, our results show a much faster dynamics in comparison with the nanosecond lifetimes previously reported for a monolayer MoS_2 EHL regime (28). These results highlight the difference between both works, since Yu *et al.* (28) achieved the EHL phase by a direct to indirect band gap transition mechanism and our EHP is achieved by directly excitation by using a short laser pulse. Finally, the two-pulse excitation correlation measurements of bilayer and trilayer WSe_2 and monolayer $MoSe_2$ are shown in Figure 8.6, revealing similar time scales for both electron-phonon and phonon-lattice thermalizations.

In summary, we reported room temperature EHP PL emission in mono and multilayer WSe_2 and monolayer $MoSe_2$ samples under high carrier densities generated by femtosecond pulsed laser excitation. We observed a large PL broadening coming from

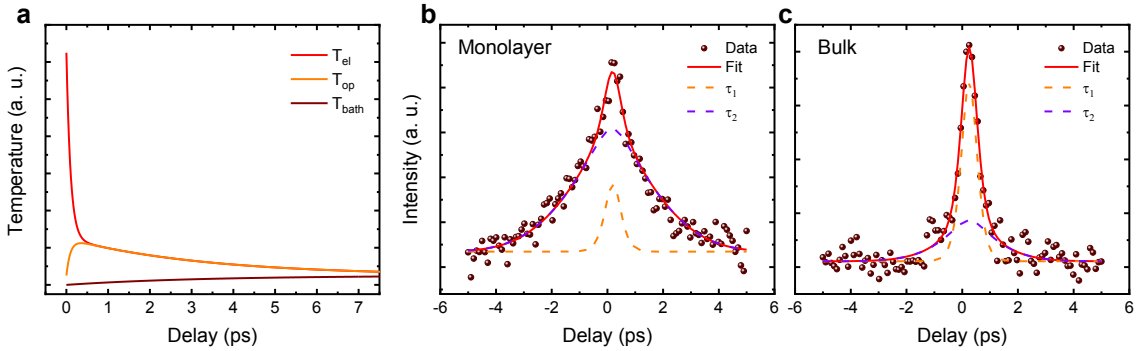

Figure 8.5 – **Two-pulse excitation correlation measurements in monolayer and bulk WSe_2 samples. a** Schematic illustration of the temporal evolution of the thermalization between the electronic temperature T_{el} with the temperatures from the optical phonons T_{op} and the lattice bath T_{bath}. **b,c** Intensity profiles of the two-pulse excitation correlation measurements for the monolayer (**b**) and bulk (**c**) WSe_2 samples. The scatter data show the intensity profile of the PL signal with respect to the temporal delay between the incident laser pulses. We collected energies around 1.97 eV, above the monolayer and bulk band gaps by using a combination of shortpass and bandpass filters. The temporal fits are shown in red, while the separated contributions of both time responses are displayed in the orange and purple dashed lines. A fast time scale of less than 100 fs and a slower one of $\sim$ 4 ps are observed.

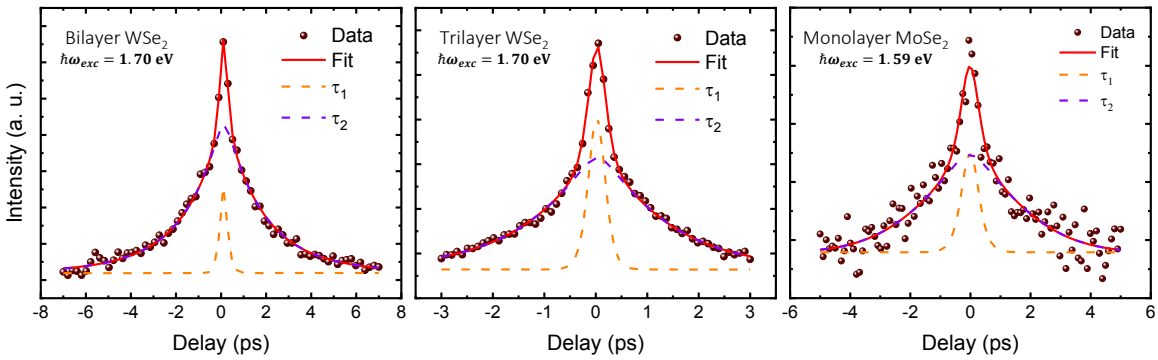

Figure 8.6 – **Two-pulse excitation correlation measurements in bilayer and trilayer WSe_2 and monolayer $MoSe_2$ samples. a-c** Intensity profiles of the two-pulse excitation correlation measurements for the bilayer (**a**) and trilayer (**b**) WSe_2 and monolayer $MoSe_2$ (**c**) samples. The scatter data show the intensity profile of the PL signal with respect to the temporal delay between the incident laser pulses. We collected energies around 1.97 eV for WSe_2 samples and 1.88 eV for the $MoSe_2$ sample, above their band gaps by using a combination of shortpass and bandpass filters. The temporal fits are shown in red, while the separated contributions of both time responses are displayed in the orange and purple dashed lines. A fast time scale of less than 100 fs and a slower one of 3–4 ps are observed.

a gradual exciton Mott transition into an EHP phase that occurs at a critical density on the order of 10^{13} cm^{-2}. Moreover, we found indications of an indirect to direct band gap transition in WSe_2 multilayers that leads to a noticeable enhancement in the light emission efficiency. We have computed the PL of both excitonic and EHP regimes based on microscopic many-particle theory and showed a good qualitative agreement with the experimental results. The thermal distribution of the plasma regime was related to the pump fluences where electronic temperatures up to 1400 K were reached. The dynamics of the EHP thermalization was probed by two-pulse excitation correlation measurements and showed a fast time response of less than 100 fs together with a slower component of few ps which were interpreted in terms of the electron-phonon and phonon-lattice bath thermalizations, respectively. As expected, this ultrafast response of the EHP is distinct from previous reported EHL lifetimes in TMDs. Our results open a wide range of possibilities not only for applications in light emitting devices such as TMD nanolasers but also in studying many body interactions at the high carrier density regime in 2D materials and their heterostructures.

8.2 Electron-hole plasma emission of 2D TMD heterostructures

In the last section we have presented and discussed about the room temperature EHP formation in mono and multilayer TMD samples through pulsed excitations. Subsequently, we were interested in employing this approach to probe TMD heterostructures in this high excitation regime. An EHP formation with the PL broadening signature has already been reported for a $MoSe_2/WSe_2$ vertical heterostructure at low temperature, in which the interlayer excitons were dissociated in a plasma of electrons and holes localized in separate layers (27). Moreover, low temperature pump-probe measurements revealed a fast expansion of the EHP also in a $MoSe_2/WSe_2$ vertical heterostructure (394). These outcomes shed light in the potential of TMD vertical heterostructures for emitting devices and for charge transport at high densities, and thus evidences the importance of room temperature investigations of their EHP regimes. Besides, the absence of studies at these high pump fluences in TMD lateral heterojunctions shows that it is also a demanding task to probe them with high excitation densities (246).

Here we report PL mapping measurements at densities above the Mott threshold in monolayer and bilayer $MoSe_2/WSe_2$ lateral heterostructures, which were also probed by spectroscopy experiments. In addition, we have performed similar PL mapping and spectroscopy measurements in the EHP regime in $MoSe_2/WSe_2$ vertical heterostructures. The experimental results of this section are concluded and its manuscript is to be submitted.

8.2.1 EHP PL mapping of a monolayer TMD lateral heterostructure

The first heterostructure sample analyzed in this work is a three-junction monolayer $MoSe_2/WSe_2$ lateral heterostructure sample synthesized by Prof. Prasana Sahoo group from the Indian Institute of Technology Kharagpur through the one-pot method (253) (growth details are described in Ref. (253)). The one-pot growth method provides an abrupt transition of a few nm from one TMD domain to another (253). However, this transition width varies when TMDs order is changed. For instance, the transition from the WSe_2 to the $MoSe_2$ domain (in the growth direction) is extremely sharp ($\sim$ 1 nm), while the reverse transition displays a small alloy formation with approximately 6 nm (253). Figure 8.7a shows the schematic representation of the three-junction monolayer $MoSe_2/WSe_2$ lateral heterostructure. In addition, optical images and PL and Raman characterization of the studied samples are displayed in Appendix Figure C.6, which confirms the thickness nature of both materials.

Similarly to the results presented in the last section, here we used a pulsed excitation below the materials band gap to probe the samples. Figures 8.7b-h show EHP PL images of a monolayer $MoSe_2/WSe_2$ lateral heterostructure for distinct pulsed excitation wavelengths (λ_{exc}) and an incident pump power of 75 mW. In order to collect the light emission associated only with the EHP PL emission we placed a 620/60 nm (λ_{det}) band pass filter in front of a photomultiplier tube (PMT). The high pump power used here is capable of generating charge densities as high as 10^{15} cm^{-2} (calculated by Equation 8.1) without damaging the sample. This is possible because the pixel dwell time of the EHP PL images of Figure 8.7 are on the order of a few μs. An intensity dependence of the EHP PL with the excitation wavelength is well noticed in Figures 8.7b-h. As expected, the PL intensity in the whole sample decreases by decreasing the laser excitation energy. Besides, the relative PL intensity of the $MoSe_2$ domains increase with respect to the WSe_2 domains due to its lower band gap energy, which explains the noted intensity inversion between these materials. Nonetheless, the most remarkable feature observed here is the enhanced EHP PL intensity at heterojunctions shown in Figures 8.7d-f. The signal at heterojunctions is stronger when the PL intensities of both domains are similar, reaching an enhancement factor greater than 2 for a 820 nm excitation wavelength, as shown in the intensity profile plot of Figure 8.7i. Moreover, the intensity profile plot also reveals different enhancements at distinct heterojunctions. The strongest enhancement is noticed at the interfaces in which there is an alloy formation (from $MoSe_2$ to WSe_2), while the sharp heterojunction (from WSe_2 to $MoSe_2$) displays a weaker enhancement. Finally, Figure 8.7i also compares the EHP PL intensity profile for distinct excitation wavelengths, in which it can be observed a shift in the position of the enhanced signal. This shift can also be noted in Figures 8.7c,g related to the excitation wavelengths of 810 and 830 nm, respectively, whereupon the brighter lines are slightly shifted from the heterojunction to the domain with the stronger

emission. We have also checked the polarization dependence of the emitted EHP PL with respect to the excitation laser polarization, as shown in Appendix Figure C.7. As the EHP PL emission is not polarized, our observed enhancement at the heterojunctions cannot be explained by a coherent interference between each domain signal. It is worth to comment that this EHP PL enhancement at heterojunctions was observed for several $MoSe_2/WSe_2$ lateral heterostructure monolayers pumped by distinct incident powers and detecting their emission at different energy ranges, as displayed in Appendix Figures C.8, C.9 and C.10.

To have a better visualization of the excitation wavelength dependence of the monolayer $MoSe_2/WSe_2$ lateral heterostructure EHP PL, we extracted the intensities from both materials and at the interface for the distinct measured excitation wavelengths as shown in Figure 8.7j. The intensities were extracted from the EHP PL images displayed in Figures 8.7b-h by taking the mean value over $MoSe_2$, WSe_2 and heterojunction areas. From low to higher excitation wavelengths, the EHP PL intensity from $MoSe_2$, WSe_2 and at the heterojunction decreases monotonically. The general behaviour can be understood in terms of the sub band gap excitation, whereas the multiphonon upconversion process responsible for generating excited carriers becomes weaker for increasing excitation wavelengths. Furthermore, we have also performed spectroscopy measurements of the EHP PL in the $MoSe_2$, WSe_2 and heterojunction regions to check this enhancement effect, as shown in Figure 8.7k. Since the spectroscopy measurements take much longer times (15 s integration time), the incident power is lowered to 33 mW in order to avoid sample damage. For this power, the excitation wavelength in which the enhancement at the heterojunction is more evident is at 805 nm. It is possible to observe that the three regions have a broad spectrum ranging up to 500 nm, and that there is indeed a stronger signal from the heterojunction for this wavelength range, confirming the features observed in the mapping measurements.

8.2.2 EHP PL mapping of a bilayer TMD lateral heterostructure

To study the influence of the sample thickness in the EHP PL emission, we performed similar EHP PL mapping measurements for a bilayer $MoSe_2/WSe_2$ lateral heterostructure. Figures 8.8a-i show EHP PL images of a bilayer $MoSe_2/WSe_2$ lateral heterostructure for distinct excitation wavelengths, an incident pump power of 40 mW and a 620/60 nm band pass filter placed in front of the PMT. An EHP PL enhancement at heterojunctions can also be observed for this bilayer lateral heterostructure, as displayed in Figures 8.8d-f. However, conversely to the monotonic decreasing in the EHP PL intensity by decreasing the excitation wavelength presented by the monolayer lateral heterostructure (Figure 8.7), a distinguish excitation wavelength dependence is noticed for the bilayer $MoSe_2/WSe_2$ lateral heterostructure. Figure 8.8j shows the EHP PL intensity graph as a function of the excitation wavelength for bilayer WSe_2 and $MoSe_2$ regions and their heterojunction. It can be noted a resonant response at 820 and 840 nm for WSe_2 and $MoSe_2$

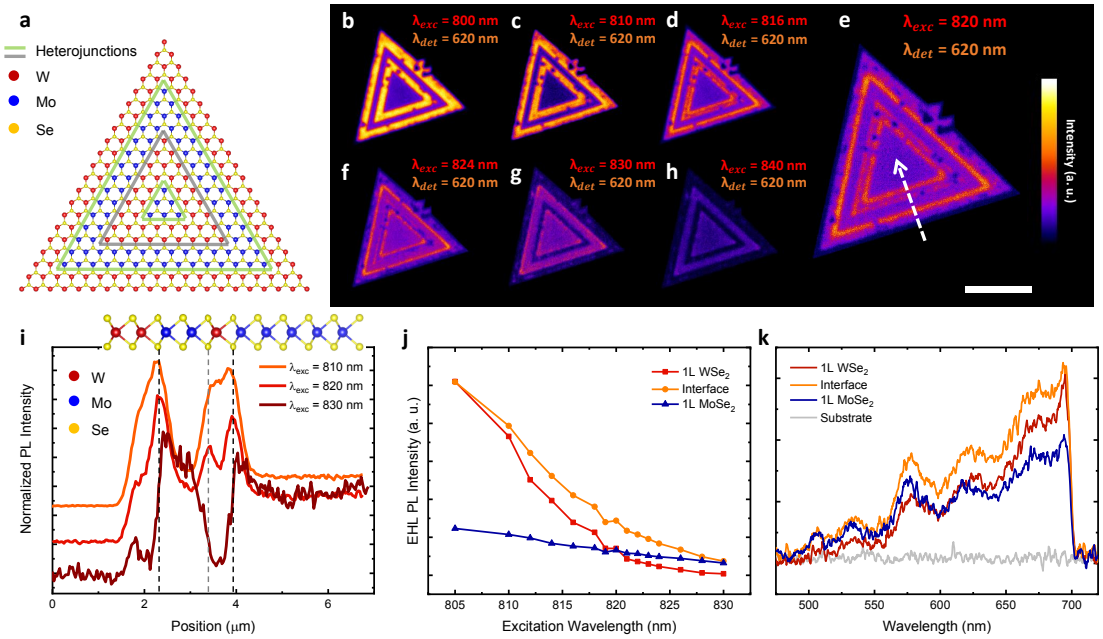

Figure 8.7 – **a** Schematic representation of a three-junction monolayer $MoSe_2/WSe_2$ lateral heterostructure, with heterojunctions highlighted in green and gray. EHP PL mapping of a monolayer $MoSe_2/WSe_2$ lateral heterostructure for 800 nm (**b**), 810 nm (**c**), 816 nm (**d**), 820 nm (**e**), 824 nm (**f**), 830 nm (**g**), and 840 nm (**h**) excitation wavelengths and 75 mW incident power. The EHP PL signal was collect by a PMT with a 620/60 nm band pass filter. **i** EHP PL intensity profile plot in the direction showed in the arrow of (**e**) for a 810, 820 and 830 nm excitation wavelengths. **j** EHP PL intensity as a function of the excitation wavelength of a monolayer $MoSe_2/WSe_2$ lateral heterostructure. The PL intensities of the WSe_2, $MoSe_2$ and interface regions clearly show the excitation wavelength dependence features observed in the PL images of (**b-h**). **k** EHP PL spectroscopy measurements of a monolayer $MoSe_2/WSe_2$ lateral heterostructure with a 805 nm excitation, an incident power of 33 mW and a 700 nm short pass filter placed in front of the spectrometer. The spectra taken in the WSe_2, $MoSe_2$ and interface regions confirm the enhanced emission at the heterojunction. The substrate signal is also presented to show that the emission is indeed from the material. Scale bar relative to (**d**): 5 μm.

domains, respectively. These resonances endorse the relation between the EHP PL intensity and broadening with the material absorption. Moreover, as well as for the monolayer lateral heterostructure, the enhanced EHP PL emission at the bilayer heterojunction happens for the excitation wavelengths in which the intensities from the individual domains are similar. Hence, we demonstrated that atomically thin $MoSe_2/WSe_2$ lateral interfaces present a remarkable luminescence emission at high excitation densities. Since this emission can be tuned by the excitation wavelength, incident power and sample thickness, our results evidence a great potential for these heterojunctions for tunable emitting devices at high pumping regimes.

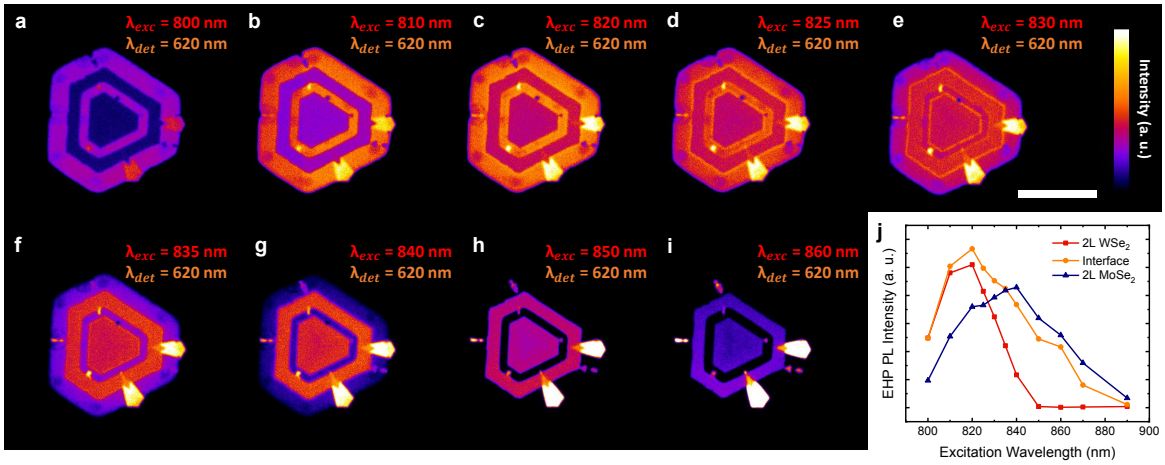

Figure 8.8 – EHP PL mapping of a bilayer $MoSe_2/WSe_2$ lateral heterostructure for 800 nm (**a**), 810 nm (**b**), 820 nm (**c**), 825 nm (**d**), 830 nm (**e**), 835 nm (**f**), 840 nm (**g**), 850 nm (**h**), and 860 nm (**i**) excitation wavelengths and a 40 mW incident power. The EHP PL signal was collect by a PMT with a 620/60 nm band pass filter. **j** EHP PL intensity as a function of the excitation wavelength of a bilayer $MoSe_2/WSe_2$ lateral heterostructure. The PL intensities of the WSe_2, $MoSe_2$ and interface regions clearly show the excitation wavelength dependence features observed in the PL images of (**a-i**). Scale bar relative to (**e**): 20 μm.

8.2.3 EHP PL in TMD vertical heterostructures

In order to further explore if the EHP PL intensity is enhanced for other heterostructure geometries, our collaborators Prof. Leonardo Campos, Felipe Murta and Gabriel Bargas from UFMG fabricated distinct $MoSe_2/WSe_2$ vertical heterostructure through a pick-up and stacking process (367) after isolating the 2D samples by a mechanical exfoliation method (1). The Raman characterization of the samples is presented in Appendix Figures C.11 and C.12. Figure 8.9a shows the optical image of a vertical heterostructure sample with a thin hBN on top, in which $MoSe_2$ bilayer (2L) and WSe_2 trilayer (3L) regions are highlighted and the studied heterostructure is at their intersected area. Firstly, we performed EHP PL mapping measurements in this sample for 800, 820 and 840 nm excitations, as shown in Figures 8.9b-d. These measurements were carried out for an incident power of 30 mW and with 690 nm short pass and 560 nm long pass filters placed in front of the PMT to collect the light emission associated only with the EHP regime. As well as for the lateral heterostructures, Figures 8.9b-d show an enhanced EHP PL emission from the vertical heterostructure (highlighted in the white rectangle) with respect to the individual TMDs. In addition, the relative intensity between $MoSe_2$ and WSe_2 domains also exhibits a similar cross-over around 820 nm (in which their intensities are similar). In order to corroborate these features, EHP PL spectroscopy measurements were also performed in the 2L $MoSe_2$, 3L WSe_2 and 2L $MoSe_2$/3L WSe_2 regions of this sample, as displayed in Figures 8.9e-g. The spectra were carried out with similar conditions of the mapping measurements, i.e., for 800, 820 and 840 nm excitations, with an incident power

of 30 mW and at a 600-730 nm spectral range. We can also observe an enhanced emission from the heterostructure and an inversion in the relative EHP PL intensity between $MoSe_2$ and WSe_2 domains, confirming the mappings results. Moreover, as underlined in the optical image of Figure 8.9a, there is another heterostructure region in this studied sample composed by a 2L $MoSe_2$ and a monolayer (1L) WSe_2. And as can be noticed in the EHP PL mappings of Figures 8.9b-d, this 2L $MoSe_2$/1L WSe_2 heterostructure region also exhibits an increased emission with respect to the individual TMDs.

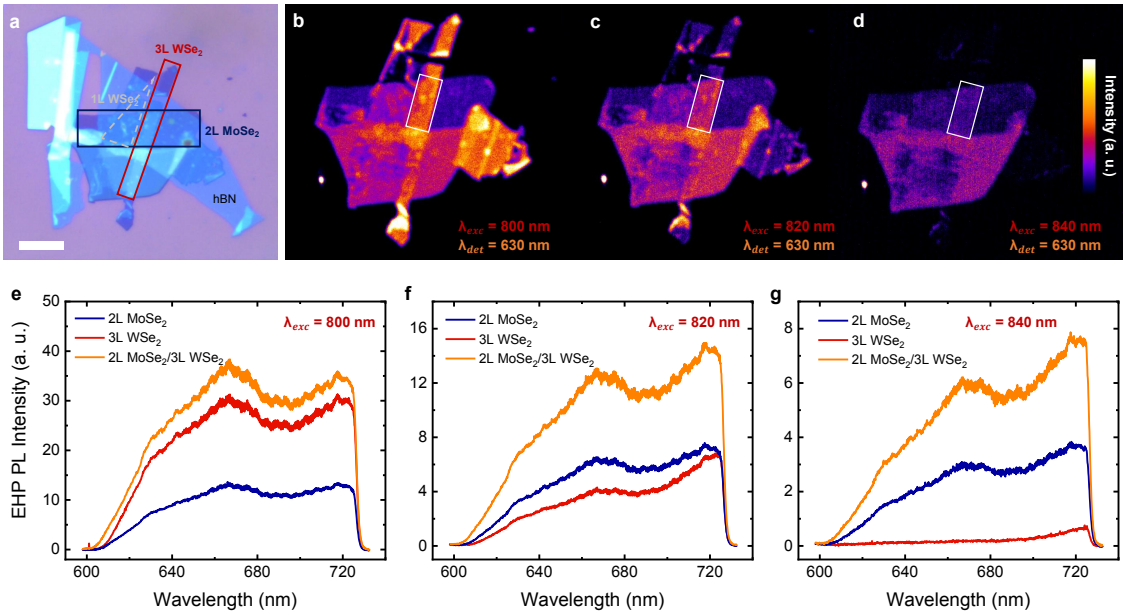

Figure 8.9 – **a** Optical image of the vertical heterostructure with the 2L $MoSe_2$ and 3L WSe_2 regions highlighted by blue and red rectangles, respectively. Monolayer WSe_2 region is also underlined by the gray dashed triangle. Scale bar: 10 μm. **b-d** EHP PL mapping of the 2L $MoSe_2$/3L WSe_2 vertical heterostructure for 800 nm (**b**), 820 nm (**c**) and 840 nm (**d**) excitation wavelengths and a 30 mW incident power. The EHP PL signal was collect by a PMT with 690 nm short pass and 560 nm long pass filters in front of it. The highlighted white rectangle indicate the heterostructure region. An intensity dependence with the excitation wavelength is clearly observed, in which a remarkable enhancement at the heterostructure emission is noted when the intensities from both domains become similar. **e-g** EHP PL spectroscopy measurements of 2L $MoSe_2$, 3L WSe_2 and their vertical heterostructure for 800 nm (**e**), 820 nm (**f**) and 840 nm (**g**) excitation wavelengths and a 30 mW incident power. The spectra taken in the WSe_2, $MoSe_2$ and heterostructure regions confirm the enhancement observed in the PL images.

To check if this enhancement effect is valid for other heterostructures, we have also investigated a 1L $MoSe_2$/1L WSe_2 sample. The optical image of this heterostructure is displayed in Appendix Figure C.12. PL spectroscopy experiments were performed in the 1L $MoSe_2$, 1L WSe_2 and 1L $MoSe_2$/1L WSe_2 regions of this sample in the excitonic and EHP regimes. Figure 8.10a shows the exciton PL spectra taken with a CW 633 nm excitation and with an incident power of 0.5 mW. Besides the well known PL peaks of 1L

$MoSe_2$ and 1L WSe_2 materials, a noticeable quenching in the PL emission of their vertical heterostructure is observed, in agreement with previous reports (395). In contrast, the EHP PL spectra presented in Figure 8.10b — performed with a 800 nm excitation and a 30 mW incident power — exhibit a strong enhancement of the heterostructure emission in comparison with the individual TMDs. Therefore, while Wang *et al.* (27) have investigated the low temperature EHP interlayer emission in a similar monolayer heterostructure, here we present the room temperature EHP PL at the intralayer transition energy range for distinct $MoSe_2/WSe_2$ vertical heterostructures, revealing a significant enhancement for all of them.

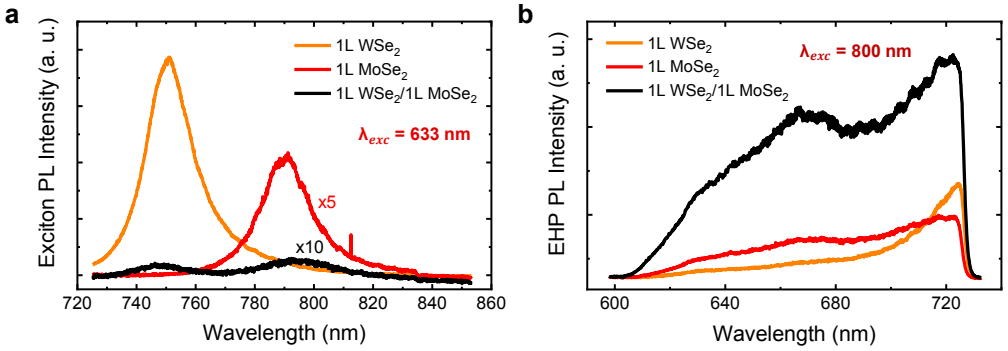

Figure 8.10 – **a** Exciton PL spectroscopy measurement for the 1L $MoSe_2$, 1L WSe_2 and their vertical heterostructure at a low excitation density regime and with a CW 633 nm laser. The excitonic spectra present a significant quenching of the vertical heterostructure emission with respect to the individual monolayers. **b** EHP PL spectroscopy measurement for the same materials for a pulsed 800 nm excitation and with a 30 mW incident power. In contrast to the excitonic PL, the EHP spectra shows an enhanced emission at the heterostructure.

8.2.4 Discussion on the EHP PL intensity enhancement at heterostructures

An important question that can be raised is why we observe a higher EHP PL emission at all lateral and vertical heterostructures. As reported in the last section, larger EHP density reflects in higher EHP PL emission. Therefore it is fair to suppose that at the heterostructures there is a greater EHP density, as shown schematically in Figures 8.11a,b. Different mechanisms can lead to charge accumulation at the heterostructures: i) higher absorption coefficients at the pump energies used; ii) enhancement of the charge lifetimes and iii) charge localization at the lateral heterojunction. The material light absorption plays a major role in the EHP formation and emission, as it directly reflects on the number of generated charge carriers (374). The $MoSe_2/WSe_2$ vertical and lateral heterostructures display a type II band alignment (238, 355), showing an interlayer transition channel with a lower energy, as displayed in Figure 8.11c. Hence, it is expected a higher absorption in the heterostructures for these sub band gap excitations, leading to an enhanced EHP PL in both lateral and vertical heterojunctions in comparison with the individual materials.

Also, different works have shown that this type II band alignment increases the lifetime of excitons due to momentum mismatch (355). Such process can help to achieve higher exciton concentration necessary to the EHP formation as shown in Ref. (129). Besides, the charge carrier density also depends on the area that they are generated. Since the heterojunctions of the measured lateral heterostructures occupy a nanoscale localized area, it is expected that they present a greater density of charge carriers. In addition, the vertical heterostructure presents a higher number of available electronic states at the conduction band, favoring an increased absorption. Although the microscopic mechanism and the relative importance of the different possible process for the EHP formation and emission deserves further theoretical work, our experimental results show that in contrast to normal excitonic PL emission that is quenched at the heterostructures (395), the EHP PL emission is in fact enhanced.

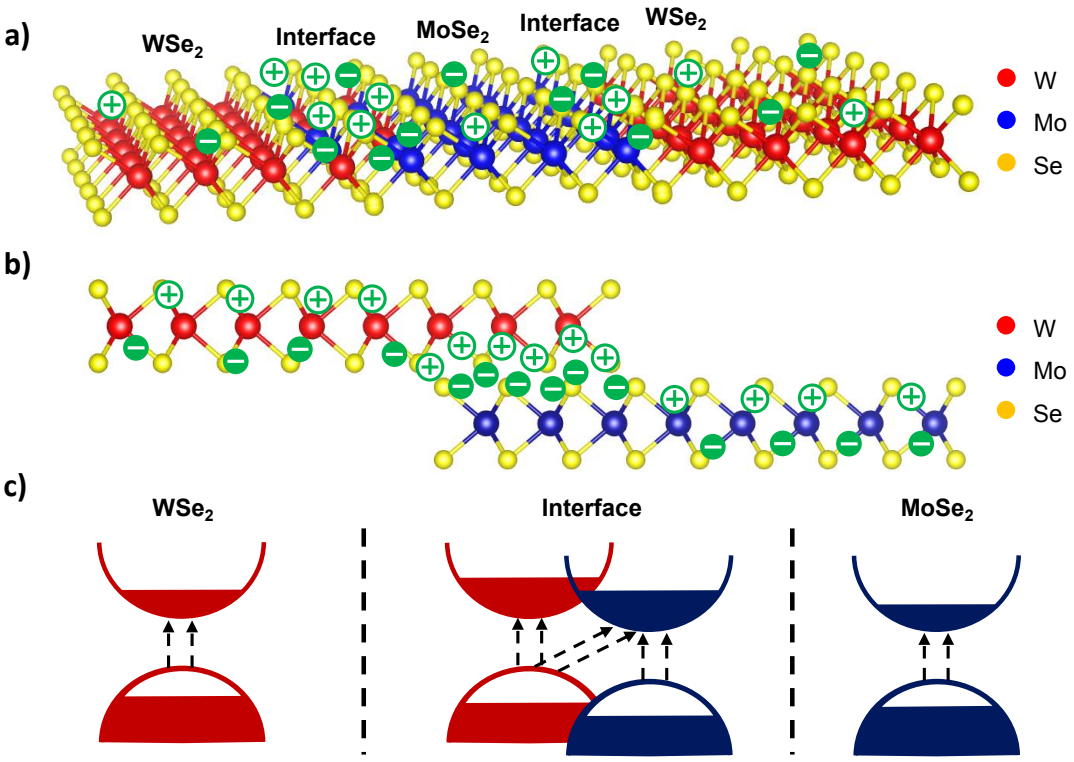

Figure 8.11 – Schematic representation of the charge carrier density in lateral (**a**) and vertical (**b**) $MoSe_2/WSe_2$ heterostructures in the EHP regime. Heterojunction and heterostructure regions present a higher density of charge carriers that is responsible for the enhanced EHP PL intensity. **b** Band structure representation of $MoSe_2$ and WSe_2 monolayers and their heterostructure. Due to the type II alignement of $MoSe_2$ and WSe_2, their heterostructure presents a lower energy interlayer transition channel that contributes with the higher absorption and charge carrier densities at the heterostructure regions.

In summary, EHP PL mapping measurements revealed an enhanced intensity at heterojunctions of monolayer and bilayer $MoSe_2/WSe_2$ lateral heterostructures and at $MoSe_2/WSe_2$ vertical heterostructures. These results were corroborated by EHP PL

spectroscopy measurements, that also showed an enhanced signal at heterojunctions and heterostructure regions. This enhancement can be related to the lower energy interlayer absorption channel and increased carrier lifetimes at the heterojunctions presented in these $MoSe_2/WSe_2$ vertical and lateral type II heterostructures, that leads to an increased charge carrier generation. Besides, the nanoscale localization of the lateral heterojunctions as well as the higher available electronic states of the vertical heterostructure also contribute to the enhanced EHP PL emission. Our work can trigger further theoretical works to understand the microscopical mechanism of EHP formation and emission and to envision future optoelectronic devices that need to be operated at the high carrier density regime.

8.3 Second-harmonic generation imaging of TMD lateral heterostructures

The heterojunctions of 2D TMD lateral heterostructures (LHs) discussed in the last section have been widely investigated by different techniques such as scanning transmission electron microscopy (STEM) (247, 248, 254, 50, 253, 251, 252, 249, 250, 255) and scanning probe microscopy (SPM) (254, 256), as well as Raman and photoluminescence (PL) spectroscopy (247, 248, 254, 50, 253, 251, 252, 249, 250, 255). Nevertheless, nonlinear optical responses in such nanostructures has been barely explored (50, 251). Here, we systematically image the second-harmonic emission in distinct TMD lateral heterostructures to investigate their nonlinear optical responses. The following results are published in Ref. (346).

8.3.1 SHG enhancement at the interfaces of $MoSe_2/WSe_2$ 1L-LHs

As discussed in Chapter 3, the development of the one-pot growth of 2D TMD LHs via sequential edge-epitaxy by Sahoo *et al.* (253) enabled the high-quality and controllable fabrication of these heterostructures, features that were not simultaneously achieved by single-step (247, 248, 249), two-step (250, 251) and multi-step (252) growth methods. The LHs grown by the one-pot method presented pure TMD domains as well as defect-free and sharp heterojunctions (253, 244, 396, 397). Nonetheless, these LHs has not been probed by SHG so far. Therefore, here we studied samples similar to those presented in the last section, grown by the one-pot method by our Indian collaborators.

Figure 8.12a shows an optical image of a three-junction 1L-LH composed by $MoSe_2$ and WSe_2 regions, and its schematic atomic structure. From the center to the edge the regions are based on $MoSe_2$-WSe_2-$MoSe_2$-WSe_2, where the 1L-$MoSe_2$ regions have a darker contrast with respect to the 1L-WSe_2 regions. As shown by Sahoo *et al.* (253), each region consists of pure 1L-$MoSe_2$ or 1L-WSe_2 domains. In the junctions of the materials there is a chemical transition that displays different behaviors for each type of interface. As commented in the last section, the 1L-WSe_2 $\rightarrow$ 1L-$MoSe_2$ interface is

atomically sharp, presenting an average width of 1 nm (4 atomic columns). The 1L-$MoSe_2$ → 1L-WSe_2 interfaces, in its turn, have a smoother chemical transition with some degree of alloy formation, with an average width of 6 nm (21 atomic columns) (253).

Figures 8.12b-d show the SH intensity images of the same 1L-LH in Figure 8.12a for three different emission wavelengths: 425, 440, and 455 nm, respectively. Comparing these images, we can observe that the relative SH intensity of the materials change with the wavelength: 1L-WSe_2 has a greater SH intensity at 425 nm (Figure 8.12b), both materials have approximately the same SH intensities at 440 nm (Figure 8.12c), and 1L-$MoSe_2$ has a greater SH intensity at 455 nm (Figure 8.12d). In addition, it can be noted a remarkable SH enhancement at the materials interface, as can be clearly seen in Figure 8.12c, when the SH intensities of both materials are similar. The SH intensity profile at the inset of Figure 8.12c shows that the SH intensity is enhanced by approximately 23% at the atomically sharp interfaces between the TMDs domains.

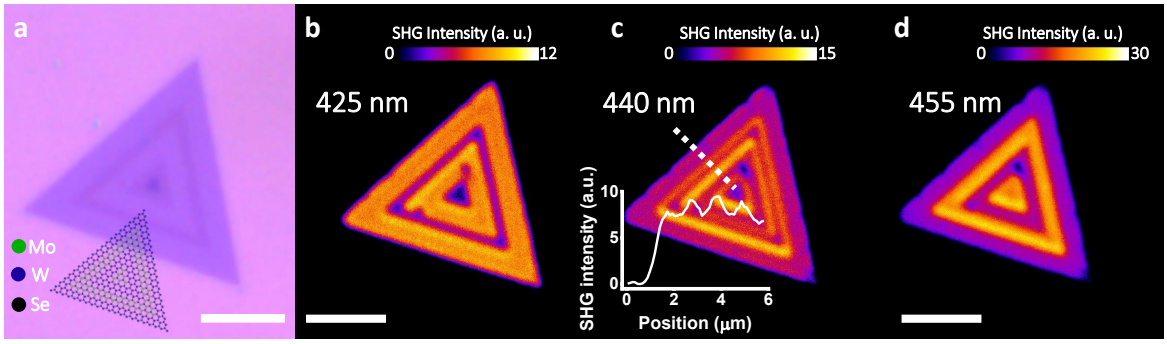

Figure 8.12 – **Optical and Second Harmonic imaging of a $MoSe_2$-WSe_2 based monolayer lateral heterostructure**. **a** Optical image and schematic atomic structure of a three-junction $MoSe_2$-WSe_2 based 1L-LH. The 1L-$MoSe_2$ domain have a darker contrast with respect to the 1L-WSe_2 domain. From the center to the edge the regions are based on $MoSe_2$-WSe_2-$MoSe_2$-WSe_2. **b-d** SH intensity images of the same 1L-LH sample collected at three different emission wavelengths. It can be noticed a greater SH intensity in the 1L-WSe_2 domain at 425 nm (**b**), approximately the same SH intensity in both domains at 440 nm (**c**) and a greater SH intensity in the 1L-$MoSe_2$ domain at 455 nm (**d**). An enhancement of the SH intensity emerges at the heterojunctions when the SH intensities of both domains are similar. It is clearly noticed in the intensity profile of the dashed line shown in the inset of (**c**). Scale bar: 5 μm.

8.3.2 SHG interference model at TMD LHs interfaces

As shown by Yin *et al.* (331), the crystal orientations of adjacent domains play an important role in the behavior of the SH signal at their interface. Therefore, to obtain better insights of the SH emission of our LHs, we performed a polarization-resolved SH measurement, that is widely used to ascertain the crystal orientation of 2D materials (19, 20, 21). For this measurement, we placed a rotable half-wave plate (690-1200 nm)

before the objective to control the incident laser polarization at the sample and a fixed analyzer in front of the photomultiplier tube (PMT) in the horizontal direction. Figure 8.13a shows the polarization resolved measurement of the same 1L-LH from Figure 8.12 for a 440 nm SH emission wavelength. As expected, the measurements reveal the SH four petals pattern, in which the intensities were extracted by taking the mean value over each analyzed region. We can notice that all petals from the 1L-WSe_2 and 1L-$MoSe_2$ domains and from their interface overlap, implying that they have parallel crystal orientations. It is important to note that 180^o crystal rotation would also give the same result for the SH polarization dependence. However, we do not observe the destructive interference between the domains as previous works (331, 333). Moreover, it has been shown that the 1L-LHs domains have the same crystal orientations (248, 249, 250, 247, 50, 251, 253).

To gain further information about the observed enhancement in the SH emission at the interfaces, we performed a set of measurements in the same 1L-LH with varying the pump wavelength. Since the SHG images are limited by optical resolution of 500 nm and the interfaces have a few nm width, we have deconvoluted the SHG images with a 2D Gaussian profile function of our system as presented in Appendix Figure C.13 to improve the spatial resolution. Then, the mean values of the SH intensity at both materials domains (1L-WSe_2 and 1L-$MoSe_2$) and at their interface from the deconvoluted images were extracted for all measured wavelengths and presented in Figure 8.13b. We can observe that for wavelengths below 435 nm the SH intensity from 1L-WSe_2 domain predominates, whereas for wavelengths above 435 nm the 1L-$MoSe_2$ region has a greater SH intensity. The reason for this intensity behavior is due to the resonance of the two-photon process with the C exciton energy. As shown by Li *et al.* (377), the absorption maximum at the C exciton for 1L-WSe_2 and 1L-$MoSe_2$ are, respectively, 427 and 477 nm. Thereby, each material is expected to have a greater SH intensity around its absorption peak wavelength. Besides that, at 435 nm, the absorption cross section for both materials are similar, giving rise to the same SH intensity as observed in Figures 8.12c and 8.13b. Moreover, Figure 8.13b reveals that the SH intensity enhancement at the interfaces can be clearly observed for SH wavelengths between 425 and 455 nm, having a higher intensity compared to the SH emission from the domains. This enhancement becomes stronger around 435 nm, where the SH intensities of both materials are similar, and disappear below 425 and above 455 nm, where there is a substantial difference between the SH intensities of the materials.

To understand the observed SH enhancement, Figure 8.13c shows a schematic illustration of the SHG at the 1L-LH. The pump laser with frequency ω excites the sample that emits a SH signal with frequency 2ω. When the laser beam is centered at the interface, the SH emission has contributions from both materials. As shown by Hsu *et al.* (327), the intensity of the SHG at the interface can be modeled as a coherent superposition of each material signal. Therefore, the electric field of the interface region $\vec{E}_{int}(2\omega)$ is

the superposition of the electric field of both materials: $\vec{E}_{int}(2\omega) = \frac{\vec{E}_{Mo}(2\omega) + \vec{E}_{W}(2\omega)}{\sqrt{2}}$. This $(1/\sqrt{2})$ factor arises because each material contributes with half of its total emission intensity, that is proportional to the square of the absolute value of the electric field ($I \propto |\vec{E}|^2$). Hence, the total SH intensity at the interface is given by:

$$I_{int} = \frac{I_{Mo}}{2} + \frac{I_W}{2} + \gamma\sqrt{I_{Mo}I_W}, \tag{8.6}$$

in which I_{Mo} and I_W are the SH intensities from 1L-$MoSe_2$ and 1L-WSe_2 domains, respectively, and I_{int} is the SH intensity at the interface. The γ factor is introduced here to account for the phase difference between the two materials. This phase difference can be due to different crystallographic orientations (331) or due to a intrinsic phase difference of different $\chi^{(2)}$ of the materials as shown by Kim *et al.*(328). Since both materials have the same crystallographic orientations (253), a deviation from $\gamma = 1$ should be due to a phase difference coming from the distinct $\chi^{(2)}$ of both materials. In order to check if such simple model explains our findings, we calculated from 8.6 the expected SH interface intensity as a function of wavelength and using the measured I_{Mo} and I_W values, as shown in Figure 8.13b. The behavior of the interface SH intensity calculated by the interference model is in a reasonable agreement with the measured interface SH intensity for $\gamma = 0.5$. It is worth to comment that although we verify that the phase difference of SH fields of the two materials is important to explain our data, the exact value of this phase difference is not reliable due to limited spatial resolution of our experimental setup and small fluctuations in intensity for different interfaces as shown in Figure 8.12c.

To have a further experimental check that interference is the origin of the SH enhancement at the interfaces, we performed a set of SH measurements for a 440 nm emission wavelength by blocking the emitted light from one of the 1L-TMD domains as shown in Figure 8.14. When the SH is generated at the LH interface, the SHG beam has contributions from both domains that interfere with each other at the PMT detector. Therefore, it is expected that if we block the SH emission from one of the domains, the interference should disappear. To prove that, we have placed a movable sharp and straight object parallel to one of the $MoSe_2$-WSe_2 1L-LH interfaces before the PMT detector as shown schematically at the bottom of Figure 8.14. Figure 8.14a shows the SH image with a clear SH enhancement at the interface without blocking the SH emissions. When the SH emission from one of the 1L-WSe_2 domains starts to be blocked, the SH intensity begins to decrease as shown in Figure 8.14b. If the blocking of the SH emission at the 1L-WSe_2 domain is increased, the SH enhancement at the adjacent interface is not visible anymore, as revealed in Figure 8.14c, confirming that this SHG enhancement at the interface comes from interference.

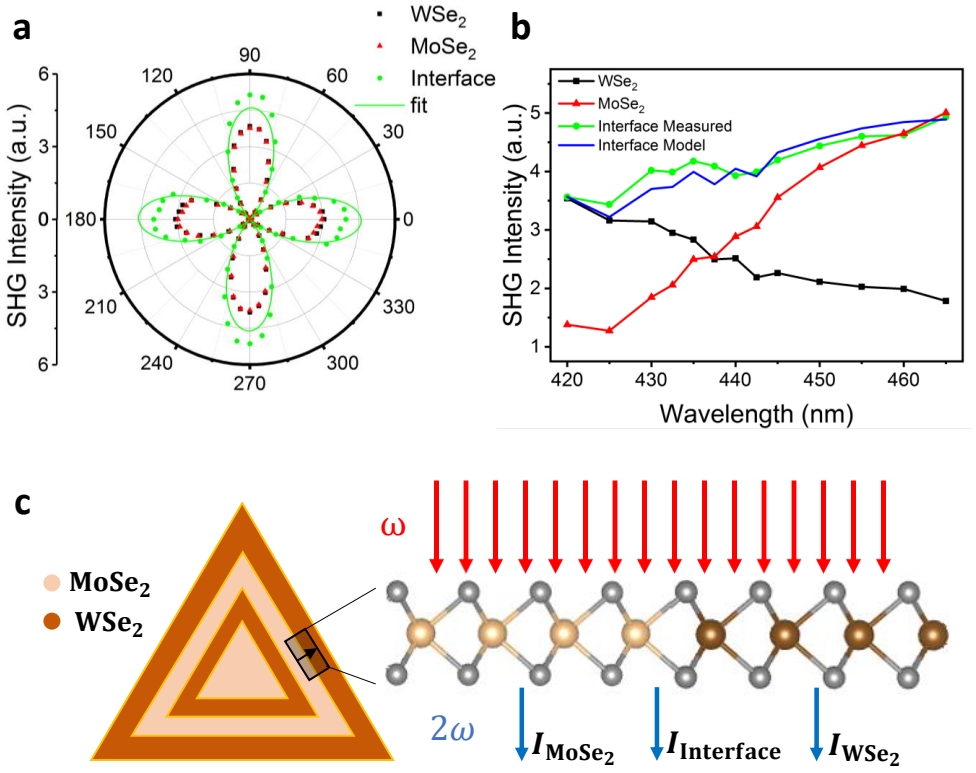

Figure 8.13 – **Second Harmonic polarization and wavelength dependent measurements in the $MoSe_2$-WSe_2 based monolayer lateral heterostructure**. **a** Polarization-resolved SH measurement from the 1L-$MoSe_2$ and 1L-WSe_2 domains and from their interface for a 440 nm SH emission wavelength. The interface displays a greater SH intensity while both materials domains show similar SH intensities. Furthermore, the overlap of the four petals pattern for these three regions shows that they all have the same crystal orientation. **b** SH intensity as a function of the emission wavelength for the three regions cited above. It is noticeable the greater SH intensity at the interface where the SH intensities of both materials are similar (425-455 nm). **c** A schematic illustration of the SHG at the 1L-LH: a laser beam with frequency ω excites the sample that generate a SH emission with frequency 2ω.

8.3.3 SHG enhancement at the interfaces of MoS_2/WS_2 LHs

In order to verify if the SHG can be used to probe other types of heterojunction interfaces, we also performed measurements in other LHs based on different TMDs (MoS_2 and WS_2) and for different number of layers. First, we performed SH measurements in a $MoSe_2$ and WSe_2 based 2L-LH. However, we did not observe any SH signal in our measurements, which led us to infer that this $MoSe_2$ and WSe_2 based 2L-LH has AB stacking. 2L-TMDs with AB stacking belong to the D_{3d} point group and have inversion symmetry due to the geometry of the stacking. As SHG is a second-order nonlinear process, they exhibit only weak SH emission, since the second order susceptibility is zero for materials with inversion symmetry (within dipole approximation) (317).

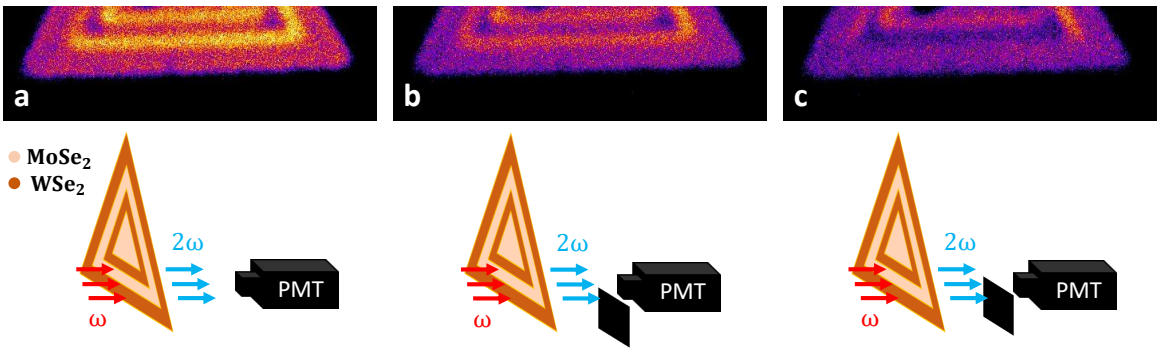

Figure 8.14 – **Interference pattern evidence in the $MoSe_2$-WSe_2 based monolayer lateral heterostructure**. **a-c** Schematic illustrations of a gradually blocked SH emission measurements and their respective SH images. In the absence of the blocking object (**a**) or with it barely blocking part of the 1L-WSe_2 domain SH emission (**b**), the SH enhancement at the interface is observed. Once there is a substantial blocking of the 1L-WSe_2 domain SH emission (**c**), the interference pattern in the adjacent interface vanish. All SH images were collected at a 440 nm emission wavelength, where there is a clear SH intensity enhancement at the interfaces.

On the other hand, Figure 8.15 shows the measurements of MoS_2 and WS_2 based 1L- and 2L-LHs with finite SH signal. Figures 8.15a-c show SH intensity images of a MoS_2 and WS_2 based single-junction 1L-LH. The 1L-MoS_2 domain is in the center of the LH while the 1L-WS_2 domain is at the edge. Although the intensity ratio between both materials change with the emission wavelength, the 1L-WS_2 SH intensity is always greater and no enhancement of the SH emission was observed at the interfaces. Figures 8.15e-g show SH intensity images of a MoS_2 and WS_2 based three-junction 2L-LH with AA stacking. From the center to the edge the regions are composed by MoS_2-WS_2-MoS_2-WS_2. For this 2L-LH there is a clear change in the predominant material with stronger SH emission as a function of wavelength. 2L-WS_2 has a larger SH intensity at 405 nm (Figure 8.15e), both materials have approximately the same SH intensities at 430 nm (Figure 8.15f) and 2L-MoS_2 has larger SH intensity at 440 nm (Figure 8.15g). It is possible to observe in the inset of Figure 8.15f that there is an evident SH enhancement at the interfaces when the SH intensities at both domains are similar.

As done for the selenide TMDs based 1L-LH, we performed a set of SH measurements varying the pump laser wavelength for both 1L- and 2L-LHs based on the sulfide TMDs. Figure 8.15d shows the 1L-MoS_2 and 1L-WS_2 domains SH profiles, where it is possible to observe that the WS_2 domain have a greater SH intensity over the whole wavelength interval measured. This is different from what is observed at the $MoSe_2$-WSe_2 based 1L-LH SH profiles (Figure 8.13b), where there is an inversion in the domain with predominant SH emission. Therefore, although the interference model (8.6) remains valid for the MoS_2-WS_2 based 1L-LH, the absence of a wavelength range where the SH intensities of both domains are similar explains why there is no visible enhancement in the SH

emission at the interfaces, since the interference is not completely constructive ($\gamma < 1$). It is worth to note that the lack of an intersecting point between the 1L-MoS_2 and 1L-WS_2 SH profiles is also observed in their absorption spectra for this same wavelength range (377).

Conversely, the MoS_2-WS_2 based 2L-LH presented a clear SH enhancement at their interfaces (Figure 8.15f). Hence, we have deconvoluted their SH images with the 2D Gaussian profile function of our system to improve the heterojunctions resolution. The intensities of both materials and of the interface for the wavelength dependent measurements were extract in the same way as before and their SH profiles are shown in Figure 8.15h. We have also calculated the expected value of the interface intensity for this MoS_2-WS_2 based 2L-LH using the interference model (8.6), and it is also shown in Figure 8.15h. We can notice that the interference model is in agreement with the measured SH intensities values at the interface by using $\gamma = 0.16$. Also in Figure 8.15h, we can observe two crossing points between the SH profiles of MoS_2 and WS_2 domains at 428 and 445 nm. This behavior is similar to the theoretical prediction (235) of the absorption spectra of these AA stacking materials, which presents two intersecting points at 424 and 454 nm for the same wavelength range.

In summary, we have observed a constructive interference emerging from the coherent superposition of the SH signal from each material at their atomically sharp interfaces for different TMD LHs. Performing polarization resolved and energy dependence measurements we were able to model this interference pattern and notice a phase difference between materials in the LHs due to their different $\chi^{(2)}$. For the $MoSe_2$-WSe_2 based 1L-LH and the MoS_2-WS_2 based 2L-LH, we have observed an enhancement of the SH emission at the interface with respect to the SH emission from both materials for a certain pump wavelength range. This enhancement only occurs when the SH emission from each material is similar in intensity, leading to a highlighted constructive interference. However, even with no enhanced SH signal, the constructive interference is also supposed to happen at the interfaces, as in the MoS_2-WS_2 based 1L-LH. Therefore, our model enable us to infer that any LH would present a constructive interference at their interfaces if their domains have the same crystal orientations, but it might be not visible as in the case of MoS_2-WS_2 based 1L-LH. Moreover, our results show that SHG, a non-destructive optical technique, can also be used to image sharp interfaces of nanometric widths in LHs based on 2D materials.

8.4 Partial Conclusions

Nonlinear optical spectroscopy and imaging techniques are a powerful tool to probe 2D TMDs and their heterostructures. Here we showed a pathway to generate EHP

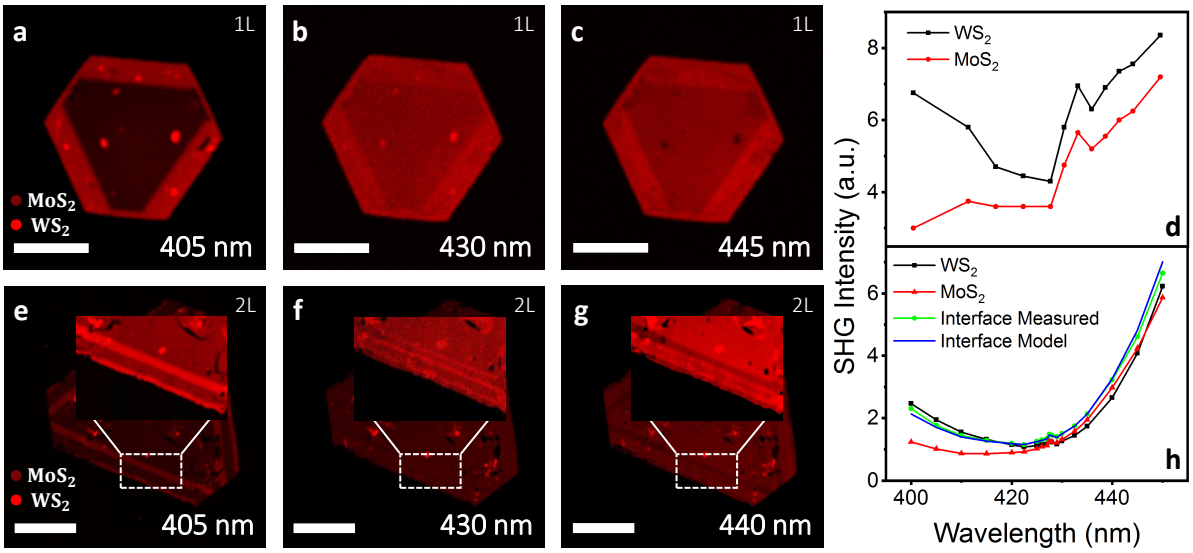

Figure 8.15 – **Second Harmonic intensity images and wavelength dependent measurements of MoS_2-WS_2 based monolayer and bilayer lateral heterostructures**. **a-c** SH intensity images of the MoS_2-WS_2 based 1L-LH for three different emission wavelengths: 405 nm (**a**), 430 nm (**b**), and 445 nm (**c**). The 1L-MoS_2 domain is in the center of the LH while the 1L-WS_2 domain is at the edge. **d** SH intensity of the 1L-LH as a function of the emission wavelength for both materials. We can notice that the 1L-WS_2 SH intensity is greater for all the wavelengths measured, implying in no enhancement of the interface SH signal. **e-g** SH intensity images of the MoS_2-WS_2 based 2L-LH for three different emission wavelengths: 405 nm (**e**), 430 nm (**f**), and 440 nm (**g**). From the center to the edge the regions are composed by MoS_2-WS_2-MoS_2-WS_2. The insets show more clearly the heterojunctions in the region indicated by the dashed lines. **h** SH intensity of the 2L-LH as a function of the emission wavelength for both materials, their interface, and the interference model using $\gamma = 0.16$. For the 2L-LH there is an evident enhancement of the interface SH intensity around 430 nm, where the SH intensities of both materials are similar. Scale bar: 10 μm (**a-c**) and 20 μm (**e-g**).

states in 2D WSe_2 and $MoSe_2$ samples by a sub band gap pulsed excitation. A remarkable broadening in the EHP PL emission of these samples and an indirect to direct band gap transition in the WSe_2 multilayers was observed at high excitation densities regimes. The dynamics of the EHP thermalization was also investigated, showing an ultrafast coupling between electrons and optical phonons and a slower cooling of few ps with the lattice. Subsequently, we used this sub band gap pulsed excitation approach to map the EHP PL in 2D TMD lateral and vertical heterostructures. They showed an enhanced PL emission in this high charge carrier density regime in comparison with the individual TMDs. This enhancement was corroborated by EHP PL spectroscopy measurements, and accounted to the higher absorption in the heterostructure regions. Our results on the EHP light emission in TMDs contribute to the understanding of both fundamental phenomena and application possibilities for these 2D TMDs and their heterostructures at high excitation conditions. In addition, this EHP state can be generated to study defects in TMDs as

well. For instance, we have preliminary results showing a noticeable enhancement of the EHP light emission in a WSe_2 monolayer on top of nanopilars owing to the charge carrier confinement in these strained regions. Finally, we also carried out SHG measurements on 2D TMD lateral heterostructures to provide the first nonlinear optical investigation of their heterojunctions. We showed an enhanced SH emission at the lateral heterostructures interfaces due to a coherent interference between the SH signals from each TMD. Hence, we presented an optical method to probe atomically sharp heterojunctions, revealing a tunable nonlinear response by varying the emission wavelength.

9 Summary

In this thesis we performed a broad optical characterization of 2D TMDs focusing on the impact of defects and many-body effects. We first provided a thorough review on the reported optical signatures of defects in TMDs revealed by distinct optical techniques, underlining topics that still lack investigations. Subsequently, we initially probed distinct defects in these materials, both intentionally introduced to tune the TMDs properties as well as unintentionally emerged during the growth or aging processes. The studied engineered defects were based in the introduction of vanadium atoms as substitutional dopants in WS_2 and WSe_2 monolayers, which induces a room temperature ferromagnetic ordering in these samples. Therefore, we employed distinct linear and nonlinear optical techniques such as photoluminescence, resonant Raman, resonant four-wave mixing, resonant second-harmonic generation and differential reflectance spectroscopies to study the optical modifications in WS_2 and WSe_2 monolayers with respect to their vanadium concentrations. The V-doped WS_2 samples presented a splitting of the A exciton PL peak in two peaks — in which the lower (higher) energy PL peak is related to an optical transition to an unoccupied (occupied) band —, a blueshifting in the B exciton energy and no modification in the C exciton energy. V-doped WSe_2 samples also displayed the emergence of a lower energy PL peak under vanadium doping. However, this peak is associated with a vanadium mid gap state. We carried out magneto-optical experiments to study the valley Zeeman splitting of this defect peak. A noticeable magnetic response was observed, with an associate g-factor of -51.6 due to the significant magnetic moments of the vanadium states. This valley Zeeman effect was also studied in aged WS_2 and WSe_2 monolayers, which also showed a defect lower energy PL peak owing to multiple mid gap states induced by adsorbed defects. We performed magneto-optical measurements in these aged TMDs, revealing a strong spin polarization and a noticeable effective g-factor related to the defect states that we explained in terms of a spin-flip mechanism induced by external magnetic fields.

Subsequently, we performed a nano-optical investigation of grain boundaries, strain and edges defects in grown MoS_2 monolayers by tip-enhanced photoluminescence and Raman spectroscopies. We unveiled the nanometric aspect of the light emission in grain boundaries, showing an increased exciton population and a suppression of trion formation in these defective regions. Moreover, localized strain fields were probed and related to an expected thermal expansion coefficient and lattice constant mismatch between the monolayer and the substrate. Finally, two distinct MoS_2 samples presented different optical responses within a region of less than 50 nm of width at their edges. While one of them showed an enhanced and blueshifted emission at the edges due to defect passivation, the other sample displayed a redshifted PL corresponding to a frequency redshift in the E_{2g}

and 2LA Raman modes owing to a local strain associated with a topographic suspension of the edge.

To study many-body effects in 2D TMDs, we employed nonlinear optical experiments by using pulsed excitations. We demonstrated that a sub band gap pulsed excitation is able to induce an electron-hole plasma state in 2D WSe_2 and $MoSe_2$ samples, leading to a remarkable broadening of their light emission. Moreover, the high excitation densities generated in WSe_2 multilayers provoked an indirect to a direct band gap renormalization, which was responsible for a significant enhancement of the photoluminescence intensity in these multilayer samples. In the sequence, we mapped the electron-hole plasma photoluminescence of 2D TMD lateral and vertical heterostructures. An enhanced emission from the lateral heterojunctions and vertical heterostructures with respect to the individual TMDs was observed, which was accounted on a higher absorption at these interface regions. Lastly, second-harmonic generation imaging also showed an enhanced signal at the heterojunction of distinct TMD lateral heterostructures due to a coherent superposition between the second-harmonic emission from each TMD.

Therefore, this thesis presents important advances in the understanding of the role of distinct defects in the optical and magneto-optical properties of TMD monolayers as well as the response of 2D TMDs and their heterostructures under high excitation densities, providing an step toward their application in different optoelectronic and spintronic devices.

LIST OF PUBLICATIONS

- Sousa, F. B., Lafeta, L., Cadore, A. R., Sahoo, P. K., and Malard, L. M. (2021). Revealing atomically sharp interfaces of two-dimensional lateral heterostructures by second harmonic generation. *2D Materials*, 8(3), 035051.

- Rosa, B. L., Fujisawa, K., Santos, J. C., Zhang, T., Matos, M. J., Sousa, F. B., Barbosa, T. C., Lafeta, L., Ramos, S. L. L. M., Carvalho, B. R., Chacham, H., Neves, B. R. A., Terrones, M., and Malard, L. M. (2022). Investigation of spatially localized defects in synthetic WS_2 monolayers. *Physical Review B*, 106(11), 115301.

- Sousa, F. B., Perea-Causin, R., Hartmann, S., Lafetá, L., Rosa, B., Brem, S., Palekas, C., Reitzenstein, S., Hartschuh, A., Malic, E., and Malard, L. M. (2023). Ultrafast hot electron–hole plasma photoluminescence in two-dimensional semiconductors. *Nanoscale*, 15(15), 7154-7163.

- Sousa, F. B., Zheng, B., Liu, M., Resende, G. C., Zhou, D., Pimenta, M. A., Terrones, M., Crespi, V., and Malard, L. M. (2024). Effects of vanadium doping on the optical response and electronic structure of WS_2 monolayers. *Advanced Optical Materials*, DOI: 10.1002/adom.202400235 (accepted for publication).

- Palekar, C. C., Junior, P. E. F., Rosa, B., Sousa, F. B., Malard, L. M., Fabian, J., and Reitzenstein, S. (2023). Amplification of interlayer exciton emission in twisted $WSe_2/WSe_2/MoSe_2$ heterotrilayers. *arXiv preprint* arXiv:2311.02509.

- Sousa, F. B., Nadas, R. B., Martins, R., Barboza, A. P., Soares, J. S., Neves, B. R., Silvestre, I., Jorio, A., and Malard, L. M. (2024). Nano-optical investigation of grain boundaries, strain and edges in CVD grown MoS_2 monolayers. *arXiv preprint* arXiv:2401.11984.

- Sousa, F. B., Ames, A., Liu, M., Gastelois, P. L., Oliveira, V. A., Zhou, D., Matos, M. J. S., Chacham, H., Terrones, M., Teodoro, M. D., and Malard, L. M. (2024). Strong magneto-optical responses of an ensemble of defect-bound excitons in aged WS_2 and WSe_2 monolayers. *arXiv preprint* arXiv: 2404.04131.

- Sousa, F. B., et al. Giant valley Zeeman splitting in V-doped WSe_2 monolayers. To be published.

- Sousa, F. B., et al. Enhanced light emission in lateral $MoSe_2/WSe_2$ heterostructures in the electron-hole plasma regime. To be published.

- Sousa, F. B., et al. Optical spectroscopy studies of defects in atomically thin transition metal dichalcogenides. To be published.

- Menescal, F., Sousa, F. B., et al. Optical investigation of spatially inhomogeneous doping effects in vanadium doped WS_2 monolayers. To be published.

BIBLIOGRAPHY

1 Novoselov, K S, A K Geim, S V Morozov, D Jiang, M I Katsnelson, I V Grigorieva, S V Dubonos, and A A Firsov: *Two-dimensional gas of massless Dirac fermions in graphene*. Nature, 438(7065):197–200, 2005, ISSN 1476-4687. <https://doi.org/10.1038/nature04233>. Cited 2 times in pages 38 e 159.

2 Wallace, P R: *The Band Theory of Graphite*. Physical Review, 71(9):622–634, may 1947. <https://link.aps.org/doi/10.1103/PhysRev.71.622>. Cited in page 38.

3 Bolotin, K I, K J Sikes, Z Jiang, M Klima, G Fudenberg, J Hone, P Kim, and H L Stormer: *Ultrahigh electron mobility in suspended graphene*. Solid State Communications, 146(9):351–355, 2008, ISSN 0038-1098. <https://www.sciencedirect.com/science/article/pii/S0038109808001178>. Cited in page 38.

4 Morozov, S V, K S Novoselov, M I Katsnelson, F Schedin, D C Elias, J A Jaszczak, and A K Geim: *Giant Intrinsic Carrier Mobilities in Graphene and Its Bilayer*. Physical Review Letters, 100(1):16602, jan 2008. <https://link.aps.org/doi/10.1103/PhysRevLett.100.016602>. Cited in page 38.

5 Lee, Changgu, Xiaoding Wei, Jeffrey W Kysar, and James Hone: *Measurement of the Elastic Properties and Intrinsic Strength of Monolayer Graphene*. Science, 321(5887):385 LP – 388, jul 2008. <http://science.sciencemag.org/content/321/5887/385.abstract>. Cited in page 38.

6 Novoselov, K S, A K Geim, S V Morozov, D Jiang, Y Zhang, S V Dubonos, I V Grigorieva, and A A Firsov: *Electric Field Effect in Atomically Thin Carbon Films*. Science, 306(5696):666 LP – 669, oct 2004. <http://science.sciencemag.org/content/306/5696/666.abstract>. Cited in page 38.

7 Novoselov, K S, Z Jiang, Y Zhang, S V Morozov, H L Stormer, U Zeitler, J C Maan, G S Boebinger, P Kim, and A K Geim: *Room-Temperature Quantum Hall Effect in Graphene*. Science, 315(5817):1379 LP – 1379, mar 2007. <http://science.sciencemag.org/content/315/5817/1379.abstract>. Cited in page 38.

8 Novoselov, K S, D Jiang, F Schedin, T J Booth, V V Khotkevich, S V Morozov, and A K Geim: *Two-dimensional atomic crystals*. Proceedings of the National Academy of Sciences of the United States of America, 102(30):10451 LP – 10453, jul 2005. <http://www.pnas.org/content/102/30/10451.abstract>. Cited in page 38.

9 Dean, C R, A F Young, I Meric, C Lee, L Wang, S Sorgenfrei, K Watanabe, T Taniguchi, P Kim, K L Shepard, and J Hone: *Boron nitride substrates for high-quality graphene electronics*. Nature Nanotechnology, 5(10):722–726, 2010, ISSN 1748-3395. <https://doi.org/10.1038/nnano.2010.172>. Cited 2 times in pages 38 e 68.

10 Mak, Kin Fai, Changgu Lee, James Hone, Jie Shan, and Tony F. Heinz: *Atomically Thin* MoS_2*: A New Direct-Gap Semiconductor*. Phys. Rev. Lett., 105:136805, Sep 2010. <https://link.aps.org/doi/10.1103/PhysRevLett.105.136805>. Cited 4 times in pages 38, 40, 42 e 44.

11 Splendiani, Andrea, Liang Sun, Yuanbo Zhang, Tianshu Li, Jonghwan Kim, Chi Yung Chim, Giulia Galli, and Feng Wang: *Emerging Photoluminescence in Monolayer MoS2*. Nano Letters, 10(4):1271–1275, apr 2010, ISSN 1530-6984. <https://doi.org/10.1021/nl903868w>. Cited 6 times in pages 8, 38, 40, 42, 44 e 45.

12 Mak, Kin Fai, Keliang He, Jie Shan, and Tony F Heinz: *Control of valley polarization in monolayer MoS2 by optical helicity*. Nature Nanotechnology, 7(8):494–498, 2012, ISSN 1748-3395. <https://doi.org/10.1038/nnano.2012.96>. Cited 7 times in pages 9, 38, 47, 53, 55, 56 e 57.

13 Zeng, Hualing, Junfeng Dai, Wang Yao, Di Xiao, and Xiaodong Cui: *Valley polarization in MoS2 monolayers by optical pumping*. Nature Nanotechnology, 7(8):490–493, 2012, ISSN 1748-3395. <https://doi.org/10.1038/nnano.2012.95>. Cited 3 times in pages 38, 53 e 56.

14 Cao, Ting, Gang Wang, Wenpeng Han, Huiqi Ye, Chuanrui Zhu, Junren Shi, Qian Niu, Pingheng Tan, Enge Wang, Baoli Liu, and Ji Feng: *Valley-selective circular dichroism of monolayer molybdenum disulphide*. Nature Communications, 3(1):887, 2012, ISSN 2041-1723. <https://doi.org/10.1038/ncomms1882>. Cited 3 times in pages 38, 47 e 53.

15 Qiu, Diana Y, Felipe H da Jornada, and Steven G Louie: *Optical Spectrum of MoS_2: Many-Body Effects and Diversity of Exciton States*. Physical Review Letters, 111(21):216805, nov 2013. <https://link.aps.org/doi/10.1103/PhysRevLett.111.216805>. Cited 2 times in pages 38 e 47.

16 Chernikov, Alexey, Timothy C Berkelbach, Heather M Hill, Albert Rigosi, Yilei Li, Ozgur Burak Aslan, David R Reichman, Mark S Hybertsen, and Tony F Heinz: *Exciton Binding Energy and Nonhydrogenic Rydberg Series in Monolayer* WS_2. Physical Review Letters, 113(7):76802, aug 2014. <https://link.aps.org/doi/10.1103/PhysRevLett.113.076802>. Cited 4 times in pages 38, 39, 44 e 47.

17 He, Keliang, Nardeep Kumar, Liang Zhao, Zefang Wang, Kin Fai Mak, Hui Zhao, and Jie Shan: *Tightly Bound Excitons in Monolayer* WSe_2. Physical Review Letters, 113(2):26803, jul 2014. <https://link.aps.org/doi/10.1103/PhysRevLett.113.026803>. Cited 2 times in pages 38 e 47.

18 Ye, Ziliang, Ting Cao, Kevin O'Brien, Hanyu Zhu, Xiaobo Yin, Yuan Wang, Steven G Louie, and Xiang Zhang: *Probing excitonic dark states in single-layer tungsten disulphide*. Nature, 513(7517):214–218, 2014, ISSN 1476-4687. <https://doi.org/10.1038/nature13734>. Cited 2 times in pages 38 e 47.

19 Li, Yilei, Yi Rao, Kin Fai Mak, Yumeng You, Shuyuan Wang, Cory R Dean, and Tony F Heinz: *Probing Symmetry Properties of Few-Layer MoS2 and h-BN by Optical Second-Harmonic Generation*. Nano Letters, 13(7):3329–3333, jul 2013, ISSN 1530-6984. <https://doi.org/10.1021/nl401561r>. Cited 4 times in pages 38, 40, 94 e 164.

20 Malard, Leandro M., Thonimar V. Alencar, Ana Paula M. Barboza, Kin Fai Mak, and Ana M. de Paula: *Observation of intense second harmonic generation from* MoS_2 *atomic crystals*. Phys. Rev. B, 87:201401, May 2013. <https://link.aps.org/doi/10.1103/PhysRevB.87.201401>. Cited 8 times in pages 12, 38, 40, 94, 95, 110, 133 e 164.

21 Kumar, Nardeep, Sina Najmaei, Qiannan Cui, Frank Ceballos, Pulickel M. Ajayan, Jun Lou, and Hui Zhao: *Second harmonic microscopy of monolayer MoS_2*. Phys. Rev. B, 87:161403, Apr 2013. <https://link.aps.org/doi/10.1103/PhysRevB.87.161403>. Cited 4 times in pages 38, 40, 94 e 164.

22 Wang, Gang, Alexey Chernikov, Mikhail M Glazov, Tony F Heinz, Xavier Marie, Thierry Amand, and Bernhard Urbaszek: *Colloquium: Excitons in atomically thin transition metal dichalcogenides*. Reviews of Modern Physics, 90(2):21001, apr 2018. <https://link.aps.org/doi/10.1103/RevModPhys.90.021001>. Cited 5 times in pages 38, 45, 46, 47 e 105.

23 Mueller, Thomas and Ermin Malic: *Exciton Physics and Device Application of Two-Dimensional Transition Metal Dichalcogenide Semiconductors*. npj 2D Materials and Applications, 2(1):29, 2018, ISSN 2397-7132. <https://doi.org/10.1038/s41699-018-0074-2>. Cited 3 times in pages 38, 45 e 47.

24 Fox, Mark: *Optical Properties of Solids*, volume 2. Oxford University Press, 2010, ISBN 9780199573363. Cited 7 times in pages 8, 38, 45, 46, 47, 55 e 71.

25 Chichibu, S, T Azuhata, T Sota, and S Nakamura: *Spontaneous emission of localized excitons in InGaN single and multiquantum well structures*. Applied Physics Letters, 69(27):4188–4190, dec 1996, ISSN 0003-6951. <https://doi.org/10.1063/1.116981>. Cited 2 times in pages 38 e 47.

26 Chernikov, Alexey, Claudia Ruppert, Heather M Hill, Albert F Rigosi, and Tony F Heinz: *Population Inversion and Giant Bandgap Renormalization in Atomically Thin WS2 Layers*. Nature Photonics, 9(7):466–470, 2015, ISSN 1749-4893. <https://doi.org/10.1038/nphoton.2015.104>. Cited 5 times in pages 39, 45, 52, 144 e 151.

27 Jue, Wang, Ardelean Jenny, Bai Yusong, Steinhoff Alexander, Florian Matthias, Jahnke Frank, Xu Xiaodong, Kira Mackillo, Hone James, and Zhu X.-Y.: *Optical Generation of High Carrier Densities in 2D Semiconductor Heterobilayers*. Science Advances, 5(9):eaax0145, jul 2019. <https://doi.org/10.1126/sciadv.aax0145>. Cited 10 times in pages 8, 39, 52, 53, 144, 145, 146, 151, 155 e 161.

28 Yu, Yiling, Alexander W Bataller, Robert Younts, Yifei Yu, Guoqing Li, Alexander A Puretzky, David B Geohegan, Kenan Gundogdu, and Linyou Cao: *Room-Temperature Electron–Hole Liquid in Monolayer MoS2*. ACS Nano, 13(9):10351–10358, sep 2019, ISSN 1936-0851. <https://doi.org/10.1021/acsnano.9b04124>. Cited 9 times in pages 8, 39, 52, 53, 144, 145, 146, 148 e 153.

29 Choi, Wonbong, Nitin Choudhary, Gang Hee Han, Juhong Park, Deji Akinwande, and Young Hee Lee: *Recent development of two-dimensional transition metal dichalcogenides and their applications*. Materials Today, 20(3):116–130, 2017, ISSN 1369-7021. <https://www.sciencedirect.com/science/article/pii/S1369702116302917>. Cited in page 39.

30 Chakraborty, Suman Kumar, Baisali Kundu, Biswajeet Nayak, Saroj Prasad Dash, and Prasana Kumar Sahoo: *Challenges and opportunities in 2D heterostructures for electronic and optoelectronic devices*. iScience, 25(3):103942, 2022, ISSN 2589-0042. <https://www.sciencedirect.com/science/article/pii/S2589004222002127>. Cited 2 times in pages 39 e 43.

31 Liu, Fang: *Mechanical exfoliation of large area 2D materials from vdW crystals*. Progress in Surface Science, 96(2):100626, 2021, ISSN 0079-6816. <https://www.sciencedirect.com/science/article/pii/S0079681621000149>. Cited 2 times in pages 39 e 42.

32 Zhang, Yu, Yuyu Yao, Marshet Getaye Sendeku, Lei Yin, Xueying Zhan, Feng Wang, Zhenxing Wang, and Jun He: *Recent Progress in CVD Growth of 2D Transition Metal Dichalcogenides and Related Heterostructures*. Advanced Materials, 31(41):1901694, oct 2019, ISSN 0935-9648. <https://doi.org/10.1002/adma.201901694>. Cited 4 times in pages 39, 60, 67 e 106.

33 Aras, F Gonca, Alp Yilmaz, H Gunalp Tasdelen, Ayberk Ozden, Feridun Ay, Nihan Kosku Perkgoz, and Aydan Yeltik: *A review on recent advances of chemical vapor deposition technique for monolayer transition metal dichalcogenides (MX2: Mo, W; S, Se, Te)*. Materials Science in Semiconductor Processing, 148:106829, 2022, ISSN 1369-8001. <https://www.sciencedirect.com/science/article/pii/S1369800122003687>. Cited in page 39.

34 Lin, Zhong, Bruno R Carvalho, Ethan Kahn, Ruitao Lv, Rahul Rao, Humberto Terrones, Marcos A Pimenta, and Mauricio Terrones: *Defect engineering of two-dimensional transition metal dichalcogenides*. 2D Materials, 3(2):022002, apr 2016. Cited 10 times in pages 39, 43, 60, 61, 62, 63, 64, 105, 122 e 138.

35 Liang, Qijie, Qian Zhang, Xiaoxu Zhao, Meizhuang Liu, and Andrew T S Wee: *Defect Engineering of Two-Dimensional Transition-Metal Dichalcogenides: Applications, Challenges, and Opportunities*. ACS Nano, 15(2):2165–2181, feb 2021, ISSN 1936-0851. <https://doi.org/10.1021/acsnano.0c09666>. Cited 5 times in pages 39, 43, 60, 61 e 105.

36 Cheng, Y C, Z Y Zhu, W B Mi, Z B Guo, and U Schwingenschlögl: *Prediction of two-dimensional diluted magnetic semiconductors: Doped monolayer MoS_2 systems*. Physical Review B, 87(10):100401, mar 2013. <https://link.aps.org/doi/10.1103/PhysRevB.87.100401>. Cited 2 times in pages 39 e 66.

37 Ramasubramaniam, Ashwin and Doron Naveh: *Mn-doped monolayer MoS_2: An atomically thin dilute magnetic semiconductor*. Physical Review B, 87(19):195201, may 2013. <https://link.aps.org/doi/10.1103/PhysRevB.87.195201>. Cited 3 times in pages 39, 66 e 105.

38 Yue, Qu, Shengli Chang, Shiqiao Qin, and Jingbo Li: *Functionalization of monolayer MoS2 by substitutional doping: A first-principles study*. Physics Letters A, 377(19):1362–1367, 2013, ISSN 0375-9601. <https://www.sciencedirect.com/science/article/pii/S0375960113003198>. Cited 2 times in pages 39 e 66.

39 Mishra, Rohan, Wu Zhou, Stephen J Pennycook, Sokrates T Pantelides, and Juan Carlos Idrobo: *Long-range ferromagnetic ordering in manganese-doped two-dimensional dichalcogenides*. Physical Review B, 88(14):144409, oct 2013. <https://link.aps.org/doi/10.1103/PhysRevB.88.144409>. Cited 2 times in pages 39 e 66.

40 Zhou, Jiadong, Junhao Lin, Hunter Sims, Chongyun Jiang, Chunxiao Cong, John A Brehm, Zhaowei Zhang, Lin Niu, Yu Chen, Yao Zhou, Yanlong Wang, Fucai Liu, Chao Zhu, Ting Yu, Kazu Suenaga, Rohan Mishra, Sokrates T Pantelides, Zhen Gang Zhu, Weibo Gao, Zheng Liu, and Wu Zhou: *Synthesis of Co-Doped MoS2 Monolayers*

with Enhanced Valley Splitting. Advanced Materials, 32(11):1906536, mar 2020, ISSN 0935-9648. <https://doi.org/10.1002/adma.201906536>. Cited 8 times in pages 10, 12, 39, 75, 76, 87, 88 e 119.

41 Li, Qi, Xiaoxu Zhao, Longjiang Deng, Zhongtai Shi, Sheng Liu, Qilin Wei, Linbo Zhang, Yingchun Cheng, Li Zhang, Haipeng Lu, Weibo Gao, Wei Huang, Cheng Wei Qiu, Gang Xiang, Stephen John Pennycook, Qihua Xiong, Kian Ping Loh, and Bo Peng: *Enhanced Valley Zeeman Splitting in Fe-Doped Monolayer MoS2*. ACS Nano, 14(4):4636–4645, apr 2020, ISSN 1936-0851. <https://doi.org/10.1021/acsnano.0c00291>. Cited 7 times in pages 12, 39, 75, 87, 88, 119 e 136.

42 Yun, Seok Joon, Dinh Loc Duong, Doan Manh Ha, Kirandeep Singh, Thanh Luan Phan, Wooseon Choi, Young Min Kim, and Young Hee Lee: *Ferromagnetic Order at Room Temperature in Monolayer WSe2 Semiconductor via Vanadium Dopant*. Advanced Science, 7(9):1903076, may 2020, ISSN 2198-3844. <https://doi.org/10.1002/advs.201903076>. Cited 6 times in pages 10, 39, 66, 67, 105 e 116.

43 Pham, Yen Thi Hai, Mingzu Liu, Valery Ortiz Jimenez, Zhuohang Yu, Vijaysankar Kalappattil, Fu Zhang, Ke Wang, Teague Williams, Mauricio Terrones, and Manh Huong Phan: *Tunable Ferromagnetism and Thermally Induced Spin Flip in Vanadium-Doped Tungsten Diselenide Monolayers at Room Temperature*. Advanced Materials, 32(45):2003607, nov 2020, ISSN 0935-9648. <https://doi.org/10.1002/adma.202003607>. Cited 7 times in pages 10, 39, 63, 66, 67, 105 e 116.

44 Zhang, Fu, Boyang Zheng, Amritanand Sebastian, David H Olson, Mingzu Liu, Kazunori Fujisawa, Yen Thi Hai Pham, Valery Ortiz Jimenez, Vijaysankar Kalappattil, Leixin Miao, Tianyi Zhang, Rahul Pendurthi, Yu Lei, Ana Laura Elías, Yuanxi Wang, Nasim Alem, Patrick E Hopkins, Saptarshi Das, Vincent H Crespi, Manh Huong Phan, and Mauricio Terrones: *Monolayer Vanadium-Doped Tungsten Disulfide: A Room-Temperature Dilute Magnetic Semiconductor*. Advanced Science, 7(24):2001174, dec 2020, ISSN 2198-3844. <https://doi.org/10.1002/advs.202001174>. Cited 9 times in pages 10, 39, 63, 66, 67, 75, 105, 106 e 108.

45 Shen, Dingyi, Bei Zhao, Zucheng Zhang, Hongmei Zhang, Xiangdong Yang, Ziwei Huang, Bailing Li, Rong Song, Yejun Jin, Ruixia Wu, Bo Li, Jia Li, and Xidong Duan: *Synthesis of Group VIII Magnetic Transition-Metal-Doped Monolayer MoSe2*. ACS Nano, 16(7):10623–10631, jul 2022, ISSN 1936-0851. <https://doi.org/10.1021/acsnano.2c02214>. Cited in page 39.

46 Geim, A K and I V Grigorieva: *Van der Waals heterostructures*. Nature, 499(7459):419–425, 2013, ISSN 1476-4687. <https://doi.org/10.1038/nature12385>. Cited 5 times in pages 10, 39, 60, 67 e 68.

47 Novoselov, K S, A Mishchenko, A Carvalho, and A H Castro Neto: *2D materials and van der Waals heterostructures*. Science, 353(6298):aac9439, jul 2016. <http://science.sciencemag.org/content/353/6298/aac9439.abstract>. Cited 3 times in pages 39, 60 e 67.

48 Liu, Yuan, Nathan O Weiss, Xidong Duan, Hung Chieh Cheng, Yu Huang, and Xiangfeng Duan: *Van der Waals heterostructures and devices*. Nature Reviews Materials, 1(9):16042, 2016, ISSN 2058-8437. <https://doi.org/10.1038/natrevmats.2016.42>. Cited 3 times in pages 39, 60 e 67.

49 Li, Ming Yang, Chang Hsiao Chen, Yumeng Shi, and Lain Jong Li: *Heterostructures based on two-dimensional layered materials and their potential applications.* Materials Today, 19(6):322–335, 2016, ISSN 1369-7021. <https://www.sciencedirect.com/science/article/pii/S1369702115003776>. Cited 4 times in pages 39, 60, 67 e 69.

50 Zhang, Xin Quan, Chin Hao Lin, Yu Wen Tseng, Kuan Hua Huang, and Yi Hsien Lee: *Synthesis of Lateral Heterostructures of Semiconducting Atomic Layers.* Nano Letters, 15(1):410–415, jan 2015, ISSN 1530-6984. <https://doi.org/10.1021/nl503744f>. Cited 4 times in pages 40, 70, 163 e 165.

51 Kozawa, Daichi, Rajeev Kumar, Alexandra Carvalho, Kiran Kumar Amara, Weijie Zhao, Shunfeng Wang, Minglin Toh, Ricardo M Ribeiro, A H Castro Neto, Kazunari Matsuda, and Goki Eda: *Photocarrier relaxation pathway in two-dimensional semiconducting transition metal dichalcogenides.* Nature Communications, 5(1):4543, 2014, ISSN 2041-1723. <https://doi.org/10.1038/ncomms5543>. Cited 3 times in pages 8, 40 e 48.

52 Corro, Elena del, Humberto Terrones, Ana Elias, Cristiano Fantini, Simin Feng, Minh An Nguyen, Thomas E Mallouk, Mauricio Terrones, and Marcos A Pimenta: *Excited Excitonic States in 1L, 2L, 3L, and Bulk WSe2 Observed by Resonant Raman Spectroscopy.* ACS Nano, 8(9):9629–9635, sep 2014, ISSN 1936-0851. <https://doi.org/10.1021/nn504088g>. Cited 4 times in pages 11, 40, 79 e 80.

53 Carvalho, Bruno R, Yuanxi Wang, Sandro Mignuzzi, Debdulal Roy, Mauricio Terrones, Cristiano Fantini, Vincent H Crespi, Leandro M Malard, and Marcos A Pimenta: *Intervalley scattering by acoustic phonons in two-dimensional MoS2 revealed by double-resonance Raman spectroscopy.* Nature Communications, 8(1):14670, 2017, ISSN 2041-1723. <https://doi.org/10.1038/ncomms14670>. Cited 3 times in pages 40, 139 e 141.

54 Selig, Malte, Gunnar Berghäuser, Archana Raja, Philipp Nagler, Christian Schüller, Tony F Heinz, Tobias Korn, Alexey Chernikov, Ermin Malic, and Andreas Knorr: *Excitonic linewidth and coherence lifetime in monolayer transition metal dichalcogenides.* Nature Communications, 7(1):13279, 2016, ISSN 2041-1723. <https://doi.org/10.1038/ncomms13279>. Cited in page 40.

55 Selig, Malte, Gunnar Berghäuser, Marten Richter, Rudolf Bratschitsch, Andreas Knorr, and Ermin Malic: *Dark and bright exciton formation, thermalization, and photoluminescence in monolayer transition metal dichalcogenides.* 2D Materials, 5(3):35017, 2018, ISSN 2053-1583. <http://dx.doi.org/10.1088/2053-1583/aabea3>. Cited 2 times in pages 40 e 148.

56 Malard, Leandro M, Lucas Lafeta, Renan S Cunha, Rafael Nadas, Andreij Gadelha, Luiz Gustavo Cançado, and Ado Jorio: *Studying 2D materials with advanced Raman spectroscopy: CARS, SRS and TERS.* Physical Chemistry Chemical Physics, 23(41):23428–23444, 2021, ISSN 1463-9076. <http://dx.doi.org/10.1039/D1CP03240B>. Cited 3 times in pages 40, 83 e 132.

57 Kim, Youngbum and Jeongyong Kim: *Near-field optical imaging and spectroscopy of 2D-TMDs.* Nanophotonics, 10(13):3397–3415, 2021. Cited 3 times in pages 40, 83 e 132.

58 Shao, Jiaqi and Weitao Su: *Tip-enhanced nanoscopy of two-dimensional transition metal dichalcogenides: progress and perspectives*. Nanoscale, 14(46):17119–17133, 2022, ISSN 2040-3364. <http://dx.doi.org/10.1039/D2NR04864G>. Cited 3 times in pages 40, 83 e 132.

59 Kwon, Soyeong, Jin Myung Kim, Peiwen J Ma, Weilin Guan, and SungWoo Nam: *Near-Field Nano-Optical Imaging of van der Waals Materials*. Advanced Physics Research, n/a(n/a):2300009, may 2023, ISSN 2751-1200. <https://doi.org/10.1002/apxr.202300009>. Cited 3 times in pages 40, 83 e 132.

60 Wen, Xinglin, Zibo Gong, and Dehui Li: *Nonlinear optics of two-dimensional transition metal dichalcogenides*. InfoMat, 1(3):317–337, sep 2019, ISSN 2567-3165. <https://doi.org/10.1002/inf2.12024>. Cited in page 40.

61 Lafeta, Lucas, Aurea Corradi, Tianyi Zhang, Ethan Kahn, Ismail Bilgin, Bruno R Carvalho, Swastik Kar, Mauricio Terrones, and Leandro M Malard: *Second- and third-order optical susceptibilities across excitons states in 2D monolayer transition metal dichalcogenides*. 2D Materials, 8(3):35010, 2021, ISSN 2053-1583. <http://dx.doi.org/10.1088/2053-1583/abeed4>. Cited 5 times in pages 13, 40, 96, 97 e 106.

62 Radisavljevic, B, A Radenovic, J Brivio, V Giacometti, and A Kis: *Single-layer MoS2 transistors*. Nature Nanotechnology, 6(3):147–150, 2011, ISSN 1748-3395. <https://doi.org/10.1038/nnano.2010.279>. Cited 2 times in pages 8 e 42.

63 Tang, Qing and De en Jiang: *Stabilization and Band-Gap Tuning of the 1T-MoS2 Monolayer by Covalent Functionalization*. Chemistry of Materials, 27(10):3743–3748, may 2015, ISSN 0897-4756. <https://doi.org/10.1021/acs.chemmater.5b00986>. Cited 2 times in pages 8 e 43.

64 Joensen, Per, R F Frindt, and S.Roy Morrison: *Single-layer MoS2*. Materials Research Bulletin, 21(4):457–461, 1986, ISSN 0025-5408. <https://www.sciencedirect.com/science/article/pii/0025540886900115>. Cited in page 42.

65 Gao, Enlai, Shao Zhen Lin, Zhao Qin, Markus J Buehler, Xi Qiao Feng, and Zhiping Xu: *Mechanical exfoliation of two-dimensional materials*. Journal of the Mechanics and Physics of Solids, 115:248–262, 2018, ISSN 0022-5096. <https://www.sciencedirect.com/science/article/pii/S0022509618300280>. Cited in page 42.

66 Huang, Yuan, Yu Hao Pan, Rong Yang, Li Hong Bao, Lei Meng, Hai Lan Luo, Yong Qing Cai, Guo Dong Liu, Wen Juan Zhao, Zhang Zhou, Liang Mei Wu, Zhi Li Zhu, Ming Huang, Li Wei Liu, Lei Liu, Peng Cheng, Ke Hui Wu, Shi Bing Tian, Chang Zhi Gu, You Guo Shi, Yan Feng Guo, Zhi Gang Cheng, Jiang Ping Hu, Lin Zhao, Guan Hua Yang, Eli Sutter, Peter Sutter, Ye Liang Wang, Wei Ji, Xing Jiang Zhou, and Hong Jun Gao: *Universal mechanical exfoliation of large-area 2D crystals*. Nature Communications, 11(1):2453, 2020, ISSN 2041-1723. <https://doi.org/10.1038/s41467-020-16266-w>. Cited in page 42.

67 Li, Yangang, Guizhi Kuang, Zhongjie Jiao, Lin Yao, and Ruihuan Duan: *Recent progress on the mechanical exfoliation of 2D transition metal dichalcogenides*. Materials Research Express, 9(12):122001, 2022, ISSN 2053-1591. <https://dx.doi.org/10.1088/2053-1591/aca6c6>. Cited in page 42.

68 Liu, Keng Ku, Wenjing Zhang, Yi Hsien Lee, Yu Chuan Lin, Mu Tung Chang, Ching Yuan Su, Chia Seng Chang, Hai Li, Yumeng Shi, Hua Zhang, Chao Sung Lai, and Lain Jong Li: *Growth of Large-Area and Highly Crystalline MoS2 Thin Layers on Insulating Substrates*. Nano Letters, 12(3):1538–1544, mar 2012, ISSN 1530-6984. <https://doi.org/10.1021/nl2043612>. Cited in page 43.

69 Zhan, Yongjie, Zheng Liu, Sina Najmaei, Pulickel M Ajayan, and Jun Lou: *Large-Area Vapor-Phase Growth and Characterization of MoS2 Atomic Layers on a SiO2 Substrate*. Small, 8(7):966–971, apr 2012, ISSN 1613-6810. <https://doi.org/10.1002/smll.201102654>. Cited in page 43.

70 Najmaei, Sina, Zheng Liu, Wu Zhou, Xiaolong Zou, Gang Shi, Sidong Lei, Boris I Yakobson, Juan Carlos Idrobo, Pulickel M Ajayan, and Jun Lou: *Vapour phase growth and grain boundary structure of molybdenum disulphide atomic layers*. Nature Materials, 12(8):754–759, 2013, ISSN 1476-4660. <https://doi.org/10.1038/nmat3673>. Cited in page 43.

71 Zande, Arend M van der, Pinshane Y Huang, Daniel A Chenet, Timothy C Berkelbach, YuMeng You, Gwan Hyoung Lee, Tony F Heinz, David R Reichman, David A Muller, and James C Hone: *Grains and grain boundaries in highly crystalline monolayer molybdenum disulphide*. Nature Materials, 12(6):554–561, 2013, ISSN 1476-4660. <https://doi.org/10.1038/nmat3633>. Cited 8 times in pages 10, 43, 64, 76, 77, 132, 133 e 134.

72 Zhang, Yi, Tay Rong Chang, Bo Zhou, Yong Tao Cui, Hao Yan, Zhongkai Liu, Felix Schmitt, James Lee, Rob Moore, Yulin Chen, Hsin Lin, Horng Tay Jeng, Sung Kwan Mo, Zahid Hussain, Arun Bansil, and Zhi Xun Shen: *Direct observation of the transition from indirect to direct bandgap in atomically thin epitaxial MoSe2*. Nature Nanotechnology, 9(2):111–115, 2014, ISSN 1748-3395. <https://doi.org/10.1038/nnano.2013.277>. Cited in page 43.

73 Xenogiannopoulou, E, P Tsipas, K E Aretouli, D Tsoutsou, S A Giamini, C Bazioti, G P Dimitrakopulos, Ph. Komninou, S Brems, C Huyghebaert, I P Radu, and A Dimoulas: *High-quality, large-area MoSe2 and MoSe2/Bi2Se3 heterostructures on AlN(0001)/Si(111) substrates by molecular beam epitaxy*. Nanoscale, 7(17):7896–7905, 2015, ISSN 2040-3364. <http://dx.doi.org/10.1039/C4NR06874B>. Cited in page 43.

74 Liu, H J, L Jiao, L Xie, F Yang, J L Chen, W K Ho, C L Gao, J F Jia, X D Cui, and M H Xie: *Molecular-beam epitaxy of monolayer and bilayer WSe 2 : a scanning tunneling microscopy/spectroscopy study and deduction of exciton binding energy*. 2D Materials, 2(3):34004, 2015, ISSN 2053-1583. <http://dx.doi.org/10.1088/2053-1583/2/3/034004>. Cited in page 43.

75 Gutiérrez, Humberto R., Nestor Perea-López, Ana Laura Elías, Ayse Berkdemir, Bei Wang, Ruitao Lv, Florentino López-Urías, Vincent H. Crespi, Humberto Terrones, and Mauricio Terrones: *Extraordinary Room-Temperature Photoluminescence in Triangular WS_2 Monolayers*. Nano Letters, 13(8):3447–3454, 2013. PMID: 23194096. Cited in page 43.

76 Cong, Chunxiao, Jingzhi Shang, Xing Wu, Bingchen Cao, Namphung Peimyoo, Caiyu Qiu, Litao Sun, and Ting Yu: *Synthesis and Optical Properties of Large-Area*

Single-Crystalline 2D Semiconductor WS_2 Monolayer from Chemical Vapor Deposition. Advanced Optical Materials, 2(2):131–136, 2014. Cited in page 43.

77 Nan, Haiyan, Zilu Wang, Wenhui Wang, Zheng Liang, Yan Lu, Qian Chen, Daowei He, Pingheng Tan, Feng Miao, Xinran Wang, Jinlan Wang, and Zhenhua Ni: *Strong Photoluminescence Enhancement of MoS_2 through Defect Engineering and Oxygen Bonding*. ACS Nano, 8(6):5738–5745, 2014. PMID: 24836121. Cited 2 times in pages 43 e 75.

78 Liu, Hongwei, Junpeng Lu, Kenneth Ho, Zhenliang Hu, Zhiya Dang, Alexandra Carvalho, Hui Ru Tan, Eng Soon Tok, and Chorng Haur Sow: *Fluorescence Concentric Triangles: A Case of Chemical Heterogeneity in WS_2 Atomic Monolayer*. Nano Letters, 16(9):5559–5567, 2016. PMID: 27479127. Cited in page 43.

79 Kim, Min Su, Seok Joon Yun, Yongjun Lee, Changwon Seo, Gang Hee Han, Ki Kang Kim, Young Hee Lee, and Jeongyong Kim: *Biexciton Emission from Edges and Grain Boundaries of Triangular WS_2 Monolayers*. ACS Nano, 10(2):2399–2405, 2016. PMID: 26758415. Cited 3 times in pages 43, 76 e 133.

80 McCreary, Kathleen M., Aubrey T. Hanbicki, Simranjeet Singh, Roland K. Kawakami, Glenn G. Jernigan, Masa Ishigami, Amy Ng, Todd H. Brintlinger, Rhonda M. Stroud, and Berend T. Jonker: *The Effect of Preparation Conditions on Raman and Photoluminescence of Monolayer WS_2*. Scientific Reports, 6(1):35154, 2016. Cited 2 times in pages 43 e 106.

81 Lin, Yung Chang, Shisheng Li, Hannu Pekka Komsa, Li Jen Chang, Arkady V. Krasheninnikov, Goki Eda, and Kazu Suenaga: *Revealing the Atomic Defects of WS_2 Governing Its Distinct Optical Emissions*. Advanced Functional Materials, 28(4):1704210, 2018. Cited in page 43.

82 Cai, Shuang, Weiwei Zhao, Amina Zafar, Zhangting Wu, Yi Tao, Kedong Bi, Zhiyong Wei, Zhenhua Ni, and Yunfei Chen: *Photoluminescence characterization of the grain boundary thermal stability in chemical vapor deposition grown WS_2*. Materials Research Express, 4(10):106202, oct 2017. Cited in page 43.

83 Carozo, Victor, Yuanxi Wang, Kazunori Fujisawa, Bruno R. Carvalho, Amber McCreary, Simin Feng, Zhong Lin, Chanjing Zhou, Néstor Perea-López, Ana Laura Elías, Bernd Kabius, Vincent H. Crespi, and Mauricio Terrones: *Optical identification of sulfur vacancies: Bound excitons at the edges of monolayer tungsten disulfide*. Science Advances, 3(4), 2017. Cited 5 times in pages 10, 43, 62, 74 e 75.

84 Li, Tianshu and Giulia Galli: *Electronic Properties of MoS2 Nanoparticles*. The Journal of Physical Chemistry C, 111(44):16192–16196, nov 2007, ISSN 1932-7447. <https://doi.org/10.1021/jp075424v>. Cited in page 43.

85 Lebègue, S and O Eriksson: *Electronic structure of two-dimensional crystals from ab initio theory*. Physical Review B, 79(11):115409, mar 2009. <https://link.aps.org/doi/10.1103/PhysRevB.79.115409>. Cited in page 43.

86 Pei, Jiajie, Jiong Yang, Tanju Yildirim, Han Zhang, and Yuerui Lu: *Many-Body Complexes in 2D Semiconductors*. Advanced Materials, 31(2):1706945, jan 2019, ISSN 0935-9648. <https://doi.org/10.1002/adma.201706945>. Cited 2 times in pages 43 e 45.

87 Tongay, Sefaattin, Jian Zhou, Can Ataca, Kelvin Lo, Tyler S Matthews, Jingbo Li, Jeffrey C Grossman, and Junqiao Wu: *Thermally Driven Crossover from Indirect toward Direct Bandgap in 2D Semiconductors: MoSe2 versus MoS2.* Nano Letters, 12(11):5576–5580, nov 2012, ISSN 1530-6984. <https://doi.org/10.1021/nl302584w>. Cited in page 44.

88 Zhao, Weijie, Zohreh Ghorannevis, Leiqiang Chu, Minglin Toh, Christian Kloc, Ping Heng Tan, and Goki Eda: *Evolution of Electronic Structure in Atomically Thin Sheets of WS2 and WSe2.* ACS Nano, 7(1):791–797, jan 2013, ISSN 1936-0851. <https://doi.org/10.1021/nn305275h>. Cited 2 times in pages 44 e 108.

89 Yun, Won Seok, S W Han, Soon Cheol Hong, In Gee Kim, and J D Lee: *Thickness and strain effects on electronic structures of transition metal dichalcogenides: 2H-MX_2 semiconductors (M = Mo, W; X = S, Se, Te).* Physical Review B, 85(3):33305, jan 2012. <https://link.aps.org/doi/10.1103/PhysRevB.85.033305>. Cited in page 44.

90 Sundaram, R S, M Engel, A Lombardo, R Krupke, A C Ferrari, Ph. Avouris, and M Steiner: *Electroluminescence in Single Layer MoS2.* Nano Letters, 13(4):1416–1421, apr 2013, ISSN 1530-6984. <https://doi.org/10.1021/nl400516a>. Cited in page 44.

91 Lopez-Sanchez, Oriol, Dominik Lembke, Metin Kayci, Aleksandra Radenovic, and Andras Kis: *Ultrasensitive photodetectors based on monolayer MoS2.* Nature Nanotechnology, 8(7):497–501, 2013, ISSN 1748-3395. <https://doi.org/10.1038/nnano.2013.100>. Cited in page 44.

92 Britnell, L, R M Ribeiro, A Eckmann, R Jalil, B D Belle, A Mishchenko, Y. J. Kim, R V Gorbachev, T Georgiou, S V Morozov, A N Grigorenko, A K Geim, C Casiraghi, A H Castro Neto, and K S Novoselov: *Strong Light-Matter Interactions in Heterostructures of Atomically Thin Films.* Science, 340(6138):1311 LP – 1314, jun 2013. <http://science.sciencemag.org/content/340/6138/1311.abstract>. Cited in page 44.

93 Fontana, Marcio, Tristan Deppe, Anthony K Boyd, Mohamed Rinzan, Amy Y Liu, Makarand Paranjape, and Paola Barbara: *Electron-hole transport and photovoltaic effect in gated MoS2 Schottky junctions.* Scientific Reports, 3(1):1634, 2013, ISSN 2045-2322. <https://doi.org/10.1038/srep01634>. Cited in page 44.

94 Zhu, Z Y, Y C Cheng, and U Schwingenschlögl: *Giant spin-orbit-induced spin splitting in two-dimensional transition-metal dichalcogenide semiconductors.* Physical Review B, 84(15):153402, oct 2011. <https://link.aps.org/doi/10.1103/PhysRevB.84.153402>. Cited 7 times in pages 9, 44, 47, 53, 54, 55 e 58.

95 Kormányos, Andor, Guido Burkard, Martin Gmitra, Jaroslav Fabian, Viktor Zólyomi, Neil D Drummond, and Vladimir Fal'ko: *$k \cdot p$ theory for two-dimensional transition metal dichalcogenide semiconductors.* 2D Materials, 2(2):22001, 2015, ISSN 2053-1583. <https://dx.doi.org/10.1088/2053-1583/2/2/022001>. Cited 4 times in pages 8, 44, 53 e 54.

96 Ramasubramaniam, Ashwin: *Large excitonic effects in monolayers of molybdenum and tungsten dichalcogenides.* Physical Review B, 86(11):115409, sep 2012. <https://link.aps.org/doi/10.1103/PhysRevB.86.115409>. Cited in page 47.

97 Cheiwchanchamnangij, Tawinan and Walter R L Lambrecht: *Quasiparticle band structure calculation of monolayer, bilayer, and bulk MoS_2*. Physical Review B, 85(20):205302, may 2012. <https://link.aps.org/doi/10.1103/PhysRevB.85.205302>. Cited in page 47.

98 Xiao, Di, Gui Bin Liu, Wanxiang Feng, Xiaodong Xu, and Wang Yao: *Coupled Spin and Valley Physics in Monolayers of* MoS_2 *and Other Group-VI Dichalcogenides*. Physical Review Letters, 108(19):196802, may 2012. <https://link.aps.org/doi/10.1103/PhysRevLett.108.196802>. Cited 6 times in pages 9, 47, 53, 54, 56 e 68.

99 You, Yumeng, Xiao Xiao Zhang, Timothy C Berkelbach, Mark S Hybertsen, David R Reichman, and Tony F Heinz: *Observation of biexcitons in monolayer WSe2*. Nature Physics, 11(6):477–481, 2015, ISSN 1745-2481. <https://doi.org/10.1038/nphys3324>. Cited in page 48.

100 Mak, Kin Fai, Keliang He, Changgu Lee, Gwan Hyoung Lee, James Hone, Tony F Heinz, and Jie Shan: *Tightly bound trions in monolayer MoS2*. Nature Materials, 12(3):207–211, 2013, ISSN 1476-4660. <https://doi.org/10.1038/nmat3505>. Cited in page 48.

101 Ross, Jason S, Sanfeng Wu, Hongyi Yu, Nirmal J Ghimire, Aaron M Jones, Grant Aivazian, Jiaqiang Yan, David G Mandrus, Di Xiao, Wang Yao, and Xiaodong Xu: *Electrical control of neutral and charged excitons in a monolayer semiconductor*. Nature Communications, 4(1):1474, 2013, ISSN 2041-1723. <https://doi.org/10.1038/ncomms2498>. Cited in page 48.

102 Klingshirn, C. Berlin, Heidelberg. Cited 3 times in pages 49, 50 e 51.

103 Pelant, Ivan and Jan Valenta: *Luminescence Spectroscopy of Semiconductors*, feb 2012, ISBN 9780199588336. <https://doi.org/10.1093/acprof:oso/9780199588336.001.0001>. Cited 4 times in pages 49, 50, 51 e 145.

104 Matsuzaki, Ryosuke, Haruka Soma, Kanae Fukuoka, Kanako Kodama, Akifumi Asahara, Tohru Suemoto, Yutaka Adachi, and Takashi Uchino: *Purely excitonic lasing in ZnO microcrystals: Temperature-induced transition between exciton-exciton and exciton-electron scattering*. Physical Review B, 96(12):125306, sep 2017. <https://link.aps.org/doi/10.1103/PhysRevB.96.125306>. Cited in page 50.

105 Weng, Guoen, Jiao Tian, Shiming Chen, Juanjuan Xue, Jiyu Yan, Xiaobo Hu, Shaoqiang Chen, Ziqiang Zhu, and Junhao Chu: *Giant reduction of the random lasing threshold in CH3NH3PbBr3 perovskite thin films by using a patterned sapphire substrate*. Nanoscale, 11(22):10636–10645, 2019, ISSN 2040-3364. <http://dx.doi.org/10.1039/C9NR00863B>. Cited in page 50.

106 Liu, Zhen, Qiuyu Shang, Chun Li, Liyun Zhao, Yan Gao, Qi Li, Jie Chen, Shuai Zhang, Xinfeng Liu, Yingshuang Fu, and Qing Zhang: *Temperature-dependent photoluminescence and lasing properties of CsPbBr3 nanowires*. Applied Physics Letters, 114(10):101902, mar 2019, ISSN 0003-6951. <https://doi.org/10.1063/1.5082759>. Cited in page 50.

107 Du, Wenna, Shuai Zhang, Jia Shi, Jie Chen, Zhiyong Wu, Yang Mi, Zhixiong Liu, Yuanzheng Li, Xinyu Sui, Rui Wang, Xiaohui Qiu, Tom Wu, Yunfeng Xiao, Qing Zhang, and Xinfeng Liu: *Strong Exciton–Photon Coupling and Lasing Behavior in All-Inorganic CsPbBr3 Micro/Nanowire Fabry-Pérot Cavity.* ACS Photonics, 5(5):2051–2059, may 2018. <https://doi.org/10.1021/acsphotonics.7b01593>. Cited in page 50.

108 Klingshirn, Claus, Robert Hauschild, Johannes Fallert, and Heinz Kalt: *Room-temperature stimulated emission of ZnO: Alternatives to excitonic lasing.* Physical Review B, 75(11):115203, mar 2007. <https://link.aps.org/doi/10.1103/PhysRevB.75.115203>. Cited in page 51.

109 Versteegh, Marijn A M, Daniël Vanmaekelbergh, and Jaap I Dijkhuis: *Room-Temperature Laser Emission of ZnO Nanowires Explained by Many-Body Theory.* Physical Review Letters, 108(15):157402, apr 2012. <https://link.aps.org/doi/10.1103/PhysRevLett.108.157402>. Cited in page 51.

110 Röder, Robert, Themistoklis P H Sidiropoulos, Christian Tessarek, Silke Christiansen, Rupert F Oulton, and Carsten Ronning: *Ultrafast Dynamics of Lasing Semiconductor Nanowires.* Nano Letters, 15(7):4637–4643, jul 2015, ISSN 1530-6984. <https://doi.org/10.1021/acs.nanolett.5b01271>. Cited in page 51.

111 Röder, Robert and Carsten Ronning: *Review on the dynamics of semiconductor nanowire lasers.* Semiconductor Science and Technology, 33(3):33001, 2018, ISSN 0268-1242. <https://dx.doi.org/10.1088/1361-6641/aaa7be>. Cited in page 51.

112 Weng, Guoen, Jiao Tian, Shengjie Chen, Jiyu Yan, Hanbing Zhang, Yuejun Liu, Chunhu Zhao, Xiaobo Hu, Xianjia Luo, Jiahua Tao, Shaoqiang Chen, Ziqiang Zhu, Junhao Chu, and Hidefumi Akiyama: *Electron–Hole Plasma Lasing Dynamics in CsPbClmBr3-m Microplate Lasers.* ACS Photonics, 8(3):787–797, mar 2021. <https://doi.org/10.1021/acsphotonics.0c01512>. Cited in page 51.

113 Finkelstein, Gleb, Hadas Shtrikman, and Israel Bar-Joseph: *Optical Spectroscopy of a Two-Dimensional Electron Gas near the Metal-Insulator Transition.* Physical Review Letters, 74(6):976–979, feb 1995. <https://link.aps.org/doi/10.1103/PhysRevLett.74.976>. Cited in page 52.

114 Lozovik, Yu. E and O L Berman: *Phase Transitions in a System of Two Coupled Quantum Wells.* Journal of Experimental and Theoretical Physics Letters, 64(8):573–579, 1996, ISSN 1090-6487. <https://doi.org/10.1134/1.567264>. Cited in page 52.

115 Kaindl, R A, M A Carnahan, D Hägele, R Lövenich, and D S Chemla: *Ultrafast Terahertz Probes of Transient Conducting and Insulating Phases in an Electron–Hole Gas.* Nature, 423(6941):734–738, 2003, ISSN 1476-4687. <https://doi.org/10.1038/nature01676>. Cited in page 52.

116 Leon, S Ben-Tabou de and B Laikhtman: *Mott Transition, Biexciton Crossover, and Spin Ordering in the Exciton Gas in Quantum Wells.* Physical Review B, 67(23):235315, jun 2003. <https://link.aps.org/doi/10.1103/PhysRevB.67.235315>. Cited in page 52.

117 Koch, Stephan W, Walter Hoyer, Mackillo Kira, and Vladimir S Filinov: *Exciton Ionization in Semiconductors.* physica status solidi (b), 238(3):404–410, aug 2003, ISSN 0370-1972. <https://doi.org/10.1002/pssb.200303153>. Cited in page 52.

118 Huber, Rupert, Robert A Kaindl, Ben A Schmid, and Daniel S Chemla: *Broadband Terahertz Study of Excitonic Resonances in the High-Density Regime in* $GaAsAl_xGa_{1-x}As$ *Quantum Wells*. Physical Review B, 72(16):161314, oct 2005. <https://link.aps.org/doi/10.1103/PhysRevB.72.161314>. Cited in page 52.

119 Kappei, L, J Szczytko, F Morier-Genoud, and B Deveaud: *Direct Observation of the Mott Transition in an Optically Excited Semiconductor Quantum Well*. Physical Review Letters, 94(14):147403, apr 2005. <https://link.aps.org/doi/10.1103/PhysRevLett.94.147403>. Cited in page 52.

120 Amo, A, M D Martín, L Viña, A I Toropov, and K S Zhuravlev: *Photoluminescence Dynamics in GaAs Along an Optically Induced Mott Transition*. Journal of Applied Physics, 101(8):81717, apr 2007, ISSN 0021-8979. <https://doi.org/10.1063/1.2722786>. Cited in page 52.

121 Stern, M, V Garmider, V Umansky, and I Bar-Joseph: *Mott Transition of Excitons in Coupled Quantum Wells*. Physical Review Letters, 100(25):256402, jun 2008. <https://link.aps.org/doi/10.1103/PhysRevLett.100.256402>. Cited in page 52.

122 Nikolaev, V V and M E Portnoi: *Theory of the Excitonic Mott Transition in Quasi-Two-Dimensional Systems*. Superlattices and Microstructures, 43(5):460–464, 2008, ISSN 0749-6036. <https://www.sciencedirect.com/science/article/pii/S0749603607002121>. Cited in page 52.

123 Manzke, G, D Semkat, and H Stolz: *Mott Transition of Excitons in GaAs-GaAlAs Quantum Wells*. New Journal of Physics, 14(9):95002, 2012, ISSN 1367-2630. <http://dx.doi.org/10.1088/1367-2630/14/9/095002>. Cited in page 52.

124 Rossbach, G, J Levrat, G Jacopin, M Shahmohammadi, J. F. Carlin, J. D. Ganière, R Butté, B Deveaud, and N Grandjean: *High-Temperature Mott Transition in Wide-Band-Gap Semiconductor Quantum Wells*. Physical Review B, 90(20):201308, nov 2014. <https://link.aps.org/doi/10.1103/PhysRevB.90.201308>. Cited in page 52.

125 Kiršanskė, Gabija, Petru Tighineanu, Raphaël S Daveau, Javier Miguel-Sánchez, Peter Lodahl, and Søren Stobbe: *Observation of the Exciton Mott Transition in the Photoluminescence of Coupled Quantum Wells*. Physical Review B, 94(15):155438, oct 2016. <https://link.aps.org/doi/10.1103/PhysRevB.94.155438>. Cited in page 52.

126 Steinhoff, A, M Florian, M Rösner, G Schönhoff, T O Wehling, and F Jahnke: *Exciton Fission in Monolayer Transition Metal Dichalcogenide Semiconductors*. Nature Communications, 8(1):1166, 2017, ISSN 2041-1723. <https://doi.org/10.1038/s41467-017-01298-6>. Cited 2 times in pages 52 e 146.

127 Rustagi, Avinash and Alexander F Kemper: *Theoretical Phase Diagram for the Room-Temperature Electron–Hole Liquid in Photoexcited Quasi-Two-Dimensional Monolayer MoS2*. Nano Letters, 18(1):455–459, jan 2018, ISSN 1530-6984. <https://doi.org/10.1021/acs.nanolett.7b04377>. Cited in page 52.

128 Meckbach, L, T Stroucken, and S W Koch: *Giant Excitation Induced Bandgap Renormalization in TMDC Monolayers*. Applied Physics Letters, 112(6):61104, feb 2018, ISSN 0003-6951. <https://doi.org/10.1063/1.5017069>. Cited in page 52.

129 Bataller, Alexander W, Robert A Younts, Avinash Rustagi, Yiling Yu, Hossein Ardekani, Alexander Kemper, Linyou Cao, and Kenan Gundogdu: *Dense Electron–Hole Plasma Formation and Ultralong Charge Lifetime in Monolayer MoS2 via Material Tuning*. Nano Letters, 19(2):1104–1111, feb 2019, ISSN 1530-6984. <https://doi.org/10.1021/acs.nanolett.8b04408>. Cited 4 times in pages 52, 146, 151 e 162.

130 Yiling, Yu, Yu Yifei, Li Guoqing, Puretzky Alexander A., Geohegan David B., and Cao Linyou: *Giant Enhancement of Exciton Diffusivity in Two-Dimensional Semiconductors*. Science Advances, 6(51):eabb4823, jul 2020. <https://doi.org/10.1126/sciadv.abb4823>. Cited in page 52.

131 Wilmington, R L, H Ardekani, A Rustagi, A Bataller, A F Kemper, R A Younts, and K Gundogdu: *Fermi Liquid Theory Sheds Light on Hot Electron-Hole Liquid in* $1L - MoS_2$. Physical Review B, 103(7):75416, feb 2021. <https://link.aps.org/doi/10.1103/PhysRevB.103.075416>. Cited 2 times in pages 52 e 147.

132 Siday, Thomas, Fabian Sandner, Samuel Brem, Martin Zizlsperger, Raul Perea-Causin, Felix Schiegl, Svenja Nerreter, Markus Plankl, Philipp Merkl, Fabian Mooshammer, Markus A Huber, Ermin Malic, and Rupert Huber: *Ultrafast Nanoscopy of High-Density Exciton Phases in WSe2*. Nano Letters, 22(6):2561–2568, mar 2022, ISSN 1530-6984. <https://doi.org/10.1021/acs.nanolett.1c04741>. Cited 3 times in pages 52, 146 e 152.

133 Arp, Trevor B, Dennis Pleskot, Vivek Aji, and Nathaniel M Gabor: *Electron–Hole Liquid in a Van Der Waals Heterostructure Photocell at Room Temperature*. Nature Photonics, 13(4):245–250, 2019, ISSN 1749-4893. <https://doi.org/10.1038/s41566-019-0349-y>. Cited 2 times in pages 52 e 152.

134 Pekh, P L, P V Ratnikov, and A P Silin: *Electron-Hole Liquid in Monolayer Transition Metal Dichalcogenide Heterostructures*. JETP Letters, 111(2):90–95, 2020, ISSN 1090-6487. <https://doi.org/10.1134/S0021364020020101>. Cited in page 52.

135 Wang, Jue, Qianhui Shi, En Min Shih, Lin Zhou, Wenjing Wu, Yusong Bai, Daniel Rhodes, Katayun Barmak, James Hone, CoryR. Dean, and X. Y. Zhu: *Diffusivity Reveals Three Distinct Phases of Interlayer Excitons in* $MoSe_2/WSe_2$ *Heterobilayers*. Physical Review Letters, 126(10):106804, mar 2021. <https://link.aps.org/doi/10.1103/PhysRevLett.126.106804>. Cited in page 52.

136 Ratnikov, Pavel V: *Charge-Separated Electron-Hole Liquid in Transition Metal Dichalcogenide Heterostructures*. Physics Letters A, 444:128235, 2022, ISSN 0375-9601. <https://www.sciencedirect.com/science/article/pii/S0375960122003176>. Cited in page 52.

137 Lohof, F, A Steinhoff, M Florian, M Lorke, D Erben, F Jahnke, and C Gies: *Prospects and Limitations of Transition Metal Dichalcogenide Laser Gain Materials*. Nano Letters, 19(1):210–217, jan 2019, ISSN 1530-6984. <https://doi.org/10.1021/acs.nanolett.8b03729>. Cited in page 52.

138 Xiao, Di, Wang Yao, and Qian Niu: *Valley-Contrasting Physics in Graphene: Magnetic Moment and Topological Transport*. Physical Review Letters, 99(23):236809, dec 2007. <https://link.aps.org/doi/10.1103/PhysRevLett.99.236809>. Cited in page 53.

139 Rycerz, A, J Tworzydło, and C W J Beenakker: *Valley filter and valley valve in graphene*. Nature Physics, 3(3):172–175, 2007, ISSN 1745-2481. <https://doi.org/10.1038/nphys547>. Cited in page 53.

140 Yao, Wang, Di Xiao, and Qian Niu: *Valley-dependent optoelectronics from inversion symmetry breaking*. Physical Review B, 77(23):235406, jun 2008. <https://link.aps.org/doi/10.1103/PhysRevB.77.235406>. Cited in page 53.

141 Zhang, Fan, Jeil Jung, Gregory A Fiete, Qian Niu, and Allan H MacDonald: *Spontaneous Quantum Hall States in Chirally Stacked Few-Layer Graphene Systems*. Physical Review Letters, 106(15):156801, apr 2011. <https://link.aps.org/doi/10.1103/PhysRevLett.106.156801>. Cited in page 53.

142 Kośmider, K and J Fernández-Rossier: *Electronic properties of the MoS_2-WS_2 heterojunction*. Physical Review B, 87(7):75451, feb 2013. <https://link.aps.org/doi/10.1103/PhysRevB.87.075451>. Cited 3 times in pages 53, 54 e 68.

143 Song, Yang and Hanan Dery: *Transport Theory of Monolayer Transition-Metal Dichalcogenides through Symmetry*. Physical Review Letters, 111(2):26601, jul 2013. <https://link.aps.org/doi/10.1103/PhysRevLett.111.026601>. Cited in page 56.

144 Liu, Yanping, Yuanji Gao, Siyu Zhang, Jun He, Juan Yu, and Zongwen Liu: *Valleytronics in transition metal dichalcogenides materials*. Nano Research, 12(11):2695–2711, 2019, ISSN 1998-0000. <https://doi.org/10.1007/s12274-019-2497-2>. Cited in page 56.

145 Ahn, Ethan C: *2D materials for spintronic devices*. npj 2D Materials and Applications, 4(1):17, 2020, ISSN 2397-7132. <https://doi.org/10.1038/s41699-020-0152-0>. Cited in page 56.

146 Li, Yilei, Jonathan Ludwig, Tony Low, Alexey Chernikov, Xu Cui, Ghidewon Arefe, Young Duck Kim, Arend M van der Zande, Albert Rigosi, Heather M Hill, Suk Hyun Kim, James Hone, Zhiqiang Li, Dmitry Smirnov, and Tony F Heinz: *Valley Splitting and Polarization by the Zeeman Effect in Monolayer* $MoSe_2$. Physical Review Letters, 113(26):266804, dec 2014. <https://link.aps.org/doi/10.1103/PhysRevLett.113.266804>. Cited 6 times in pages 57, 58, 59, 87, 124 e 127.

147 MacNeill, David, Colin Heikes, Kin Fai Mak, Zachary Anderson, Andor Kormányos, Viktor Zólyomi, Jiwoong Park, and Daniel C Ralph: *Breaking of Valley Degeneracy by Magnetic Field in Monolayer* $MoSe_2$. Physical Review Letters, 114(3):37401, jan 2015. <https://link.aps.org/doi/10.1103/PhysRevLett.114.037401>. Cited 6 times in pages 57, 58, 59, 87, 124 e 127.

148 Srivastava, Ajit, Meinrad Sidler, Adrien V Allain, Dominik S Lembke, Andras Kis, and A Imamoğlu: *Valley Zeeman effect in elementary optical excitations of monolayer WSe2*. Nature Physics, 11(2):141–147, 2015, ISSN 1745-2481. <https://doi.org/10.1038/nphys3203>. Cited 6 times in pages 57, 58, 59, 87, 124 e 127.

149 Aivazian, G, Zhirui Gong, Aaron M Jones, Rui Lin Chu, J Yan, D G Mandrus, Chuanwei Zhang, David Cobden, Wang Yao, and X Xu: *Magnetic control of valley pseudospin in monolayer WSe2*. Nature Physics, 11(2):148–152, 2015, ISSN 1745-2481. <https://doi.org/10.1038/nphys3201>. Cited 7 times in pages 12, 57, 58, 59, 87, 124 e 127.

150 Griffiths, David J.: *Introduction to Quantum Mechanics (2nd Edition)*. Pearson Prentice Hall, April 2004, ISBN 0131118927. <https://doi.org/10.1017/9781316995433>. Cited in page 57.

151 Stier, Andreas V, Kathleen M McCreary, Berend T Jonker, Junichiro Kono, and Scott A Crooker: *Exciton diamagnetic shifts and valley Zeeman effects in monolayer WS2 and MoS2 to 65Tesla*. Nature Communications, 7(1):10643, 2016, ISSN 2041-1723. <https://doi.org/10.1038/ncomms10643>. Cited 4 times in pages 9, 58, 59 e 87.

152 Plechinger, Gerd, Philipp Nagler, Ashish Arora, Andrés Granados del Águila, Mariana V Ballottin, Tobias Frank, Philipp Steinleitner, Martin Gmitra, Jaroslav Fabian, Peter C M Christianen, Rudolf Bratschitsch, Christian Schüller, and Tobias Korn: *Excitonic Valley Effects in Monolayer WS2 under High Magnetic Fields*. Nano Letters, 16(12):7899–7904, dec 2016, ISSN 1530-6984. <https://doi.org/10.1021/acs.nanolett.6b04171>. Cited 2 times in pages 59 e 87.

153 Kuhnert, Jan, Arash Rahimi-Iman, and Wolfram Heimbrodt: *Magneto photoluminescence measurements of tungsten disulphide monolayers*. Journal of Physics: Condensed Matter, 29(8):08LT02, 2017, ISSN 0953-8984. <https://dx.doi.org/10.1088/1361-648X/aa55a9>. Cited 2 times in pages 59 e 87.

154 Nagler, Philipp, Mariana V Ballottin, Anatolie A Mitioglu, Mikhail V Durnev, Takashi Taniguchi, Kenji Watanabe, Alexey Chernikov, Christian Schüller, Mikhail M Glazov, Peter C.M. Christianen, and Tobias Korn: *Zeeman Splitting and Inverted Polarization of Biexciton Emission in Monolayer* WS_2. Physical Review Letters, 121(5):57402, aug 2018. <https://link.aps.org/doi/10.1103/PhysRevLett.121.057402>. Cited 3 times in pages 59, 87 e 88.

155 Barbone, Matteo, Alejandro R. P. Montblanch, Dhiren M Kara, Carmen Palacios-Berraquero, Alisson R Cadore, Domenico De Fazio, Benjamin Pingault, Elaheh Mostaani, Han Li, Bin Chen, Kenji Watanabe, Takashi Taniguchi, Sefaattin Tongay, Gang Wang, Andrea C Ferrari, and Mete Atatüre: *Charge-tuneable biexciton complexes in monolayer WSe2*. Nature Communications, 9(1):3721, 2018, ISSN 2041-1723. <https://doi.org/10.1038/s41467-018-05632-4>. Cited 2 times in pages 59 e 87.

156 Liu, Gui Bin, Wen Yu Shan, Yugui Yao, Wang Yao, and Di Xiao: *Three-band tight-binding model for monolayers of group-VIB transition metal dichalcogenides*. Physical Review B, 88(8):85433, aug 2013. <https://link.aps.org/doi/10.1103/PhysRevB.88.085433>. Cited in page 59.

157 Woźniak, Tomasz, Paulo E Faria Junior, Gotthard Seifert, Andrey Chaves, and Jens Kunstmann: *Exciton g factors of van der Waals heterostructures from first-principles calculations*. Physical Review B, 101(23):235408, jun 2020. <https://link.aps.org/doi/10.1103/PhysRevB.101.235408>. Cited in page 59.

158 Deilmann, Thorsten, Peter Krüger, and Michael Rohlfing: *Ab Initio Studies of Exciton g Factors: Monolayer Transition Metal Dichalcogenides in Magnetic Fields*. Physical Review Letters, 124(22):226402, jun 2020. <https://link.aps.org/doi/10.1103/PhysRevLett.124.226402>. Cited in page 59.

159 Bloch, Felix: *Über die Quantenmechanik der Elektronen in Kristallgittern*. Zeitschrift für Physik, 52(7):555–600, 1929, ISSN 0044-3328. <https://doi.org/10.1007/BF01339455>. Cited in page 60.

160 Wilson, Alan Herries and Paul Adrien Maurice Dirac: *The theory of electronic semi-conductors*. Proceedings of the Royal Society of London. Series A, Containing Papers of a Mathematical and Physical Character, 133(822):458–491, oct 1931. <https://doi.org/10.1098/rspa.1931.0162>. Cited in page 60.

161 Riordan, M and L Hoddeson: *The origins of the pn junction*. IEEE Spectrum, 34(6):46–51, 1997, ISSN 1939-9340 VO - 34. Cited in page 60.

162 Shockley, W: *The Theory of p-n Junctions in Semiconductors and p-n Junction Transistors*. Bell System Technical Journal, 28(3):435–489, jul 1949, ISSN 0005-8580. <https://doi.org/10.1002/j.1538-7305.1949.tb03645.x>. Cited in page 60.

163 Tudor Jenkins: *A brief history of ... semiconductors*. Physics Education, 40(5):430, 2005, ISSN 0031-9120. <https://dx.doi.org/10.1088/0031-9120/40/5/002>. Cited in page 60.

164 Queisser, Hans J and Eugene E Haller: *Defects in Semiconductors: Some Fatal, Some Vital*. Science, 281(5379):945–950, aug 1998. <https://doi.org/10.1126/science.281.5379.945>. Cited in page 60.

165 Lee, Young Hee: *Is it possible to create magnetic semiconductors that function at room temperature?* Science, 382(6668):eadl0823, oct 2023. <https://doi.org/10.1126/science.adl0823>. Cited 3 times in pages 60, 66 e 105.

166 Ortiz Jimenez, Valery, Yen Thi Hai Pham, Da Zhou, Mingzu Liu, Florence Ann Nugera, Vijaysankar Kalappattil, Tatiana Eggers, Khang Hoang, Dinh Loc Duong, Mauricio Terrones, Humberto Rodriguez Gutiérrez, and Manh Huong Phan: *Transition Metal Dichalcogenides: Making Atomic-Level Magnetism Tunable with Light at Room Temperature*. Advanced Science, n/a(n/a):2304792, dec 2023, ISSN 2198-3844. <https://doi.org/10.1002/advs.202304792>. Cited 4 times in pages 60, 66, 105 e 116.

167 Addou, Rafik, Luigi Colombo, and Robert M Wallace: *Surface Defects on Natural MoS2*. ACS Applied Materials & Interfaces, 7(22):11921–11929, jun 2015, ISSN 1944-8244. <https://doi.org/10.1021/acsami.5b01778>. Cited in page 60.

168 Wang, Shanshan, Alex Robertson, and Jamie H Warner: *Atomic structure of defects and dopants in 2D layered transition metal dichalcogenides*. Chemical Society Reviews, 47(17):6764–6794, 2018, ISSN 0306-0012. <http://dx.doi.org/10.1039/C8CS00236C>. Cited in page 60.

169 Zhou, Wu, Xiaolong Zou, Sina Najmaei, Zheng Liu, Yumeng Shi, Jing Kong, Jun Lou, Pulickel M Ajayan, Boris I Yakobson, and Juan Carlos Idrobo: *Intrinsic Structural Defects in Monolayer Molybdenum Disulfide*. Nano Letters, 13(6):2615–2622, jun 2013, ISSN 1530-6984. <https://doi.org/10.1021/nl4007479>. Cited 7 times in pages 9, 10, 62, 64, 65, 132 e 133.

170 Mitterreiter, Elmar, Bruno Schuler, Ana Micevic, Daniel Hernangómez-Pérez, Katja Barthelmi, Katherine A Cochrane, Jonas Kiemle, Florian Sigger, Julian Klein, Edward Wong, Edward S Barnard, Kenji Watanabe, Takashi Taniguchi, Michael Lorke, Frank Jahnke, Johnathan J Finley, Adam M Schwartzberg, Diana Y Qiu, Sivan Refaely-Abramson, Alexander W Holleitner, Alexander Weber-Bargioni, and Christoph Kastl: *The role of chalcogen vacancies for atomic defect emission in MoS2*. Nature Communications,

12(1):3822, 2021, ISSN 2041-1723. <https://doi.org/10.1038/s41467-021-24102-y>. Cited 7 times in pages 10, 62, 63, 74, 75, 122 e 127.

171 Cavallini, Massimiliano and Denis Gentili: *Atomic Vacancies in Transition Metal Dichalcogenides: Properties, Fabrication, and Limits*. ChemPlusChem, 87(3):e202100562, mar 2022, ISSN 2192-6506. <https://doi.org/10.1002/cplu.202100562>. Cited in page 62.

172 Schuler, Bruno, Diana Y Qiu, Sivan Refaely-Abramson, Christoph Kastl, Christopher T Chen, Sara Barja, Roland J Koch, D Frank Ogletree, Shaul Aloni, Adam M Schwartzberg, Jeffrey B Neaton, Steven G Louie, and Alexander Weber-Bargioni: *Large Spin-Orbit Splitting of Deep In-Gap Defect States of Engineered Sulfur Vacancies in Monolayer* WS_2. Physical Review Letters, 123(7):76801, aug 2019. <https://link.aps.org/doi/10.1103/PhysRevLett.123.076801>. Cited in page 62.

173 Mitterreiter, Elmar, Bruno Schuler, Katherine A Cochrane, Ursula Wurstbauer, Alexander Weber-Bargioni, Christoph Kastl, and Alexander W Holleitner: *Atomistic Positioning of Defects in Helium Ion Treated Single-Layer MoS2*. Nano Letters, 20(6):4437–4444, jun 2020, ISSN 1530-6984. <https://doi.org/10.1021/acs.nanolett.0c01222>. Cited in page 62.

174 Klein, J, M Lorke, M Florian, F Sigger, L Sigl, S Rey, J Wierzbowski, J Cerne, K Müller, E Mitterreiter, P Zimmermann, T Taniguchi, K Watanabe, U Wurstbauer, M Kaniber, M Knap, R Schmidt, J J Finley, and A W Holleitner: *Site-selectively generated photon emitters in monolayer MoS2 via local helium ion irradiation*. Nature Communications, 10(1):2755, 2019, ISSN 2041-1723. <https://doi.org/10.1038/s41467-019-10632-z>. Cited in page 62.

175 Schuler, Bruno, Katherine A Cochrane, Christoph Kastl, Edward S Barnard, Edward Wong, Nicholas J Borys, Adam M Schwartzberg, D Frank Ogletree, F Javier García de Abajo, and Alexander Weber-Bargioni: *Electrically driven photon emission from individual atomic defects in monolayer WS2*. Science Advances, 6(38):eabb5988, sep 2020. <https://doi.org/10.1126/sciadv.abb5988>. Cited in page 62.

176 Lin, Yu Chuan, Riccardo Torsi, David B Geohegan, Joshua A Robinson, and Kai Xiao: *Controllable Thin-Film Approaches for Doping and Alloying Transition Metal Dichalcogenides Monolayers*. Advanced Science, 8(9):2004249, may 2021, ISSN 2198-3844. <https://doi.org/10.1002/advs.202004249>. Cited 5 times in pages 9, 62, 63, 64 e 80.

177 Loh, Leyi, Zhepeng Zhang, Michel Bosman, and Goki Eda: *Substitutional doping in 2D transition metal dichalcogenides*. Nano Research, 14(6):1668–1681, 2021, ISSN 1998-0000. <https://doi.org/10.1007/s12274-020-3013-4>. Cited 3 times in pages 62, 63 e 122.

178 Rosa, Bárbara L T, Kazunori Fujisawa, Joyce C C Santos, Tianyi Zhang, Matheus J S Matos, Frederico B Sousa, Tiago C Barbosa, Lucas Lafeta, Sérgio L L M Ramos, Bruno R Carvalho, Helio Chacham, Bernardo R A Neves, Mauricio Terrones, and Leandro M Malard: *Investigation of spatially localized defects in synthetic* WS_2 *monolayers*. Physical Review B, 106(11):115301, sep 2022. <https://link.aps.org/doi/10.1103/PhysRevB.106.115301>. Cited 7 times in pages 10, 63, 64, 65, 76, 106 e 133.

179 Lu, Ang Yu, Hanyu Zhu, Jun Xiao, Chih Piao Chuu, Yimo Han, Ming Hui Chiu, Chia Chin Cheng, Chih Wen Yang, Kung Hwa Wei, Yiming Yang, Yuan Wang, Dimosthenis Sokaras, Dennis Nordlund, Peidong Yang, David A Muller, Mei Yin Chou, Xiang Zhang, and Lain Jong Li: *Janus monolayers of transition metal dichalcogenides.* Nature Nanotechnology, 12(8):744–749, 2017, ISSN 1748-3395. <https://doi.org/10.1038/nnano.2017.100>. Cited in page 63.

180 Islam, Muhammad R, Narae Kang, Udai Bhanu, Hari P Paudel, Mikhail Erementchouk, Laurene Tetard, Michael N Leuenberger, and Saiful I Khondaker: *Tuning the electrical property via defect engineering of single layer MoS2 by oxygen plasma.* Nanoscale, 6(17):10033–10039, 2014, ISSN 2040-3364. <http://dx.doi.org/10.1039/C4NR02142H>. Cited in page 63.

181 Kang, Narae, Hari P Paudel, Michael N Leuenberger, Laurene Tetard, and Saiful I Khondaker: *Photoluminescence Quenching in Single-Layer MoS2 via Oxygen Plasma Treatment.* The Journal of Physical Chemistry C, 118(36):21258–21263, sep 2014, ISSN 1932-7447. <https://doi.org/10.1021/jp506964m>. Cited in page 63.

182 Hu, Zhenliang, Jose Avila, Xinyun Wang, Jin Feng Leong, Qi Zhang, Yanpeng Liu, Maria C Asensio, Junpeng Lu, Alexandra Carvalho, Chorng Haur Sow, and Antonio Helio Castro Neto: *The Role of Oxygen Atoms on Excitons at the Edges of Monolayer WS2.* Nano Letters, 19(7):4641–4650, jul 2019, ISSN 1530-6984. <https://doi.org/10.1021/acs.nanolett.9b01670>. Cited 5 times in pages 63, 65, 75, 139 e 140.

183 Ataca, C and S Ciraci: *Functionalization of Single-Layer MoS2 Honeycomb Structures.* The Journal of Physical Chemistry C, 115(27):13303–13311, jul 2011, ISSN 1932-7447. <https://doi.org/10.1021/jp2000442>. Cited in page 63.

184 He, Jiangang, Kechen Wu, Rongjian Sa, Qiaohong Li, and Yongqin Wei: *Magnetic properties of nonmetal atoms absorbed MoS2 monolayers.* Applied Physics Letters, 96(8):82504, feb 2010, ISSN 0003-6951. <https://doi.org/10.1063/1.3318254>. Cited in page 63.

185 Dolui, Kapildeb, Ivan Rungger, Chaitanya Das Pemmaraju, and Stefano Sanvito: *Possible doping strategies for MoS_2 monolayers: An ab initio study.* Physical Review B, 88(7):75420, aug 2013. <https://link.aps.org/doi/10.1103/PhysRevB.88.075420>. Cited in page 63.

186 Majd, Zahra Ghasemi, Seyed Fardin Taghizadeh, Peiman Amiri, and Behroz Vaseghi: *Half-metallic properties of transition metals adsorbed on WS2 monolayer: A first-principles study.* Journal of Magnetism and Magnetic Materials, 481:129–135, 2019, ISSN 0304-8853. <https://www.sciencedirect.com/science/article/pii/S0304885318322959>. Cited in page 63.

187 Rogers, Christopher, Dodd Gray, Nate Bogdanowicz, and Hideo Mabuchi: *Laser annealing for radiatively broadened* $MoSe_2$ *grown by chemical vapor deposition.* Physical Review Materials, 2(9):94003, sep 2018. <https://link.aps.org/doi/10.1103/PhysRevMaterials.2.094003>. Cited in page 63.

188 Venanzi, Tommaso, Himani Arora, Artur Erbe, Alexej Pashkin, Stephan Winnerl, Manfred Helm, and Harald Schneider: *Exciton localization in MoSe2 monolayers*

induced by adsorbed gas molecules. Applied Physics Letters, 114(17):172106, may 2019, ISSN 0003-6951. <https://doi.org/10.1063/1.5094118>. Cited in page 63.

189 Xu, Xuejun, Lihui Li, Mingming Yang, Qinglin Guo, Ying Wang, Xiaoli Li, Xiujuan Zhuang, and Baolai Liang: *Localized state effect and exciton dynamics for monolayer WS2*. Optics Express, 29(4):5856–5866, 2021. <https://opg.optica.org/oe/abstract.cfm?URI=oe-29-4-5856>. Cited 4 times in pages 63, 75, 122 e 127.

190 Cadiz, F, E Courtade, C Robert, G Wang, Y Shen, H Cai, T Taniguchi, K Watanabe, H Carrere, D Lagarde, M Manca, T Amand, P Renucci, S Tongay, X Marie, and B Urbaszek: *Excitonic Linewidth Approaching the Homogeneous Limit in* MoS_2*-Based van der Waals Heterostructures*. Physical Review X, 7(2):21026, may 2017. <https://link.aps.org/doi/10.1103/PhysRevX.7.021026>. Cited in page 63.

191 Azizi, Amin, Xiaolong Zou, Peter Ercius, Zhuhua Zhang, Ana Laura Elías, Néstor Perea-López, Greg Stone, Mauricio Terrones, Boris I Yakobson, and Nasim Alem: *Dislocation motion and grain boundary migration in two-dimensional tungsten disulphide*. Nature Communications, 5(1):4867, 2014, ISSN 2041-1723. <https://doi.org/10.1038/ncomms5867>. Cited 2 times in pages 64 e 133.

192 Karvonen, Lasse, Antti Säynätjoki, Mikko J Huttunen, Anton Autere, Babak Amirsolaimani, Shisheng Li, Robert A Norwood, Nasser Peyghambarian, Harri Lipsanen, Goki Eda, Khanh Kieu, and Zhipei Sun: *Rapid visualization of grain boundaries in monolayer MoS2 by multiphoton microscopy*. Nature Communications, 8(1):15714, 2017, ISSN 2041-1723. <https://doi.org/10.1038/ncomms15714>. Cited 7 times in pages 10, 64, 76, 77, 80, 133 e 134.

193 Carvalho, Bruno R, Yuanxi Wang, Kazunori Fujisawa, Tianyi Zhang, Ethan Kahn, Ismail Bilgin, Pulickel M Ajayan, Ana M de Paula, Marcos A Pimenta, Swastik Kar, Vincent H Crespi, Mauricio Terrones, and Leandro M Malard: *Nonlinear Dark-Field Imaging of One-Dimensional Defects in Monolayer Dichalcogenides*. Nano Letters, 20(1):284–291, jan 2020, ISSN 1530-6984. <https://doi.org/10.1021/acs.nanolett.9b03795>. Cited in page 64.

194 Rong, Youmin, Kuang He, Mercè Pacios, Alex W Robertson, Harish Bhaskaran, and Jamie H Warner: *Controlled Preferential Oxidation of Grain Boundaries in Monolayer Tungsten Disulfide for Direct Optical Imaging*. ACS Nano, 9(4):3695–3703, apr 2015, ISSN 1936-0851. <https://doi.org/10.1021/acsnano.5b00852>. Cited in page 64.

195 Yang, Guanhua, Yan Shao, Jiebin Niu, Xiaolei Ma, Congyan Lu, Wei Wei, Xichen Chuai, Jiawei Wang, Jingchen Cao, Hao Huang, Guangwei Xu, Xuewen Shi, Zhuoyu Ji, Nianduan Lu, Di Geng, Jing Qi, Yun Cao, Zhongliu Liu, Liwei Liu, Yuan Huang, Lei Liao, Weiqi Dang, Zhengwei Zhang, Yuan Liu, Xidong Duan, Jiezhi Chen, Zhiqiang Fan, Xiangwei Jiang, Yeliang Wang, Ling Li, Hong Jun Gao, Xiangfeng Duan, and Ming Liu: *Possible Luttinger liquid behavior of edge transport in monolayer transition metal dichalcogenide crystals*. Nature Communications, 11(1):659, 2020, ISSN 2041-1723. <https://doi.org/10.1038/s41467-020-14383-0>. Cited 2 times in pages 10 e 65.

196 Deng, Shikai, Anirudha V Sumant, and Vikas Berry: *Strain engineering in two-dimensional nanomaterials beyond graphene*. Nano Today, 22:14–35, 2018, ISSN 1748-0132. <https://www.sciencedirect.com/science/article/pii/S1748013217306345>. Cited 2 times in pages 65 e 137.

197 Peng, Zhiwei, Xiaolin Chen, Yulong Fan, David J Srolovitz, and Dangyuan Lei: *Strain engineering of 2D semiconductors and graphene: from strain fields to band-structure tuning and photonic applications.* Light: Science & Applications, 9(1):190, 2020, ISSN 2047-7538. <https://doi.org/10.1038/s41377-020-00421-5>. Cited in page 65.

198 Li, Zhiwei, Yawei Lv, Liwang Ren, Jia Li, Lingan Kong, Yujia Zeng, Quanyang Tao, Ruixia Wu, Huifang Ma, Bei Zhao, Di Wang, Weiqi Dang, Keqiu Chen, Lei Liao, Xidong Duan, Xiangfeng Duan, and Yuan Liu: *Efficient strain modulation of 2D materials via polymer encapsulation.* Nature Communications, 11(1):1151, 2020, ISSN 2041-1723. <https://doi.org/10.1038/s41467-020-15023-3>. Cited 6 times in pages 11, 65, 76, 77, 78 e 80.

199 Tomasz Dietl: *Ferromagnetic semiconductors.* Semiconductor Science and Technology, 17(4):377, 2002, ISSN 0268-1242. <https://dx.doi.org/10.1088/0268-1242/17/4/310>. Cited in page 66.

200 Dietl, Tomasz: *A ten-year perspective on dilute magnetic semiconductors and oxides.* Nature Materials, 9(12):965–974, 2010, ISSN 1476-4660. <https://doi.org/10.1038/nmat2898>. Cited in page 66.

201 Dietl, Tomasz and Hideo Ohno: *Dilute ferromagnetic semiconductors: Physics and spintronic structures.* Reviews of Modern Physics, 86(1):187–251, mar 2014. <https://link.aps.org/doi/10.1103/RevModPhys.86.187>. Cited 2 times in pages 66 e 105.

202 Bonilla, Manuel, Sadhu Kolekar, Yujing Ma, Horacio Coy Diaz, Vijaysankar Kalappattil, Raja Das, Tatiana Eggers, Humberto R Gutierrez, Manh Huong Phan, and Matthias Batzill: *Strong room-temperature ferromagnetism in VSe2 monolayers on van der Waals substrates.* Nature Nanotechnology, 13(4):289–293, 2018, ISSN 1748-3395. <https://doi.org/10.1038/s41565-018-0063-9>. Cited in page 66.

203 O'Hara, Dante J, Tiancong Zhu, Amanda H Trout, Adam S Ahmed, Yunqiu Kelly Luo, Choong Hee Lee, Mark R Brenner, Siddharth Rajan, Jay A Gupta, David W McComb, and Roland K Kawakami: *Room Temperature Intrinsic Ferromagnetism in Epitaxial Manganese Selenide Films in the Monolayer Limit.* Nano Letters, 18(5):3125–3131, may 2018, ISSN 1530-6984. <https://doi.org/10.1021/acs.nanolett.8b00683>. Cited in page 66.

204 Huang, Bevin, Genevieve Clark, Efrén Navarro-Moratalla, Dahlia R Klein, Ran Cheng, Kyle L Seyler, Ding Zhong, Emma Schmidgall, Michael A McGuire, David H Cobden, Wang Yao, Di Xiao, Pablo Jarillo-Herrero, and Xiaodong Xu: *Layer-dependent ferromagnetism in a van der Waals crystal down to the monolayer limit.* Nature, 546(7657):270–273, 2017, ISSN 1476-4687. <https://doi.org/10.1038/nature22391>. Cited in page 66.

205 Huang, Bevin, Genevieve Clark, Dahlia R Klein, David MacNeill, Efrén Navarro-Moratalla, Kyle L Seyler, Nathan Wilson, Michael A McGuire, David H Cobden, Di Xiao, Wang Yao, Pablo Jarillo-Herrero, and Xiaodong Xu: *Electrical control of 2D magnetism in bilayer CrI3.* Nature Nanotechnology, 13(7):544–548, 2018, ISSN 1748-3395. <https://doi.org/10.1038/s41565-018-0121-3>. Cited in page 66.

206 Jiang, Shengwei, Lizhong Li, Zefang Wang, Kin Fai Mak, and Jie Shan: *Controlling magnetism in 2D CrI3 by electrostatic doping*. Nature Nanotechnology, 13(7):549–553, 2018, ISSN 1748-3395. <https://doi.org/10.1038/s41565-018-0135-x>. Cited in page 66.

207 Gong, Cheng, Lin Li, Zhenglu Li, Huiwen Ji, Alex Stern, Yang Xia, Ting Cao, Wei Bao, Chenzhe Wang, Yuan Wang, Z Q Qiu, R J Cava, Steven G Louie, Jing Xia, and Xiang Zhang: *Discovery of intrinsic ferromagnetism in two-dimensional van der Waals crystals*. Nature, 546(7657):265–269, 2017, ISSN 1476-4687. <https://doi.org/10.1038/nature22060>. Cited in page 66.

208 Fang, Mengqi and Eui Hyeok Yang: *Advances in Two-Dimensional Magnetic Semiconductors via Substitutional Doping of Transition Metal Dichalcogenides*, 2023, ISBN 1996-1944. Cited in page 66.

209 Yun, Won Seok and J D Lee: *Unexpected strong magnetism of Cu doped single-layer MoS2 and its origin*. Physical Chemistry Chemical Physics, 16(19):8990–8996, 2014, ISSN 1463-9076. <http://dx.doi.org/10.1039/C4CP00247D>. Cited in page 66.

210 Andriotis, Antonis N and Madhu Menon: *Tunable magnetic properties of transition metal doped* MoS_2. Physical Review B, 90(12):125304, sep 2014. <https://link.aps.org/doi/10.1103/PhysRevB.90.125304>. Cited in page 66.

211 Lu, Shang Chun and Jean Pierre Leburton: *Electronic structures of defects and magnetic impurities in MoS2 monolayers*. Nanoscale Research Letters, 9(1):676, 2014, ISSN 1556-276X. <https://doi.org/10.1186/1556-276X-9-676>. Cited in page 66.

212 Li, Hongping, Shuai Liu, Songlei Huang, Deqiang Yin, Changsheng Li, and Zhongchang Wang: *Impurity-induced ferromagnetism and metallicity of WS2 monolayer*. Ceramics International, 42(2, Part A):2364–2369, 2016, ISSN 0272-8842. <https://www.sciencedirect.com/science/article/pii/S0272884215019112>. Cited in page 66.

213 Wang, Yiren, Sean Li, and Jiabao Yi: *Electronic and magnetic properties of Co doped MoS2 monolayer*. Scientific Reports, 6(1):24153, 2016, ISSN 2045-2322. <https://doi.org/10.1038/srep24153>. Cited 2 times in pages 66 e 105.

214 Luo, Min, Yu Hao Shen, and Jun Hao Chu: *First-principles study of the magnetism of Ni-doped MoS2 monolayer*. Japanese Journal of Applied Physics, 55(9):93001, 2016, ISSN 1347-4065. <https://dx.doi.org/10.7567/JJAP.55.093001>. Cited in page 66.

215 Singh, Nirpendra and Udo Schwingenschlögl: *Extended Moment Formation in Monolayer WS2 Doped with 3d Transition-Metals*. ACS Applied Materials & Interfaces, 8(36):23886–23890, sep 2016, ISSN 1944-8244. <https://doi.org/10.1021/acsami.6b05670>. Cited in page 66.

216 Singh, Nirpendra and Udo Schwingenschlögl: *A Route to Permanent Valley Polarization in Monolayer MoS2*. Advanced Materials, 29(1):1600970, jan 2017, ISSN 0935-9648. <https://doi.org/10.1002/adma.201600970>. Cited in page 66.

217 Xia, Baorui, Peitao Liu, Yonggang Liu, Daqiang Gao, Desheng Xue, and Jun Ding: *Re doping induced 2H-1T phase transformation and ferromagnetism in MoS2 nanosheets*. Applied Physics Letters, 113(1):13101, jul 2018, ISSN 0003-6951. <https://doi.org/10.1063/1.5027535>. Cited in page 66.

218 Coelho, Paula Mariel, Hannu Pekka Komsa, Kinga Lasek, Vijaysankar Kalappattil, Jeyakumar Karthikeyan, Manh Huong Phan, Arkady V Krasheninnikov, and Matthias Batzill: *Room-Temperature Ferromagnetism in MoTe2 by Post-Growth Incorporation of Vanadium Impurities*. Advanced Electronic Materials, 5(5):1900044, may 2019, ISSN 2199-160X. <https://doi.org/10.1002/aelm.201900044>. Cited in page 66.

219 Gao, Yuqiang, Nirmal Ganguli, and Paul J Kelly: *Itinerant ferromagnetism in p-doped monolayers of* MoS_2. Physical Review B, 99(22):220406, jun 2019. <https://link.aps.org/doi/10.1103/PhysRevB.99.220406>. Cited in page 66.

220 Duong, Dinh Loc, Seok Joon Yun, Youngkuk Kim, Seong Gon Kim, and Young Hee Lee: *Long-range ferromagnetic ordering in vanadium-doped WSe2 semiconductor*. Applied Physics Letters, 115(24):242406, dec 2019, ISSN 0003-6951. <https://doi.org/10.1063/1.5131566>. Cited 3 times in pages 66, 108 e 114.

221 Deng, Jianjun, Zhonghao Zhou, Jinglong Chen, Zhihai Cheng, Jia Liu, and Zhiyong Wang: *Vanadium-Doped Molybdenum Diselenide Atomic Layers with Room-Temperature Ferromagnetism*. ChemPhysChem, 23(16):e202200162, aug 2022, ISSN 1439-4235. <https://doi.org/10.1002/cphc.202200162>. Cited in page 66.

222 Fu, Shichen, Kyungnam Kang, Kamran Shayan, Anthony Yoshimura, Siamak Dadras, Xiaotian Wang, Lihua Zhang, Siwei Chen, Na Liu, Apoorv Jindal, Xiangzhi Li, Abhay N Pasupathy, A Nick Vamivakas, Vincent Meunier, Stefan Strauf, and Eui Hyeok Yang: *Enabling room temperature ferromagnetism in monolayer MoS2 via in situ iron-doping*. Nature Communications, 11(1):2034, 2020, ISSN 2041-1723. <https://doi.org/10.1038/s41467-020-15877-7>. Cited 2 times in pages 66 e 75.

223 Ohya, Shinobu, Kenta Takata, and Masaaki Tanaka: *Nearly non-magnetic valence band of the ferromagnetic semiconductor GaMnAs*. Nature Physics, 7(4):342–347, 2011, ISSN 1745-2481. <https://doi.org/10.1038/nphys1905>. Cited in page 66.

224 Ruderman, M A and C Kittel: *Indirect Exchange Coupling of Nuclear Magnetic Moments by Conduction Electrons*. Physical Review, 96(1):99–102, oct 1954. <https://link.aps.org/doi/10.1103/PhysRev.96.99>. Cited in page 66.

225 Dietl, T, H Ohno, F Matsukura, J Cibert, and D Ferrand: *Zener Model Description of Ferromagnetism in Zinc-Blende Magnetic Semiconductors*. Science, 287(5455):1019–1022, feb 2000. <https://doi.org/10.1126/science.287.5455.1019>. Cited in page 66.

226 Song, Bumsub, Seok Joon Yun, Jinbao Jiang, José Avila, Kory Beach, Wooseon Choi, Young Min Kim, Duhee Yoon, Humberto Terrones, Young Jae Song, Maria C Asensio, Dinh Loc Duong, and Young Hee Lee: *Evidence of itinerant holes for long-range magnetic order in the tungsten diselenide semiconductor with vanadium dopants*. Physical Review B, 103(9):94432, mar 2021. <https://link.aps.org/doi/10.1103/PhysRevB.103.094432>. Cited 2 times in pages 66 e 114.

227 Ponomarenko, L A, A K Geim, A A Zhukov, R Jalil, S V Morozov, K S Novoselov, I V Grigorieva, E H Hill, V V Cheianov, V I Fal'ko, K Watanabe, T Taniguchi, and R V Gorbachev: *Tunable metal–insulator transition in double-layer graphene heterostructures*. Nature Physics, 7(12):958–961, 2011, ISSN 1745-2481. <https://doi.org/10.1038/nphys2114>. Cited in page 68.

228 Britnell, L, R V Gorbachev, R Jalil, B D Belle, F Schedin, A Mishchenko, T Georgiou, M I Katsnelson, L Eaves, S V Morozov, N M R Peres, J Leist, A K Geim, K S Novoselov, and L A Ponomarenko: *Field-Effect Tunneling Transistor Based on Vertical Graphene Heterostructures*. Science, 335(6071):947 LP – 950, feb 2012. <http://science.sciencemag.org/content/335/6071/947.abstract>. Cited in page 68.

229 Haigh, S J, A Gholinia, R Jalil, S Romani, L Britnell, D C Elias, K S Novoselov, L A Ponomarenko, A K Geim, and R Gorbachev: *Cross-sectional imaging of individual layers and buried interfaces of graphene-based heterostructures and superlattices*. Nature Materials, 11(9):764–767, 2012, ISSN 1476-4660. <https://doi.org/10.1038/nmat3386>. Cited in page 68.

230 Wang, Qing Hua, Kourosh Kalantar-Zadeh, Andras Kis, Jonathan N Coleman, and Michael S Strano: *Electronics and optoelectronics of two-dimensional transition metal dichalcogenides*. Nature Nanotechnology, 7(11):699–712, 2012, ISSN 1748-3395. <https://doi.org/10.1038/nnano.2012.193>. Cited in page 68.

231 Gong, Cheng, Hengji Zhang, Weihua Wang, Luigi Colombo, Robert M Wallace, and Kyeongjae Cho: *Band alignment of two-dimensional transition metal dichalcogenides: Application in tunnel field effect transistors*. Applied Physics Letters, 103(5):53513, jul 2013, ISSN 0003-6951. <https://doi.org/10.1063/1.4817409>. Cited in page 68.

232 Kang, Jun, Sefaattin Tongay, Jian Zhou, Jingbo Li, and Junqiao Wu: *Band offsets and heterostructures of two-dimensional semiconductors*. Applied Physics Letters, 102(1):12111, jan 2013, ISSN 0003-6951. <https://doi.org/10.1063/1.4774090>. Cited in page 68.

233 Terrones, Humberto, Florentino López-Urías, and Mauricio Terrones: *Novel hetero-layered materials with tunable direct band gaps by sandwiching different metal disulfides and diselenides*. Scientific Reports, 3(1):1549, 2013, ISSN 2045-2322. <https://doi.org/10.1038/srep01549>. Cited in page 68.

234 Kang, Jun, Jingbo Li, Shu Shen Li, Jian Bai Xia, and Lin Wang Wang: *Electronic Structural Moiré Pattern Effects on MoS2/MoSe2 2D Heterostructures*. Nano Letters, 13(11):5485–5490, nov 2013, ISSN 1530-6984. <https://doi.org/10.1021/nl4030648>. Cited in page 68.

235 He, Jiangang, Kerstin Hummer, and Cesare Franchini: *Stacking effects on the electronic and optical properties of bilayer transition metal dichalcogenides* MoS_2, $MoSe_2$, WS_2, *and* WSe_2. Physical Review B, 89(7):75409, feb 2014. <https://link.aps.org/doi/10.1103/PhysRevB.89.075409>. Cited 2 times in pages 68 e 169.

236 Fang, Hui, Corsin Battaglia, Carlo Carraro, Slavomir Nemsak, Burak Ozdol, Jeong Seuk Kang, Hans A Bechtel, Sujay B Desai, Florian Kronast, Ahmet A Unal, Giuseppina Conti, Catherine Conlon, Gunnar K Palsson, Michael C Martin, Andrew M Minor, Charles S Fadley, Eli Yablonovitch, Roya Maboudian, and Ali Javey: *Strong interlayer coupling in van der Waals heterostructures built from single-layer chalcogenides*. Proceedings of the National Academy of Sciences, 111(17):6198 LP – 6202, apr 2014. <http://www.pnas.org/content/111/17/6198.abstract>. Cited in page 68.

237 Chiu, Ming Hui, Ming Yang Li, Wengjing Zhang, Wei Ting Hsu, Wen Hao Chang, Mauricio Terrones, Humberto Terrones, and Lain Jong Li: *Spectroscopic Signatures for Interlayer Coupling in MoS2–WSe2 van der Waals Stacking.* ACS Nano, 8(9):9649–9656, sep 2014, ISSN 1936-0851. <https://doi.org/10.1021/nn504229z>. Cited in page 68.

238 Rivera, Pasqual, John R Schaibley, Aaron M Jones, Jason S Ross, Sanfeng Wu, Grant Aivazian, Philip Klement, Kyle Seyler, Genevieve Clark, Nirmal J Ghimire, Jiaqiang Yan, D G Mandrus, Wang Yao, and Xiaodong Xu: *Observation of long-lived interlayer excitons in monolayer MoSe2–WSe2 heterostructures.* Nature Communications, 6(1):6242, 2015, ISSN 2041-1723. <https://doi.org/10.1038/ncomms7242>. Cited 2 times in pages 68 e 161.

239 Miller, Bastian, Alexander Steinhoff, Borja Pano, Julian Klein, Frank Jahnke, Alexander Holleitner, and Ursula Wurstbauer: *Long-Lived Direct and Indirect Interlayer Excitons in van der Waals Heterostructures.* Nano Letters, 17(9):5229–5237, sep 2017, ISSN 1530-6984. <https://doi.org/10.1021/acs.nanolett.7b01304>. Cited in page 68.

240 Nagler, Philipp, Gerd Plechinger, Mariana V Ballottin, Anatolie Mitioglu, Sebastian Meier, Nicola Paradiso, Christoph Strunk, Alexey Chernikov, Peter C M Christianen, Christian Schüller, and Tobias Korn: *Interlayer exciton dynamics in a dichalcogenide monolayer heterostructure.* 2D Materials, 4(2):25112, 2017, ISSN 2053-1583. <http://dx.doi.org/10.1088/2053-1583/aa7352>. Cited in page 68.

241 Unuchek, Dmitrii, Alberto Ciarrocchi, Ahmet Avsar, Kenji Watanabe, Takashi Taniguchi, and Andras Kis: *Room-temperature electrical control of exciton flux in a van der Waals heterostructure.* Nature, 560(7718):340–344, 2018, ISSN 1476-4687. <https://doi.org/10.1038/s41586-018-0357-y>. Cited in page 68.

242 Jauregui, Luis A, Andrew Y Joe, Kateryna Pistunova, Dominik S Wild, Alexander A High, You Zhou, Giovanni Scuri, Kristiaan De Greve, Andrey Sushko, Che Hang Yu, Takashi Taniguchi, Kenji Watanabe, Daniel J Needleman, Mikhail D Lukin, Hongkun Park, and Philip Kim: *Electrical control of interlayer exciton dynamics in atomically thin heterostructures.* Science, 366(6467):870 LP – 875, nov 2019. <http://science.sciencemag.org/content/366/6467/870.abstract>. Cited in page 68.

243 Yu, Hongyi, Gui Bin Liu, Jianju Tang, Xiaodong Xu, and Wang Yao: *Moiré excitons: From programmable quantum emitter arrays to spin-orbit–coupled artificial lattices.* Science Advances, 3(11):e1701696, nov 2017. <http://advances.sciencemag.org/content/3/11/e1701696.abstract>. Cited in page 68.

244 Sahoo, Prasana Kumar, Shahriar Memaran, Florence Ann Nugera, Yan Xin, Tania Díaz Márquez, Zhengguang Lu, Wenkai Zheng, Nikolai D Zhigadlo, Dmitry Smirnov, Luis Balicas, and Humberto Rodríguez Gutiérrez: *Bilayer Lateral Heterostructures of Transition-Metal Dichalcogenides and Their Optoelectronic Response.* ACS Nano, 13(11):12372–12384, nov 2019, ISSN 1936-0851. <https://doi.org/10.1021/acsnano.9b04957>. Cited 3 times in pages 69, 132 e 163.

245 Rosati, Roberto, Ioannis Paradisanos, Libai Huang, Ziyang Gan, Antony George, Kenji Watanabe, Takashi Taniguchi, Laurent Lombez, Pierre Renucci, Andrey Turchanin, Bernhard Urbaszek, and Ermin Malic: *Interface engineering of charge-transfer excitons in 2D lateral heterostructures.* Nature Communications, 14(1):2438, 2023, ISSN 2041-1723. <https://doi.org/10.1038/s41467-023-37889-9>. Cited in page 69.

246 Malic, Ermin, Raül Perea-Causin, Roberto Rosati, Daniel Erkensten, and Samuel Brem: *Exciton transport in atomically thin semiconductors*. Nature Communications, 14(1):3430, 2023, ISSN 2041-1723. <https://doi.org/10.1038/s41467-023-38556-9>. Cited 4 times in pages 10, 69, 70 e 155.

247 Duan, Xidong, Chen Wang, Jonathan C Shaw, Rui Cheng, Yu Chen, Honglai Li, Xueping Wu, Ying Tang, Qinling Zhang, Anlian Pan, Jianhui Jiang, Ruqing Yu, Yu Huang, and Xiangfeng Duan: *Lateral epitaxial growth of two-dimensional layered semiconductor heterojunctions*. Nature Nanotechnology, 9(12):1024–1030, 2014, ISSN 1748-3395. <https://doi.org/10.1038/nnano.2014.222>. Cited 4 times in pages 69, 70, 163 e 165.

248 Gong, Yongji, Junhao Lin, Xingli Wang, Gang Shi, Sidong Lei, Zhong Lin, Xiaolong Zou, Gonglan Ye, Robert Vajtai, Boris I Yakobson, Humberto Terrones, Mauricio Terrones, Beng Kang Tay, Jun Lou, Sokrates T Pantelides, Zheng Liu, Wu Zhou, and Pulickel M Ajayan: *Vertical and in-plane heterostructures from WS2/MoS2 monolayers*. Nature Materials, 13(12):1135–1142, 2014, ISSN 1476-4660. <https://doi.org/10.1038/nmat4091>. Cited 4 times in pages 69, 70, 163 e 165.

249 Huang, Chunming, Sanfeng Wu, Ana M Sanchez, Jonathan J P Peters, Richard Beanland, Jason S Ross, Pasqual Rivera, Wang Yao, David H Cobden, and Xiaodong Xu: *Lateral heterojunctions within monolayer MoSe2–WSe2 semiconductors*. Nature Materials, 13(12):1096–1101, 2014, ISSN 1476-4660. <https://doi.org/10.1038/nmat4064>. Cited 4 times in pages 69, 70, 163 e 165.

250 Gong, Yongji, Sidong Lei, Gonglan Ye, Bo Li, Yongmin He, Kunttal Keyshar, Xiang Zhang, Qizhong Wang, Jun Lou, Zheng Liu, Robert Vajtai, Wu Zhou, and Pulickel M Ajayan: *Two-Step Growth of Two-Dimensional WSe2/MoSe2 Heterostructures*. Nano Letters, 15(9):6135–6141, sep 2015, ISSN 1530-6984. <https://doi.org/10.1021/acs.nanolett.5b02423>. Cited 4 times in pages 69, 70, 163 e 165.

251 Li, Ming Yang, Yumeng Shi, Chia Chin Cheng, Li Syuan Lu, Yung Chang Lin, Hao Lin Tang, Meng Lin Tsai, Chih Wei Chu, Kung Hwa Wei, Jr Hau He, Wen Hao Chang, Kazu Suenaga, and Lain Jong Li: *Epitaxial growth of a monolayer WSe₂-MoS₂ lateral p-n junction with an atomically sharp interface*. Science, 349(6247):524 LP – 528, jul 2015. <http://science.sciencemag.org/content/349/6247/524.abstract>. Cited 4 times in pages 69, 70, 163 e 165.

252 Zhang, Zhengwei, Peng Chen, Xidong Duan, Ketao Zang, Jun Luo, and Xiangfeng Duan: *Robust epitaxial growth of two-dimensional heterostructures, multiheterostructures, and superlattices*. Science, page eaan6814, aug 2017. <http://science.sciencemag.org/content/early/2017/08/02/science.aan6814.abstract>. Cited 3 times in pages 69, 70 e 163.

253 Sahoo, Prasana K, Shahriar Memaran, Yan Xin, Luis Balicas, and Humberto R Gutiérrez: *One-pot growth of two-dimensional lateral heterostructures via sequential edge-epitaxy*. Nature, 553(7686):63–67, 2018, ISSN 1476-4687. <https://doi.org/10.1038/nature25155>. Cited 7 times in pages 69, 70, 156, 163, 164, 165 e 166.

254 Chen, Kun, Xi Wan, Jinxiu Wen, Weiguang Xie, Zhiwen Kang, Xiaoliang Zeng, Huanjun Chen, and Jian Bin Xu: *Electronic Properties of MoS2–WS2 Heterostructures*

Synthesized with Two-Step Lateral Epitaxial Strategy. ACS Nano, 9(10):9868–9876, oct 2015, ISSN 1936-0851. <https://doi.org/10.1021/acsnano.5b03188>. Cited 2 times in pages 70 e 163.

255 Jia, Shuai, Zehua Jin, Jing Zhang, Jiangtan Yuan, Weibing Chen, Wei Feng, Pingan Hu, Pulickel M Ajayan, and Jun Lou: *Lateral Monolayer MoSe2–WSe2 p–n Heterojunctions with Giant Built-In Potentials*. Small, 16(34):2002263, aug 2020, ISSN 1613-6810. <https://doi.org/10.1002/smll.202002263>. Cited 2 times in pages 70 e 163.

256 Sahoo, Prasana K, Haonan Zong, Jiru Liu, Wenjin Xue, Xiaoyi Lai, Humberto R Gutiérrez, and Dmitri V Voronine: *Probing nano-heterogeneity and aging effects in lateral 2D heterostructures using tip-enhanced photoluminescence*. Optical Materials Express, 9(4):1620–1631, 2019. <http://www.osapublishing.org/ome/abstract.cfm?URI=ome-9-4-1620>. Cited 3 times in pages 70, 84 e 163.

257 Frisenda, Riccardo, Yue Niu, Patricia Gant, Aday J Molina-Mendoza, Robert Schmidt, Rudolf Bratschitsch, Jinxin Liu, Lei Fu, Dumitru Dumcenco, Andras Kis, David Perez De Lara, and Andres Castellanos-Gomez: *Micro-reflectance and transmittance spectroscopy: a versatile and powerful tool to characterize 2D materials*. Journal of Physics D: Applied Physics, 50(7):74002, 2017, ISSN 0022-3727. <https://dx.doi.org/10.1088/1361-6463/aa5256>. Cited in page 72.

258 Niu, Yue, Sergio Gonzalez-Abad, Riccardo Frisenda, Philipp Marauhn, Matthias Drüppel, Patricia Gant, Robert Schmidt, Najme S Taghavi, David Barcons, Aday J Molina-Mendoza, Steffen M De Vasconcellos, Rudolf Bratschitsch, David Perez De Lara, Michael Rohlfing, and Andres Castellanos-Gomez: *Thickness-Dependent Differential Reflectance Spectra of Monolayer and Few-Layer MoS2, MoSe2, WS2 and WSe2*, 2018, ISBN 2079-4991. Cited 3 times in pages 10, 72 e 73.

259 Bretscher, Hope, Zhaojun Li, James Xiao, Diana Yuan Qiu, Sivan Refaely-Abramson, Jack A Alexander-Webber, Arelo Tanoh, Ye Fan, Géraud Delport, Cyan A Williams, Samuel D Stranks, Stephan Hofmann, Jeffrey B Neaton, Steven G Louie, and Akshay Rao: *Rational Passivation of Sulfur Vacancy Defects in Two-Dimensional Transition Metal Dichalcogenides*. ACS Nano, 15(5):8780–8789, may 2021, ISSN 1936-0851. <https://doi.org/10.1021/acsnano.1c01220>. Cited in page 72.

260 Schmidt, T, K Lischka, and W Zulehner: *Excitation-power dependence of the near-band-edge photoluminescence of semiconductors*. Physical Review B, 45(16):8989–8994, apr 1992. <https://link.aps.org/doi/10.1103/PhysRevB.45.8989>. Cited 2 times in pages 74 e 106.

261 Suh, Joonki, Teck Leong Tan, Weijie Zhao, Joonsuk Park, Der Yuh Lin, Tae Eon Park, Jonghwan Kim, Chenhao Jin, Nihit Saigal, Sandip Ghosh, Zicong Marvin Wong, Yabin Chen, Feng Wang, Wladyslaw Walukiewicz, Goki Eda, and Junqiao Wu: *Reconfiguring crystal and electronic structures of MoS2 by substitutional doping*. Nature Communications, 9(1):199, 2018, ISSN 2041-1723. <https://doi.org/10.1038/s41467-017-02631-9>. Cited 3 times in pages 10, 75 e 76.

262 Qin, Ziyu, Leyi Loh, Junyong Wang, Xiaomin Xu, Qi Zhang, Benedikt Haas, Carlos Alvarez, Hanako Okuno, Justin Zhou Yong, Thorsten Schultz, Norbert Koch, Jiadong Dan,

Stephen J Pennycook, Dawen Zeng, Michel Bosman, and Goki Eda: *Growth of Nb-Doped Monolayer WS2 by Liquid-Phase Precursor Mixing*. ACS Nano, 13(9):10768–10775, sep 2019, ISSN 1936-0851. <https://doi.org/10.1021/acsnano.9b05574>. Cited in page 75.

263 Zhang, Kehao, Brian M Bersch, Jaydeep Joshi, Rafik Addou, Christopher R Cormier, Chenxi Zhang, Ke Xu, Natalie C Briggs, Ke Wang, Shruti Subramanian, Kyeongjae Cho, Susan Fullerton-Shirey, Robert M Wallace, Patrick M Vora, and Joshua A Robinson: *Tuning the Electronic and Photonic Properties of Monolayer MoS2 via In Situ Rhenium Substitutional Doping*. Advanced Functional Materials, 28(16):1706950, apr 2018, ISSN 1616-301X. <https://doi.org/10.1002/adfm.201706950>. Cited in page 75.

264 Cai, Zhengyang, Tianze Shen, Qi Zhu, Simin Feng, Qiangmin Yu, Jiaman Liu, Lei Tang, Yue Zhao, Jiangwei Wang, Bilu Liu, and Hui Ming Cheng: *Dual-Additive Assisted Chemical Vapor Deposition for the Growth of Mn-Doped 2D MoS2 with Tunable Electronic Properties*. Small, 16(15):1903181, apr 2020, ISSN 1613-6810. <https://doi.org/10.1002/smll.201903181>. Cited 3 times in pages 10, 75 e 76.

265 Kang, Kyungnam, Shichen Fu, Kamran Shayan, Yoshimura Anthony, Siamak Dadras, Xiong Yuzan, Fujisawa Kazunori, Mauricio Terrones, Wei Zhang, Stefan Strauf, Vincent Meunier, A Nick Vamivakas, and Eui Hyeok Yang: *The effects of substitutional Fe-doping on magnetism in MoS2 and WS2 monolayers*. Nanotechnology, 32(9):95708, 2021, ISSN 0957-4484. <https://dx.doi.org/10.1088/1361-6528/abcd61>. Cited 3 times in pages 10, 75 e 76.

266 Nguyen, Lan Anh T, Krishna P Dhakal, Yuhan Lee, Wooseon Choi, Tuan Dung Nguyen, Chengyun Hong, Dinh Hoa Luong, Young Min Kim, Jeongyong Kim, Myeongwon Lee, Taeyoung Choi, Andreas J Heinrich, Ji Hee Kim, Donghun Lee, Dinh Loc Duong, and Young Hee Lee: *Spin-Selective Hole–Exciton Coupling in a V-Doped WSe2 Ferromagnetic Semiconductor at Room Temperature*. ACS Nano, 15(12):20267–20277, dec 2021, ISSN 1936-0851. <https://doi.org/10.1021/acsnano.1c08375>. Cited 2 times in pages 75 e 116.

267 Nisi, Katharina, Jonas Kiemle, Lukas Powalla, Alessio Scavuzzo, Tuan Dung Nguyen, Takashi Taniguchi, Kenji Watanabe, Dinh Loc Duong, Marko Burghard, Alexander W Holleitner, and Christoph Kastl: *Defect-Engineered Magnetic Field Dependent Optoelectronics of Vanadium Doped Tungsten Diselenide Monolayers*. Advanced Optical Materials, 10(17):2102711, sep 2022, ISSN 2195-1071. <https://doi.org/10.1002/adom.202102711>. Cited 4 times in pages 75, 116, 117 e 119.

268 Zhang, Tianyi, Mingzu Liu, Kazunori Fujisawa, Michael Lucking, Kory Beach, Fu Zhang, Maruda Shanmugasundaram, Andrey Krayev, William Murray, Yu Lei, Zhuohang Yu, David Sanchez, Zhiwen Liu, Humberto Terrones, Ana Laura Elías, and Mauricio Terrones: *Spatial Control of Substitutional Dopants in Hexagonal Monolayer WS2: The Effect of Edge Termination*. Small, 19(6):2205800, feb 2023, ISSN 1613-6810. <https://doi.org/10.1002/smll.202205800>. Cited 4 times in pages 10, 75, 76 e 106.

269 Liu, Zheng, Matin Amani, Sina Najmaei, Quan Xu, Xiaolong Zou, Wu Zhou, Ting Yu, Caiyu Qiu, A Glen Birdwell, Frank J Crowne, Robert Vajtai, Boris I Yakobson, Zhenhai Xia, Madan Dubey, Pulickel M Ajayan, and Jun Lou: *Strain and structure heterogeneity in MoS2 atomic layers grown by chemical vapour deposition*. Nature Communications, 5(1):5246, 2014, ISSN 2041-1723. <https://doi.org/10.1038/ncomms6246>. Cited 2 times in pages 76 e 77.

270 Christopher, J W, M Vutukuru, D Lloyd, J S Bunch, B B Goldberg, D J Bishop, and A K Swan: *Monolayer MoS2 Strained to 1.3% With a Microelectromechanical System*. Journal of Microelectromechanical Systems, 28(2):254–263, apr 2019, ISSN 1941-0158. <https://doi.org/10.1109/JMEMS.2018.2877983>. Cited 6 times in pages 76, 77, 80, 136, 137 e 141.

271 Desai, Sujay B, Gyungseon Seol, Jeong Seuk Kang, Hui Fang, Corsin Battaglia, Rehan Kapadia, Joel W Ager, Jing Guo, and Ali Javey: *Strain-Induced Indirect to Direct Bandgap Transition in Multilayer WSe2*. Nano Letters, 14(8):4592–4597, aug 2014, ISSN 1530-6984. <https://doi.org/10.1021/nl501638a>. Cited 4 times in pages 11, 77, 78 e 147.

272 Yu, Peter Y and Manuel Cardona: *Optical Properties II BT - Fundamentals of Semiconductors: Physics and Materials Properties*. In Yu, Peter Y and Manuel Cardona (editors): *Fundamentals of Semiconductors: Physics and Materials Properties*, pages 345–426. Springer Berlin Heidelberg, Berlin, Heidelberg, 2010, ISBN 978-3-642-00710-1. <https://doi.org/10.1007/978-3-642-00710-1_7>. Cited 3 times in pages 77, 78 e 79.

273 Jorio, Ado, Mildred S Dresselhaus, Riichiro Saito, and Gene Dresselhaus: *Raman Spectroscopy in Graphene Related Systems*. John Wiley & Sons, 2011, ISBN 9783527632695. <https://doi.org/10.1002/9783527632695>. Cited 4 times in pages 79, 80, 108 e 109.

274 Corro, E del, A Botello-Méndez, Y Gillet, A L Elias, H Terrones, S Feng, C Fantini, Daniel Rhodes, N Pradhan, L Balicas, X Gonze, J. C. Charlier, M Terrones, and M A Pimenta: *Atypical Exciton–Phonon Interactions in WS2 and WSe2 Monolayers Revealed by Resonance Raman Spectroscopy*. Nano Letters, 16(4):2363–2368, apr 2016, ISSN 1530-6984. <https://doi.org/10.1021/acs.nanolett.5b05096>. Cited 4 times in pages 11, 79, 80 e 110.

275 Mignuzzi, Sandro, Andrew J Pollard, Nicola Bonini, Barry Brennan, Ian S Gilmore, Marcos A Pimenta, David Richards, and Debdulal Roy: *Effect of disorder on Raman scattering of single-layer* MoS_2. Physical Review B, 91(19):195411, may 2015. <https://link.aps.org/doi/10.1103/PhysRevB.91.195411>. Cited 3 times in pages 11, 80 e 81.

276 Zhu, C R, G Wang, B L Liu, X Marie, X F Qiao, X Zhang, X X Wu, H Fan, P H Tan, T Amand, and B Urbaszek: *Strain tuning of optical emission energy and polarization in monolayer and bilayer* MoS_2. Physical Review B, 88(12):121301, sep 2013. <https://link.aps.org/doi/10.1103/PhysRevB.88.121301>. Cited 3 times in pages 11, 80 e 82.

277 Conley, Hiram J, Bin Wang, Jed I Ziegler, Richard F Jr. Haglund, Sokrates T Pantelides, and Kirill I Bolotin: *Bandgap Engineering of Strained Monolayer and Bilayer MoS2*. Nano Letters, 13(8):3626–3630, aug 2013, ISSN 1530-6984. <https://doi.org/10.1021/nl4014748>. Cited 2 times in pages 80 e 141.

278 Chakraborty, Biswanath, Achintya Bera, D V S Muthu, Somnath Bhowmick, U V Waghmare, and A K Sood: *Symmetry-dependent phonon renormalization in monolayer* MoS_2 *transistor*. Physical Review B, 85(16):161403, apr 2012. <https://link.aps.org/doi/10.1103/PhysRevB.85.161403>. Cited 3 times in pages 11, 80 e 82.

279 Parkin, William M, Adrian Balan, Liangbo Liang, Paul Masih Das, Michael Lamparski, Carl H Naylor, Julio A Rodríguez-Manzo, A T Charlie Johnson, Vincent Meunier, and Marija Drndić: *Raman Shifts in Electron-Irradiated Monolayer MoS2*. ACS Nano, 10(4):4134–4142, apr 2016, ISSN 1936-0851. <https://doi.org/10.1021/acsnano.5b07388>. Cited in page 80.

280 Hecht, Bert and Lukas Novotny: *Principles of Nano-Optics*. Cambridge University Press, 2nd edition, 2012, ISBN 9781107005464. <https://doi.org/10.1017/CBO9780511794193>. Cited 2 times in pages 82 e 83.

281 Rodriguez, Alvaro, Tim Verhagen, Martin Kalbac, Jana Vejpravova, and Otakar Frank: *Imaging Nanoscale Inhomogeneities and Edge Delamination in As-Grown MoS2 Using Tip-Enhanced Photoluminescence*. physica status solidi (RRL) – Rapid Research Letters, 13(11):1900381, nov 2019, ISSN 1862-6254. <https://doi.org/10.1002/pssr.201900381>. Cited 5 times in pages 11, 83, 84, 132 e 139.

282 Huang, Teng Xiang, Xin Cong, Si Si Wu, Kai Qiang Lin, Xu Yao, Yu Han He, Jiang Bin Wu, Yi Fan Bao, Sheng Chao Huang, Xiang Wang, Ping Heng Tan, and Bin Ren: *Probing the edge-related properties of atomically thin MoS2 at nanoscale*. Nature Communications, 10(1):5544, 2019, ISSN 2041-1723. <https://doi.org/10.1038/s41467-019-13486-7>. Cited 4 times in pages 11, 83, 84 e 132.

283 Rahaman, Mahfujur, Raul D Rodriguez, Gerd Plechinger, Stefan Moras, Christian Schüller, Tobias Korn, and Dietrich R T Zahn: *Highly Localized Strain in a MoS2/Au Heterostructure Revealed by Tip-Enhanced Raman Spectroscopy*. Nano Letters, 17(10):6027–6033, oct 2017, ISSN 1530-6984. <https://doi.org/10.1021/acs.nanolett.7b02322>. Cited 4 times in pages 11, 84, 85 e 132.

284 Kato, Ryo, Takayuki Umakoshi, Rhea Thankam Sam, and Prabhat Verma: *Probing nanoscale defects and wrinkles in MoS2 by tip-enhanced Raman spectroscopic imaging*. Applied Physics Letters, 114(7):73105, feb 2019, ISSN 0003-6951. <https://doi.org/10.1063/1.5080255>. Cited 4 times in pages 11, 84, 85 e 132.

285 Koo, Yeonjeong, Yongchul Kim, Soo Ho Choi, Hyeongwoo Lee, Jinseong Choi, Dong Yun Lee, Mingu Kang, Hyun Seok Lee, Ki Kang Kim, Geunsik Lee, and Kyoung Duck Park: *Tip-Induced Nano-Engineering of Strain, Bandgap, and Exciton Funneling in 2D Semiconductors*. Advanced Materials, 33(17):2008234, apr 2021, ISSN 0935-9648. <https://doi.org/10.1002/adma.202008234>. Cited 3 times in pages 11, 84 e 85.

286 Shao, Jiaqi, Fei Chen, Weitao Su, Naresh Kumar, Yijie Zeng, Ling Wu, and Hong Wei Lu: *Probing Nanoscale Exciton Funneling at Wrinkles of Twisted Bilayer MoS2 Using Tip-Enhanced Photoluminescence Microscopy*. The Journal of Physical Chemistry Letters, 13(14):3304–3309, apr 2022. <https://doi.org/10.1021/acs.jpclett.2c00815>. Cited 2 times in pages 84 e 132.

287 Shao, Jiaqi, Fei Chen, Weitao Su, Yijie Zeng, and Hong Wei Lu: *Multimodal Nanoscopic Study of Atomic Diffusion and Related Localized Optoelectronic Response of WS2/MoS2 Lateral Heterojunctions*. ACS Applied Materials & Interfaces, 13(17):20361–20370, may 2021, ISSN 1944-8244. <https://doi.org/10.1021/acsami.1c03061>. Cited 2 times in pages 84 e 132.

288 Moore, David, Kiyoung Jo, Christine Nguyen, Jun Lou, Christopher Muratore, Deep Jariwala, and Nicholas R Glavin: *Uncovering topographically hidden features in 2D MoSe2 with correlated potential and optical nanoprobes.* npj 2D Materials and Applications, 4(1):44, 2020, ISSN 2397-7132. <https://doi.org/10.1038/s41699-020-00178-w>. Cited 3 times in pages 12, 85 e 86.

289 Lee, Yongjun, Seki Park, Hyun Kim, Gang Hee Han, Young Hee Lee, and Jeongyong Kim: *Characterization of the structural defects in CVD-grown monolayered MoS2 using near-field photoluminescence imaging.* Nanoscale, 7(28):11909–11914, 2015, ISSN 2040-3364. <http://dx.doi.org/10.1039/C5NR02897C>. Cited 3 times in pages 85, 132 e 133.

290 Smithe, Kirby K H, Andrey V Krayev, Connor S Bailey, Hye Ryoung Lee, Eilam Yalon, Burak Aslan, Miguel Muñoz Rojo, Sergiy Krylyuk, Payam Taheri, Albert V Davydov, Tony F Heinz, and Eric Pop: *Nanoscale Heterogeneities in Monolayer MoSe2 Revealed by Correlated Scanning Probe Microscopy and Tip-Enhanced Raman Spectroscopy.* ACS Applied Nano Materials, 1(2):572–579, feb 2018. <https://doi.org/10.1021/acsanm.7b00083>. Cited 5 times in pages 12, 85, 86, 132 e 133.

291 Su, Weitao, Naresh Kumar, Haibo Shu, Ophélie Lancry, and Marc Chaigneau: *In Situ Visualization of Optoelectronic Behavior of Grain Boundaries in Monolayer WSe2 at the Nanoscale.* The Journal of Physical Chemistry C, 125(48):26883–26891, dec 2021, ISSN 1932-7447. <https://doi.org/10.1021/acs.jpcc.1c08064>. Cited 5 times in pages 12, 85, 86, 132 e 133.

292 Wang, Yaqian, Longjiang Deng, Qilin Wei, Yi Wan, Zhen Liu, Xiao Lu, Yue Li, Lei Bi, Li Zhang, Haipeng Lu, Haiyan Chen, Peiheng Zhou, Linbo Zhang, Yingchun Cheng, Xiaoxu Zhao, Yu Ye, Wei Huang, Stephen John Pennycook, Kian Ping Loh, and Bo Peng: *Spin-Valley Locking Effect in Defect States of Monolayer MoS2.* Nano Letters, 20(3):2129–2136, mar 2020, ISSN 1530-6984. <https://doi.org/10.1021/acs.nanolett.0c00138>. Cited 4 times in pages 12, 87, 88 e 127.

293 Wang, Tianmeng, Shengnan Miao, Zhipeng Li, Yuze Meng, Zhengguang Lu, Zhen Lian, Mark Blei, Takashi Taniguchi, Kenji Watanabe, Sefaattin Tongay, Dmitry Smirnov, and Su Fei Shi: *Giant Valley-Zeeman Splitting from Spin-Singlet and Spin-Triplet Interlayer Excitons in WSe2/MoSe2 Heterostructure.* Nano Letters, 20(1):694–700, jan 2020, ISSN 1530-6984. <https://doi.org/10.1021/acs.nanolett.9b04528>. Cited in page 88.

294 Gobato, Y Galvão, C Serati de Brito, A Chaves, M A Prosnikov, T Woźniak, Shi Guo, Ingrid D Barcelos, M V Milošević, F Withers, and P C M Christianen: *Distinctive g-Factor of Moiré-Confined Excitons in van der Waals Heterostructures.* Nano Letters, 22(21):8641–8646, nov 2022, ISSN 1530-6984. <https://doi.org/10.1021/acs.nanolett.2c03008>. Cited in page 88.

295 Li, Xiangzhi, Andrew C Jones, Junho Choi, Huan Zhao, Vigneshwaran Chandrasekaran, Michael T Pettes, Andrei Piryatinski, Märta A Tschudin, Patrick Reiser, David A Broadway, Patrick Maletinsky, Nikolai Sinitsyn, Scott A Crooker, and Han Htoon: *Proximity-induced chiral quantum light generation in strain-engineered WSe2/NiPS3 heterostructures.* Nature Materials, 22(11):1311–1316, 2023, ISSN 1476-4660. <https://doi.org/10.1038/s41563-023-01645-7>. Cited in page 88.

296 Liu, Haiyang, Deyi Fu, Xu Li, Junbo Han, Xiaodie Chen, Xuefeng Wu, Baofan Sun, Weiqing Tang, Congming Ke, Yaping Wu, Zhiming Wu, and Junyong Kang: *Enhanced Valley Splitting in Monolayer WSe2 by Phase Engineering*. ACS Nano, 15(5):8244–8251, may 2021, ISSN 1936-0851. <https://doi.org/10.1021/acsnano.0c08305>. Cited in page 88.

297 Zhang, Xiao Xiao, Ting Cao, Zhengguang Lu, Yu Chuan Lin, Fan Zhang, Ying Wang, Zhiqiang Li, James C Hone, Joshua A Robinson, Dmitry Smirnov, Steven G Louie, and Tony F Heinz: *Magnetic brightening and control of dark excitons in monolayer WSe2*. Nat. Nanotechnol., 12:883, 2017. <https://doi.org/10.1038/nnano.2017.105>. Cited in page 88.

298 Robert, C, B Han, P Kapuscinski, A Delhomme, C Faugeras, T Amand, M R Molas, M Bartos, K Watanabe, T Taniguchi, B Urbaszek, M Potemski, and X Marie: *Measurement of the spin-forbidden dark excitons in MoS2 and MoSe2 monolayers*. Nature Communications, 11(1):4037, 2020, ISSN 2041-1723. <https://doi.org/10.1038/s41467-020-17608-4>. Cited in page 88.

299 Ceballos, Frank and Hui Zhao: *Ultrafast Laser Spectroscopy of Two-Dimensional Materials Beyond Graphene*. Advanced Functional Materials, 27(19):1604509, may 2017, ISSN 1616-301X. <https://doi.org/10.1002/adfm.201604509>. Cited in page 89.

300 Dal Conte, Stefano, Chiara Trovatello, Christoph Gadermaier, and Giulio Cerullo: *Ultrafast photophysics of 2D semiconductors and related heterostructures*. Trends in Chemistry, 2(1):28–42, 2020. Cited 3 times in pages 12, 89 e 90.

301 Nie, Zhaogang, Run Long, Linfeng Sun, Chung Che Huang, Jun Zhang, Qihua Xiong, Daniel W Hewak, Zexiang Shen, Oleg V Prezhdo, and Zhi Heng Loh: *Ultrafast Carrier Thermalization and Cooling Dynamics in Few-Layer MoS2*. ACS Nano, 8(10):10931–10940, oct 2014, ISSN 1936-0851. <https://doi.org/10.1021/nn504760x>. Cited in page 89.

302 Ceballos, Frank, Qiannan Cui, Matthew Z Bellus, and Hui Zhao: *Exciton formation in monolayer transition metal dichalcogenides*. Nanoscale, 8(22):11681–11688, 2016, ISSN 2040-3364. <http://dx.doi.org/10.1039/C6NR02516A>. Cited in page 89.

303 Trovatello, Chiara, Florian Katsch, Nicholas J Borys, Malte Selig, Kaiyuan Yao, Rocio Borrego-Varillas, Francesco Scotognella, Ilka Kriegel, Aiming Yan, Alex Zettl, P James Schuck, Andreas Knorr, Giulio Cerullo, and Stefano Dal Conte: *The ultrafast onset of exciton formation in 2D semiconductors*. Nature Communications, 11(1):5277, 2020, ISSN 2041-1723. <https://doi.org/10.1038/s41467-020-18835-5>. Cited in page 89.

304 Thilagam, A: *Exciton formation assisted by longitudinal optical phonons in monolayer transition metal dichalcogenides*. Journal of Applied Physics, 120(12):124306, sep 2016, ISSN 0021-8979. <https://doi.org/10.1063/1.4963123>. Cited in page 89.

305 Sun, Dezheng, Yi Rao, Georg A Reider, Gugang Chen, Yumeng You, Louis Brézin, Avetik R Harutyunyan, and Tony F Heinz: *Observation of rapid exciton–exciton annihilation in monolayer molybdenum disulfide*. Nano letters, 14(10):5625–5629, 2014. Cited 2 times in pages 89 e 90.

306 Wang, Tong, Thomas R Hopper, Navendu Mondal, Sihui Liu, Chengning Yao, Xijia Zheng, Felice Torrisi, and Artem A Bakulin: *Hot Carrier Cooling and Trapping*

in Atomically Thin WS2 Probed by Three-Pulse Femtosecond Spectroscopy. ACS Nano, 17(7):6330–6340, apr 2023, ISSN 1936-0851. <https://doi.org/10.1021/acsnano.2c10479>. Cited 2 times in pages 89 e 132.

307 Korn, T, S Heydrich, M Hirmer, J Schmutzler, and C Schüller: *Low-temperature photocarrier dynamics in monolayer MoS2*. Applied Physics Letters, 99(10):102109, sep 2011, ISSN 0003-6951. <https://doi.org/10.1063/1.3636402>. Cited 2 times in pages 89 e 90.

308 Robert, Cédric, David Lagarde, Fabian Cadiz, Gang Wang, Benjamin Lassagne, Thierry Amand, Andrea Balocchi, Pierre Renucci, Seffattin Tongay, Bernhard Urbaszek, *et al.*: *Exciton radiative lifetime in transition metal dichalcogenide monolayers*. Physical review B, 93(20):205423, 2016. Cited 2 times in pages 89 e 90.

309 Shah, Jagdeep: *Ultrafast Spectroscopy of Semiconductors and Semiconductor Nanostructures*. Springer Berlin Heidelberg, 1999, ISBN 978-3-662-03770-6. <https://doi.org/10.1007/978-3-662-03770-6_1>. Cited 2 times in pages 89 e 90.

310 Lagarde, D, L Bouet, X Marie, C R Zhu, B L Liu, T Amand, P H Tan, and B Urbaszek: *Carrier and Polarization Dynamics in Monolayer* MoS_2. Physical Review Letters, 112(4):47401, jan 2014. <https://link.aps.org/doi/10.1103/PhysRevLett.112.047401>. Cited 2 times in pages 90 e 129.

311 Wang, G, L Bouet, D Lagarde, M Vidal, A Balocchi, T Amand, X Marie, and B Urbaszek: *Valley dynamics probed through charged and neutral exciton emission in monolayer* WSe_2. Physical Review B, 90(7):75413, aug 2014. <https://link.aps.org/doi/10.1103/PhysRevB.90.075413>. Cited 4 times in pages 12, 90, 91 e 129.

312 Kumar, Nardeep, Qiannan Cui, Frank Ceballos, Dawei He, Yongsheng Wang, and Hui Zhao: *Exciton-exciton annihilation in* $MoSe_2$ *monolayers*. Physical Review B, 89(12):125427, mar 2014. <https://link.aps.org/doi/10.1103/PhysRevB.89.125427>. Cited in page 90.

313 Yuan, Long and Libai Huang: *Exciton dynamics and annihilation in WS2 2D semiconductors*. Nanoscale, 7(16):7402–7408, 2015, ISSN 2040-3364. <http://dx.doi.org/10.1039/C5NR00383K>. Cited in page 90.

314 Poellmann, Christoph, Philipp Steinleitner, Ursula Leierseder, Philipp Nagler, Gerd Plechinger, Michael Porer, R Bratschitsch, Christian Schüller, Tobias Korn, and Rupert Huber: *Resonant internal quantum transitions and femtosecond radiative decay of excitons in monolayer WSe2*. Nat. Mater., 14:889–893, 2015. <https://doi.org/10.1038/nmat4356>. Cited in page 90.

315 Wang, Haining, Changjian Zhang, and Farhan Rana: *Ultrafast Dynamics of Defect-Assisted Electron–Hole Recombination in Monolayer MoS2*. Nano Letters, 15(1):339–345, jan 2015, ISSN 1530-6984. <https://doi.org/10.1021/nl503636c>. Cited in page 90.

316 Franken, P A, A E Hill, C W Peters, and G Weinreich: *Generation of Optical Harmonics*. Physical Review Letters, 7(4):118–119, aug 1961. <https://link.aps.org/doi/10.1103/PhysRevLett.7.118>. Cited in page 91.

317 Boyd, Robert W.: *Nonlinear Optics*, volume 3. Academic Press, 2003, ISBN 9780123694706. Cited 6 times in pages 12, 91, 92, 93, 97 e 167.

318 Butet, Jérémy, Pierre François Brevet, and Olivier J F Martin: *Optical Second Harmonic Generation in Plasmonic Nanostructures: From Fundamental Principles to Advanced Applications*. ACS Nano, 9(11):10545–10562, nov 2015, ISSN 1936-0851. <https://doi.org/10.1021/acsnano.5b04373>. Cited in page 94.

319 Blake, Marea J, Brandon A Colon, and Tessa R Calhoun: *Leaving the Limits of Linearity for Light Microscopy*. The Journal of Physical Chemistry C, 124(45):24555–24565, nov 2020, ISSN 1932-7447. <https://doi.org/10.1021/acs.jpcc.0c07501>. Cited in page 94.

320 Huang, Wenjuan, Yue Xiao, Fangfang Xia, Xiangbai Chen, and Tianyou Zhai: *Second Harmonic Generation Control in 2D Layered Materials: Status and Outlook*. Advanced Functional Materials, n/a(n/a):2310726, jan 2024, ISSN 1616-301X. <https://doi.org/10.1002/adfm.202310726>. Cited 2 times in pages 94 e 144.

321 Heinz, T F, C K Chen, D Ricard, and Y R Shen: *Spectroscopy of Molecular Monolayers by Resonant Second-Harmonic Generation*. Physical Review Letters, 48(7):478–481, feb 1982. <https://link.aps.org/doi/10.1103/PhysRevLett.48.478>. Cited in page 94.

322 Shen, Y R: *Surface properties probed by second-harmonic and sum-frequency generation*. Nature, 337(6207):519–525, 1989, ISSN 1476-4687. <https://doi.org/10.1038/337519a0>. Cited in page 94.

323 Shen, Y R: *Optical Second Harmonic Generation at Interfaces*. Annual Review of Physical Chemistry, 40(1):327–350, oct 1989, ISSN 0066-426X. <https://doi.org/10.1146/annurev.pc.40.100189.001551>. Cited in page 94.

324 Cunha, Renan, Alisson Cadore, Sérgio L L M Ramos, Kenji Watanabe, Takashi Taniguchi, Sejeong Kim, Alexander S Solntsev, Igor Aharonovich, and Leandro M Malard: *Second harmonic generation in defective hexagonal boron nitride*. Journal of Physics: Condensed Matter, 32(19):19LT01, 2020, ISSN 0953-8984. <http://dx.doi.org/10.1088/1361-648X/ab6cbf>. Cited in page 94.

325 Wang, Ying, Jun Xiao, Sui Yang, Yuan Wang, and Xiang Zhang: *Second harmonic generation spectroscopy on two-dimensional materials [Invited]*. Optical Materials Express, 9(3):1136–1149, 2019. <http://www.osapublishing.org/ome/abstract.cfm?URI=ome-9-3-1136>. Cited in page 94.

326 Shree, Shivangi, Ioannis Paradisanos, Xavier Marie, Cedric Robert, and Bernhard Urbaszek: *Guide to optical spectroscopy of layered semiconductors*. Nature Reviews Physics, 3(1):39–54, 2021, ISSN 2522-5820. <https://doi.org/10.1038/s42254-020-00259-1>. Cited in page 96.

327 Hsu, Wei Ting, Zi Ang Zhao, Lain Jong Li, Chang Hsiao Chen, Ming Hui Chiu, Pi Shan Chang, Yi Chia Chou, and Wen Hao Chang: *Second Harmonic Generation from Artificially Stacked Transition Metal Dichalcogenide Twisted Bilayers*. ACS Nano, 8(3):2951–2958, mar 2014, ISSN 1936-0851. <https://doi.org/10.1021/nn500228r>. Cited 3 times in pages 12, 96 e 165.

328 Kim, Wontaek, Je Yhoung Ahn, Juseung Oh, Ji Hoon Shim, and Sunmin Ryu: *Second-Harmonic Young's Interference in Atom-Thin Heterocrystals*. Nano Letters, nov 2020, ISSN 1530-6984. <https://doi.org/10.1021/acs.nanolett.0c03763>. Cited 2 times in pages 96 e 166.

329 Yuan, Yuanjian, Peng Liu, Hongjian Wu, Haitao Chen, Weihao Zheng, Gang Peng, Zhihong Zhu, Mengjian Zhu, Jiayu Dai, Shiqiao Qin, and Kostya S Novoselov: *Probing the Twist-Controlled Interlayer Coupling in Artificially Stacked Transition Metal Dichalcogenide Bilayers by Second-Harmonic Generation*. ACS Nano, 17(18):17897–17907, sep 2023, ISSN 1936-0851. <https://doi.org/10.1021/acsnano.3c03795>. Cited in page 96.

330 Kim, Wontaek, Gyouil Jeong, Juseung Oh, Jihun Kim, Kenji Watanabe, Takashi Taniguchi, and Sunmin Ryu: *Exciton-Sensitized Second-Harmonic Generation in 2D Heterostructures*. ACS Nano, 17(20):20580–20588, oct 2023, ISSN 1936-0851. <https://doi.org/10.1021/acsnano.3c07428>. Cited in page 96.

331 Yin, Xiaobo, Ziliang Ye, Daniel A Chenet, Yu Ye, Kevin O'Brien, James C Hone, and Xiang Zhang: *Edge Nonlinear Optics on a MoS₂ Atomic Monolayer*. Science, 344(6183):488 LP – 490, may 2014. <http://science.sciencemag.org/content/344/6183/488.abstract>. Cited 5 times in pages 96, 133, 164, 165 e 166.

332 Cheng, Jingxin, Tao Jiang, Qingqing Ji, Yu Zhang, Zhiming Li, Yuwei Shan, Yanfeng Zhang, Xingao Gong, Weitao Liu, and Shiwei Wu: *Kinetic Nature of Grain Boundary Formation in As-Grown MoS2 Monolayers*. Advanced Materials, 27(27):4069–4074, jul 2015, ISSN 0935-9648. <https://doi.org/10.1002/adma.201501354>. Cited 2 times in pages 12 e 96.

333 Carvalho, Bruno R., Yuanxi Wang, Kazunori Fujisawa, Tianyi Zhang, Ethan Kahn, Ismail Bilgin, Pulickel M. Ajayan, Ana M. de Paula, Marcos A. Pimenta, Swastik Kar, Vincent H. Crespi, Mauricio Terrones, and Leandro M. Malard: *Nonlinear Dark-Field Imaging of One-Dimensional Defects in Monolayer Dichalcogenides*. Nano Letters, 20(1):284–291, 2020. <https://doi.org/10.1021/acs.nanolett.9b03795>, PMID: 31794217. Cited 3 times in pages 12, 96 e 165.

334 Mennel, Lukas, Matthias Paur, and Thomas Mueller: *Second harmonic generation in strained transition metal dichalcogenide monolayers: MoS2, MoSe2, WS2, and WSe2*. APL Photonics, 4(3):34404, dec 2018, ISSN 2378-0967. <https://doi.org/10.1063/1.5051965>. Cited 2 times in pages 12 e 96.

335 Vasconcelos, Thiago L, Bráulio S Archanjo, Bruno S Oliveira, Rogério Valaski, Rafael C Cordeiro, Helton G Medeiros, Cassiano Rabelo, Aroldo Ribeiro, Peter Ercius, Carlos A Achete, *et al.*: *Plasmon-Tunable Tip Pyramids: Monopole Nanoantennas for Near-Field Scanning Optical Microscopy*. Advanced Optical Materials, 6(20):1800528, 2018. Cited in page 99.

336 Duong, Dinh Loc, Seong Gon Kim, and Young Hee Lee: *Gate modulation of the long-range magnetic order in a vanadium-doped WSe2 semiconductor*. AIP Advances, 10(6):65220, jun 2020. <https://doi.org/10.1063/5.0010730>. Cited in page 108.

337 Sousa, Frederico B., Boyang Zheng, Mingzu Liu, Geovani C. Resende, Da Zhou, Marcos A. Pimenta, Mauricio Terrones, Vincent H. Crespi, and Leandro M. Malard: *Effects of Vanadium Doping on the Optical Response and Electronic Structure of WS_2 Monolayers*, 2024. Cited 5 times in pages 15, 16, 105, 113 e 115.

338 Zeng, Hualing, Gui Bin Liu, Junfeng Dai, Yajun Yan, Bairen Zhu, Ruicong He, Lu Xie, Shijie Xu, Xianhui Chen, Wang Yao, and Xiaodong Cui: *Optical signature of symmetry variations and spin-valley coupling in atomically thin tungsten dichalcogenides*. Scientific Reports, 3(1):1608, 2013, ISSN 2045-2322. <https://doi.org/10.1038/srep01608>. Cited 2 times in pages 106 e 147.

339 Li, Shisheng, Jinhua Hong, Bo Gao, Yung Chang Lin, Hong En Lim, Xueyi Lu, Jing Wu, Song Liu, Yoshitaka Tateyama, Yoshiki Sakuma, Kazuhito Tsukagoshi, Kazu Suenaga, and Takaaki Taniguchi: *Tunable Doping of Rhenium and Vanadium into Transition Metal Dichalcogenides for Two-Dimensional Electronics*. Advanced Science, 8(11):2004438, jun 2021, ISSN 2198-3844. <https://doi.org/10.1002/advs.202004438>. Cited in page 106.

340 Spindler, Conrad, Thomas Galvani, Ludger Wirtz, Germain Rey, and Susanne Siebentritt: *Excitation-intensity dependence of shallow and deep-level photoluminescence transitions in semiconductors*. Journal of Applied Physics, 126(17):175703, nov 2019, ISSN 0021-8979. <https://doi.org/10.1063/1.5095235>. Cited in page 106.

341 Fan, Peng, Biyuan Zheng, Xingxia Sun, Weihao Zheng, Zheyuan Xu, Cuihuan Ge, Yong Liu, Xiujuan Zhuang, Dong Li, Xiao Wang, Xiaoli Zhu, Ying Jiang, and Anlian Pan: *Trion-Induced Distinct Transient Behavior and Stokes Shift in WS2 Monolayers*. The Journal of Physical Chemistry Letters, 10(13):3763–3772, jul 2019. <https://doi.org/10.1021/acs.jpclett.9b01422>. Cited in page 108.

342 Lautenschlager, P, M Garriga, L Vina, and M Cardona: *Temperature dependence of the dielectric function and interband critical points in silicon*. Physical Review B, 36(9):4821–4830, sep 1987. <https://link.aps.org/doi/10.1103/PhysRevB.36.4821>. Cited in page 108.

343 Berkdemir, Ayse, Humberto R Gutiérrez, Andrés R Botello-Méndez, Néstor Perea-López, Ana Laura Elías, Chen Ing Chia, Bei Wang, Vincent H Crespi, Florentino López-Urías, Jean Christophe Charlier, Humberto Terrones, and Mauricio Terrones: *Identification of individual and few layers of WS2 using Raman Spectroscopy*. Scientific Reports, 3(1):1755, 2013, ISSN 2045-2322. <https://doi.org/10.1038/srep01755>. Cited in page 109.

344 Thripuranthaka, M, Ranjit V Kashid, Chandra Sekhar Rout, and Dattatray J Late: *Temperature dependent Raman spectroscopy of chemically derived few layer MoS2 and WS2 nanosheets*. Applied Physics Letters, 104(8):81911, feb 2014, ISSN 0003-6951. <https://doi.org/10.1063/1.4866782>. Cited in page 109.

345 Zhu, Bairen, Xi Chen, and Xiaodong Cui: *Exciton Binding Energy of Monolayer WS2*. Scientific Reports, 5(1):9218, 2015, ISSN 2045-2322. <https://doi.org/10.1038/srep09218>. Cited in page 110.

346 Sousa, Frederico B, Lucas Lafeta, Alisson R Cadore, Prasana K Sahoo, and Leandro M Malard: *Revealing atomically sharp interfaces of two-dimensional lateral heterostructures by second harmonic generation*. 2D Materials, 8(3):35051, 2021,

ISSN 2053-1583. <http://dx.doi.org/10.1088/2053-1583/ac0731>. Cited 2 times in pages 110 e 163.

347 Liu, Gui Bin, Wen Yu Shan, Yugui Yao, Wang Yao, and Di Xiao: *Three-Band Tight-Binding Model for Monolayers of Group-VIB Transition Metal Dichalcogenides.* Physical Review B, 88(8):085433, August 2013, ISSN 1098-0121, 1550-235X. Cited in page 112.

348 Crowley, Jason M., Jamil Tahir-Kheli, and William A. III Goddard: *Resolution of the Band Gap Prediction Problem for Materials Design.* The Journal of Physical Chemistry Letters, 7(7):1198–1203, April 2016. Cited in page 113.

349 Sousa, Frederico B., Alessandra Ames, Mingzu Liu, Pedro L. Gastelois, Vinícius A. Oliveira, Da Zhou, Matheus J. S. Matos, Helio Chacham, Mauricio Terrones, Marcio D. Teodoro, and Leandro M. Malard: *Strong magneto-optical responses of an ensemble of defect-bound excitons in aged WS_2 and WSe_2 monolayers*, 2024. Cited in page 121.

350 Tongay, Sefaattin, Joonki Suh, Can Ataca, Wen Fan, Alexander Luce, Jeong Seuk Kang, Jonathan Liu, Changhyun Ko, Rajamani Raghunathanan, Jian Zhou, Frank Ogletree, Jingbo Li, Jeffrey C Grossman, and Junqiao Wu: *Defects activated photoluminescence in two-dimensional semiconductors: interplay between bound, charged and free excitons.* Scientific Reports, 3(1):2657, 2013, ISSN 2045-2322. <https://doi.org/10.1038/srep02657>. Cited in page 122.

351 Gao, Jian, Baichang Li, Jiawei Tan, Phil Chow, Toh Ming Lu, and Nikhil Koratkar: *Aging of Transition Metal Dichalcogenide Monolayers.* ACS Nano, 10(2):2628–2635, feb 2016, ISSN 1936-0851. <https://doi.org/10.1021/acsnano.5b07677>. Cited in page 122.

352 He, Zhengyu, Xiaochen Wang, Wenshuo Xu, Yingqiu Zhou, Yuewen Sheng, Youmin Rong, Jason M Smith, and Jamie H Warner: *Revealing Defect-State Photoluminescence in Monolayer WS2 by Cryogenic Laser Processing.* ACS Nano, 10(6):5847–5855, jun 2016, ISSN 1936-0851. <https://doi.org/10.1021/acsnano.6b00714>. Cited in page 122.

353 Krustok, J, R Kaupmees, R Jaaniso, V Kiisk, I Sildos, B Li, and Y Gong: *Local strain-induced band gap fluctuations and exciton localization in aged WS2 monolayers.* AIP Advances, 7(6):65005, jun 2017, ISSN 2158-3226. <https://doi.org/10.1063/1.4985299>. Cited 2 times in pages 122 e 127.

354 Romanov, Roman I, Maxim G Kozodaev, Anna G Chernikova, Ivan V Zabrosaev, Anastasia A Chouprik, Sergey S Zarubin, Sergey M Novikov, Valentyn S Volkov, and Andrey M Markeev: *Thickness-Dependent Structural and Electrical Properties of WS2 Nanosheets Obtained via the ALD-Grown WO3 Sulfurization Technique as a Channel Material for Field-Effect Transistors.* ACS Omega, 6(50):34429–34437, dec 2021. <https://doi.org/10.1021/acsomega.1c04532>. Cited in page 122.

355 Jiang, Xiang, Qijing Zheng, Zhenggang Lan, Wissam A Saidi, Xinguo Ren, and Jin Zhao: *Real-time GW-BSE investigations on spin-valley exciton dynamics in monolayer transition metal dichalcogenide.* Science Advances, 7(10):eabf3759, mar 2021. <https://doi.org/10.1126/sciadv.abf3759>. Cited 3 times in pages 128, 161 e 162.

356 Robert, Cedric, Sangjun Park, Fabian Cadiz, Laurent Lombez, Lei Ren, Hans Tornatzky, Alistair Rowe, Daniel Paget, Fausto Sirotti, Min Yang, Dinh Van

Tuan, Takashi Taniguchi, Bernhard Urbaszek, Kenji Watanabe, Thierry Amand, Hanan Dery, and Xavier Marie: *Spin/valley pumping of resident electrons in WSe2 and WS2 monolayers*. Nature Communications, 12(1):5455, 2021, ISSN 2041-1723. <https://doi.org/10.1038/s41467-021-25747-5>. Cited in page 128.

357 Slobodeniuk, A O and D M Basko: *Spin–flip processes and radiative decay of dark intravalley excitons in transition metal dichalcogenide monolayers*. 2D Materials, 3(3):35009, 2016, ISSN 2053-1583. <https://dx.doi.org/10.1088/2053-1583/3/3/035009>. Cited in page 128.

358 Su, Weitao, Naresh Kumar, Sandro Mignuzzi, Jason Crain, and Debdulal Roy: *Nanoscale mapping of excitonic processes in single-layer MoS2 using tip-enhanced photoluminescence microscopy*. Nanoscale, 8(20):10564–10569, 2016, ISSN 2040-3364. <http://dx.doi.org/10.1039/C5NR07378B>. Cited in page 132.

359 Okuno, Yoshito, Ophélie Lancry, Agnès Tempez, Cristina Cairone, Matteo Bosi, Filippo Fabbri, and Marc Chaigneau: *Probing the nanoscale light emission properties of a CVD-grown MoS2 monolayer by tip-enhanced photoluminescence*. Nanoscale, 10(29):14055–14059, 2018, ISSN 2040-3364. <http://dx.doi.org/10.1039/C8NR02421A>. Cited in page 132.

360 Gadelha, Andreij C, Joyce C C Santos, Cassiano Rabelo, Thiago L Vasconcelos, Rafael S Alencar, Vitor Monken, Hudson L S Miranda, Luiz A Cury, Ygor M Jaques, Raphael M Tromer, Douglas S Galvão, Luiz G Cançado, Bernardo R A Neves, and Ado Jorio: *Locally-enhanced optical properties in a hybrid organic/inorganic (coronene/MoS2) Van der Waals heterostructure*. 2D Materials, 10(2):25015, 2023, ISSN 2053-1583. <https://dx.doi.org/10.1088/2053-1583/acbc8a>. Cited in page 132.

361 Lee, Yongjun, Seok Joon Yun, Youngbum Kim, Min Su Kim, Gang Hee Han, A K Sood, and Jeongyong Kim: *Near-field spectral mapping of individual exciton complexes of monolayer WS2 correlated with local defects and charge population*. Nanoscale, 9(6):2272–2278, 2017, ISSN 2040-3364. <http://dx.doi.org/10.1039/C6NR08813A>. Cited in page 132.

362 Buscema, Michele, Gary A Steele, Herre S J van der Zant, and Andres Castellanos-Gomez: *The effect of the substrate on the Raman and photoluminescence emission of single-layer MoS2*. Nano Research, 7(4):561–571, 2014, ISSN 1998-0000. <https://doi.org/10.1007/s12274-014-0424-0>. Cited in page 132.

363 Senkić, Ana, Josip Bajo, Antonio Supina, Borna Radatović, and Nataša Vujičić: *Effects of CVD growth parameters on global and local optical properties of MoS2 monolayers*. Materials Chemistry and Physics, 296:127185, 2023, ISSN 0254-0584. <https://www.sciencedirect.com/science/article/pii/S0254058422014912>. Cited in page 132.

364 Sousa, Frederico B., Rafael Battistella Nadas, Rafael Martins, Ana P. M. Barboza, Jaqueline S. Soares, Bernardo R. A. Neves, Ive Silvestre, Ado Jorio, and Leandro M. Malard: *Nano-optical investigation of grain boundaries, strain and edges in CVD grown MoS_2 monolayers*, 2024. Cited in page 132.

365 Ly, Thuc Hue, Ming Hui Chiu, Ming Yang Li, Jiong Zhao, David J Perello, Magdalena Ola Cichocka, Hye Min Oh, Sang Hoon Chae, Hye Yun Jeong, Fei Yao,

Lain Jong Li, and Young Hee Lee: *Observing Grain Boundaries in CVD-Grown Monolayer Transition Metal Dichalcogenides*. ACS Nano, 8(11):11401–11408, nov 2014, ISSN 1936-0851. <https://doi.org/10.1021/nn504470q>. Cited in page 133.

366 Mouri, Shinichiro, Yuhei Miyauchi, and Kazunari Matsuda: *Tunable Photoluminescence of Monolayer MoS2 via Chemical Doping*. Nano Letters, 13(12):5944–5948, dec 2013, ISSN 1530-6984. <https://doi.org/10.1021/nl403036h>. Cited in page 134.

367 Gadelha, Andreij C, Thiago L Vasconcelos, Luiz G Cançado, and Ado Jorio: *Nano-optical Imaging of In-Plane Homojunctions in Graphene and MoS2 van der Waals Heterostructures on Talc and SiO2*. The Journal of Physical Chemistry Letters, 12(31):7625–7631, aug 2021. <https://doi.org/10.1021/acs.jpclett.1c01804>. Cited 2 times in pages 134 e 159.

368 Nadas, Rafael Battistella, Andreij C Gadelha, Tiago C Barbosa, Cassiano Rabelo, Thiago de Lourenço e Vasconcelos, Vitor Monken, Ary V R Portes, Kenji Watanabe, Takashi Taniguchi, Jhonattan C Ramirez, Leonardo C Campos, Riichiro Saito, Luiz Gustavo Cançado, and Ado Jorio: *Spatially Coherent Tip-Enhanced Raman Spectroscopy Measurements of Electron–Phonon Interaction in a Graphene Device*. Nano Letters, 23(19):8827–8832, oct 2023, ISSN 1530-6984. <https://doi.org/10.1021/acs.nanolett.3c00851>. Cited in page 134.

369 Bao, Wei, Nicholas J Borys, Changhyun Ko, Joonki Suh, Wen Fan, Andrew Thron, Yingjie Zhang, Alexander Buyanin, Jie Zhang, Stefano Cabrini, Paul D Ashby, Alexander Weber-Bargioni, Sefaattin Tongay, Shaul Aloni, D Frank Ogletree, Junqiao Wu, Miquel B Salmeron, and P James Schuck: *Visualizing nanoscale excitonic relaxation properties of disordered edges and grain boundaries in monolayer molybdenum disulfide*. Nature Communications, 6(1):7993, 2015, ISSN 2041-1723. <https://doi.org/10.1038/ncomms8993>. Cited in page 134.

370 Liu, Lei, Jewook Park, David A Siegel, Kevin F McCarty, Kendal W Clark, Wan Deng, Leonardo Basile, Juan Carlos Idrobo, An Ping Li, and Gong Gu: *Heteroepitaxial Growth of Two-Dimensional Hexagonal Boron Nitride Templated by Graphene Edges*. Science, 343(6167):163 LP – 167, jan 2014. <http://science.sciencemag.org/content/343/6167/163.abstract>. Cited in page 136.

371 Castellanos-Gomez, Andres, Vibhor Singh, Herre S J van der Zant, and Gary A Steele: *Mechanics of freely-suspended ultrathin layered materials*. Annalen der Physik, 527(1-2):27–44, jan 2015, ISSN 0003-3804. <https://doi.org/10.1002/andp.201400153>. Cited in page 136.

372 Birmingham, Blake, Jiangtan Yuan, Matthias Filez, Donglong Fu, Jonathan Hu, Jun Lou, Marlan O Scully, Bert M Weckhuysen, and Zhenrong Zhang: *Spatially-Resolved Photoluminescence of Monolayer MoS2 under Controlled Environment for Ambient Optoelectronic Applications*. ACS Applied Nano Materials, 1(11):6226–6235, nov 2018. <https://doi.org/10.1021/acsanm.8b01422>. Cited 2 times in pages 139 e 140.

373 Kumar, Pawan, Dipanwita Chatterjee, Takuya Maeda, Ahin Roy, Kenji Kaneko, and Viswanath Balakrishnan: *Scalable faceted voids with luminescent enhanced edges in WS2 monolayers*. Nanoscale, 10(34):16321–16331, 2018, ISSN 2040-3364. <http://dx.doi.org/10.1039/C8NR02246A>. Cited in page 139.

374 Sousa, Frederico B, Raül Perea-Causin, Sean Hartmann, Lucas Lafetá, Bárbara Rosa, Samuel Brem, Chirag Palekar, Stephan Reitzenstein, Achim Hartschuh, Ermin Malic, and Leandro M Malard: *Ultrafast hot electron–hole plasma photoluminescence in two-dimensional semiconductors*. Nanoscale, pages –, 2023. <http://dx.doi.org/10.1039/D2NR06732C>. Cited 4 times in pages 23, 144, 151 e 161.

375 Klingshirn, Claus F.: *Semiconductor Optics*. Springer: Berlin, 2012, ISBN 978-3-540-38345-1. Cited 2 times in pages 145 e 148.

376 Jadczak, J, L Bryja, J Kutrowska-Girzycka, P Kapuściński, M Bieniek, Y. S. Huang, and P Hawrylak: *Room temperature multi-phonon upconversion photoluminescence in monolayer semiconductor WS2*. Nature Communications, 10(1):107, 2019, ISSN 2041-1723. <https://doi.org/10.1038/s41467-018-07994-1>. Cited in page 145.

377 Li, Yilei, Alexey Chernikov, Xian Zhang, Albert Rigosi, Heather M Hill, Arend M van der Zande, Daniel A Chenet, En Min Shih, James Hone, and Tony F Heinz: *Measurement of the optical dielectric function of monolayer transition-metal dichalcogenides: MoS_2, $MoSe_2$, WS_2, and WSe_2*. Physical Review B, 90(20):205422, nov 2014. Cited 3 times in pages 146, 165 e 169.

378 Erben, D, A Steinhoff, C Gies, G Schönhoff, T O Wehling, and F Jahnke: *Excitation-Induced Transition to Indirect Band Gaps in Atomically Thin Transition-Metal Dichalcogenide Semiconductors*. Physical Review B, 98(3):35434, jul 2018. <https://link.aps.org/doi/10.1103/PhysRevB.98.035434>. Cited in page 147.

379 Tonndorf, Philipp, Robert Schmidt, Philipp Böttger, Xiao Zhang, Janna Börner, Andreas Liebig, Manfred Albrecht, Christian Kloc, Ovidiu Gordan, Dietrich R T Zahn, Steffen Michaelis de Vasconcellos, and Rudolf Bratschitsch: *Photoluminescence emission and Raman response of monolayer MoS2, MoSe2, and WSe2*. Optics Express, 21(4):4908–4916, 2013. <http://www.opticsexpress.org/abstract.cfm?URI=oe-21-4-4908>. Cited in page 147.

380 Li, Yuanzheng, Xinshu Li, Tong Yu, Guochun Yang, Heyu Chen, Cen Zhang, Qiushi Feng, Jiangang Ma, Weizhen Liu, Haiyang Xu, Yichun Liu, and Xinfeng Liu: *Accurate Identification of Layer Number for Few-Layer WS_2 and WSe_2 via Spectroscopic Study*. Nanotechnology, 29(12):124001, 2018, ISSN 0957-4484. <http://dx.doi.org/10.1088/1361-6528/aaa923>. Cited in page 147.

381 Hoyer, W, C Ell, M Kira, S W Koch, S Chatterjee, S Mosor, G Khitrova, H M Gibbs, and H Stolz: *Many-Body Dynamics and Exciton Formation Studied by Time-Resolved Photoluminescence*. Physical Review B, 72(7):75324, aug 2005. <https://link.aps.org/doi/10.1103/PhysRevB.72.075324>. Cited in page 148.

382 Winzer, Torben, Richard Ciesielski, Matthias Handloser, Alberto Comin, Achim Hartschuh, and Ermin Malic: *Microscopic View on the Ultrafast Photoluminescence from Photoexcited Graphene*. Nano Letters, 15(2):1141–1145, feb 2015, ISSN 1530-6984. <https://doi.org/10.1021/nl504176z>. Cited in page 148.

383 Brem, Samuel, August Ekman, Dominik Christiansen, Florian Katsch, Malte Selig, Cedric Robert, Xavier Marie, Bernhard Urbaszek, Andreas Knorr, and Ermin Malic: *Phonon-Assisted Photoluminescence from Indirect Excitons in Monolayers of Transition-Metal Dichalcogenides*. Nano Letters, 20(4):2849–2856, apr 2020, ISSN 1530-6984. <https://doi.org/10.1021/acs.nanolett.0c00633>. Cited in page 148.

384 Rosati, Roberto, Koloman Wagner, Samuel Brem, Raül Perea-Causín, Edith Wietek, Jonas Zipfel, Jonas D Ziegler, Malte Selig, Takashi Taniguchi, Kenji Watanabe, Andreas Knorr, Alexey Chernikov, and Ermin Malic: *Temporal Evolution of Low-Temperature Phonon Sidebands in Transition Metal Dichalcogenides.* ACS Photonics, 7(10):2756–2764, oct 2020. <https://doi.org/10.1021/acsphotonics.0c00866>. Cited in page 148.

385 Erkensten, Daniel, Samuel Brem, Koloman Wagner, Roland Gillen, Raül Perea-Causín, Jonas D Ziegler, Takashi Taniguchi, Kenji Watanabe, Janina Maultzsch, Alexey Chernikov, and Ermin Malic: *Dark Exciton-Exciton Annihilation in Monolayer* WSe_2. Physical Review B, 104(24):L241406, dec 2021. <https://link.aps.org/doi/10.1103/PhysRevB.104.L241406>. Cited in page 148.

386 Koch, S W, M Kira, G Khitrova, and H M Gibbs: *Semiconductor Excitons in New Light.* Nature Materials, 5(7):523–531, 2006, ISSN 1476-4660. <https://doi.org/10.1038/nmat1658>. Cited in page 148.

387 Katsch, Florian, Malte Selig, and Andreas Knorr: *Exciton-Scattering-Induced Dephasing in Two-Dimensional Semiconductors.* Physical Review Letters, 124(25):257402, jun 2020. <https://link.aps.org/doi/10.1103/PhysRevLett.124.257402>. Cited in page 148.

388 Erkensten, Daniel, Samuel Brem, and Ermin Malic: *Exciton-Exciton Interaction in Transition Metal Dichalcogenide Monolayers and Van Der Waals Heterostructures.* Physical Review B, 103(4):45426, jan 2021. <https://link.aps.org/doi/10.1103/PhysRevB.103.045426>. Cited in page 148.

389 Lui, Chun Hung, Kin Fai Mak, Jie Shan, and Tony F Heinz: *Ultrafast Photoluminescence from Graphene.* Physical Review Letters, 105(12):127404, sep 2010. <https://link.aps.org/doi/10.1103/PhysRevLett.105.127404>. Cited 2 times in pages 151 e 152.

390 Liu, Wei Tao, S W Wu, P J Schuck, M Salmeron, Y R Shen, and F Wang: *Nonlinear Broadband Photoluminescence of Graphene Induced by Femtosecond Laser Irradiation.* Physical Review B, 82(8):81408, aug 2010. <https://link.aps.org/doi/10.1103/PhysRevB.82.081408>. Cited 2 times in pages 151 e 153.

391 Stöhr, Rainer J, Roman Kolesov, Jens Pflaum, and Jörg Wrachtrup: *Fluorescence of Laser-Created Electron-Hole Plasma in Graphene.* Physical Review B, 82(12):121408, sep 2010. <https://link.aps.org/doi/10.1103/PhysRevB.82.121408>. Cited in page 151.

392 Hwang, E H, Ben Yu Kuang Hu, and S Das Sarma: *Inelastic Carrier Lifetime in Graphene.* Physical Review B, 76(11):115434, sep 2007. <https://link.aps.org/doi/10.1103/PhysRevB.76.115434>. Cited in page 152.

393 Jeong, Tae Young, Byung Moon Jin, Sonny H Rhim, Lamjed Debbichi, Jaesung Park, Yu Dong Jang, Hyang Rok Lee, Dong Hun Chae, Donghan Lee, Yong Hoon Kim, Suyong Jung, and Ki Ju Yee: *Coherent Lattice Vibrations in Mono- and Few-Layer WSe2.* ACS Nano, 10(5):5560–5566, may 2016, ISSN 1936-0851. <https://doi.org/10.1021/acsnano.6b02253>. Cited in page 153.

394 Choi, Junho, Jacob Embley, Daria D Blach, Raül Perea-Causín, Daniel Erkensten, Dong Seob Kim, Long Yuan, Woo Young Yoon, Takashi Taniguchi, Kenji Watanabe,

Keiji Ueno, Emanuel Tutuc, Samuel Brem, Ermin Malic, Xiaoqin Li, and Libai Huang: *Fermi Pressure and Coulomb Repulsion Driven Rapid Hot Plasma Expansion in a van der Waals Heterostructure*. Nano Letters, 23(10):4399–4405, may 2023, ISSN 1530-6984. <https://doi.org/10.1021/acs.nanolett.3c00678>. Cited in page 155.

395 Hanbicki, Aubrey T, Hsun Jen Chuang, Matthew R Rosenberger, C Stephen Hellberg, Saujan V Sivaram, Kathleen M McCreary, Igor I Mazin, and Berend T Jonker: *Double Indirect Interlayer Exciton in a MoSe2/WSe2 van der Waals Heterostructure*. ACS Nano, 12(5):4719–4726, may 2018, ISSN 1936-0851. <https://doi.org/10.1021/acsnano.8b01369>. Cited 2 times in pages 161 e 162.

396 Xue, Wenjin, Prasana K Sahoo, Jiru Liu, Haonan Zong, Xiaoyi Lai, Sharad Ambardar, and Dmitri V Voronine: *Nano-optical imaging of monolayer MoSe2-WSe2 lateral heterostructure with subwavelength domains*. Journal of Vacuum Science & Technology A, 36(5):05G502, jul 2018, ISSN 0734-2101. <https://doi.org/10.1116/1.5035437>. Cited in page 163.

397 Berweger, Samuel, Hanyu Zhang, Prasana K Sahoo, Benjamin M Kupp, Jeffrey L Blackburn, Elisa M Miller, Thomas M Wallis, Dmitri V Voronine, Pavel Kabos, and Sanjini U Nanayakkara: *Spatially Resolved Persistent Photoconductivity in MoS2–WS2 Lateral Heterostructures*. ACS Nano, 14(10):14080–14090, oct 2020, ISSN 1936-0851. <https://doi.org/10.1021/acsnano.0c06745>. Cited in page 163.

Appendix

A Supplementary Information for Chapter 6

A.1 Supplementary Information for section 6.1

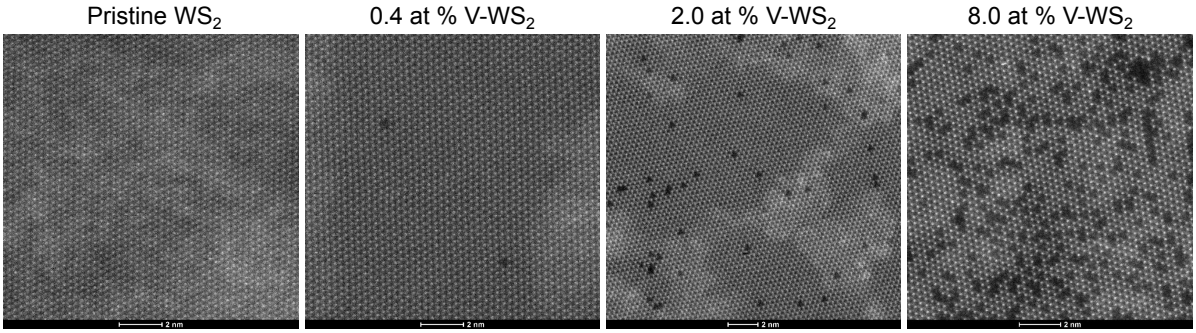

Figure A.1 – **a-d** HAADF-STEM images for pristine WS_2 (**a**) and 0.4 at% (**b**), 2 at% (**c**), and 8 at% (**d**) vanadium doped WS_2 monolayers. Scale bars: 2 nm.

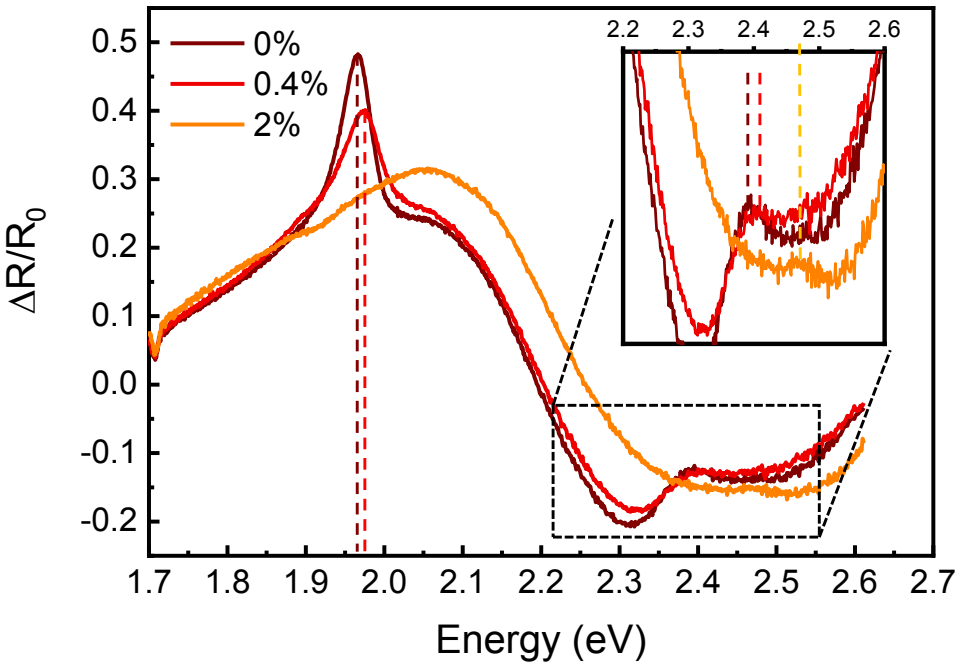

Figure A.2 – Differential reflectance measurement of a pristine (brown), 0.4 at% (red), and 2 at%, (orange) V-doped WS_2 monolayers. The absorption responses in the A and B excitons spectral regions are shown. A blueshift for both A and B exction peaks under increasing vanadium concentration can be noted.

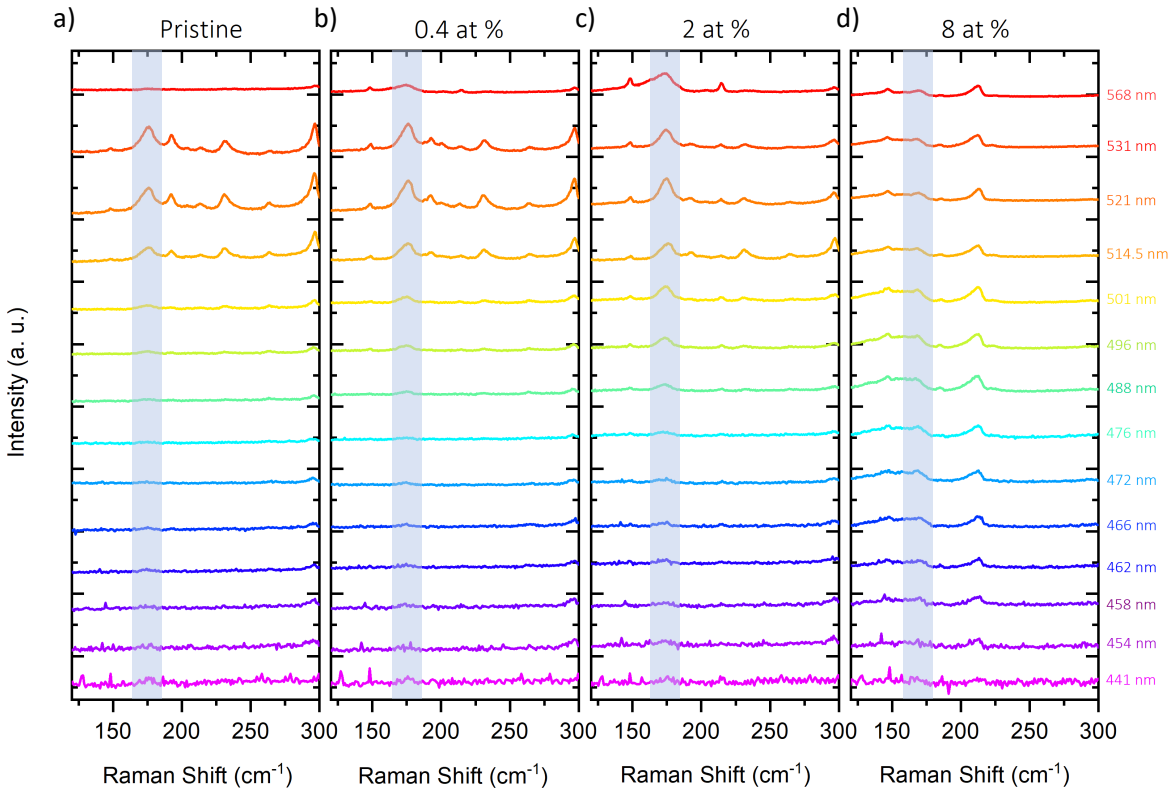

Figure A.3 – **a-d** Lower frequency Raman spectra for pristine WS_2 (**a**) and 0.4 at% (**b**), 2 at% (**c**), and 8 at% (**d**) vanadium doped WS_2 monolayers under 14 different excitation energies. The excitation wavelengths are on the right side of each spectrum of the 8 at% V-doped WS_2 monolayer (**d**). All spectra were normalized by the silicon peak intensity considering its Raman cross-section for each laser line. The LA(M) mode is highlighted.

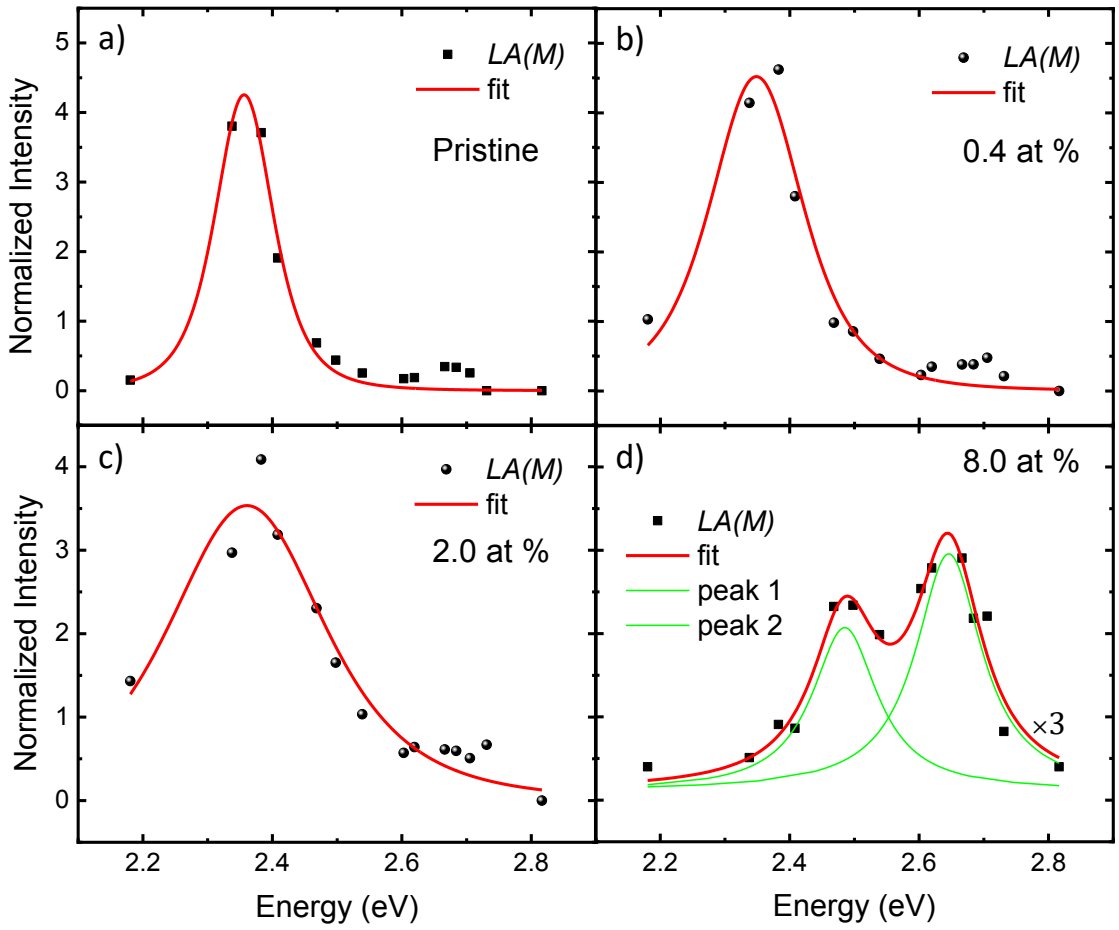

Figure A.4 – **a-d** Raman excitation profiles of the *LA* Raman mode - highlighted in gray in Figure A.3 – for the (**a**) pristine, (**b**) 0.4 at%, (**c**) 2 at%, and (**d**) 8 at% V-doped WS_2 monolayers. The Raman excitation profiles were fitted by the Raman Fermi golden rule equation presented in Chapter 6.

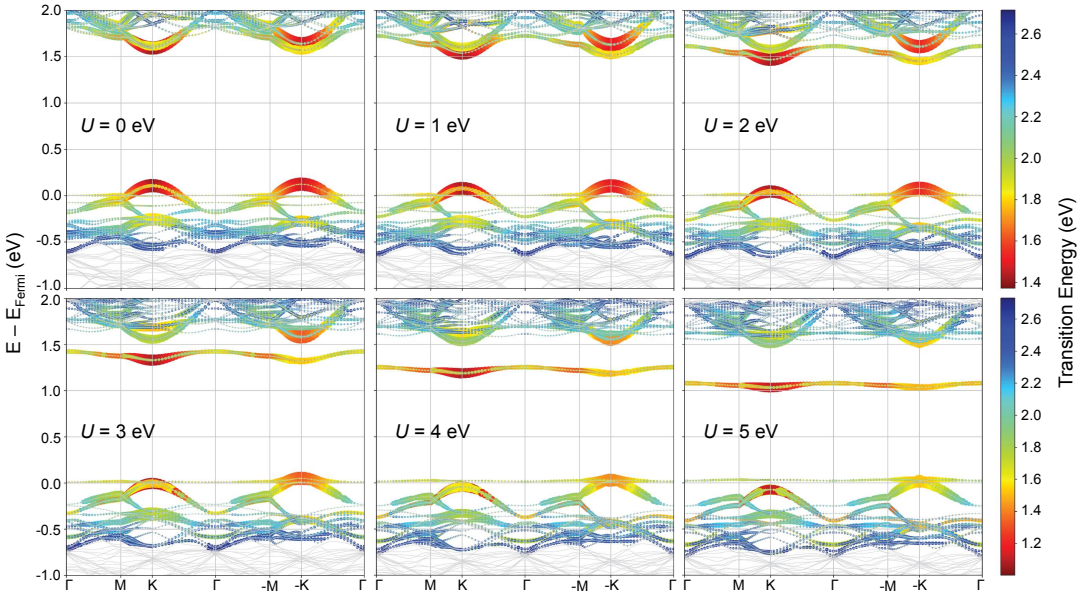

Figure A.5 – Band structure of V-doped WS_2 for distinct Hubbard U values. Colored circles represent the energies (color) and the magnitude of the transition dipole moments (size) of selected bands around band edges. A pair of identical circles is assigned to the initial and final states for each transition.

A.2 Supplementary Information for section 6.2

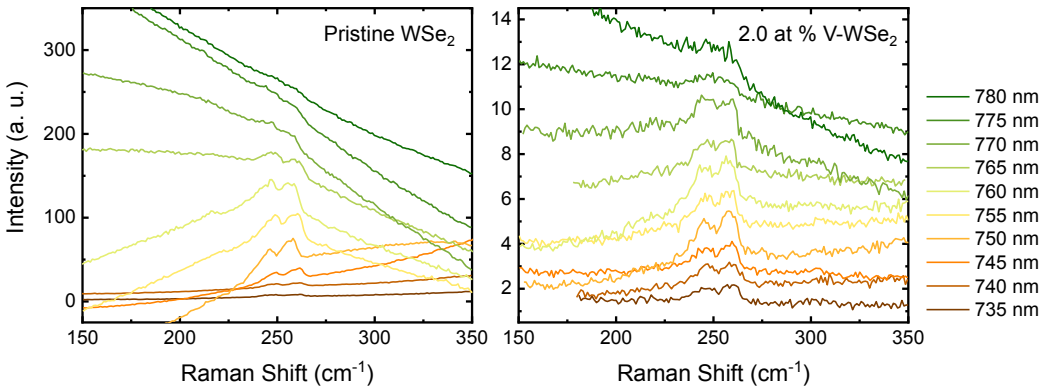

Figure A.6 – Raman spectra for pristine and 4 at% vanadium doped WSe_2 monolayers under 10 different excitation wavelengths in the near infrared range.

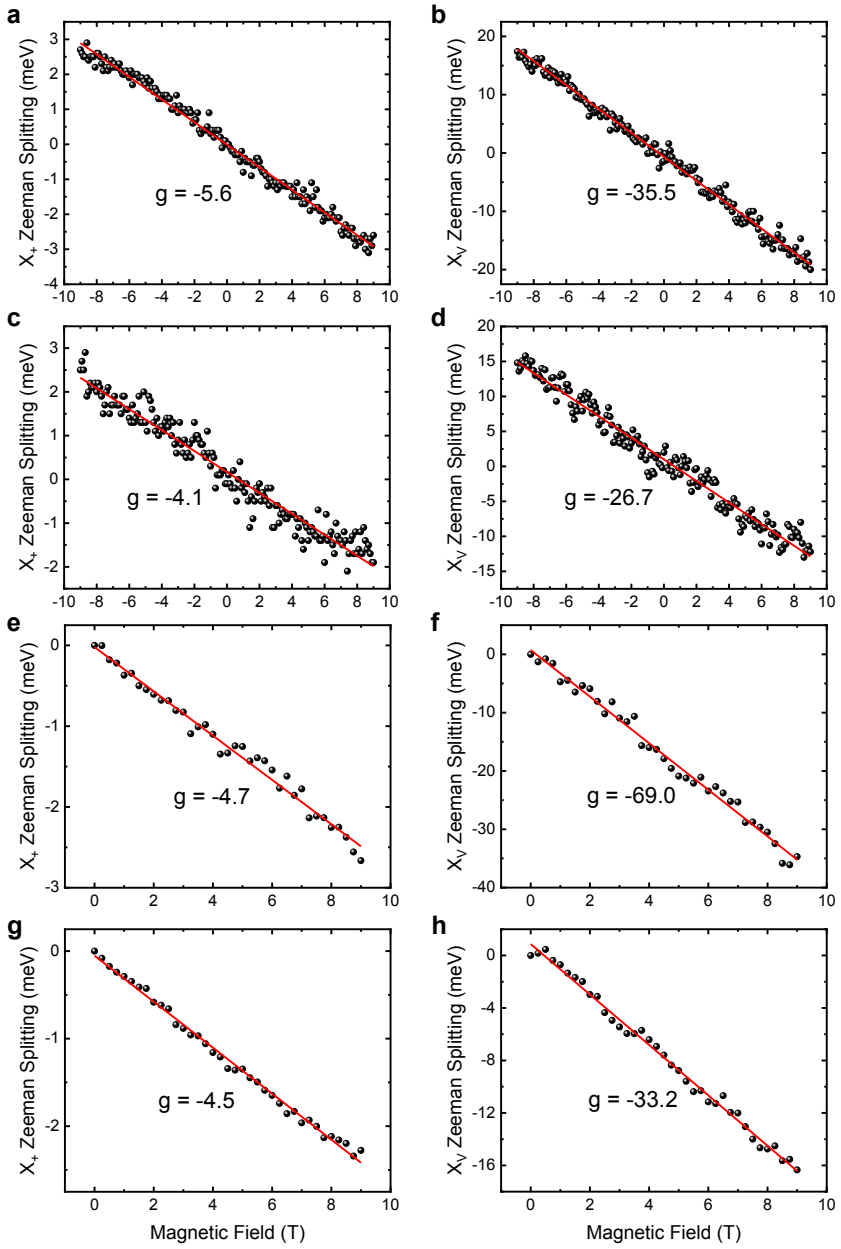

Figure A.7 – Zeeman splittings related to trion (X_+) and defect-bound exciton (X_V) transitions for a 4 at% vanadium doped WSe_2 monolayer. These measurements were performed in different flakes and at distinct regions of these flakes. The respective g-factors confirm the giant Zeeman splitting associated with the defective PL peak.

A.3 Supplementary Information for section 6.3

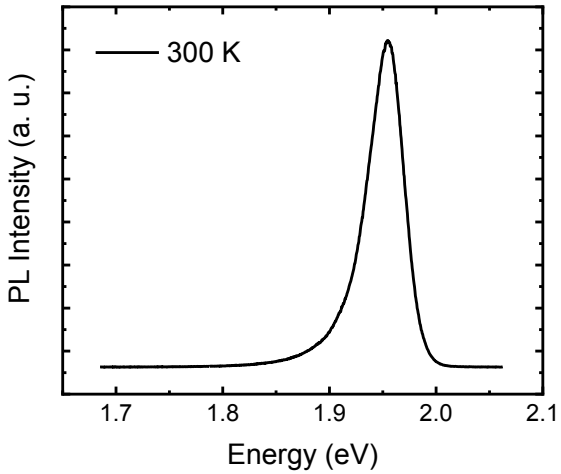

Figure A.8 – Room temperature PL spectra of the aged WS_2 monolayer showing no defect-bound exciton peak.

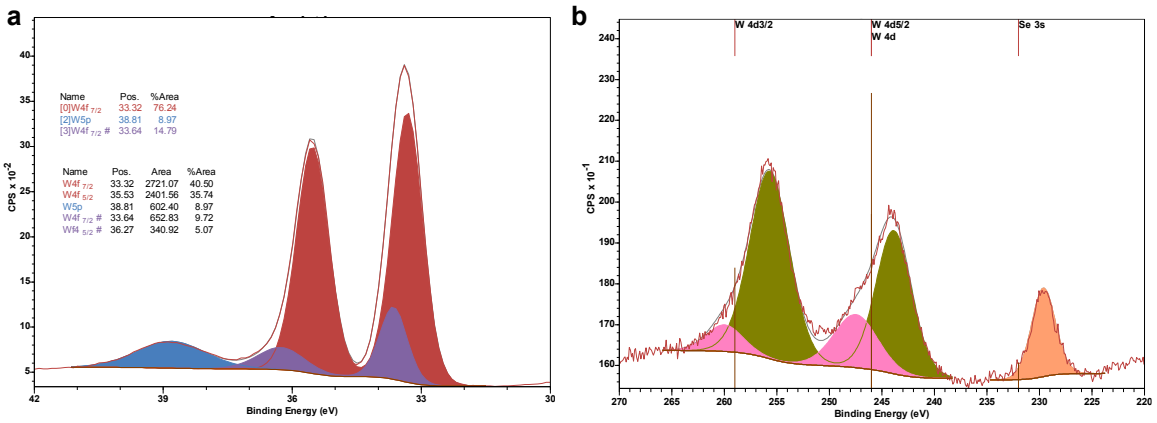

Figure A.9 – **a** XPS spectrum of W 4f and W 5p core-level peaks for an aged WS_2 monolayer. The W 4f displays two W $4f_7/2$ and W $4f_5/2$ doublets associated to W of the main WS_2 structure (red fitted peaks) and to W at defect sites (blue fitted peaks). **b** XPS spectrum of W 4d and Se 2s core-level peaks for an aged WSe_2 monolayer. The W 4d display two W $4d_5/2$ and W $4d_3/2$ doublets associated to W of the main WSe_2 structure (green fitted peaks) and to W at defect sites (pink fitted peaks).

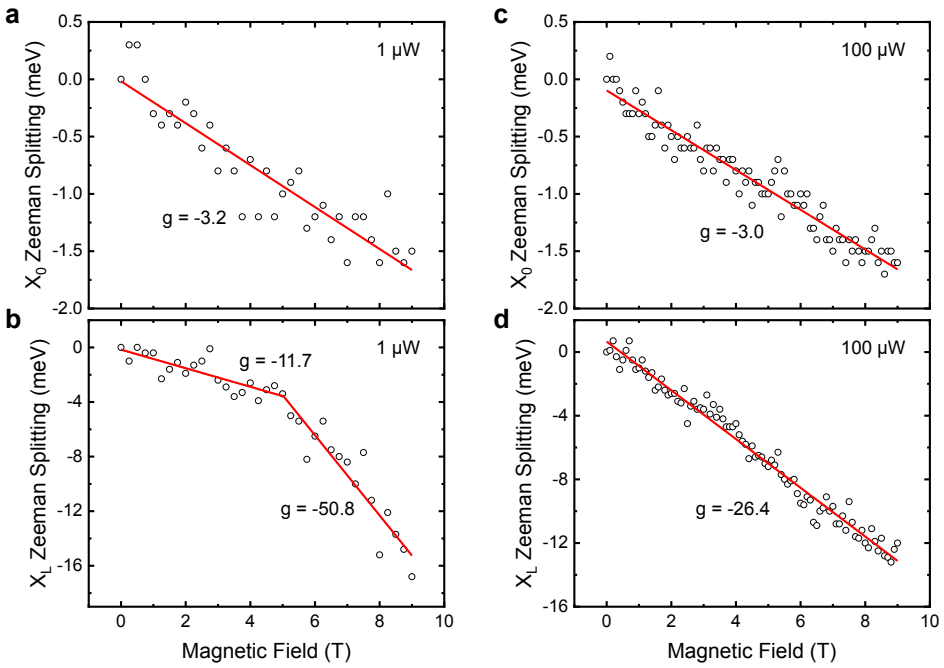

Figure A.10 – **a** Zeeman splittings related to exciton (X_0) and defect-bound exciton (X_L) transitions for an aged WS_2 monolayer measured with an incident power of 1 μW. For this lower pumping power there are two splittings regimes related to the defective PL peak: a weaker one up to 5 T and a stronger one from 5 T. **a** Zeeman splittings related to exciton (X_0) and defect-bound exciton (X_L) transitions for an aged WS_2 monolayer measured with an incident power of 100 μW. These measurements were performed in a different flake from that presented in Figure 6.14, confirming the great g-factor associated with the defective PL peak.

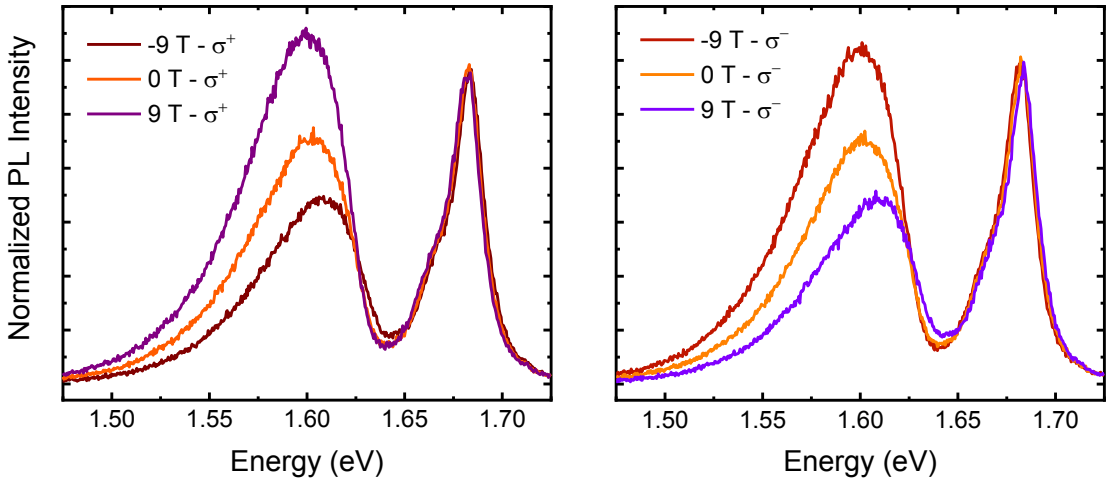

Figure A.11 – **a,b** PL spectra of an aged WS_2 monolayer for a linearly polarized excitation and σ^+ (**a**) and σ^- (**b**) detections with external magnetic fields of -9, 0 and 9 T. The spectra are normalized by the free exciton peak intensity.

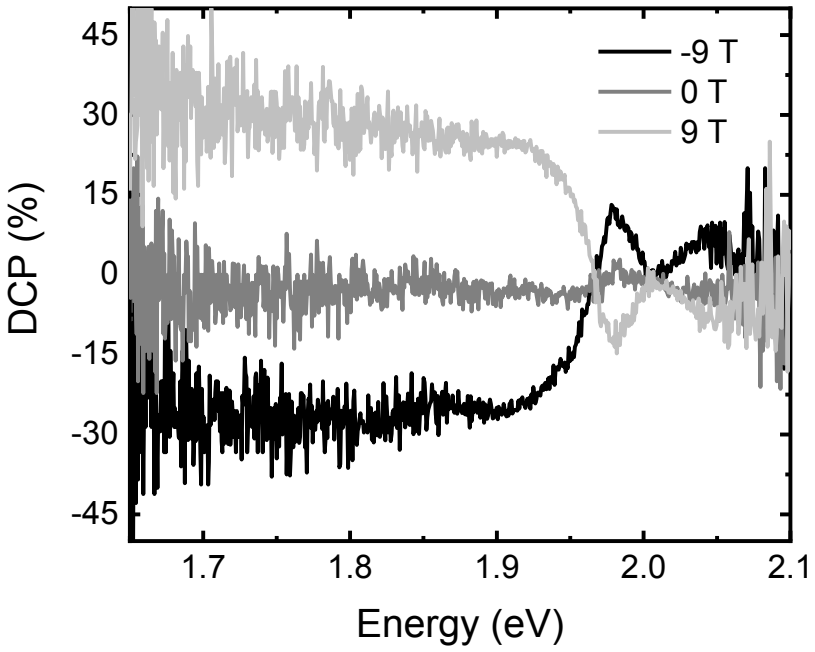

Figure A.12 – Degree of circular polarization of an aged WS_2 monolayer for -9, 0 and 9 T between the σ^+ and σ^- PL spectra shown in Figures 6.14a,b.

B Supplementary Information for Chapter 7

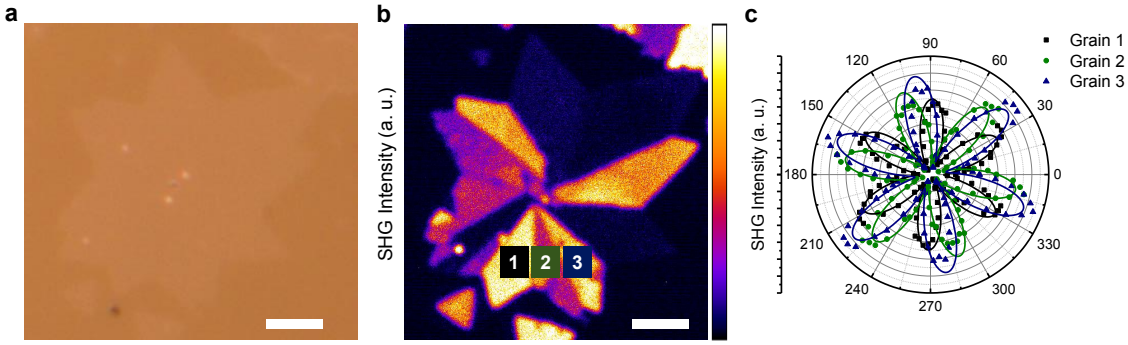

Figure B.1 – **a** Optical image of MoS_2 monolayer sample A1 shown in Figure 7.1. **b** SHG intensity image of MoS_2 monolayer sample A1 with the 3 studied grains highlighted. Scale bars: 5 μm. **c** Polarized SHG measurement for grains 1, 2 and 3 of MoS_2 monolayer sample A1. The relative orientations between them are: $\theta_{1,2} = 21°$, $\theta_{1,3} = 11°$ and $\theta_{2,3} = 10°$.

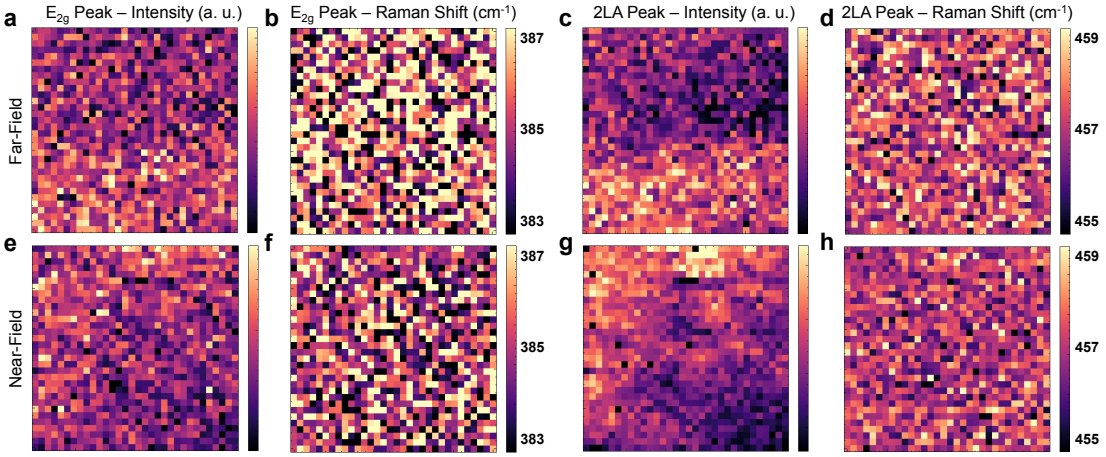

Figure B.2 – **a-d** Far-field E_{2g} intensity (**a**), E_{2g} frequency (**b**), 2LA intensity (**c**), and 2LA frequency (**d**) maps of MoS_2 monolayer sample A2. **e-h** Near-field E_{2g} intensity (**e**), E_{2g} frequency (**f**), 2LA intensity (**g**), and 2LA frequency (**h**) maps of MoS_2 monolayer sample A2. These maps are from the same region of the exciton maps of Figure 7.3.

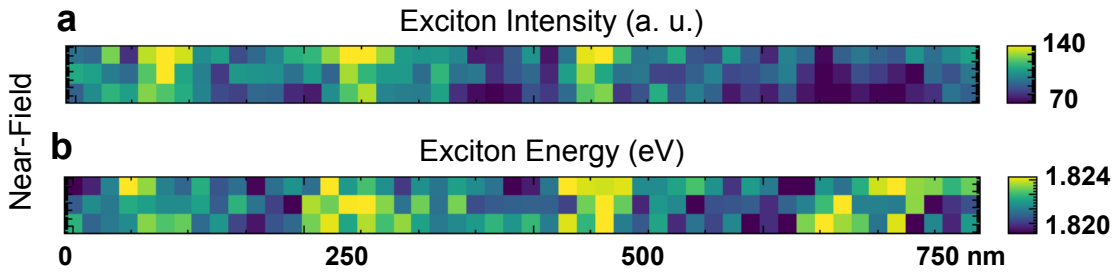

Figure B.3 – **a,b** Near-field exciton intensity (**a**) and exciton energy (**b**) maps of MoS_2 monolayer sample A2 showing localized strain fields in a different sample region.

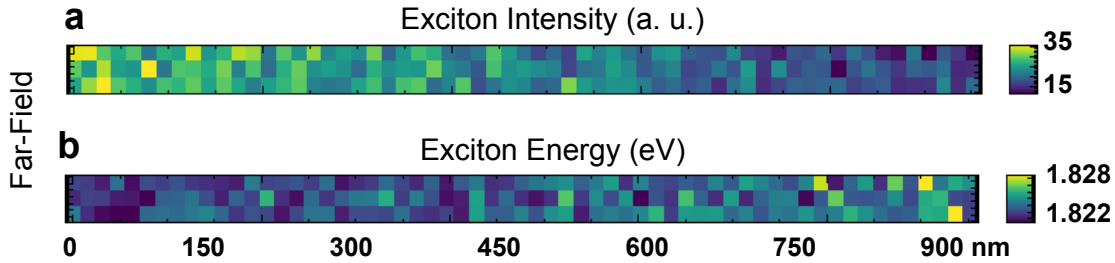

Figure B.4 – **a,b** Far-field exciton intensity (**a**) and exciton energy (**b**) maps at the edge of MoS_2 monolayer sample A2 showing no localized optical features. These maps are from the same region of the maps of Figure 7.5.

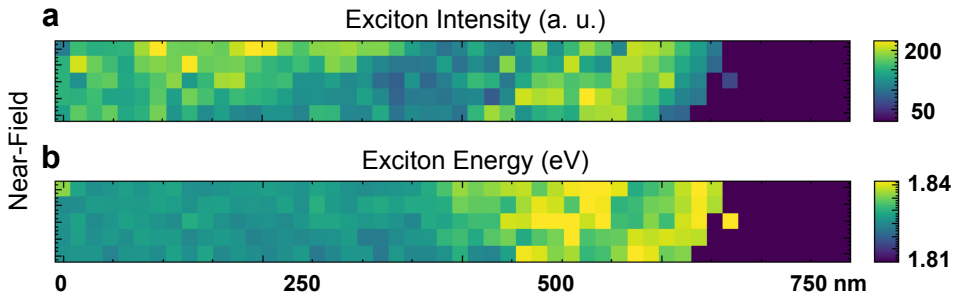

Figure B.5 – **a,b** Near-field exciton intensity (**a**) and exciton energy (**b**) maps in another edge region of MoS_2 monolayer sample A2 showing similar PL enhancement and blueshift features presented at the edge region of Figure 7.5.

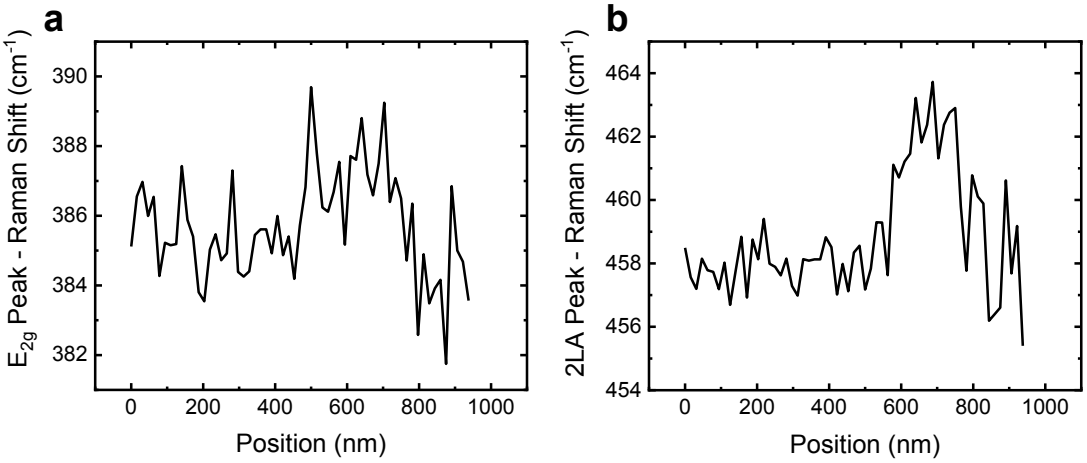

Figure B.6 – **a,b** E_{2g} (**a**) and 2LA (**b**) frequency profiles along the edge of MoS_2 monolayer sample A2.

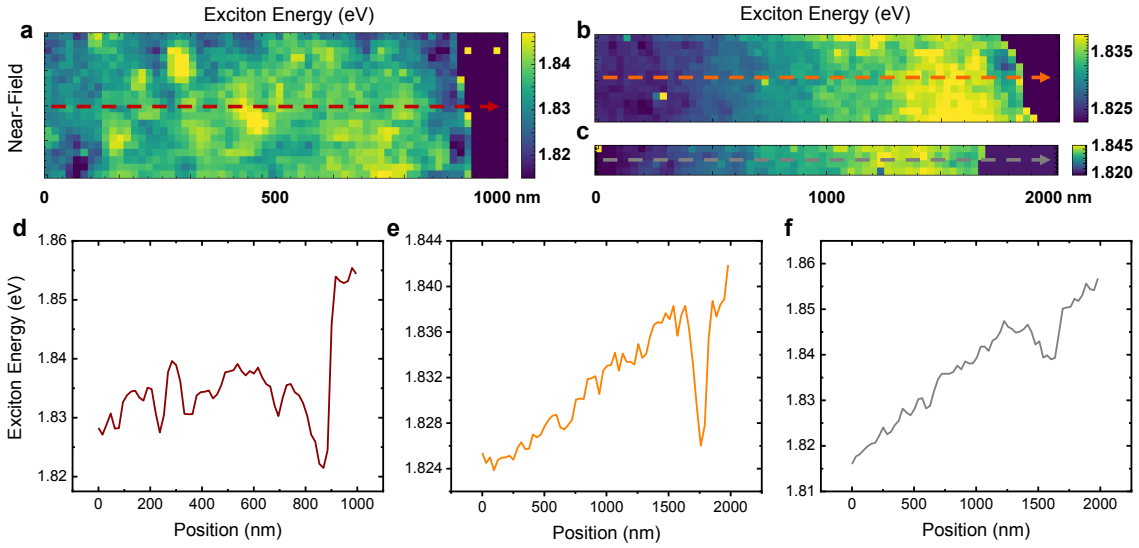

Figure B.7 – **a-c** Near-field exciton energy maps in other edge regions of MoS_2 monolayer sample A1 showing a similar PL redshift response presented at the edge region of Figure 7.6. **d-f** Exciton energy profiles along the edges of (**a-c**) highlighting the PL redshift feature. The profiles colors correspond to the dashed arrow colors of (**a-c**).

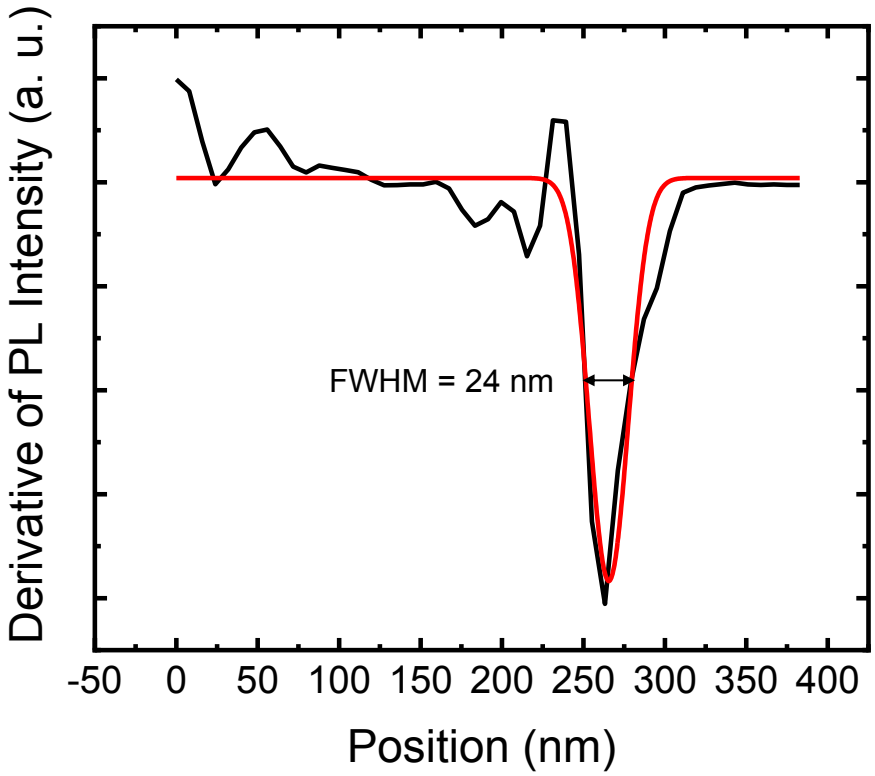

Figure B.8 – To extract the spatial resolution of the near-field measurements we differentiated the PL intensity profile along the edge (in black) of Figure 7.6 and fitted it with a Gaussian function (in red). The spatial resolution of the measurement is the fitted full width at half maximum (FWHM) = 24 nm.

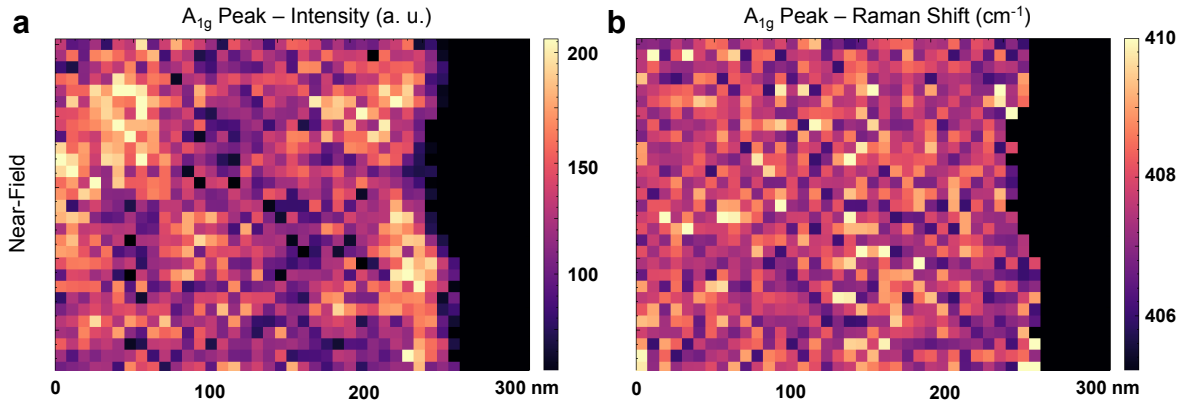

Figure B.9 – **a,b** Near-field A_{1g} intensity (**a**) and frequency (**b**) maps at the edge of MoS_2 monolayer sample A1. These maps are from the same region of E_{2g} and 2LA maps of Figure 7.7.

C Supplementary Information for Chapter 8

C.1 Supplementary Information for section 8.1

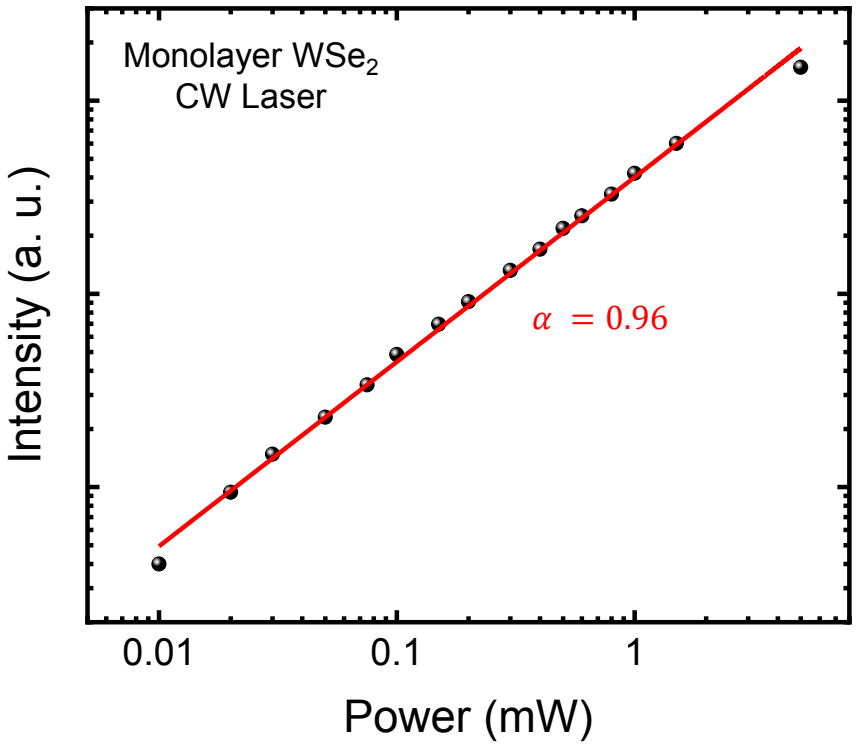

Figure C.1 – Power dependence of the photoluminescence (PL) intensity of a monolayer WSe_2 under CW excitation. The 0.96 coefficient shows the linear dependence with the incident power. The axes are in a logarithm scale.

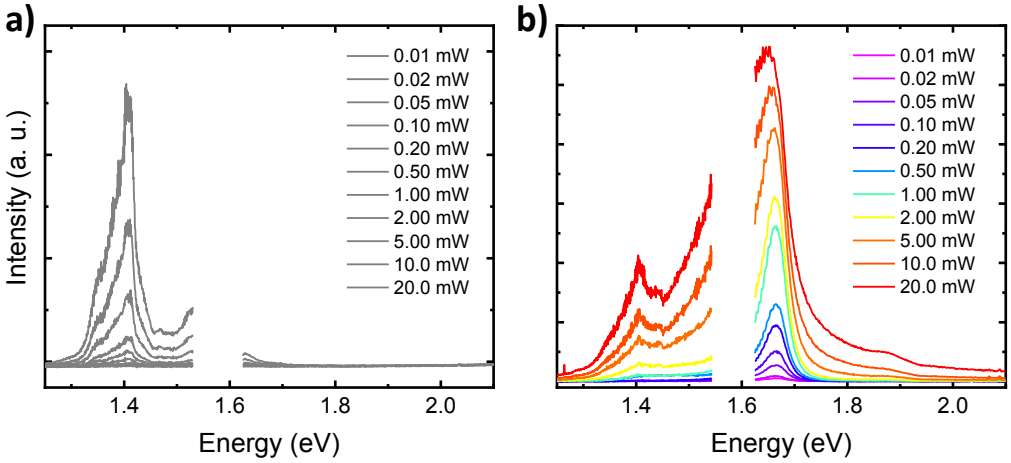

Figure C.2 – **a** Light emission from the quartz substrate under a pulsed excitation for distinct incident powers. **b** Raw PL spectra for the monolayer WSe_2. The substrate peak around 1.4 eV can be noted for all spectra. In order to extract this substrate contribution, for each pump power we subtracted the quartz spectra from the samples spectra. The same was done for the multilayer WSe_2 samples.

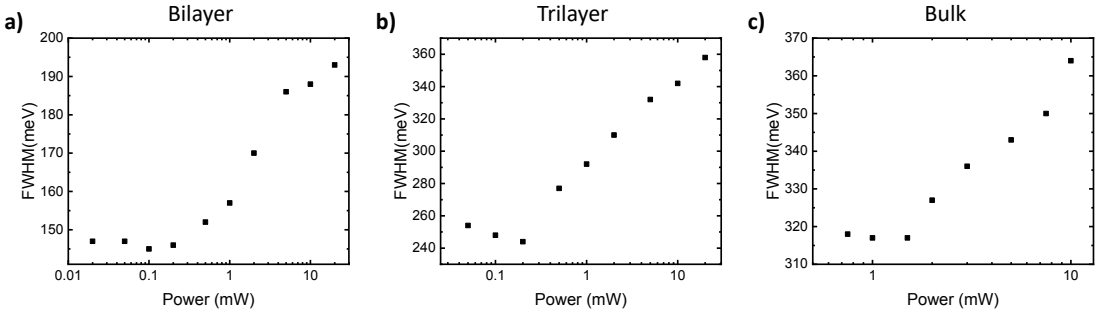

Figure C.3 – **a-c** Power dependence of the PL FWHM in a bilayer (**a**), trilayer (**b**) and bulk (**c**) WSe_2 samples. For all samples there is a critical pump power value in which the FWHM starts to increase revealing the exciton Mott transition to an EHP phase.

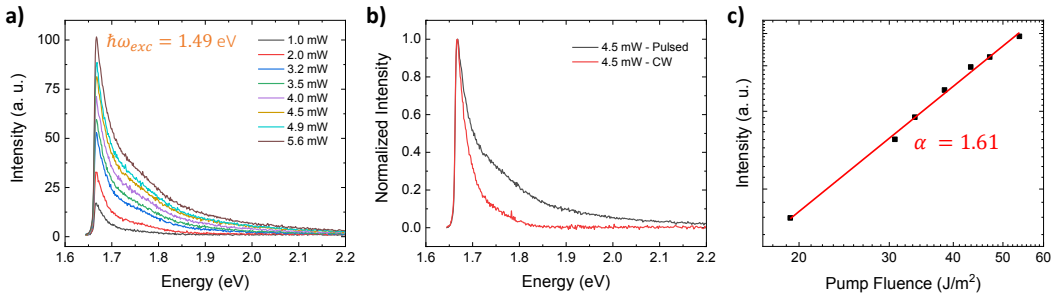

Figure C.4 – **a** PL spectra above the band gap of a monolayer $MoSe_2$ for distinct incident powers and a pulsed excitation energy of 1.49 eV. **b** Comparison of monolayer $MoSe_2$ PL spectra with pulsed and CW excitation to show the broadening of the PL spectra when the material is excited to an EHP phase. **c** Pump fluence dependence of the PL intensity revealing the nonlinearity of the effect. The axes in (**c**) are displayed in a logarithm scale.

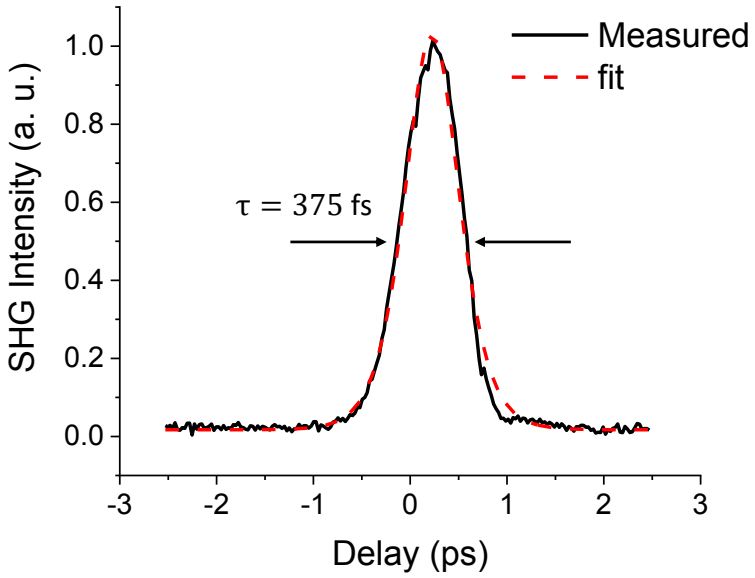

Figure C.5 – To extract the instrument response function (IRF) — that is mainly driven by the laser pulse width — we performed a second-harmonic generation (SHG) autocorrelation measurement in a $MoSe_2$ monolayer with the same optical setup of the two-pulse excitation correlation measurement. The SHG signal was directed to the spectrometer and its intensity as a function of the temporal pulse separation is shown in the graph above. The autocorrelation data was fitted by a $sech^2(t/\tau)$ function (red dashed line) and yielded a laser pulse width value of $\tau = 375$ fs. In order to deconvolute the temporal response of the EHP PL signal from the laser pulse width response, we fitted our two-pulse excitation correlation data with the convolution of the intensity model function (Equation 8.5) with the $sech^2(t/\tau)$ function (IRF). This IRF deconvolution improved our temporal resolution to 100 fs.

C.2 Supplementary Information for section 8.2

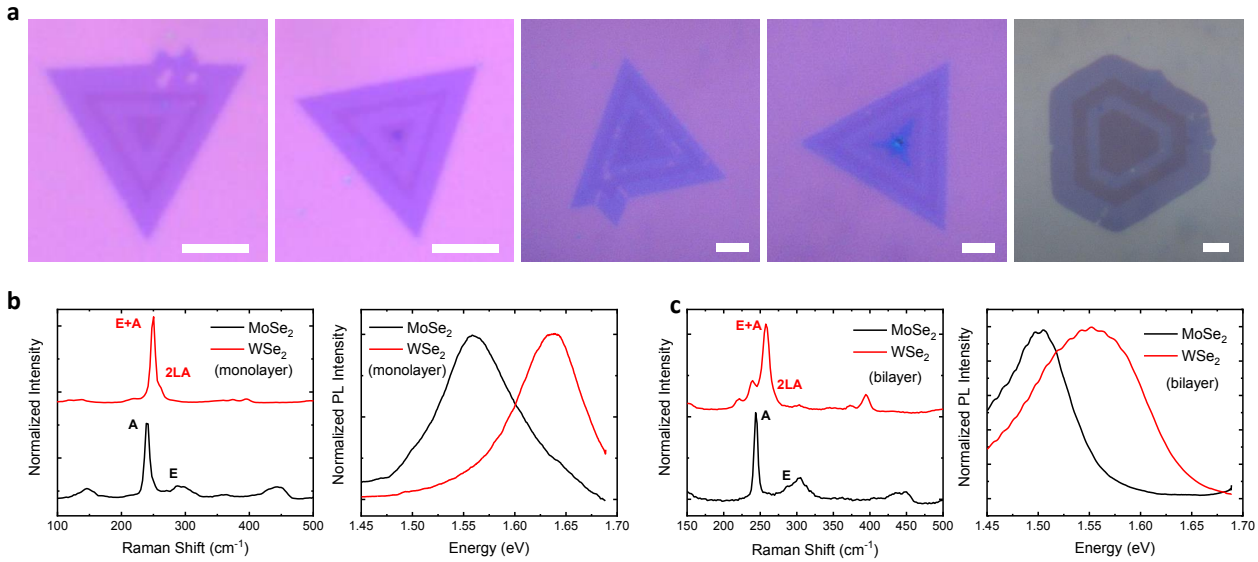

Figure C.6 – **a** Optical images of distinct monolayer and a bilayer (last one) $MoSe_2/WSe_2$ lateral heterostructures studied in this work. The alternation of $MoSe_2$ and WSe_2 domains from the center to the edge can be observed, in which $MoSe_2$ regions are darker with respect to WSe_2 regions. Scale bars: 5 μm. **b** Raman spectra of monolayer $MoSe_2$ (in black) and WSe_2 (in red) regions. The $MoSe_2$ Raman spectrum presents A_{1g} and E^1_{2g} modes at 241 and 281 cm^{-1}, respectively, while the WSe_2 displays its degenerated A_{1g} and E^1_{2g} modes at 249 cm^{-1} and 2LA mode at 257 cm^{-1}. **c** Normalized PL spectra of monolayer $MoSe_2$ (in black) and WSe_2 (in red) regions. Their single PL peaks are located at 1.56 and 1.64 eV for $MoSe_2$ and WSe_2, respectively. **d** Raman spectra of $MoSe_2$ (in black) and WSe_2 (in red) regions. The $MoSe_2$ Raman spectrum presents A_{1g} and E^1_{2g} modes at 243 and 285 cm^{-1}, respectively, while the WSe_2 displays its degenerated A_{1g} and E^1_{2g} modes at 255 cm^{-1} and 2LA mode at 263 cm^{-1}. **e** Normalized PL spectra of $MoSe_2$ (in black) and WSe_2 (in red) regions. Their indirect transition PL peaks are located at 1.50 and 1.55 eV for $MoSe_2$ and WSe_2, respectively.

C.3 Supplementary Information for section 8.3

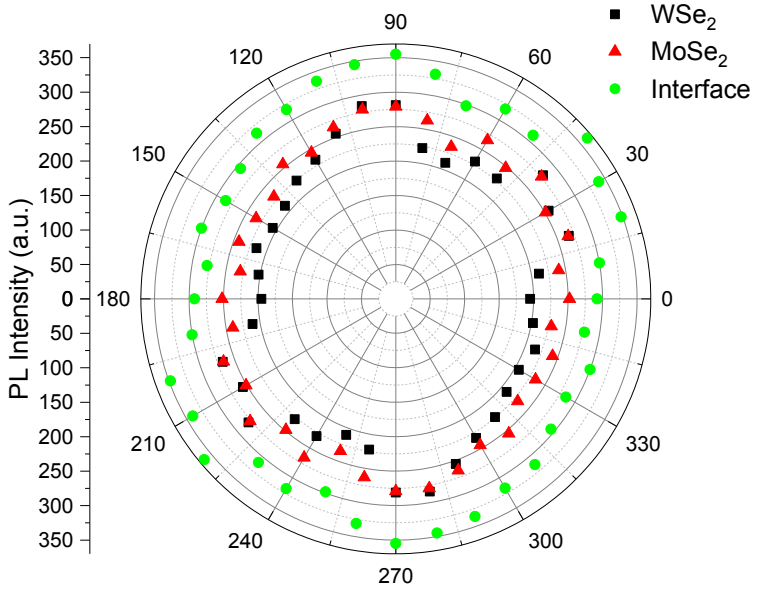

Figure C.7 – Polarization-resolved EHP PL measurement of the monolayer $MoSe_2/WSe_2$ lateral heterostructure. The graph displays polarized plots of both domains and from their interface for a 804 nm excitation laser wavelength and 50 mW pumping power. No polarization dependence was observed for the EHP PL emission.

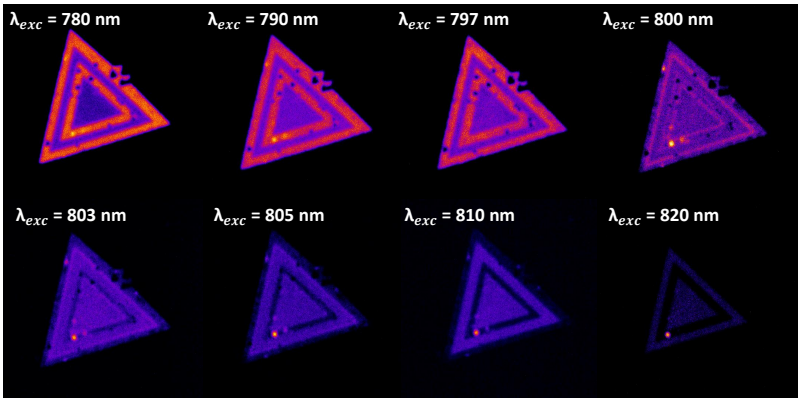

Figure C.8 – EHP PL imaging of a monolayer $MoSe_2/WSe_2$ lateral heterostructure for several excitation wavelengths, a 50 mW pumping power and collecting the PL signal with a 620/60 nm band pass filter in front of the PMT. This monolayer sample is the same presented in Figure 8.7. However, here the excitation wavelength in which the enhanced emission at the heterojunction is maximum is 800 nm due to the distinct incident power.

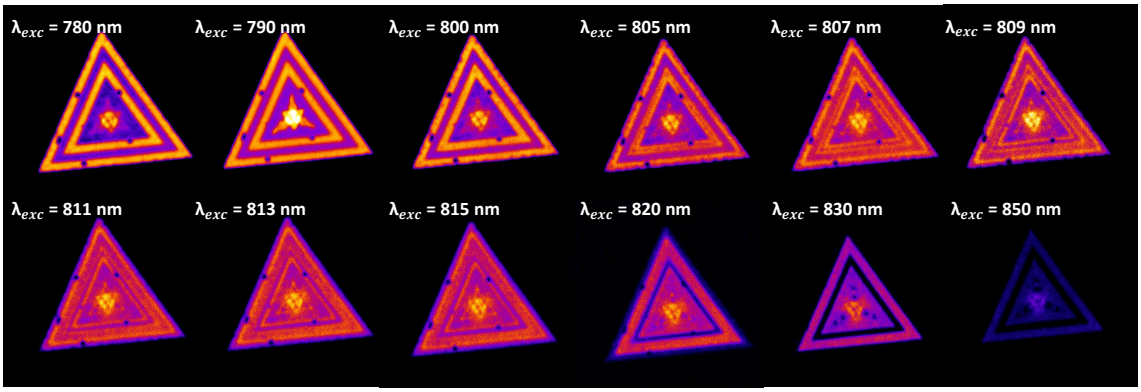

Figure C.9 – EHP PL imaging of a monolayer $MoSe_2/WSe_2$ lateral heterostructure for several excitation wavelengths, a 50 mW pumping power and collecting the PL signal with 690 nm short pass and 560 nm long pass filters in front of the PMT. This monolayer sample is not the same presented in Figure 8.7. Although the pumping power used to probe it was the same used in the mappings of Figure S5, here the excitation wavelength in which the enhanced emission at the heterojunction is maximum is 809 nm due to the distinct wavelength range of detection.

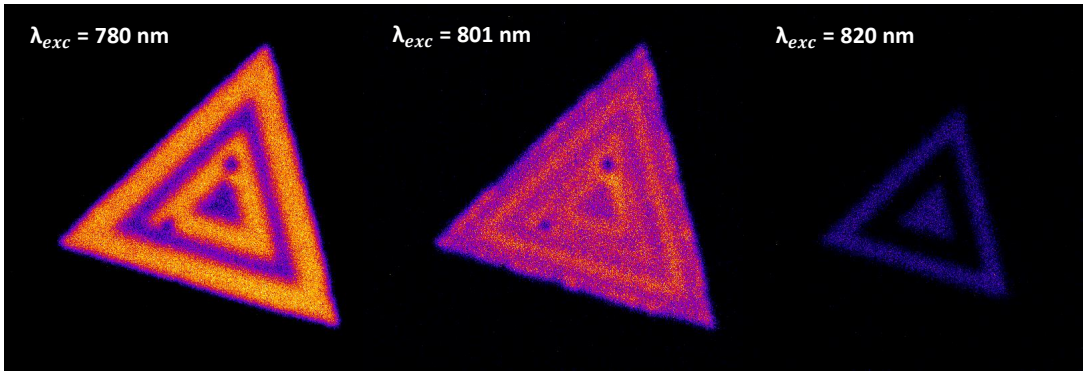

Figure C.10 – EHP PL imaging of a monolayer $MoSe_2/WSe_2$ lateral heterostructure for different excitation wavelengths, a 50 mW pumping power and collecting the PL signal with a 620/60 nm band pass filter in front of the PMT. This monolayer sample is not the same presented in Figure 8.7. For these scanning measurements, the excitation wavelength in which the enhanced emission at the heterojunction is maximum is 801 nm.

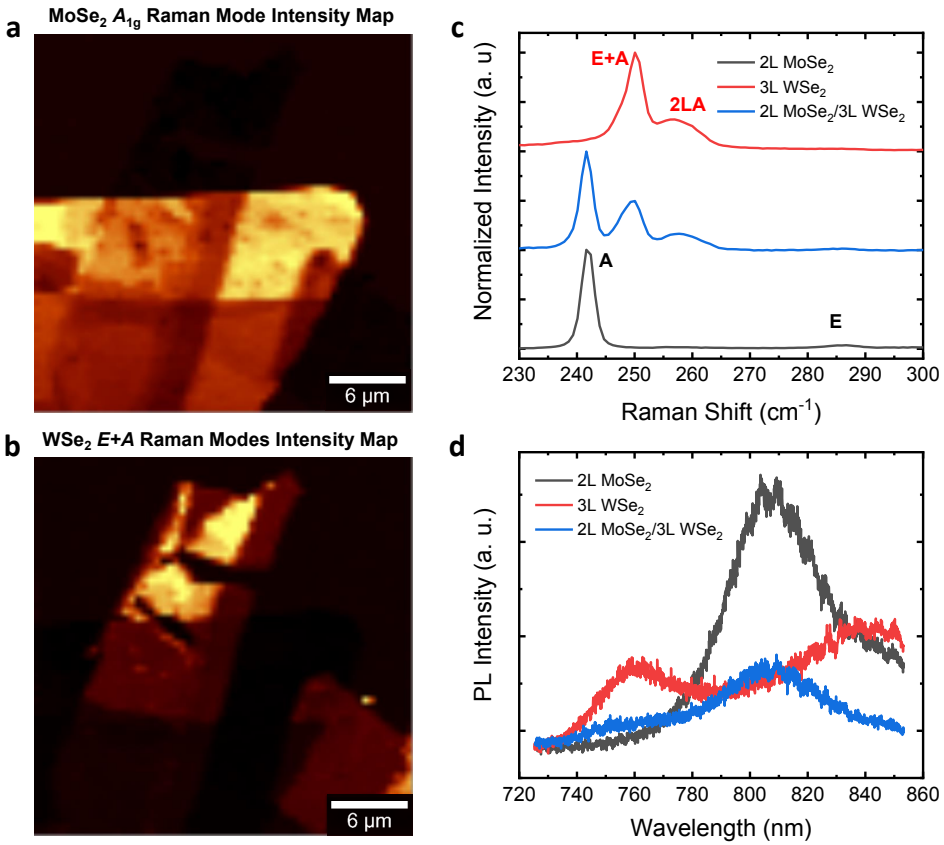

Figure C.11 – **a,b** Intensity maps of 2L $MoSe_2$ A_{1g} Raman mode (**a**) and 3L WSe_2 E^1_{2g}+A_{1g} Raman modes (**b**), highlighting their regions. The Raman intensity maps were extracted from a hyperspectral Raman measurement. **c** Raman spectra of bilayer $MoSe_2$ (in black), trilayer WSe_2 (in red) and heterostructure (in blue) regions. The bilayer $MoSe_2$ Raman spectrum presents A_{1g} and E^1_{2g} modes at 242 and 285 cm^{-1}, respectively, while the trilayer WSe_2 displays its degenerated A_{1g} and E^1_{2g} modes at 250 cm^{-1} and 2LA mode at 257 cm^{-1}. Besides, the heterostructure region shows the sum of both bilayer $MoSe_2$ and trilayer WSe_2 Raman spectra. **d** PL spectra of bilayer $MoSe_2$ (in black), trilayer WSe_2 (in red) and heterostructure (in blue) regions. Bilayer $MoSe_2$ and trilayer WSe_2 PL spectra display two peaks related to their indirect and direct transitions, while the heterostructure PL spectrum is composed by the sum of the PL spectra of both TMDs. Moreover, a quenching in the PL intensity at the heterostructure with respect to bilayer $MoSe_2$ and trilayer WSe_2 PL intensities can be observed.

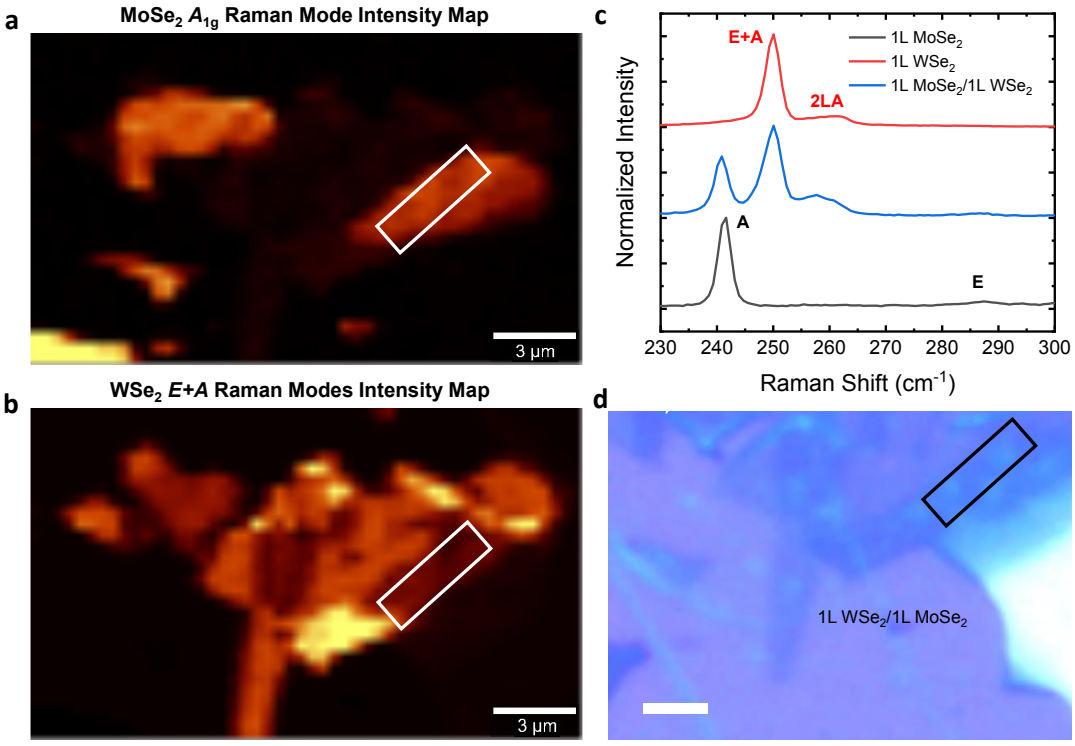

Figure C.12 – **a,b** Intensity maps of 1L $MoSe_2$ A_{1g} Raman mode (**a**) and 1L WSe_2 E^1_{2g}+A_{1g} Raman modes (**b**), highlighting their regions. The Raman intensity maps were extracted from the hyperspectral Raman measurement and the vertical heterostructure region is underlined in white. **c** Raman spectra of monolayer $MoSe_2$ (in black), monolayer WSe_2 (in red) and heterostructure (in blue) regions. The monolayer $MoSe_2$ Raman spectrum presents A_{1g} and E^1_{2g} modes at 241 and 282 cm^{-1}, respectively, while the WSe_2 displays its degenerated A_{1g} and E^1_{2g} modes at 250 cm^{-1} and 2LA mode at 256 cm^{-1}. Besides, the heterostructure region shows the sum of both $MoSe_2$ and WSe_2 Raman spectra. **d** Optical image of the sample with the monolayer vertical heterostructure highlighted in black. Scale bar: 2 μm.

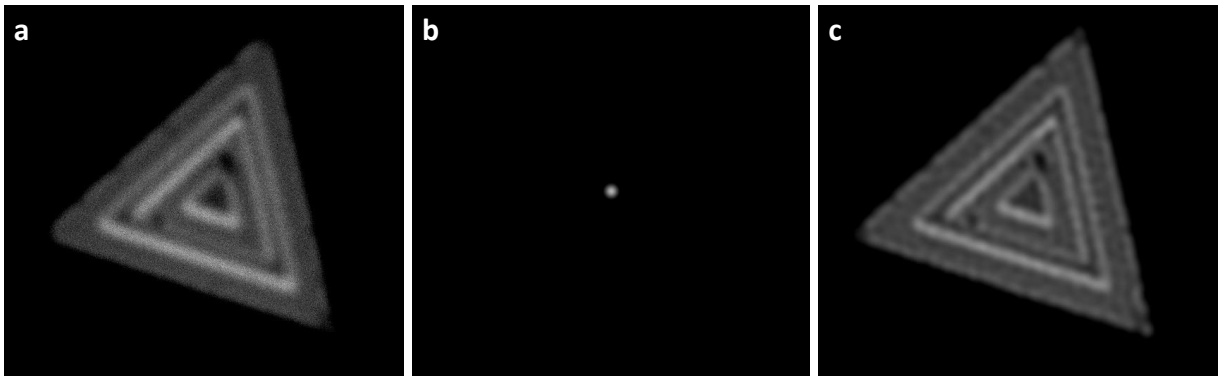

Figure C.13 – In order to increase the spatial resolution of our measurements we deconvoluted the SH images with a 2D Gaussian profile function as our deconvolution input image. For this 2D Gaussian profile we set its full width at half maximum (FWHM) as the spatial resolution of the system, set by the laser spot width. Figures (**a-c**) illustrates this deconvolution procedure, where (**a**) is the raw SH image, (**b**) is the 2D Gaussian profile function of our system, and (**c**) is the deconvoluted image. It is noticeable that the spatial resolution, mainly from the interfaces, was indeed improved by comparing the raw and deconvoluted images. Whereas we have a spatial resolution of 500 nm in the raw image, after the deconvolution this value decrease to 270 nm. This deconvolution was made for all SH images of selenide TMD 1L-LHs and sulfide TMD 2L-LHs for the wavelength dependence measurements.